Design, synthesis and applications of multi-functional MRI contrast agents for bio-imaging

Thesis submitted for the degree of

Doctor of Philosophy

at the University of Leicester

by

Adil Hussein Ali

Department of Chemistry

University of Leicester

2018

Abstract

Multimodal imaging agents have the potential to be detected in both MRI and optical imaging experiments allowing for visualisation of biological systems from the cellular level up to the whole body. This thesis reports a series of second generation MRI contrast agents with monometallic and heteronuclear Ln-DO3A based complexes for different bio-imaging techniques.

Herein, a series of novel dual-mode optical / MR imaging agents have been synthesised using Ir(III) and Pt(II) as emissive metals. Mono-gadolinium **Ir(ppy)$_2$GdL1** with q = 2 exhibits r_1 = 7.5 mM^{-1} s^{-1} and two photon excitation at 850 nm gives rise to emission in the range 500-600 nm suggesting that it may be suitable for investigating *in vitro* CA co-localisation. The slow tumbling and presence of multinuclear Gd(III) units in **IrGdL6L1** gives a ~3 fold increase in relaxivity *cf.* mono-gadolinium **GdL1**. The photophysical properties of the Ir(III) core complex are tuned to optimise the imaging probe by modifying the (N^C) cyclometallated or the (N^N') ancillary ligand. The water soluble dual-mode **PtGdL10** with q = 1 gives r_1 = 4.0 mM^{-1} s^{-1} and displays interesting emission characteristics in both its monomer and excimer forms.

A number of europium-based carbonate sensors have been prepared, exploiting the inner-sphere water molecule displacement by bidentate carbonate anions. Incorporating a carbonate independent luminescent Re(I) core enables a ratiometric determination of carbonate ions *in vitro*. **RepyEuL1** exhibits log K = 2.33 for $NaHCO_3$, with a clear change in photoluminesence colour from green to yellow on binding carbonate. The Re(I) emission was tuned by OMe and CF_3 substitution around the pyridine of regular pyridine-2-yl-1H-1,2,3-triazol-1-yl (pyta) or using the inverse triazole-4-yl ligand (tapy) for the complexation.

High molecular weight CAs **FeGdL1** and **CoGdL1** have been synthesised. These multinuclear complexes show a three-fold enhancement in relaxivity *cf.* mono **GdL1** parent complex at 400 MHz, 9.4 T.

Finally, a new CA (**GdL8**) based on Gd-DO3A with a *N*-methylsulfonamide pendant arm was produced, which has a changeable hydration number, allowing pH to be reported in the range 6 to 8 reversibly. **GdL8** exhibits a blood brain barrier permeability with pH response in *in vivo* cerebral stroke studies.

Dedication

Dedicated to my mother and father.

Acknowledgments

Firstly, I would like to express my sincere gratitude to my fabulous supervisors, Dr Mark Lowe and Prof. Paul Cullis for the opportunity they have given me, and in doing so their support and certainly their patience with my foolish mistakes, particularly in the first few months. In particular, Dr Lowe without your guidance, ideas, motivation and your smile I would never have reached this point. I could not have imagined having a better advisor and mentor for my studies.

Secondly, a massive thank you goes out to Mick Lee for keeping things running smoothly in the lab and the fine tuning involved in getting me such fine mass spectra. Huge thanks also to Dr Gerry Griffith for his invaluable knowledge of NMR spectroscopy and his help in running T_1 experiments. As well big thanks to Dr Vincenzo Marra and Dr Michael Kelly.

Naturally, this section would not be complete without a shout-out to the rest of the 2.14 Lab Ph.D students (Vicki, Sarab, Lucy, Yana, Nada and Adhit).

I'd also like to thank the people I've worked with over the past few years – there's too many to mention, but you know who you are. Thanks for creating a great working atmosphere in the lab and for all the support you offered, it got me through the last four years.

I gratefully acknowledge the funding received towards my PhD from the HCEDiraq and MODiraq. Thank you for your generous sponsorship over the last five years.

Last but not the least, I would like to thank my family: my parents and my brothers and sister for supporting me spiritually throughout the writing of this thesis and my life in general.

AHA.

Table of Contents

Abbreviations

°C	Degrees Celsius
a.u.	Arbitrary Units
Abs	Absorbance
AcOH	Acetic Acid
B.M.	Bohr Magnetons
b.p.	Boiling point
bpy	2,2-Bipyridyl
cf.	Confer (compare)
CN	Coordination Number
CuAAC	Copper(I)-catalysed Azide-Alkyne Cycloaddition
CuOAc	Copper(I)Acetate
d	Doublet (NMR)
DCM	Dichloromethane
DELFIA®	Dissociation Enhanced Lanthanide Fluoroimmunoassay
DIPEA	N,N-Diisopropylethylamine
DMF	N,N-Dimethylformamide
DO3A	1,4,7-tris(carboxymethyl)-1,4,7,10-tetraazacyclodecane
DOTA	1,4,7,10-tetra(carboxymethyl)-1,4,7,10-tetraazacyclodecane
e.g.	exempli gratia (for example)
ED	Electric Dipole
EDG	Electron Donating Group
EDTA	Ethylenediaminetetraacetato
equiv.	Equivalents
ESI	Electrospray Ionisation
EtOAc	Ethyl Acetate
EtOH	Ethanol
EWG	Electron Withdrawing Group
FID	Free Induction Decay
FRET	Förster Resonance Energy Transfer
g	Gram
GdBCA	Gd(III)-based contrast agent

HEPES	4-(2-hydroxyethyl)-1-piperazineethanesulfonic acid (buffer) solution)
HOMO	Highest occupied molecular orbital
HPLC	High Performance Liquid Chromatography
h	Hour
HRMS	High Resolution Mass Spectrometry
I	Intensity
I_0	Incident Radiant Power, Intensity at Time = 0
IL	Intra-ligand
in vitro	In an artificial environment outside a living organism
in vivo	Within a living organism
IR	Infra-red
ISC	Inter-system crossing
K	Kelvin
K	Stability constant
LUMO	Lowest Unoccupied Molecular Orbital
LA	Lactic Acid
M	Molar (mol dm^{-3})
m	Multiplet (NMR Spectroscopy)
m/z	Mass-to-charge Ratio
MALDI	Matrix Assisted Laser Desorption Ionisation
MC	Metal-centred
MeCN	Acetonitrile
MeOH	Methanol
MCAO	Middle cerebral artery occlusion
mg	Milligram
m	Minute
mL	Millilitre
MLC	Metal-ligand Complex
MLCT	Metal-to-ligand Charge Transfer
m.p.	Melting point

mM	Millimolar (mmol dm^{-3})
mmol	Millimole
mol	Mole
MS	Mass Spectrometry
MW	Microwave
MW.	Molecular Weight
NaAsc	Sodium Ascorbate
NIR	Near Infra-red
NMR	Nuclear Magnetic Resonance
ns	Nanosecond
OLED	Organic Light Emitting Diode
PBS	phosphate Buffered Saline
phta	Phenyl-1*H*-1,2,3-triazol-1-yl
ppy	2-Phenylpyridine
py	pyridine
pyta	Pyridin-2-yl-1*H*-1,2,3-triazol-1-yl
q	Quartet (NMR Spectroscopy)
q	Number of inner sphere water molecules/ hydration state
RF	Radio Frequency
RP-HPLC	Reversed-Phase High Performance Liquid Chromatography
rt	Room temperature
R_1	Relaxation rate
r_1	Relaxivity
s	Seconds
s	Singlet (NMR Spectroscopy)
s br	Broad Singlet
SAP	Square Antiprismatic
S_0	Singlet Ground state
tapy	Pyridine-2-yl-1*H*-1,2,3-triazol-4-yl
t	Triplet (NMR Spectroscopy)
^{t}Bu	tert-butyl group

TFA	Trifluoroacetic Acid
TBA	*tert*-Butyl alcohol
THF	Tetrahydrofuran
TMS	Tetramethysilane
TMS-acetylene	Trimethylsilylacetylene
TCSPC	Time-Correlated Single Photon Counting
TPE	Two-Photon Microscopy
t_R	Retention Time
TSAP	Twisted Square Antiprismatic
T_1	Triplet electronic excited state
T_1	Longitudinal relaxation
T_2	Transverse relaxation
UV	Ultraviolet
via	By means of
vs.	Versus
k_r	Rate constant for radiative energy
k_{nr}	Rate constant for nonradative energy
η	Refractive Index
Λ	Lambda Configuration Chirality, Left Hand
Δ	Delta Configuration Chirality, right Hand
λ_{em}	Emission Wavelength
λ_{ex}	Excitation Wavelength
μ	Magnetic moment
μM	Micromolar (μmol dm^{-3})
τ	Fluorescence Lifetime
τ_c	Correlation time
τ_m	Mean residence lifetime of a water molecule
τ_R	Molecular reorientation time
Φ	Fluorescence Quantum Yield

Index of Compounds

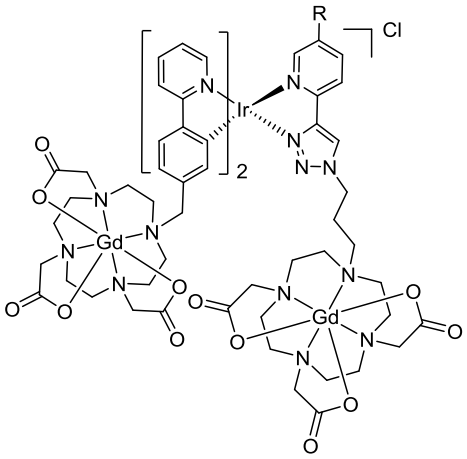

R = H = **IrGdL6L1**
R = CF_3 = **IrGdL6L3**

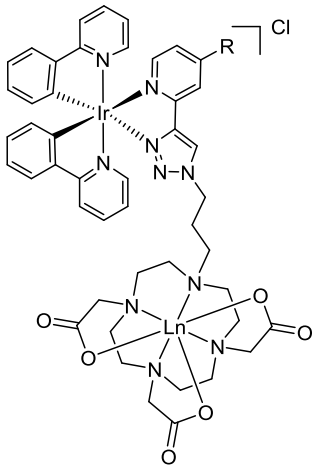

R = H **= Ir(ppy)$_2$GdL1**
R = OMe **= Ir(ppy)$_2$EuL11**

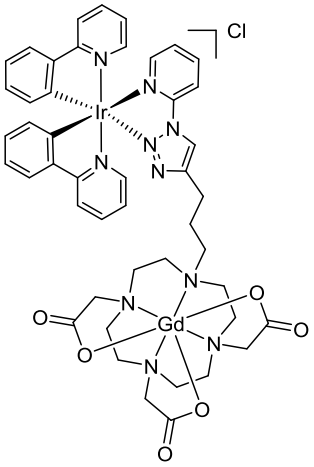

Ir(ppy)$_2$GdL5

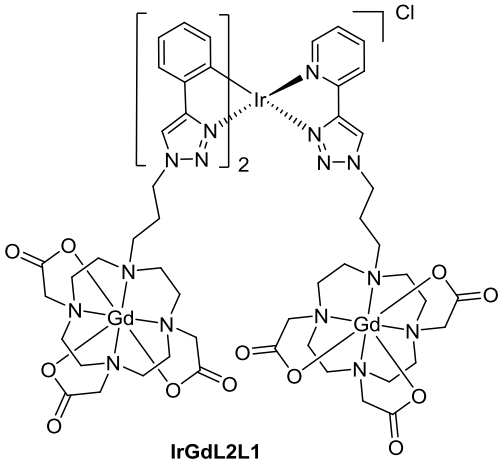

IrGdL2L1

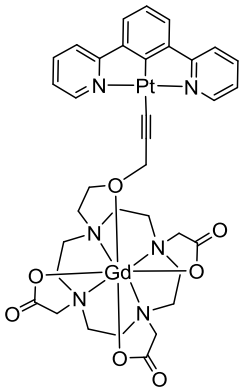

PtGdL10

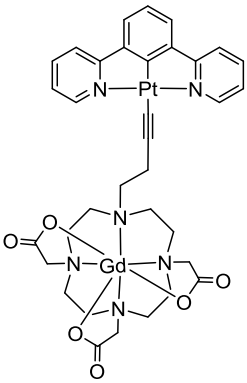

PtGdL9

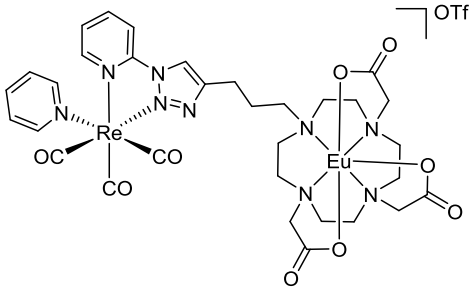

RepyEuL5

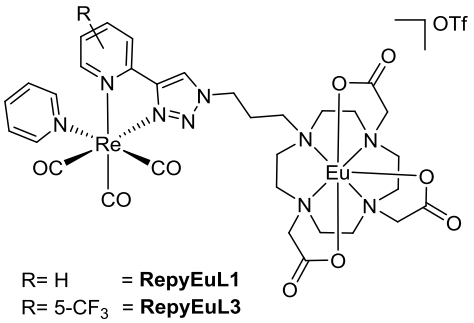

R= H = **RepyEuL1**
R= 5-CF_3 = **RepyEuL3**
R= 4-CF_3 = **RepyEuL4**
R= 4-OMe = **RepyEuL11**

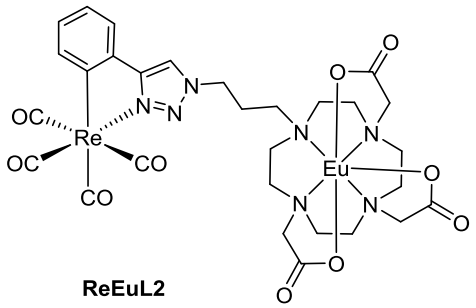

ReEuL2

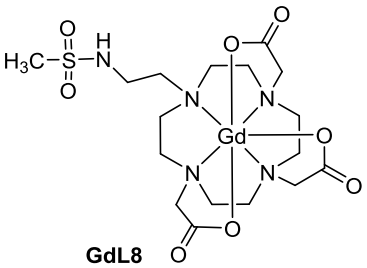

GdL8

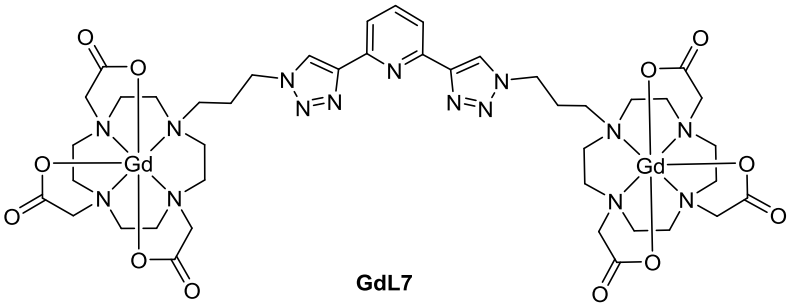

GdL7

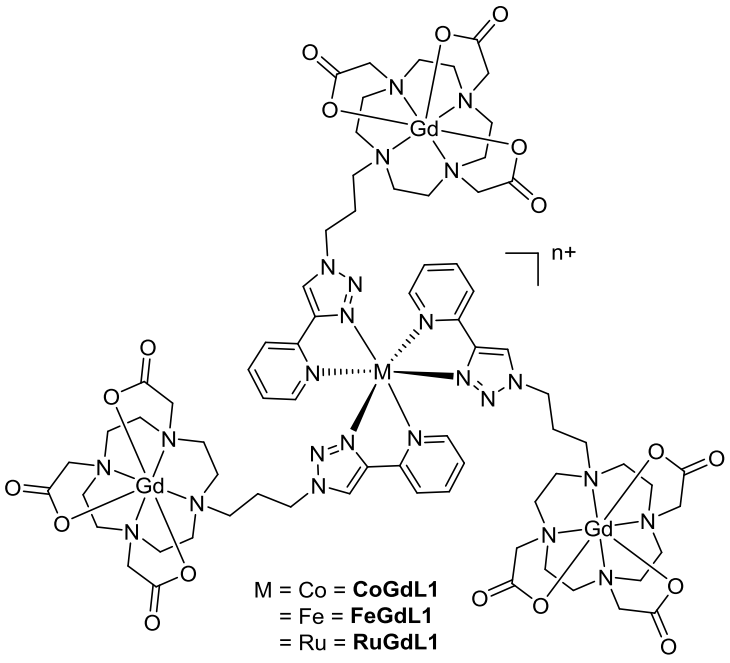

M = Co = **CoGdL1**
= Fe = **FeGdL1**
= Ru = **RuGdL1**

Chapter 1
Introduction

1.1 Molecular Imaging Probes

Molecular imaging (MI) is a type of medical imaging, providing a highly-detailed depiction at the cellular, subcellular, or even molecular level in biological systems enabling visualisation, diagnosis and monitoring of numerous abnormalities such as cancer, neurological and cardiovascular diseases.[1, 2] The use of MI probes for imaging the cell body has seen considerable growth over the last decade, to the point of gaining highly detailed 3D images to 1 μm resolution. Non-invasive diagnostic methods are safer and more useful than invasive methods in terms of earlier detection and treatment of malignant tumours. Imaging modalities can be generally divided into two categories: ultrasound and computed tomography (CT), which can provide anatomical images for organs (physical structure). Imaging modalities such as Positron Emission Tomography (PET), Single Photon Emission Computed Tomography (SPECT) and Magnetic Resonance Imaging (MRI) can monitor the biological functions of diseases and track physiological responses *in vivo*.[3] MI probes can be employed in each imaging technique to produce signal or/and enhance the quality of results, for instance ^{18}F, ^{11}C, ^{64}Cu are used in PET and Cy5.5 near-IR fluorescent dyes in optical imaging (OI), whereas in MRI, Gd(III) chelates, and iron oxide nanoparticles are used. These probes can be designed with targeting moieties such as: small molecules, peptides, proteins, antibodies and nanoparticles; these can increase the selectivity and the sensitivity inside the living system as in Fig. 1.1. In addition, two modalities can be joined simultaneously to gain complementary data.[4]

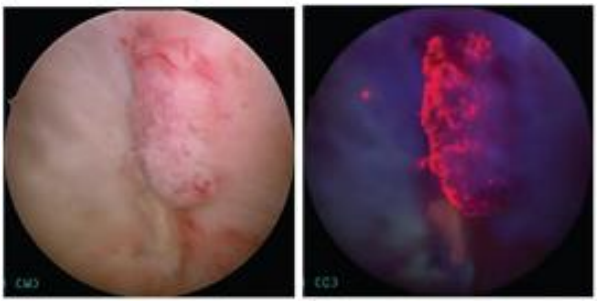

Figure 1.1: The use of a cancer-specific molecular targeting agent for optical imaging to differentiate between healthy and cancerous bladder cells. Left picture under visible light, right under UV. Light, *with permission from Science Traslational Medicine*.[5]

1.2 Magnetic Resonance Imaging (MRI)

The principle of nuclear magnetic resonance (NMR) was discovered first by F. Bloch and E. Purcell in 1946, and for this discovery, they were awarded the Nobel Prize in 1952.[6] More recently, NMR spectroscopy has been applied as an imaging technique as pioneered by P.C. Lauterbur and P. Mansfield, who in 2003 jointly won the Nobel Prize for Physiology or Medicine. Nuclear magnetic resonance imaging, abbreviated to MRI in the clinical field, has the advantage of being able to penetrate bony and air-filled structures, and visualise biosystems in 3D. It essentially visualises water protons due to their high abundance at > 70% in live bodies. This modality is considered safer compared with PET/CT due to the non-ionising radiation used, and it has the capability of exhibiting excellent contrast between normal soft tissue and abnormalities. Although MRI was applied primarily for brain and spinal cord examination, the rapid development of imaging techniques has extended its role into chest, abdomen and skeletal imaging. Moreover, it is capable of collecting information about the physiological state of tissues subtly.[7]

1.2.1 ***Principles of NMR***

The principle of NMR spectroscopy depends totally on the physical concept of angular momentum. An object, in this case a nucleus/proton with a certain mass orbiting on a circular path around a reference point with velocity, v, will obtain the magnetic properties shown in Fig. 1.2.

Figure 1.2: Magnetic Properties of the proton nucleus of the Hydrogen Atom.

As depicted in Fig. 1.2. the proton behaves like a spinning magnet with a north and a south pole, as a result of this motion, each nuclear particle will possess spin angular momentum,| I |, the magnitude of which for the Z axis is;

$$|I| = m_I.\left(h/_{2\pi}\right), \quad m_I = \sqrt{I(I+1)} \tag{1}$$

Where h is the Planck constant (equal to 6.6 x 10^{-34} J s), m_I is the magnetic quantum number, and I is the spin quantum number which can take values of I, I - 1,…,-I. 2I +1 is the total number of orientations. The spin quantum number, I, consists of the sum of the individual contributions of each of the unpaired protons and neutrons present, each possessing spin of ± ½. A nucleus such as ^{12}C with I = 0 cannot be imaged by NMR spectroscopy, *cf*. ^{1}H where has I = ½.

Due to all nucleons being charged, the tendency is to have a magnetic dipole moment. The nuclear magneton, μ_{mN}, is used to express the magnitude of the magnetic dipole moment of the nucleus, where a + or – sign indicates whether the magnetic dipole moment is aligned or opposed to the direction of angular momentum. The nuclear magnetic moment, μ, can be found through the expression:

$$\mu = \gamma I \tag{2}$$

Where γ is the gyromagnetic ratio, and its characteristic of each articular nucleus as shown in Table 1.1. Eventually, each value of m_I corresponds to a different orientation of the nuclear spin and, therefore, nuclear magnetic moment.

As with angular momentum, the nuclear magnetic moment is quantised and can exist only in distinct energy levels, as described by Equ. (3).

$$\mu_z = \gamma m_I\left(h/_{2\pi}\right) \tag{3}$$

Nucleus type	Mag. Dipole Moment (μN)	Nuclear spin number, I	Gyromagnetic Ratio γ (rad. $S^{-1}.T^{-1}$)	Larmor freq. ($MHz.T^{-1}$)
^{1}H	2.79	1/2	$2.7x10^{8}$	42.6
^{2}H	0.85	1	$4.1x10^{7}$	6.5
^{13}C	0.70	1/2	$6.7x10^{7}$	10.7
^{14}C	0.40	1	$1.9x10^{7}$	3.1
^{23}Na	2.21	3/2	$7.1x10^{7}$	11.7
^{31}P	1.13	1/2	$1.1x10^{8}$	17.2

Table 1.1. Magnetic properties of nuclei commonly observed by NMR spectroscopy (where μ_N is the nuclear magneton, 5.05079 x 10^{-27} *J* T^{-1}

For, a proton with I = ½, two energy levels will separate. When a proton is placed in a magnetic field, the nuclei with spin angular momentum will behave as bar magnets and will align themselves along the external magnetic field, B_o, which by convention is oriented along the z-axis. The z-components of the magnetic moment will align either parallel or antiparallel with the magnetic field, as per Fig. 1.3.

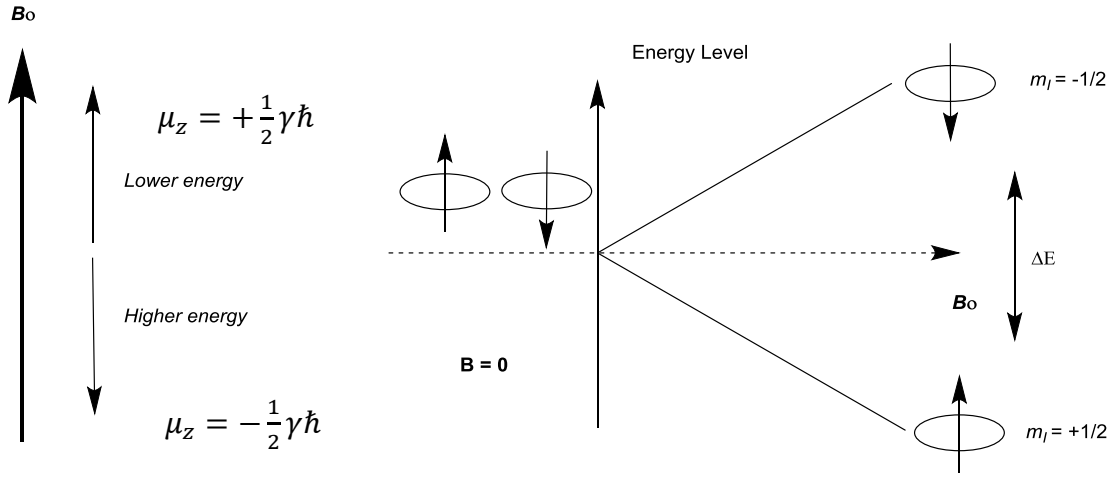

Figure 1.3. Energy diagram for spin = ½ nucleus in the absence of an external magnetic field (B = 0). The application of a magnetic field produces a difference in energy between the two spin states through Zeeman splitting.

The selection rule for an NMR transition between the m_I states is:

$$\Delta m_I = \pm 1 \tag{4}$$

The interaction μ_z with B_0 produces a difference in energy, ΔE, between the two states. The energy difference of the eigenstates is directly proportional to the applied magnetic field according to the following Equ. (5):

$$\Delta E = -\mu_z B_o = -m_I \hbar \gamma B_o \tag{5}$$

The nucleus must be supplied with the certain energy, ΔE, in the form of electromagnetic radiation (Larmor frequency) in order for a transition into a higher energy state to occur for example MRI with 64 MHz needs 1.5 T. Likewise, if a transition is to a lower energy state, electromagnetic radiation equal to the energy difference ΔE will be emitted.[8] The angular frequency, ω_o, for the electromagnetic radiation of a m_I-state transition is:

$$\omega_o = \gamma B_o \tag{6}$$

In a magnetic field, μ revolves around B_o with angular velocity,ω_L Fig. 1.4.

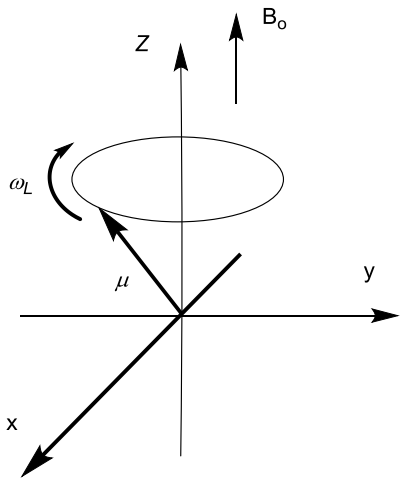

Figure 1.4: Angular velocity of nuclei.

$$\omega_L = -\gamma B_o \tag{7}$$

The angular velocity, ω_L, is known as the Larmor frequency, and it is identical to the angular frequency, ω_o, required for an energy transition to take place. For this reason, the angular frequency is also known as the Larmor frequency.

1.2.2 *NMR Signal*

NMR signal depends on abundance of population m_I states from lower to higher energy. A Boltzmann distribution is utilised to compute the relative populations of the higher energy, N^+, and lower energy, N^-, m_I states equ. (8).

$$\frac{N_{upper}}{N_{lower}} = e^{\frac{-\Delta E}{kT}} \tag{8}$$

Where ΔE is the energy difference between the m_I states, k is the Boltzmann constant (1.3805 x 10^{-23} J K^{-1}) and T is the temperature in Kelvin. In the presence of a strong external magnetic field, the nuclear spins of protons randomly spin around the *x*,*y*-plane. When a 90° radio frequency (RF) pulse, B_1, is applied equivalent to the Larmor frequency along the *x*,*y*-plane, it will pull the individual spins toward the direction of the applied field, which is known as precession. One of the drawbacks in this technique is low percentage of coherence which leads to diminished sensitivity of this analysis. The net magnetisation, *M*, will overturn onto the *x*,*y*-plane if the RF field is applied for sufficient time, which means there is no difference between m_I states population, and the *z* component of the net magnetization is zero ($M_z = 0$) around B_o. 90° RF pulse application, leads to conversion of the m_I states that

are equally populated as longitudinal magnetisation to transverse magnetisation. Finally, a 180° RF pulse is applied, the population is inverted. The spins will continue to possess around B_o until the RF field is removed, after t (seconds), spin relaxation processes will cause loss of coherence and return to the ground state until $M_z = -M_o$, as in Fig. 1.5. The individual spins begin to precess about the x,y-plane at different resonant frequencies, emitting a radio frequency to the NMR spectrometer detector coils, which detects only transverse magnetisation. As equilibrium is re-established, the coils detect a loss in radio frequency known as free induction decay (FID), which is transformed into an NMR spectrum by a Fourier transformation.[9,10]

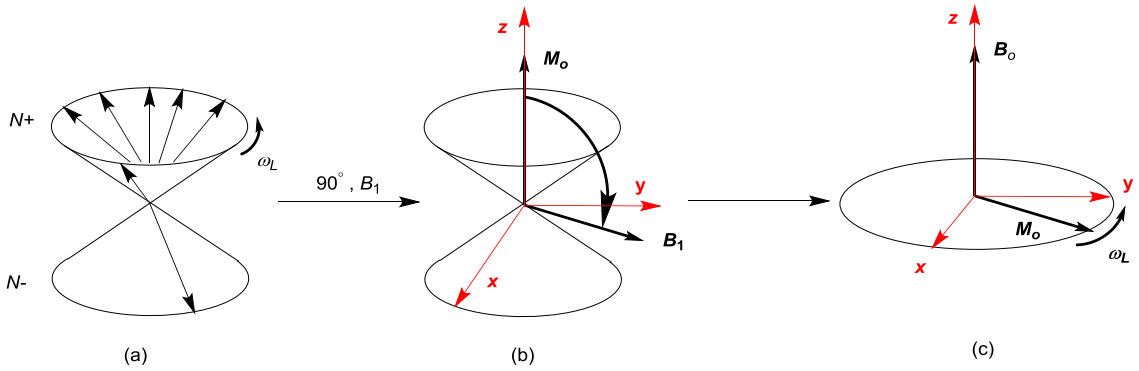

Figure 1.5: Coherence of individual spins following a 90° RF pulse. (a) The equilibrium Boltzmann distribution of spins when nuclei are placed in a magnetic field. (b) The net magnetisation, M, flips 90° onto the x,y-plane. (c) The m_I states are now all in the same phase and precess around the magnetic field, B_o, at Larmor frequency, ω_L.

1.2.3 *Longitudinal (Spin-Lattice) Relaxation Time, T_1*

The time taken for M_z to return to its equilibrium state is the spin-lattice (or longitudinal) relaxation time, T_1, and this governs the rate of transferring energy from the nuclear spin system to the neighbouring molecules (the lattice). There are three rules for T_1 energy transfer: (i) the nuclei is expected to gain or lose the energy which causes a *fluctuating magnetic field*, (ii) the latter must be at the Larmor frequency, v_o, (iii) only the x,y components of the local field can cause T_1 relaxation. This is affected by temperature due to the rate of the molecular motion. The net magnetisation, M_o, at equilibrium is directed along the applied magnetic field, B_o. The equation for the return to equilibrium following this process is:

$$M_z = M_o\left(1 - e^{-\tau/T_1}\right) \tag{9}$$

Where τ is the delay time following the 90° RF pulse.

1.2.4 *Measurement of T_1: The Inversion Recovery Experiment*

The standard method for measuring T_1 by a pulsed NMR technique is known as *inversion-recovery*. Firstly, the sample is subjected to a 180° RF pulse which induces a magnetisation inversion along the *z*-axis. At a specific time, τ, spin-lattice relaxation occurs, causing M_z to go from a value of $-M_o$ through zero to its equilibrium value of M_o as in Fig. 1.6. A 90° RF pulse is then employed and the FID (Free Induction Decay) is recorded, a process which can be repeated with a series of delay times, τ, allowing the determination of the T_1 value. The latter can be quantified by plotting $\ln[I(\infty)-I(\tau)]$ vs. τ. (where $\ln I(\infty)$ is the intensity of the fully relaxed sample).

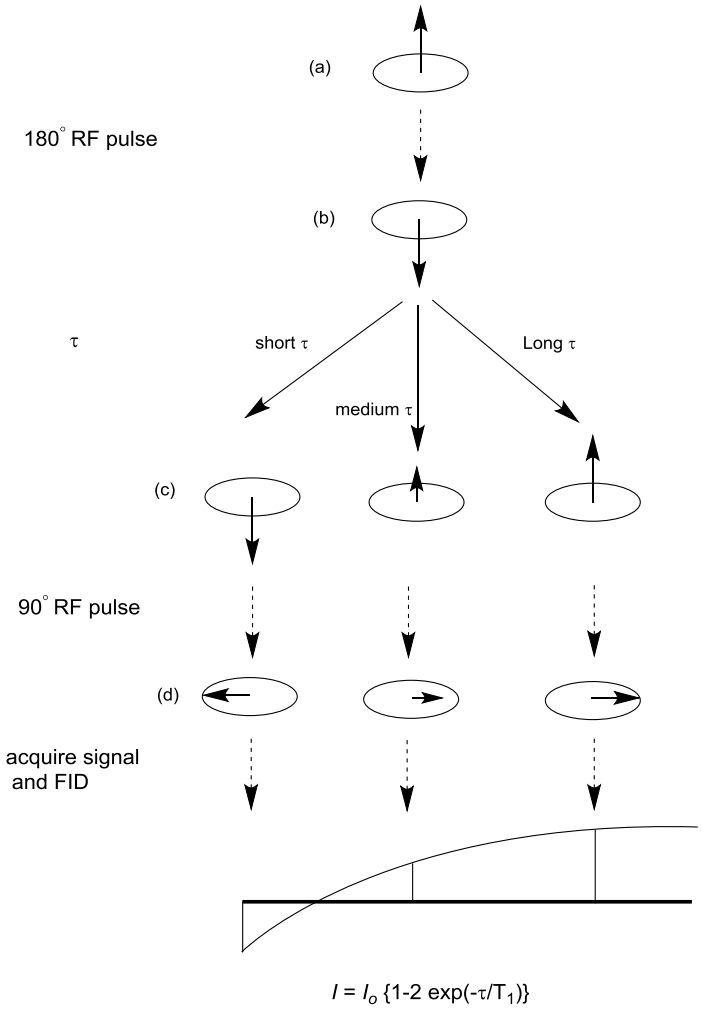

Figure 1.6: The inversion recovery experiment. (a) The M_z component of the net magnetisation is in line with the magnetic field, B_o, and, thus $M_o = M_z$. (b) M_z flipped across the z-axis following a 180° RF pulse. (c) The M_z returning to equilibrium following a delay time, τ, where above a shorter delay is employed, τ_1, compared to the longer delay τ_2 below. (d) M_z is flipped onto the x,y-plane following a 90° RF pulse, from where a FID is detected and the signal intensity is recorded.

1.2.5 *Transverse (Spin-Spin) Relaxation Time, T_2*

Spin-spin (or *transverse*) relaxation time, T_2, is used to quantify the rate of loss of coherence around the *x,y*-plane. After a 90° pulse, the spins precess in one direction. This coherence is gradually lost due to field inhomogeneities and/or direct interactions between the spins without energy transfer to the lattice as adopted in Fig. 1.7. This process is related to T_1 relaxation, because it is impossible to increase the *z*-magnetization without a decrease in the magnetization in the *x,y*-plane. Interestingly, the T_2 relaxation time is always shorter than that of T_1.[11]

So far it has been assumed that the varying frequencies of the spins away from the Larmor frequencies arise only due to interactions within the sample.

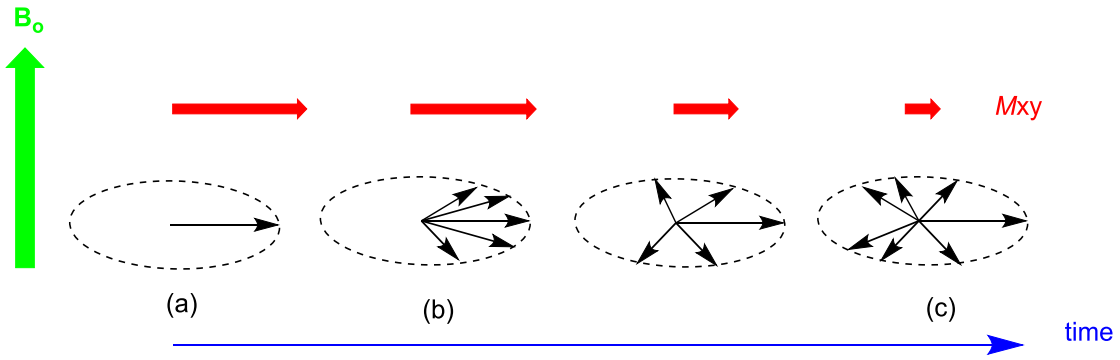

Figure 1.7: Transverse relaxation (a) the spins are flipped onto the x,y-plane following a 90° RF pulse. (b) the net magnetisation processes around the x,y-plane at Larmor frequency. (c) the spins start to return to equilibrium, restoring transverse magnetization M_{xy}, as they "fan out" around the x,y-plane.

It is important, however, to bear in mind the bulk inhomogeneity of the magnet, ΔB_o, i.e., the field varies at different locations of the sample, and contributes to the observed transverse relaxation time in an NMR signal, T^*_2.

$$\frac{1}{T_2^*} = \frac{1}{T_2} + \gamma \Delta B_o \qquad (10)$$

1.2.6 *Magnetic Field Gradients*

In a gradient field, conductive scanners (G_x, G_y and G_z) are employed to generate three-dimensional images from the voltage induced by the precessing transverse magnetisation. Its function is specifically to encode the observed nuclear

spin densities. These *physical gradient coils* exhibit further feeble magnetic fields than the main magnetic field (B_0) and vary linearly across, X-gradient coil will produce sagittal images, Y-gradient coil will produce coronal images, and Z-gradient coil will produce axial images, as in Fig. 1.8. They can be turned on in combinations to create a linear gradient in any arbitrary direction in space. According to the Larmor equation, if a magnetic field varies across space, the *precession frequency* of the protons will vary as well.

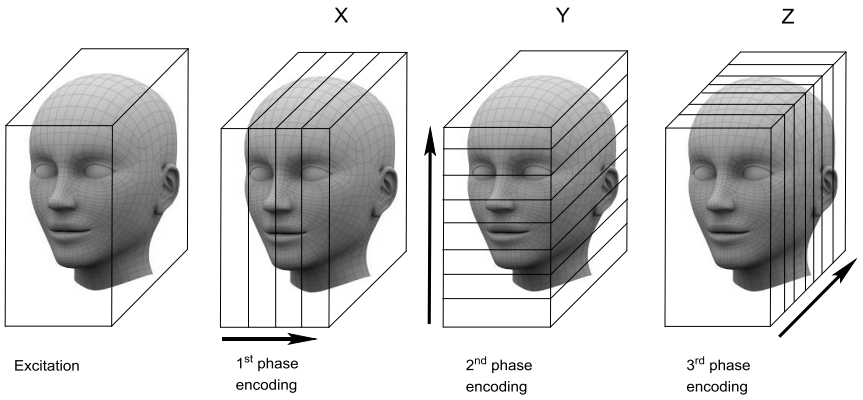

Figure 1.8: The x, y, or z (axial, coronal, and sagittal) directions of gradient coils.

1.2.7 *Image Contrast*

A biological system (hard and soft tissues) contains different concentrations of water molecules or density of protons (hydrogen atoms) according to tissue type, and as consequence a variable water proton spin density will be obtained at different regions of the body, as per Table 1.2. It was seen in Sections 1.2.3 - 1.2.5 that signal intensities are affected by both T_1 and T_2. As a consequence, an MRI image will have contrast brightness, bright images for tissues with high proton signal intensities, dark for low signal, and grey in an intermediate case. Such data can be collected by three mechanisms, *i.e.* T_1 recovery, T_2 decay, and proton density, PD (the hydrogen concentration within a sample of tissue). In the human brain, grey matter proton density is higher than white matter 85 pu and 70 pu respectively, so they will have different T_1 values and contrasting brightness. As reported in Table 1.2 tissues have different T_1 values, this variation in image brightness is key to diagnosing a biological abnormality.

Tissue	T_1(ms) 1.5 T	Proton density
Liver -Normal tissue	493	91
-Tumours	905	
Bone -Normal marrow	732	~5
- Osteosarcoma	973	
Arterial blood	1441	72
CSF	2650	100
Brain		
-Greymatter	921	85
-Meningioma	979	90
-White matter	787	70

*(CSF) is Cerebrospinal fluid, PD is expressed in percentage units (pu).

Table 1.2: Shows T_1 relaxation times and proton intensities for various tissues.[12]

1.2.8 *T1-Weighted Imaging*

The mechanisms behind the T_1 relaxation time have been previously discussed (Section 1.2.3). The T_1-weighted image is derived from the longitudinal relaxation times of tissues. It can visualise tissue with a high fat content depending on T_1 recorded values (*e.g.*, white matter) which appear brighter in comparison with CSF. The scanning parameters are those of a short repetition time and short echo time to minimize T_2 relaxation effects. This method is suitable for visualising anatomy.

1.2.9 *T2-Weighted Imaging*

T_2-weighted imaging is used to visualise anatomical structures depending on their T_2 values. The scanning parameters are set to use a long repetition time and long echo time to minimise T_1 relaxation effects. In this type of scan, a tissue that is filled with water (e.g., CSF compartments) appears bright in comparison with fatty tissue (e.g., white matter). It is suitable as well for pathological studies since most (though not all) lesions are associated with an increase in water content. Fig. 1.9 demonstrates human brain images depending on visualising T_1, T_2 and PD.

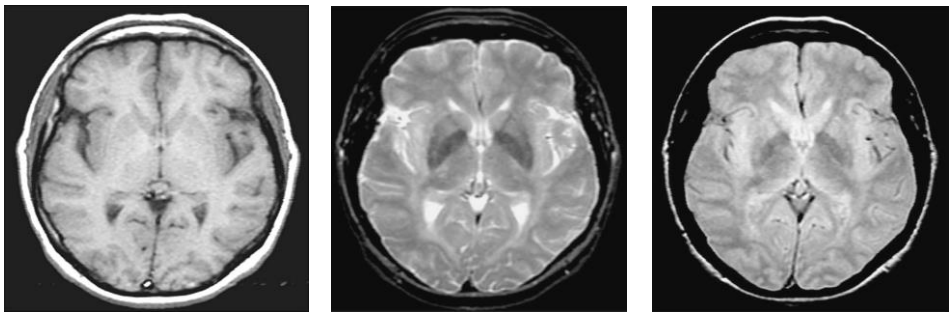

Figure 1.9: comparing three types of imaging T_1(left), T_2 (middle) and (right) PD, *with permission from John Wiley & Sons*.[13]

In MR imaging modality, it is necessary to obtain a highly resolved depiction (μm) to help physicians in their diagnoses. This method is highly dependent on the longitudinal and transverse relaxation times of the water protons present. So, the MR image can be enhanced by inducing short water proton relaxation processes. This can be accomplished by injecting agents into the patient's blood in a dose can be as low as 0.1 mmol kg^{-1} body mass, which has a positive effect on the water proton relaxation times, is MRI contrast agents.

1.3 MRI Contrast Agents

In MRI, excellent FID intensity can be imparted by the presence of paramagnetic contrast agents (CAs). It is complexes of metal ions such as Mn(II), Gd(III) that are applied to T_1-weighted imaging, or ferromagnetic iron oxide or superparamagnetic materials, such as superparamagnetic iron oxide (SPIO) for T_2-weighted imaging.[14] Since the MRI technique images body water protons, it is not the contrast agent *per se* which is seen in the image; rather its effect on the longitudinal relaxation (T_1) and transverse relaxation (T_2) of surrounding water proton nuclei. High stability, solubility and functionality are the most desirable features in the synthesis of contrast agents.[15]

1.3.1 *Gd(III)-Based Contrast Agents*

Gadolinium(III) has been widely applied for T_1 relaxation time enhancement, due to seven unpaired *f*-electrons, a long electron spin relaxation time, symmetrical ground *S*-state and large effective magnetic moment, μ_{eff} = 7.94 B.M. Unlike Dy(III) with an incredibly rapid electronic relaxation rate and larger magnetic moment, Gd(III) shows electronic relaxation more closely in tune with the proton's frequency, lacking orbital contributions to electron angular momentum giving an electronic

relaxation time much longer than those of other Ln(III) ions (T_{1e}≥ 2 x 10^{-10} s, at room temperature).[16] Since gadopentetate dimeglumine (Magnevist®) was approved 1988, now more than 100 million doses are administered annually.[17] Gd(III)-based contrast agent (GdBCA) has a much greater effects on T_1 than T_2, therefore it is considered the for best T_1-weighted images (positive agents). An increase in transverse relaxation rate leads to a decrease in MR image intensity, and such T_2 contrast agents are referred to as negative agents.[16,18]

The first approaches towards synthesis of these kind of agents, produced very stable agents, *i.e.*, CAs with high thermodynamic stability and kinetic inertness. Gd(III) is similar to Ca(II) in terms of its ionic radius (1.05 Å and 1.12 Å for Gd(III) and Ca(II), respectively) and coordination number (typically C.N ≥ 8). Therefore, Gd(III) has unfortunately proved itself an excellent replacement for Ca(II) in the coordination of biological sites. Free trivalent gadolinium inhibits calcium transfer processes in the human body, which leads to bone deposition, blockage of voltage-gated Ca^{2+} channels, develops inorganic Gd-phosphate precipitates and can result in gadolinium-induced fibrosis (GIF).[19, 20]

CAs are complexes, which can be classified in many ways (i) type of ligand, (ii) type of metal centre, (iii) bio-application and distribution, or (iv) magnetic properties (positive or negative CA), amongst others. The most important classification, is according to the type of chelate, as a remarkable indicator of the stability.[21] Generally speaking, both linear and macrocyclic chelates are used in CAs synthesis, but non-macrocyclic chelates have lower kinetic stability in the solution with high transmetalation probability *in vivo*.[22] Macrocyclic chelates are widely favourable, due to their exceptionally inertness to dissociation, kinetically inertness and ease of modification compared to liner chelators. Lanthanides generally show coordination numbers of 9, nevertheless, it can easily reach 11 or 12. This scenario can be satisfied and produce stable agents by using cyclen derivatives with three or four acetate arms, such as 1,4,7,10-tetra-azacyclododecane-1,4,7,10-tetraacetic acid (DOTA) or even phosphate arms (DOTP). There are currently numerous commercial agents available for different purposes. ProHance® (gadoteridol), Omniscan® (gadodiamide), and Optimark® (gadoversetamide) were approved between 1992 and 1999. In addition, three extracellular fluid agents (MultiHance®, Eovist® and

Ablavar®), one hepatobiliary (Gadavist®) and one blood pool (Dotarem®), these contrast agents were approved between 2004 and 2013, Dotarem® has already been adopted to use in Europe and numerous countries.[23] Fig. 1.10 depicts the GdBCAs that have been approved by the FDA for clinical use.[16] Table 1.3 shows the association constant as log K_{ML}, (pH 7.4) the acid dissociation rate constant, k_{obs} and the half-life at pH 1.0 for selective commercially available contrast agents.[24]

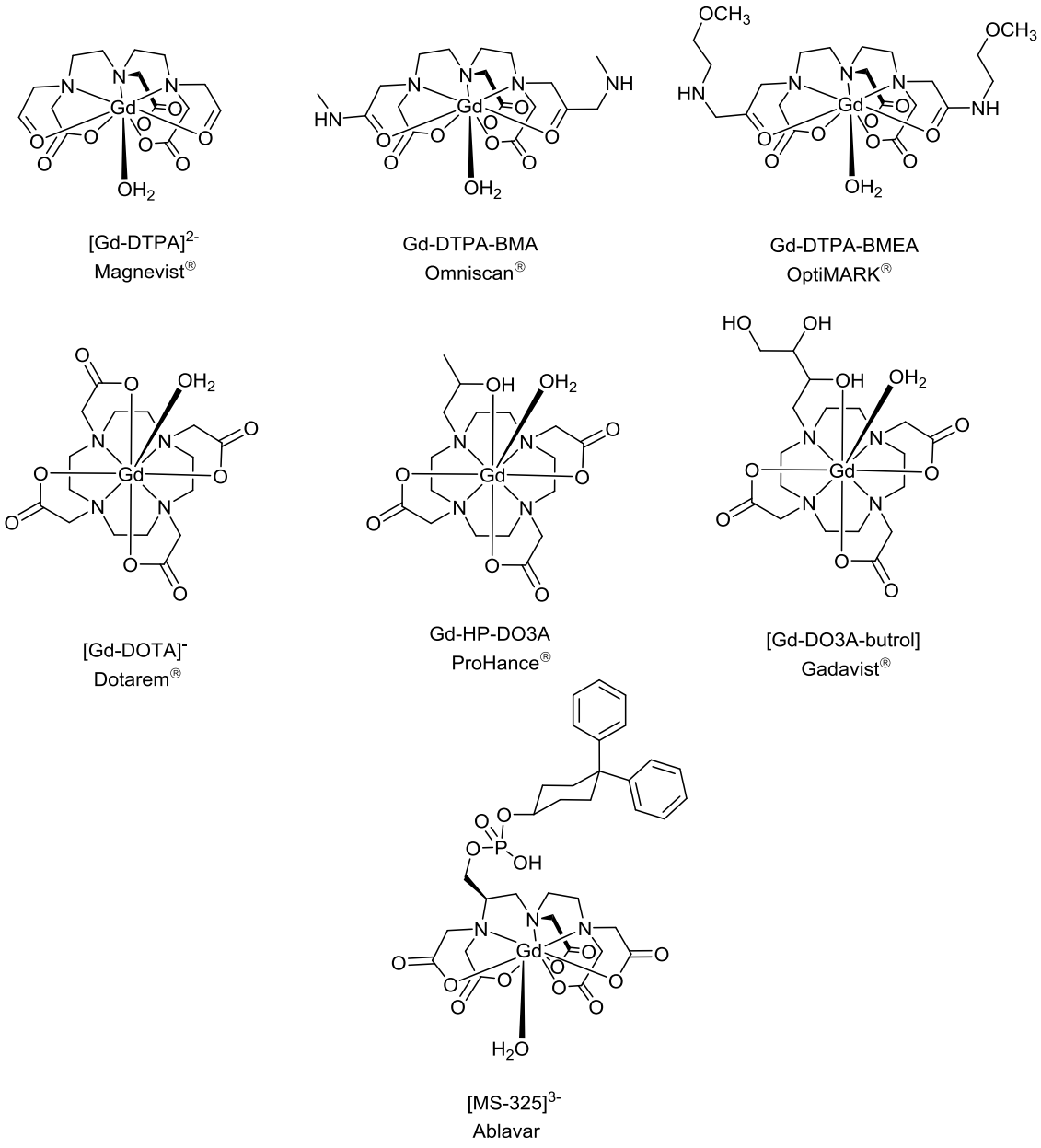

Figure 1.10: Sample of commercially available contrast agents.

Contrast Agent	Chemical Name	log K_{ML}	k_{obs} (10^{-3} s^{-1})	$t_{½}$
Magnevist®	$[Gd\text{-}DTPA]^{2-}$	22.1	1.2	10 min
Omniscan®	Gd-DTPA-BMA	16.9	20	35 s
OptiMARK®	Gd-DTPA-BMEA	16.6	N/A	< 5 s
Dotarem®	$[Gd\text{-}DOTA]^{-}$	25.8	0.021	>1 month
ProHance®	Gd-HP-DO3A	23.8	0.063	3 h
Gadavist®	Gd-BT-DO3A	21.8	N/A	7.9 h

Table 1.3: Association constants, log K_{ML}, acid dissociation rate constants, k_{obs}, and half life, $t_{½}$(at 25 °C in 0.1 N HCl) for various commercially available contrast agents.[25]

1.3.2 *Stability and Toxicity of Contrast Agents*

The thermodynamic stability of a contrast agent is an indication of the equilibrium between Gd(III) [M] and the chelate [L] with the complex [ML] in aqueous solution:

$$[M] + [L] \leftrightarrows [ML] \tag{11}$$

Toxicity of these complexes depends on the release of Gd(III) ions in the solution, which can be found in complexes low with *K*, which is defined as:

$$K = [\mathrm{ML}] / [\mathrm{M}][\mathrm{L}] \tag{12}$$

Despite 1,4,7-tris(carboxymethyl)-1,4,7,10-tetraazcyclododacne (DO3A) having a slightly low stability constant compared to DOTA (21.10 and 25.3 respectively), it is still favourable to use in biological research due to its hydration number.[26-28] There are different parameters that can have extreme effects on CA stability inside the body: abundance of biological cations such as Cu(II), Zn(II) and Ca(II), as they tend to compete with the coordinated Gd(III); negative ions, for instance PO_4^{3-}, CO_3^{2-} and OH^- can coordinate with Gd(III) instead of the chelate; and biological processes leading to Gd(III) ion liberation. Transmetalation is highly relevant with linear chelating ligands due to insignificant kinetic stability.[25] In summary, the factors that can affect nonlinear CAs stability are: (i) ligand size, as can be clearly seen with macrocyclic polyamine ligands, where NOTA~TETA < TRITA < DOTA (this is related to the chelate cavity itself, as the NOTA cavity size is insufficient for large Ln(III) ions); (ii) the basicity and bonding of nitrogen atoms,

for example, replacing acetate side-chains with phosphate groups increases DOTA stability log K_{therm} about 7.8, in that DOTA < DO3AP < DO2A2P < DOA3P < DOTP;[29](iii) the total charge on the ligand also plays a significant role, for instance, as the number of negative charge increases, the Ln-complex stability increases. This can be demonstrated by comparing related ligands stability of $[Ln(DOTA)]^-$ which is significantly affected by reducing the acetate side-chain number as well; (iv) the number of water molecules associated with the CA, hydration numbers , q, has a significant effect on thermodynamic and kinetic stability; (v) biological cations such as Zn(II), Cu(II), Ca(II) and H^+ can transmetalate Gd(III) in vivo, the preferential binding selectivity for Gd(III), K_{sel}, indicates the selectivity and stability of chelate toward these ions which can be found through equ. (13). Table 1.4 reports selected results in this regard.[30]

$$K_{sel} = K_{ML}\left[\frac{K_{H^+L}}{[H^+]} + \frac{K_{CaL}}{[Ca^{2+}]} + \frac{K_{CuL}}{[Cu^{2+}]} + \frac{K_{ZnL}}{[Zn^{2+}]}\right] \quad (13)$$

Contrast Agent	Ligand	K_{sel}	K_{CaL}	K_{CuL}	K_{ZnL}
Magnevist®	DTPA	7.04	10.75	21.38	18.29
Omniscan®	DTPA-BMA	9.04	7.17	13.03	12.04
OptiMARK®	DTPA-BMEA	-	-	-	-
Dotarem®	DOTA	8.30	17.23	22.63	21.05
ProHance®	GD-HP-DO3A	6.95	14.83	22.84	19.37
Gadovist®	Gd-BT-DO3A	4.13	11.74	22.87	19.26

Table 1.4. Association constants for various commercially available contrast agent ligands with selected metal ions.

1.3.3 *Water Proton Relaxivity,* r_1

The dipole-dipole interaction between unpaired Gd(III) electrons and bulk water is the key function of how Gd-CAs work. This dipolar mechanism generates a local magnetic field that alters both the longitudinal and transverse relaxation rates of water protons. The exchange between bulk water with q (water molecules coordinated directly to the metal centre) is governed by a $1/r^6$ distance between the

paramagnetic metal ion and water molecule.[31] CA water moieties can be categorised into three groups: inner-sphere water, R_{1p}^{IS} , which coordinate directly to the metal centre, and have a residency time of 1-10,000 ns; second sphere, R_{1p}^{SS}, is the water molecules hydrogen-bonded to the CA's carboxylate or phosphate groups, it contributing accounts 40% of the overall relaxivity with characterised residency of about 10 ps;[32] and the outer-sphere waters, R_{1p}^{OS}, which are diffused around the complex at over 4 Å separations. However, the CA total relaxation rate (R_1) is related to all three hydration spheres:

$$R_{IP}^{obs} = R_1^{IS} + R_1^{OS} + R_1^{SS} \tag{14}$$

The bulk water proton longitudinal (R_1) and transverse (R_2) relaxation rates can be found by Equ. (15).

$$R_1^{IS} = \left(\frac{1}{T_1}\right)^{IS} = \frac{Cq}{55.6}\left[\frac{1}{(T_{1m}+\tau_m)}\right] \tag{15}$$

Where C is the concentration of the paramagnetic ion, q, is the number of coordinated (inner sphere) water molecules, T_{1M} is the longitudinal relaxation time of the inner sphere waters and τ_m is the life time to water exchange. It is clear from Equ. (15) that there are several strategies that can be used to increase inner-sphere water relaxivity, such as increasing the CA concentration, exchange rate, k_{ex} ($1/\tau_m$) and the number of inner sphere water or by decreasing T_{1M}. According to Solomon-Bloemberen theory, to improve the T_{1M} Gd-CAs efficiency, a greater number of water molecules, q, with long rotational correlation time, τ_R, as well as optimum water residence life-time, τ_m, should be designed.

In summary, Fig. 1.11 demonstrates the inner and outer sphere contribution to bulk water relaxivity.[24, 31] In terms of increasing the number of ligated waters, it is feasible to focus on inner- sphere waters, taking in consideration the stability of the CA in the biological system.

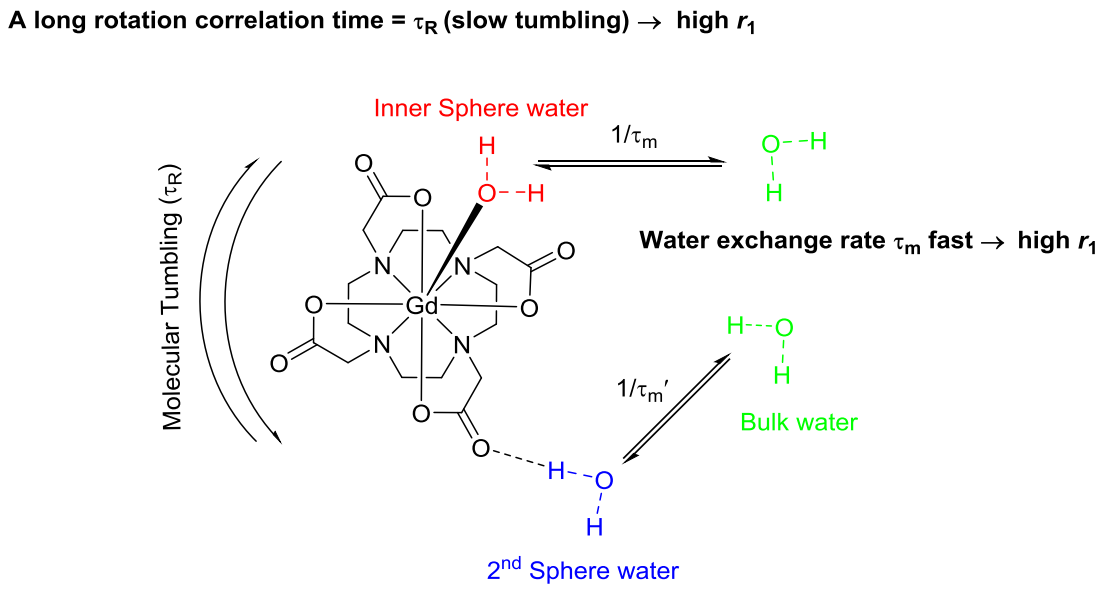

Figure 1.11: Molecular parameters that influence inner- and 2nd-sphere relaxivity.

1.4 Relaxivity Enhancement

The efficiency of a contrast agent is defined by its relaxivity, r_1; the total paramagnetic relaxation rate enhancement of the water protons per unit concentration of the contrast agent ($mM^{-1}s^{-1}$), Equ. (16).

$$r_1 = R_{1p}/[Gd] \tag{16}$$

According to Solomon and Bloembergen Equ. (17), there are three major parameters that must be taken in consideration to increase Gd-CA efficiency.[33]

$$\frac{1}{T_{1M}} = \frac{2}{15}\frac{\gamma_H I^2 g^2 S(S+1)\beta^2}{r_{Gd-H}^6}\left[\frac{7\tau_{c2}}{(1+\omega_S^2\tau_{C2}^2)} + \frac{3\tau_{c1}}{(1+\omega_I^2\tau_{C1}^2)}\right] \tag{17}$$

Where, γ_H, is the proton gyromagnetic ratio, g ,is the electron g-factor, β, is the Bohr Magneton, S, is the total electron spin, r_{Gd-H}, is the distance between the Gd(III) centre and proton of a coordinated water molecule, τ_c, is the correlation times for dipole–dipole. ω_I and ω_S denote the nuclear and electronic Larmor precession frequencies respectively ($\omega = \gamma B$, B is the magnetic field).[16]

1.4.1 *Hydration Number (q) and Gd-H Distance (r_{Gd-H})*

The efficiency of any contrast agent depends heavily on the number of inner-sphere proton and its relaxivity. The measured relaxivity of Gd-DO3A is r_1 = 4.8 mM^{-}

$^1s^{-1}$ (20 MHz, 40°C), under the same conditions, Gd-DOTA has a relaxivity of r_1 = 3.5 $mM^{-1}s^{-1}$, this is related the difference in hydration states.[34] However, more than one inner sphere water makes the CA favourable for endogenous biological chelators such as phosphates or bicarbonates binding, see Section (1.3.2). Until now, clinically approved cyclen-based CAs are of the type q = 1, for instance Gd-DOTA (Dotarem®), Gd-HP-DO3A (ProHance®) and Gd-BT-DO3A (Gagovist®). Toth *et al*. showed that the water exchange rate of $[Gd(DO3A)(H_2O)_2]$ was significantly slower than the Gd(III) aqueous ion, nevertheless still twice as fast as for $[Gd(DOTA)(H_2O)]$(k_{ex}^{298} = 11 x 10^6 and 4.8 x 10^6 s^{-1}, respectively).[35] According to Equ. (17), as the relaxivity of the water proton also depends on the distance between the Gd(III) and the inner sphere water proton ($r_{Gd\text{-}H}$), it has been established that shortening this distance increases the relaxivity. It has also been reported that the most favourable distance ranges between 2.7-3.5 Å, which can be measured: either by an indirect method from fitting NMRD data and ENDOR spectroscopy, or by direct determination using neutron diffraction on single crystals and isotopic exchange methods. 1D and 2D pulsed ENDOR studies show that this distance does not depend on the co-ligand or total charge. In addition, it been found CAs with 8- or 9-coordinate and $r_{Gd\text{-}H}$ distance around 3.1 Å has higher steric crowding to facilitate the release of the Ln(III) bound waters, lowering the water exchange lifetime. [31]

1.4.2 ***Rotational Correlation Time (τ_R)***

In clinical settings, scanners typically of magnetic field strengths 0.24 - 1.65 T are applied, compatible with the proton Larmor frequency of 10 - 70 MHz. At these parameters, the electronic contribution is almost dispersed. The correlation time, τ_c, is totally dependent on the water exchange lifetime, τ_m, and the rotational correlation time, τ_R, as in Equ. (18).

$$\frac{1}{\tau_c} = \frac{1}{\tau_R} + \frac{1}{\tau_{1e}} + \frac{1}{\tau_m} \qquad (18)$$

Where (τ_R) is the required time for any molecule to rotate 57° back and forth. As mentioned in Section (1.3.3), reducing the rate of molecular tumbling gives

higher relaxivities. There are various methods to makes τ_R longer: for spherical rigid molecules it can be estimated using Debye‑Stokes equation (19).[36]

$$\tau_R = \frac{4\pi a^3 \eta}{3k_B T} \quad (19)$$

In this correlation, *a,* is the value of the molecular radius and η is the viscosity, k_B, Boltzmann's constant, *T* is the temperature. First, increasing the viscosity of the medium this involves with raising the viscosity of extracellular fluid (the medium), which is impossible. Second, coupling to polymers, dendrimers or biological molecules macromolecules to increase the molecular size, for instance Giardiello *et al*., synthesised diphenylphosphinamide-Gd-DO3A which is covalently attached through a linker to human serum albumin HSA (albumin is the most abundant protein in plasma, and its concentration is 600 –700 μM). They noticed that the relaxivity was improved by 15% upon slowing molecular reorientation, regardless of the fact that the protein blocks water access to the agent.[37] In the same scenario, Caravan *et al.*, introduced Ablavar (Fig. 1.10) as a blood pool contrast agent which shows excellent affinity toward HSA because of two phenyl groups with limited hepatic clearance related to the charged phosphodiester linkage. This linear Gd(III) chelator exhibits high half-life retention ~18.5 hr with plasma relaxivity 27.7 $mM^{-1}s^{-1}$ (1.5 T, 37 °C).[38] It has been noted that multimeric MR agents cannot achieve an optimal r_1 (< 40 mM^{-1} s^{-1}) even when containing polygadolinium agents. For example **1** has 24 terminal GdDOTA-monoamide groups (Fig. 1.12) with MW. 17,500, with total relaxivity per Gd(III) 16.4 $mM^{-1}s^{-1}$ which is consider much lower than expected comparing with Ablavar with 46.1 mM^{-1} s^{-1} when coupled to HSA. The reason is the single amide bond in each GdDOTA-monoamide unit lowering water exchange (t_M = 1 μs), also unrestricted motional flexibility of each appended unit. The local rotational correlation time felt by each Gd(III) is only about 760 ps, which is about 3.5 times longer than a typical low Mwt Gd(III) chelate (GdDOTA-1-Bz-NO_2).[39]

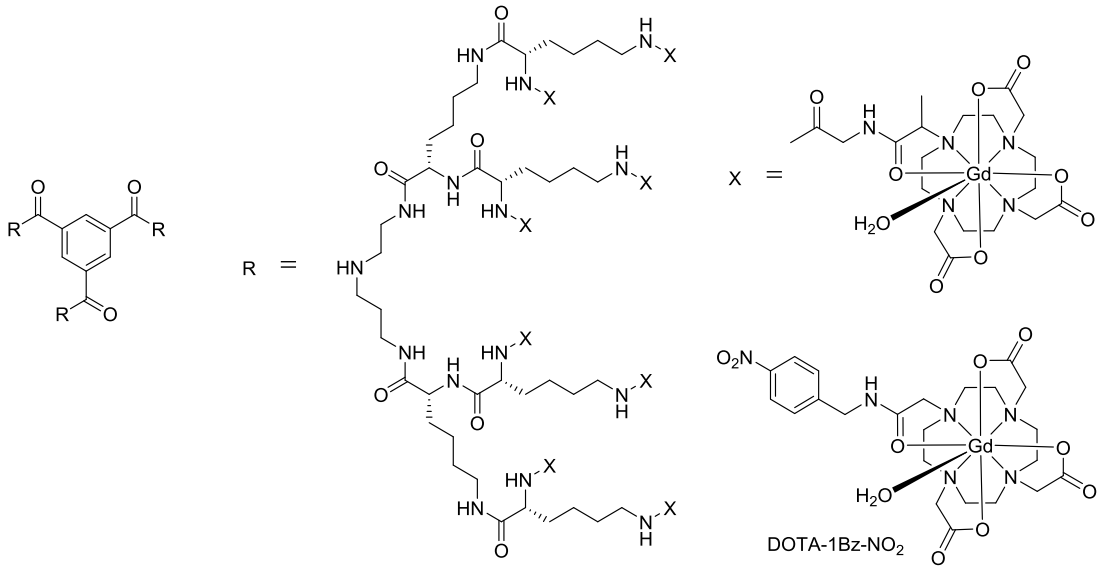

Figure 1.12: Structures of **1** and DOTa-1Bz-NO_2.

Fig.1.13 shows that at higher fields, CAs with intermediate molecular weights and shorter τ_M are preferable.[40] It is also widely appreciated that the maximum value of r_1 for a Gd(III)-based agent undergoing slow molecular rotation is smaller at higher magnetic field. Additionally, the coupling with a macromolecule can be beneficial depending upon the function of the contrast agent. Blood Pool Agents (BPAs), for instance have been designed to remain in the blood stream for longer times to diagnose vascular abnormalities via Magnetic Resonance Angiography (MRA). So, it is necessary to have a large molecular weight (> 20 kDa) to prolong residency and prevent infiltration into the interstitium by selecting a protein with a high molecular weight.[41]

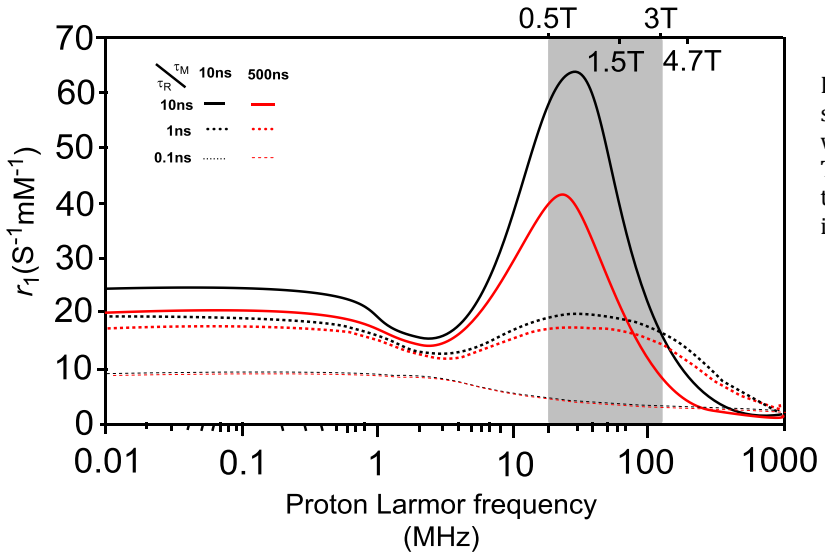

Figure 1.13: ^{1}H NMRD simulations of relaxivity with varying τ_R 0.1 to 10 ns. The shaded area shows the typical magnetic fields used in medicine.

1.4.3 *Water Residency Time (τ_m)*

The water exchange lifetime is the third factor that directly effects the relaxivity. The exchange rate, $k_{ex} = 1/\tau_m$, τ_m, can be defined as the lifetime for which a bulk water can be coordinated directly to a metal centre. It is considered the key for transferring the relaxivity to the bulk water. A CA can work efficiently when the residency time ranges between 10 - 40 ns. It needs to be short enough to allow all water molecules to coordinate to the Gd(III), otherwise the T_1 enhancement will be concentrated purely on the inner sphere waters.[42] Contrast agents can be altered to be bio selective to various ions such Cu(II), Ca(II) and Zn(II) which can lead to enhancement of the relaxivity upon an increase in water exchange rate, or alternatively, creation of a more organised second sphere of water in close proximity to the inner sphere water, the result for example increase in relaxivity about 20%.[43]

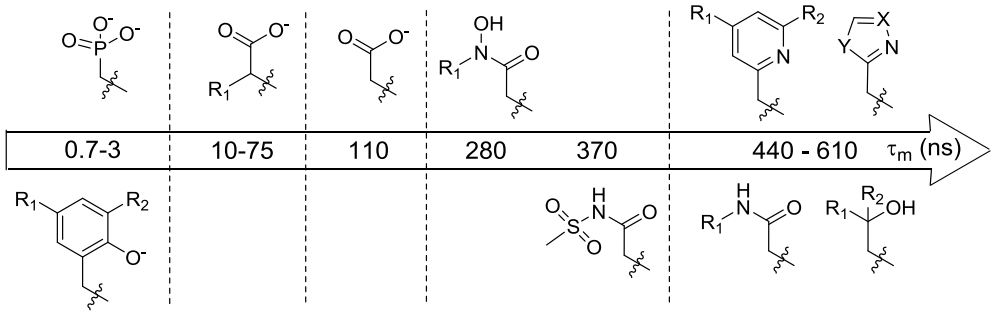

Figure 1.14: The effect of stitution different arms on exchange rate.

There are a number of elements that effect the τ_m value such as: complex charge, solvent accessibility, steric hindrance of the metal centre and the water exchange mechanism.[44] The negative charge and the donor group creates a negative 'cloud' charge that weakens the ligation between the metal and water molecule. Noticeably, excellent exchange rates has been observed with α-substituted acetate groups as outlined in a pattern in Fig. 1.14. [45] Macrocyclic contrast agents with α-substituted acids groups (DO3A = 1.0 ± 0.1 10^6 s^{-1}) exhibits longer exchange rate compared to $[Gd(H_2O)_8]^{3+}$ (8.30 ± 0.95 x 10^8 s^{-1}), due to stable complexes with higher ΔS^* and ΔH^* are formed (ΔS^* and ΔH^* are the entropy and enthalpy of activation for the exchange process) that lacks a dissociative process and breaking the metal-water bond.[46] On the other hand, the amide pendant groups offered an opportunity to increase the second-sphere relaxivity, but the amide donors served

to slow inner-sphere water exchange and decrease inner-sphere relaxivity due to increase in the basicity of nitrogen atoms.

When $[Gd(DOTA)]^-$ is solvated, it has been noticed that it exists in four interchangeable coordination geometries, related as two enantiomeric pairs: the mono-capped antiprismatic geometry (SAP) and the mono-capped twisted square antiprismatic geometry (TSAP), as per Fig. 1.15. It has been reported that of the two configurations, TSAP has the faster water exchange rate by 50 times, because of greater steric crowding around the metal centre leads to form weak ligation with inner-sphere water.[47] The conversion between the four stereoisomers occurs either by cooperative ring inversion ($\lambda \leftrightarrows \delta$) or via the mutual rotation of acetate arms ($\Delta \leftrightarrows \Lambda$) therefore it is noted as *i.e.*, $\Delta\delta\delta\delta\delta/\Lambda\lambda\lambda\lambda\lambda$ and $\Delta\lambda\lambda\lambda\lambda/\Lambda\delta\delta\delta\delta$.

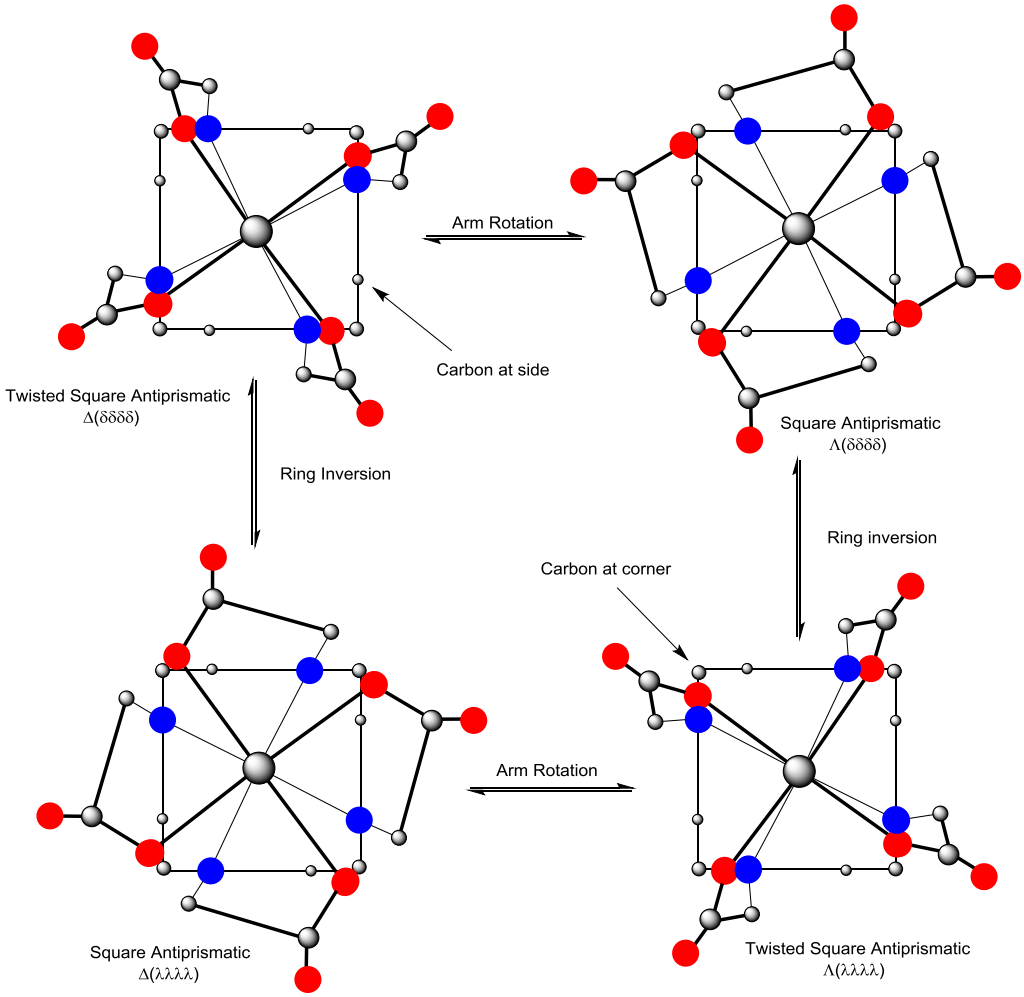

Figure 1.15: $[Ln\text{-}DOTA]^-$ Stereoisomeric structures present in solution. The TSAP isomer has a more "open" coordination cage with a smaller twisting angle between the O4 and N4 planes ~25°, while the SAP isomer has a large twisting angle of ~39° and a close structure.[48]

Recently, Opina and co-workers developed rigidified, symmetrical ligands that incorporate polymethylated groups into the DOTA chelate seeking protein structure determination, as per Fig. 1.16.[48] The complexes with the lanthanide series, showed the square antiprismatic (ΛδδδδδΛδδδδδ) form to be the major isomer for lighter Ln(III) complexes, and the twisted square antiprismatic (ΔδδδδδΔδδδδδ) isomer to be predominant with the heavier lanthanides. It can be related to the size of the Ln(III) and methyl-methyl repulsion that stabilises the TSP isomer.

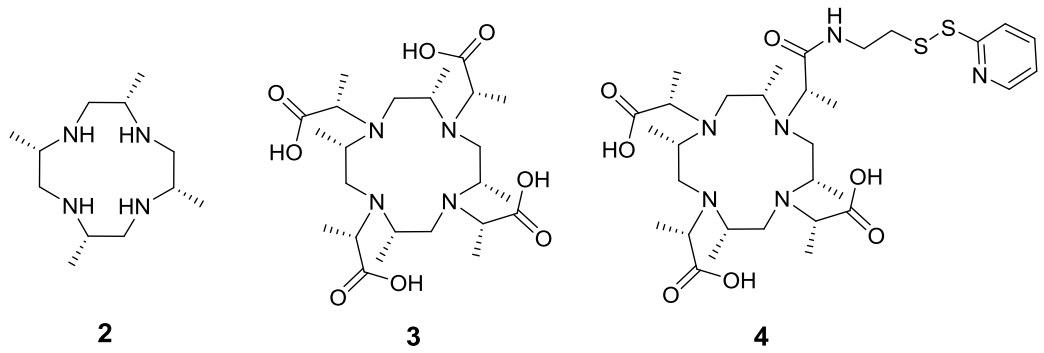

Figure 1.16: Chemical structures of **2**, **3**, and **4**

The reason for the easy conversion between stereoisomers is related to the energetic stabilities and Ln(III)-N distances; for example, Pr-**3** has a longer Pr-N bond length 0.05Å than in DOTA. This indicates that the methyl groups lead to greater steric repulsion. In addition, the exchange rate between the two isomers is considerably increased (up to 9-fold) when the temperature is increased by 55 K.[48] Caravan *et al*. also studied a series of Gd(DOTAlaP) moieties with different substituents Fig. 1.17. They found an enhancement in terms of second-sphere relaxivity compared to Gd(DOTAla), they also found that different R- derivatives on the alanine can block water coordination and produce q = 0 complexes. However, Gd(**5)** and **Gd(6a)** display high water exchange rates and short τ_M values compared to commercial CAs and previous work in the literature (Table 1.5). [49]

	6	**7**	**Gd(DOTAa) -OH**	**Gd(DOTAa) -amide**	**Gd(DOT)**	**Gd(DOP)**
$^{298}k_{ex}$ **x** 10^6 **s**$^{-1}$	97±3	103±2	61	29	4.6	71
$^{310}\tau_M$ **ns**	8.1±0.3	6.4±0.1	8.6	17	97	4.1

Table 1.5. The five complexes exchange rate and residency lifetime.

Interestingly, **Gd(6a)**, **Gd(6b)** and **Gd(7b)** show no inner-sphere water ligation due to high steric hindrance of these groups; however, in these complexes, the second-sphere water plays a crucial role in the relaxivity sequence **Gd(5)** < **Gd(7a)** ≈**Gd(6a)** < **Gd(6b)**. It also was noted that anionic and neutral propionate analogues have no effect on the water exchange lifetime, in contrast to acetate and acetamide substitution.[50]

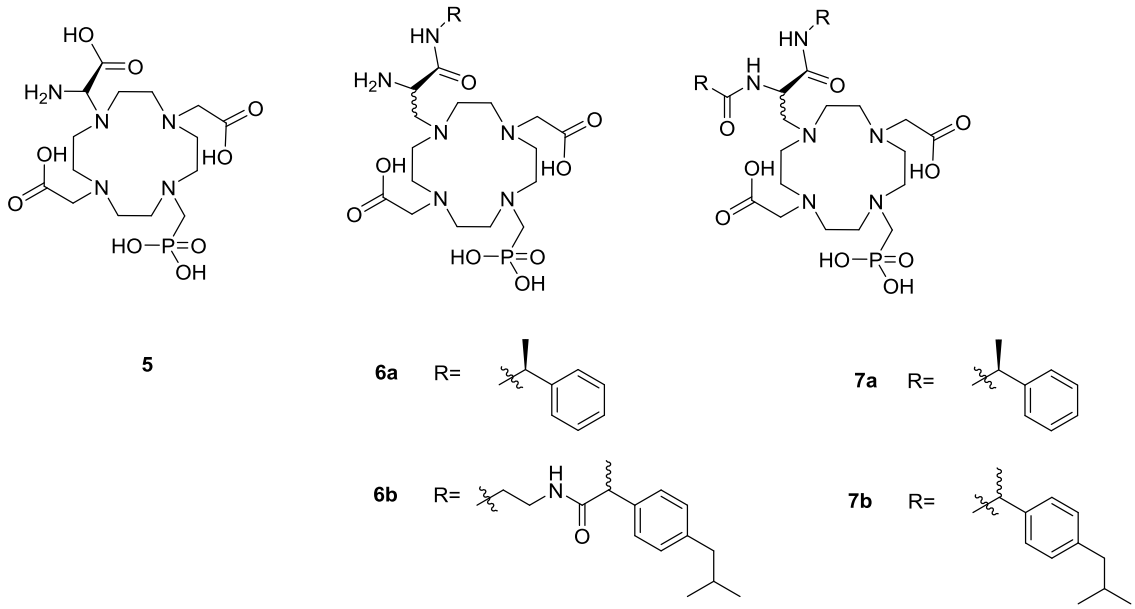

Figure 1.17: The DOTPAla ligands.

1.5 Lanthanides

1.5.1 *Introduction and Properties of the Lanthanides*

The rare earth elements (REE) constitute the lanthanide series and the elements Sc and Y, giving 17 highly electropositive heavy elements. The Lanthanide series comprises lanthanum, La (atomic number 57), to lutetium, Lu (71), with electronic configurations consisting of a xenon core with periodical filling of the seven sub-orbitals, from $4f^0$ to $4f^{14}$. The lanthanides show trivalency (3+), with the exception of Ce, which is also tetravalent (4+) and Eu, and Yb and Sm which can exist as (2+) ions. They can be classified in two ways: the light rare earth elements (LREEs) which includes the elements from La-Gd, and the heavy rare earth elements (HREEs) which have paired electrons, and comprise Tb-Lu as well as Y, due to it having similar chemical and physical properties.[51] The ionic radii drop dramatically from 1.032Å to 0.861Å for La(III) to Lu(III), respectively; this phenomenon is called

the *Lanthanide contraction*. It results from the imperfect shielding properties of the 4*f* orbitals, the effective nuclear charge, Z_{eff}, increases along the lanthanides series.[52]

Lanthanide ions are generally paramagnetic elements, with the exceptions of La(III) and Lu(III), due to the presence of unpaired electrons in the 4*f* orbitals. With the exception of Gd(III), the magnetic moments do not fellow the "spin only" formula as in Equ. (20).

$$\mu = 2\sqrt{S(S+1)} \tag{20}$$

Where S is the total spin angular momentum present of the ion. In the case of heavy metals, paramagnetism is significantly affected by orbital contributions, as in Equ. (21).

$$\mu_{eff} = g_J\sqrt{J(J+1)} \tag{21}$$

Where
$$g_J = 1 + \left(\frac{S(S+1)-L(L+1)+J(J+1)}{2J(J+1)}\right) \tag{22}$$

Where S is the total spin angular momentum, L is the total orbital angular momentum, J is the total angular momentum and g_J is the Landé splitting factor. In the Lanthanides, all three couplings are expressed in the magnetic moment, due to the 4*f*-orbitals being totally shielded by the outer shells of 5s and 5*p* electrons. Trivalent gadolinium has an $^8S_{7/2}$ ground state term, a long electron-spin relaxation time without orbital contribution promotes it as the best paramagnetic ion option in MRI.[53]

1.5.2 *Lanthanide Coordination Chemistry*

Lanthanides are hard Lewis acids with high hydration enthalpies that increase with increasing atomic number, which means multiple-hard Lewis bases such as (carboxylate, ammonia and hydroxide) are required to overcome the desolvation energy and produce a highly stable complex.[54]

In aqueous solution, Ln(III) can form highly stable Ln(III) aqueous complexes, with coordination numbers typically of 9 for the larger ions (La(III)-Nd(III)) and 8 for the smaller ions (Dy(III)-Lu(III)). However, Ln(III) will undergo hydrolysis at pH > 6, resulting in insoluble $Ln(OH)_3$, which is considered an important method of

excluding excess Ln(III) from aqueous solution.[55] On the other hand, its complexes can be dissociated at low pH < 3 due to protonation of pendant carboxylate arms and nitrogen atoms.[56]

1.5.3 *Lanthanide Luminescence*

Lanthanides, especially Eu(III) and Tb(III), have been extensively used in industry and medicine (Fig. 1.18) due to their remarkable photophysical properties, which include narrow emission lines, long life time and high photostability.[57]

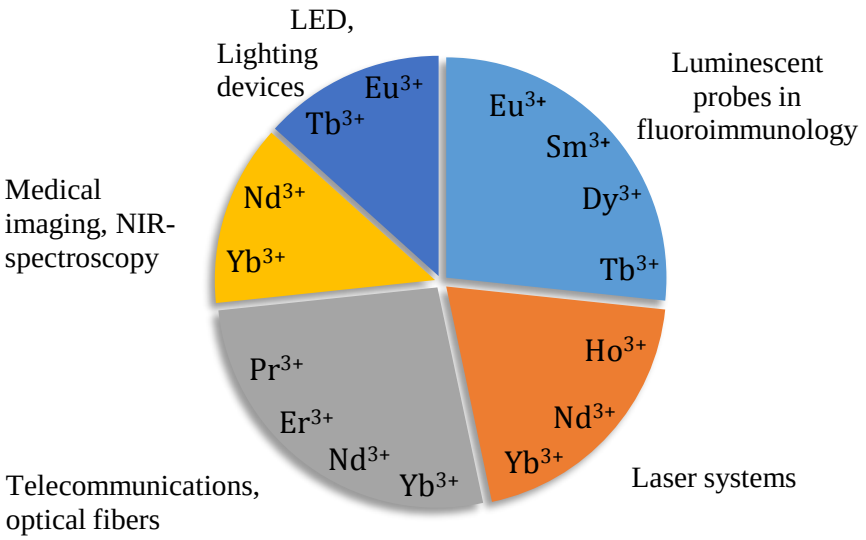

Figure 1.18: Type of emission and related applications of lanthanides.[58]

Lanthanide emission emerges from three types of electronic transition: (i) *f-f* : which can be diagnosed as line-like emission, and is considered the most important type of luminescence; however, it is a forbidden transition, as per the Laporte rule, with low absorption coefficients around 1 M^{-1} cm^{-1}; (ii) *f-d*: transitions, which are broader, fully allowed transitions arising from the transition of excited electrons between the *f* and d subshells. They are largely dependent on the metal environment due to the existing 5*d* orbitals in the outer shell, so it can directly interact with the ligand orbitals; (iii) charge-transfer transitions, both metal to ligand charge transfer (MLCT) and (metal to metal charge transfer) LMCT. Although LMCT typically has low energy it can be seen with Eu(III) and Yb(III).[59] The 4*f* subshell is buried in lanthanide ions, and is well shielded by the 5s and 5*p* orbitals; as a consequence, *f-f*

emission is protected from ligand field effects. Lanthanides emit in the visible and near-IR regions of the electromagnetic spectrum, with the exceptions of La(III) and Lu(III) ($4f^{0}$ and $4f^{14}$, respectively), due to small crystal field splitting energy. Nevertheless, Gd(III) emits in the UV region but it requires a high excitation energy of up to 32000 cm^{-1}.[60]

There are different interelectronic repulsions leading to the emergence of several energy sublevels. For instance, in the Eu(III) ion, the electronic configuration is divided into several terms because of the repulsion between the electrons within the orbitals (electron-electron repulsion). Then, these terms are split into *J*-levels due to spin-orbit coupling ($J = L+S \rightarrow L-S$), which are separated by around 10^3 cm^{-1}. These values represent the free ion levels, which can be suggested by the term symbols *S*, *L* and *J* by $^{2S+1}L_J$, where $2S+1$ is the spin multiplicity, *L* is the total orbital angular momentum and *J* the total angular momentum. The *J*-levels however, can be split into sublevels because of the crystal field, as in the Fig. 1.19 for Eu(III). [61]

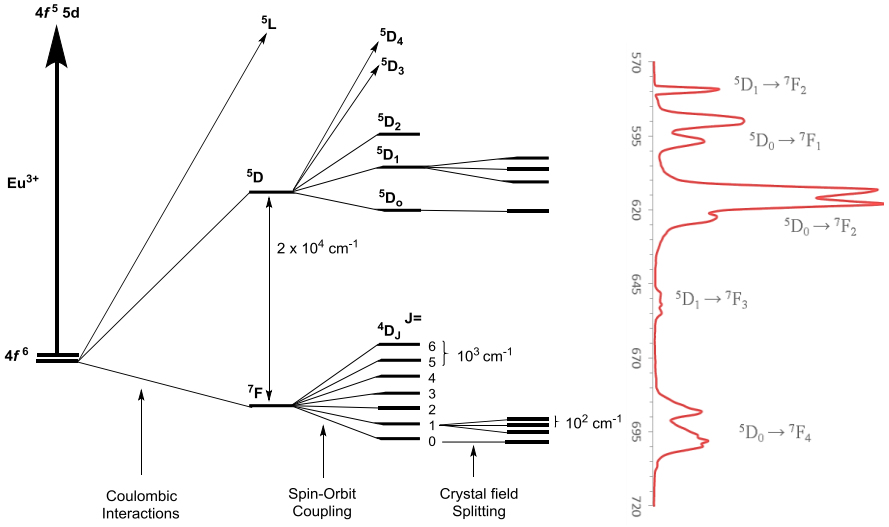

Figure 1.19: Eu(III) ion splitting sublevels and its emission (**EuL6**).

The Gd(III) ion shows a large ΔE at around 311 nm, or 32000 cm^{-1} ($^8S_{7/2}$ to $^6P_{7/2}$) which obviously needs considerable energy to achieve excitation (Fig. 1.20). The maximum emission, λ_{max}, for the Gd(III) ion occurs in the UV region, in the same typical emission region as organic chromophores. So, it is natural to use Eu(III) or Tb(III) (similar chemical properties) instead of Gd(III) to measure the excited state lifetime for *q* determination. Eu(III) and Tb(III) possess large energy gaps without

any intermediate sublevels, are highly photobleaching resistant and have a long luminescence lifetime in aqueous solution.

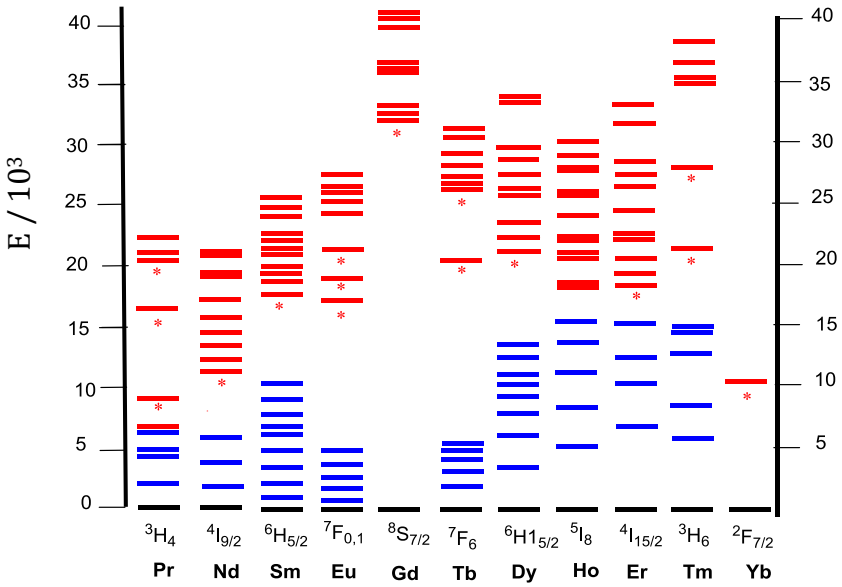

Figure 1.20: Energy diagram depicting the ground (blue) and excited electronic approximate energy levels (red) of a number of aqueous lanthanide ions.

The red and green emission colour for Eu(III) and Tb(III) respectively are widely used for bioanalysis and time-resolved fluorescence detection.[62] Their sharp emission peaks possess longer lifetime about a six-fold than the organic chromophores and a large Stokes shift, which gives a great signal-to-noise ratio detection in bioanalytical applications (Table 1.6). However, in order to record Ln(III) emission in its complexes, high direct excitation energy or indirect excitation (antenna) are required.[63]

Ln(III)	Ground State	Excited State	Excited State Energy (cm^{-1})	ΔE (cm^{-1})	τ(ms)	λ_{max} (cm^{-1})	Emission colour
Sm	^6H_J	$^4G_{5/2}$	17,900	7,400	6.26	590	Orange
Eu	^7F_J	$^5D_0$	17,277	12,300	9.67	620	Red
Gd	$^8S_{7/2}$	$^6P_{7/2}$	32,000	32,000	10.9	312	UV
Tb	^7F_J	$^5D_4$	20,500	14,800	9.02	550	Green
Dy	6H$_J$	4F$_{9/2}$	21,100	7,850	1.85	570	Yellow-orange

Table 1.6: Luminescent properties of selected aqueous Ln(III) ions (Sm(III) and Eu(III)and Gd(III) CN = 9 H_2O, Tb(III) and Dy(III), CN = 8 H_2O).

1.5.4 *Luminescent Quenching and Lifetime Studies for Eu/Tb*

The luminescence of trivalent lanthanides Eu/Tb ions can be quenched by the environment, such as solvents that contain O-H, N-H and C-H bonds. This process involves the transfer of vibrational energy from the excited state to vibrational energy levels of the oscillator. It is found that Ln(III) quenching dependents upon the efficient interaction between excited state and the ground state manifolds, for instance $^5D_0$ of Eu(III) of 12300 cm^{-1} with the v = 3 vibrational overtone of O-H in H_2O. Franck-Condon principle states that population of vibrational states will decrease dramatically with increasing energy levels, due to poor overlap of the ground and vibrational wavefunctions. Therefore, Tb(III) in aqueous media with $^5D_4$ excited state 14800 cm^{-1} overlaps less with the v = 4 vibrational level of H_2O, resulting in less efficient energy and hence longer emission lifetimes in comparison to Eu(III), as per Fig. 1.21. It has also been established for Eu/Tb complexes, that energy transfer to O-D oscillators is 200 times slower than to O-H, due to the lower vibrational frequency of the O-D bond; $\Delta\nu_{OH}$ and $\Delta\nu_{OD}$ are at 3,405 cm^{-1} and 2,520 cm^{-1}, respectively, with no anharmonicity assumed in the vibrational ladder. In addition, the quenching is directly proportional to the number of OH oscillators that are coordinating with the complex. Recording emission intensity vs. time in both H_2O and D_2O enables the measurement of the first-order decay constants, k_{H_2O} and k_{D_2O}, which are applied to Eqs. (23) and (24) in order to calculate the hydration state value, q.[64,65]

$$q_{Eu} = 1.2[(k_{H_2O} - k_{D_2O}) - 0.25] \quad (23)$$

$$q_{Tb} = 5\,[(k_{H_2O} - k_{D_2O}) - 0.06] \quad (24)$$

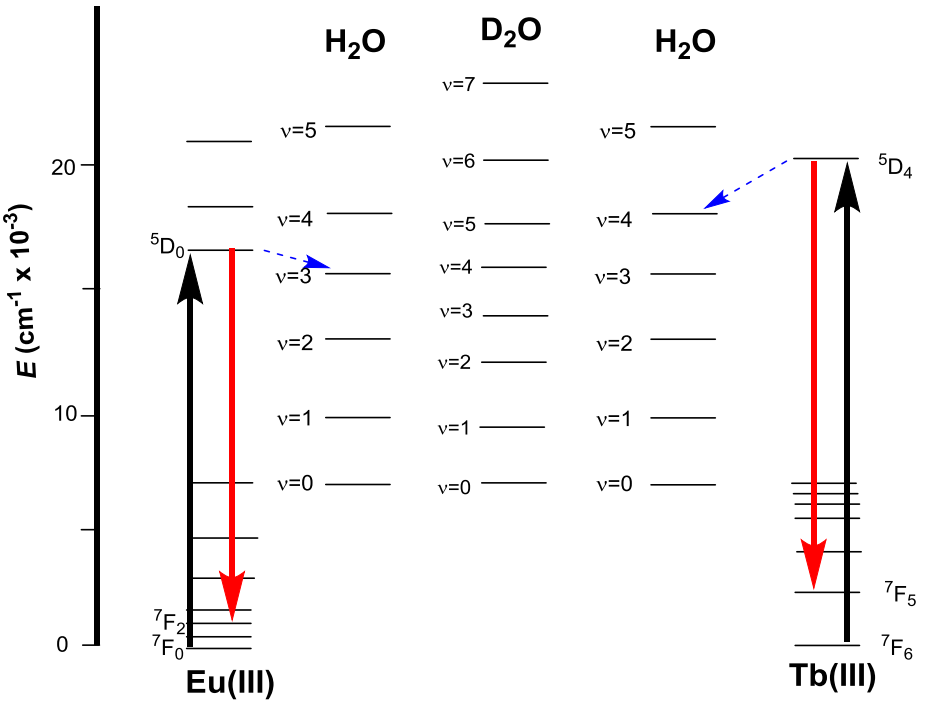

Figure 1.21: Vibrational quenching of Eu(III) and Tb(III) excited states. Excitation (black arrow) occurs from the ground to the excited state ($^7F_0$ to $^5D_0$ for Eu(III) and $^7F_6$ to $^5D_4$ for Tb(III)) followed by emission, shown by the $\Delta J = 2$ transition for Eu(III) (red arrow, $^5D_0$ to $^7F_2 \sim 615$ nm) and $\Delta J = 1$ for Tb(III) (green arrow, $^5D_4$ to $^7F_5 \sim 545$ nm). There is greater overlap between the v = 3 vibrational level of H_2O with the $^5D_0$ excited state of Eu(III) than with the $^5D_4$ excited state of Tb(III) resulting in greater quenching and a shorter lifetime for Eu(III) emission via radiationless energy transfer (blue dashed arrow). The overlap of the v = 4 and v = 5 vibrational levels of D_2O with the excited states of Eu(III) and Tb(III) respectively results in reduced quenching and longer emission lifetimes in this media.

1.5.5 *Sensitised Emission*

As a consequence of such small absorption coefficients $\varepsilon < 1$ $M^{-1}cm^{-1}$, Eu/Tb need high energy excitation source such as argon lasers, for instance, Eu(III) can be directly excited at 395 nm. However, this method is considered inefficient for bioanalyses use due to the possibility of destroying the biological cells and expensive equipment required. A solution is to use a polydentate-chelate grafted with a chromophore (antenna) that has a high absorbance coefficient in the UV-Vis region which transfers efficient energy to the neighbour lanthanide ion.[66] This antenna should be an organic chromophore with a high excitation coefficient, ε, such as a polyphenyl or pyridine group. The mechanism of transferring the energy begins with absorbing energy by the antenna (chromophore) and the electrons in the ground state being excited and promoted to its singlet excited state, S_1. This is followed by intersystem crossing (ISC) to the chromophore triplet excited state, T_1,

with a reversal in electron spin direction. Finally, the excited electrons in T_1 loses its energy gradually as light (phosphorescence) or/and can be transferred to the ^5D excited state of Ln(III) by energy transfer as depicted in Fig. 1.22.[60]

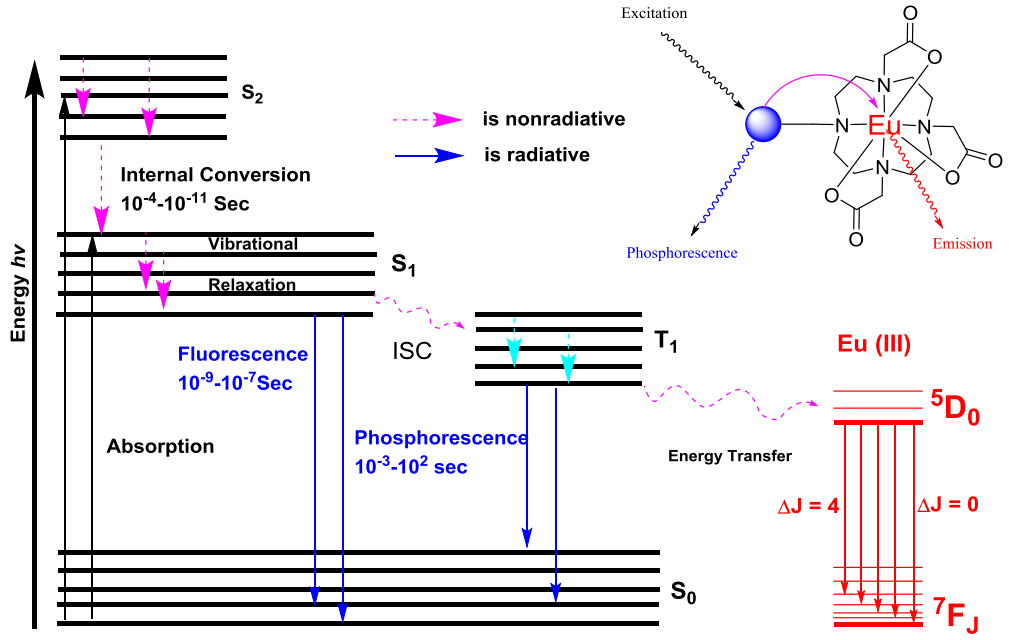

Figure 1.22: Jabloński diagram demonstrating Eu(III) sensitised emission. The excitation (black solid arrows) of an organic chromophore to its S_1 and S_2 state followed by short-lived fluorescence (blue solid arrows). ISC to the chromophore, T_1, (pink dotted arrow), followed by the associated phosphorescence (blue solid arrows). Energy transfer from T_1 to the $^5D_0$ excited state of Eu(III) occurs as T_1 is higher in energy (pink, dashed arrow), resulting in enhanced Eu(III) emission (red, solid arrows). BET (hollow arrows) Inset; schematic representation of an organic antenna bearing Eu-DO3A species.

A Jabloński diagram indicates the possibility of a back energy transfer process (BET). This is can occur if the triplet excited state T_1 is energetically close to a singlet excited state (S_1 or S_2) or to the ^5D Ln(III)'s excited state. In order to obtain excellent sensitising, a decent energy gap is recommended 1500-2000 cm^{-1} between T_1 and ^5D.[67,68] For example, the less energy for exciting Eu(III) and Tb(III) from the ^5D excited state to the *J* levels of the ground term ^7F is 17500 cm^{-1} and 20400 cm^{-1} respectively.

The process of transferring energy between the donor (antenna) and the acceptor Eu^{3+}/Tb^{3+} follows one of two mechanisms. The first involves dipole-dipole exchange, also known as Förster energy transfer, whilst the second involves with electron transfer, also called Dexter energy transfer. The latter requires a wavefunction overlap between the donor and acceptor, which means it can only

occur at short distances; typically within 10 Å. While the dipole-dipole mechanism shows chromophore-metal distance dependence, inversely proportional to the sixth power of the distance between donor and acceptor.[69]

A further advantage of sensitised lanthanide emission is the long luminescence lifetime that is obtained. The incorporation of a delay time, around 200 μs, following initial chromophore excitation allows for the organic fluorescence to be gated-out completely, leaving only the Ln(III) spectrum to be recorded, as per Fig. 1.23. This gives the advantage of excluding short-lived auto fluorescence initiated from biological materials and scattered excitation light. The principle has led to the development of time-resolved immunoassay probes, such as the widely used DELFIA® (dissociation enhanced lanthanide fluoroimmunoassay) method developed by PerkinElmer.[62]

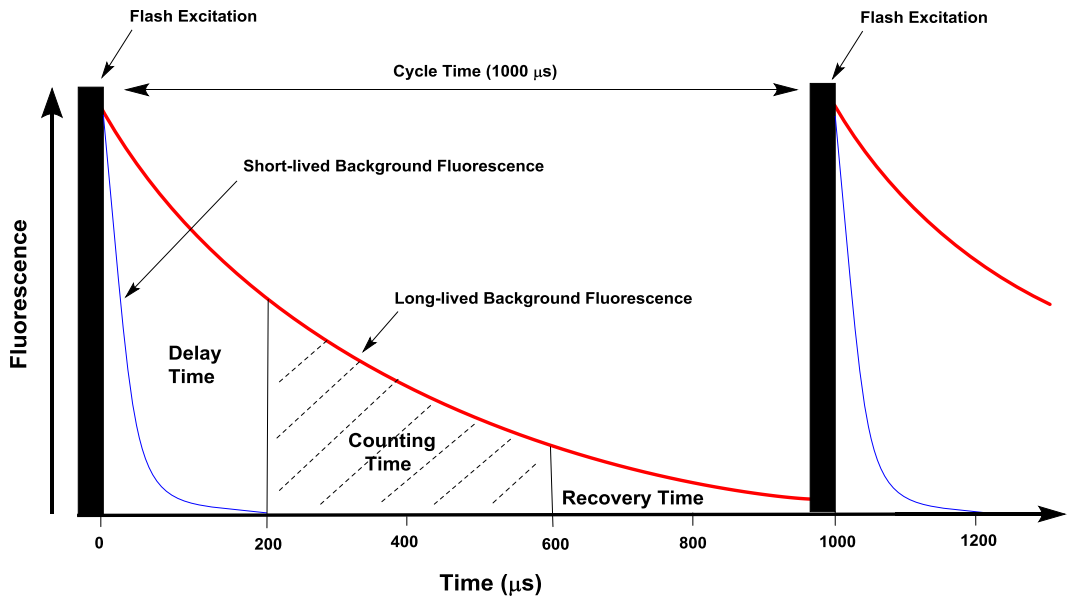

Figure 1.23: Illustration of the principles of time-resolved fluorometry. A delay time of 200 μs is applied to the sample following flash lamp excitation. The organic background fluorescence (blue) has reduced to near zero leaving only lanthanide fluorescence (red) to be measured during the 400 μs counting time. Further excitation occurs after 1000 μs and the experiment is repeated.

Recently, Patra and coworkers. synthesised organelle-specific targeted Eu/Tb luminescent probes **8** (Fig. 1.24) that can stain nucleoli through Pt-DNA crosslinking.[70] The Pt–quinoline ^{3}MLCT excited states act as antennae to sensitize the excited states of Ln(III) via efficient ET at 315 nm excitation. Taking advantage of the significant photobleching resistance, this bioprobe shows excellent stability

and high overall quantum yield ($\varphi_{overall}$) 4.9% and 4.1% with Eu and Tb respectively even though the metal centre is coordinated to one H_2O moiety, compared to only 0.3% for free nucleoli stain SYTO® RNASelect dye.

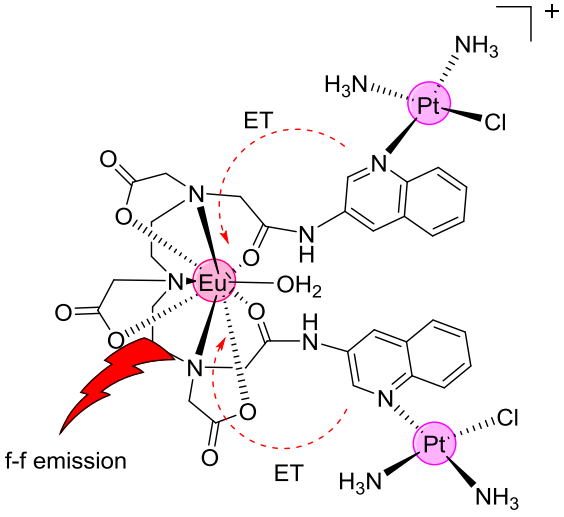

Figure 1.24: **8** structure.

1.5.6 ***Luminescent Lanthanide Probes***

The use of lanthanides in medicine has increased in recent times owing to both magnetic and emission properties. Optical imaging probes containing trivalent lanthanides with macrocyclic chelates, are usually grafted with high excitation chromophores (e.g., ≥ 30,000 cm^{-1}) or complexes that produce ligand-to-metal charge transfer (LMCT) to use for different purposes and applications.[71]

Liang and co-workers recently developed a smart luminescence probe that can detect low H_2S concentrations in biological systems.[72] As shown in Fig. 1.25, the **Eu(8)** complex emits when the pyridine chelate coordinates directly to Eu(III) in the presence of H_2S, this energy transfer occurs. The presence of Cu^{2+} in the aza-18-crown-6 cavity blocks the sensitising by Inter-Ligand Charge transfer (ILCT). H_2S addition removes copper as CuS, followed by a 40-fold emission enhancement. The high selective probe displays significant change in $\Delta J = 2$/ $\Delta J = 1$ intensity due to the lower symmetry of the final structure.

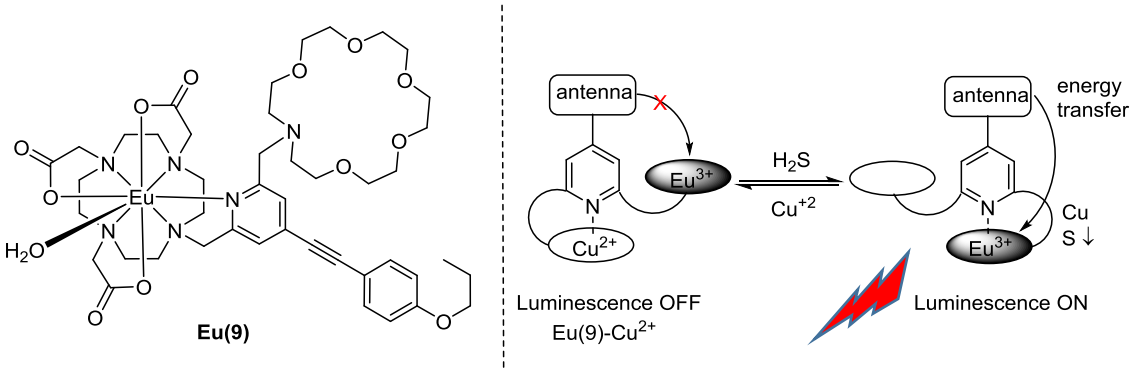

Figure 1.25: The structure of **Eu(1)** and an illustration of the design of a reversible Eu-based luminescence probe (**Eu(9)–Cu²⁺**) for H_2S detection.

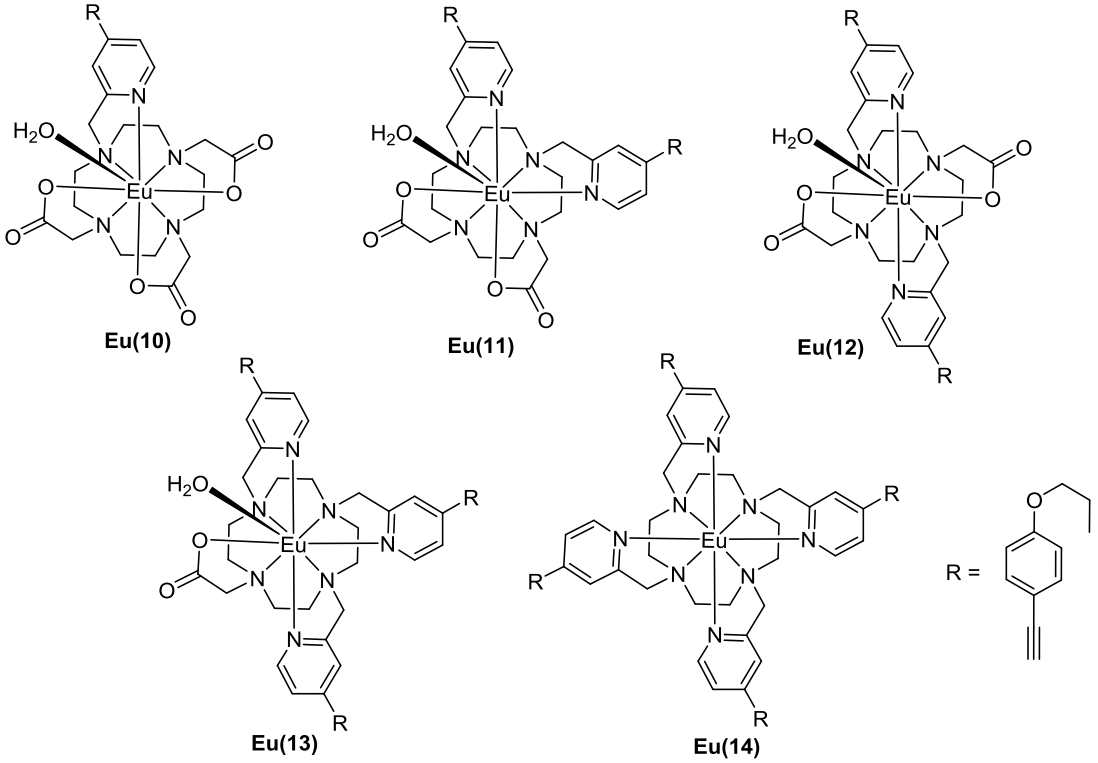

Figure 1.26: The molecular structures of the five cyclen-based europium complexes.

It has been assumed that increasing the number of antenna will enhance the harvesting of light, which will eventually have an effect on quantum yield, overall absorption coefficient and energy-transfer sensitization of Ln(III) emission. Liang *et al.*, examined chelator cyclen-based Eu(III) complexes with different number and distribution of the same pyridine appendant, as per Fig. 1.26.[68] Surprisingly adequate, **Eu(13)** with an overall positively doubled charge was found to be the best

energy-transfer sensitization system, most likely the T_1 energy level of the chromophores close to the ^7D_J excited states of Eu(III).

In terms of examining and matching of ligand to metal energy transfer level, Routledge *et al*., prepared three aryl ketone chromophores-DO3A chelates with various lanthanides as in Fig. 1.27.[73] **Eu(14)** and **Eu(16)** show the most intense emission with triplet excited states 19,900 cm^{-1} and 19,500 cm^{-1} respectively. Because of these T_1 energies are close to $^7D_0$ Eu/Tb excited state, it shows the efficient energy transfer with less back energy or quenching the T_1 by nonradative decay. On the other hand, **Eu(15)** gives a higher energy gap excess of 4000 cm^{-1} between the triplet excited state and the highest excited state of Eu(III), these values explain the differences in quantum yields (up to 18% in water). At low pH it was found the keto non-ionic form complexes are photoemissive unlike the enolate form, due to the formation of LMCT state that induces lower energy than the emissive $^5D_0$ state of Eu(III) 17277 cm^{-1}.

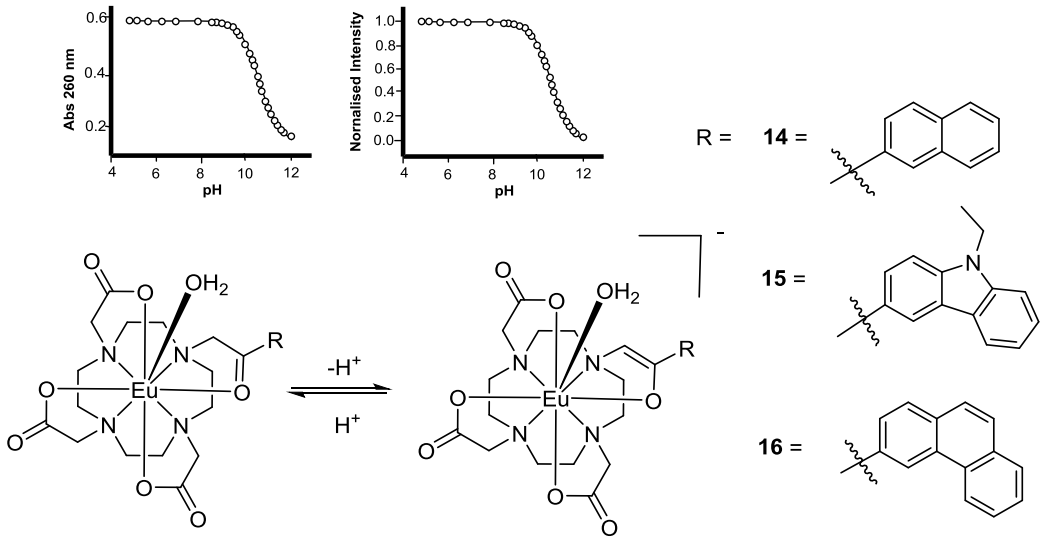

Figure 1.27: Acid base structure of **Eu(14) - (16)** complexes and UV-Vis absorption and emission data for **Eu(15)**.

These results are supported with ^1H NMR spectrum data upon coordinating these ligands with Yb(III), which proves at low pH ($pK_a = 10.5 \pm 0.1$), the aromaticity has been extended in the system. Previous results for **Eu-(14)** and **Eu-(16)** recommended that these complexes could be used as a pH luminescent probes. Since Ln(III) sensitisation depends totally on the presence of a high absorption coefficient moiety, it has been found the emission can be sensitised by direct coordination of

the metal centre to a T_1 ligand with a high triplet excited state. The latter transfers its energy to the metal centre through a Förster mechanism depending on the distance between them.[74] Another strategy can be utilised to produce selective biologically relevant ions sensors, by removing the coordinated antenna as indicator for the presence of specific bidentate ligands. Recently, Vaněk *et al*., synthesised highly selective carbonate sensors that depend on dipicolinic acid (PA) substitution with the CO_3^{2-} anion, as in Fig. 1.28.[75]

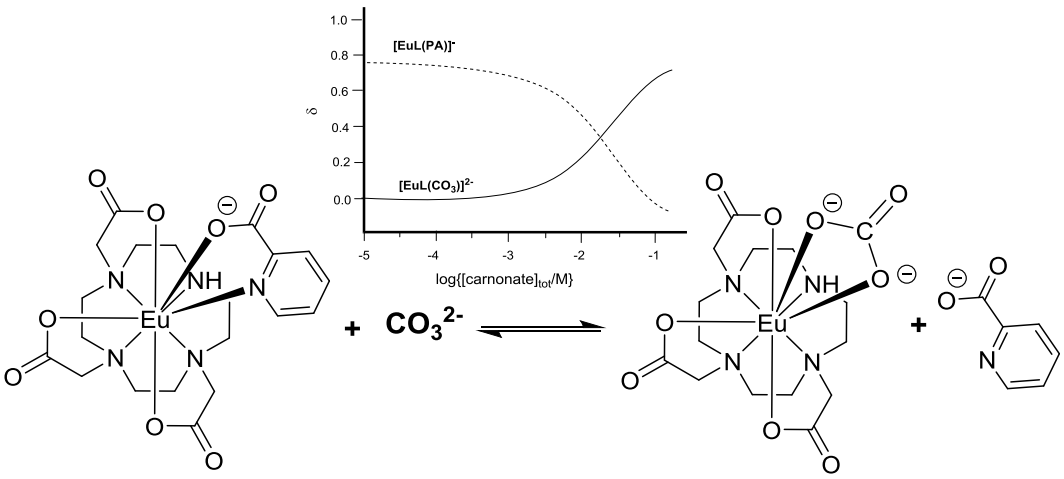

Figure 1.28: Carbonate sensor mechanism and emission exchange profile.

1.6 'Click' Chemistry with Lanthanide Chelates

Copper(I)-catalysed azide-alkyne cycloaddition (CuAAC) ''click chemistry'' has gained considerable attention due to high productivity, cheap raw materials and high stability toward H_2O/O_2 under most synthesis conditions. The Meldal, Afokin and Sharpless publication in 2002 introduced this reaction with Cu(I) (Scheme 1.2), which accelerates the rate of the reactions by 10^7 orders of magnitude compared to purely thermal cycloaddition reactions observed without metal catalysts:[76,77]

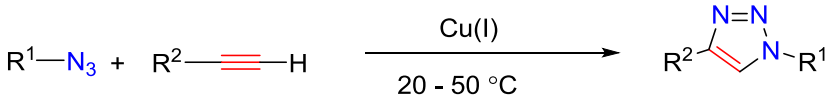

Scheme 1.1: Copper Catalysed azide-alkyne cycloaddion.

The reaction has been widely employed for several fields, including: organic, dendrimer and polymer synthesis. In pharmacology, 1,2,3-triazole compounds offer numerous biological applications such as: anti-allergic, anti-bacterial and anti-HIV

activity has been observed.[78] The catalytic cycle for Cu(I) is shown in Scheme 1.2 with a prediction of a dinuclear copper intermediate species.[79]

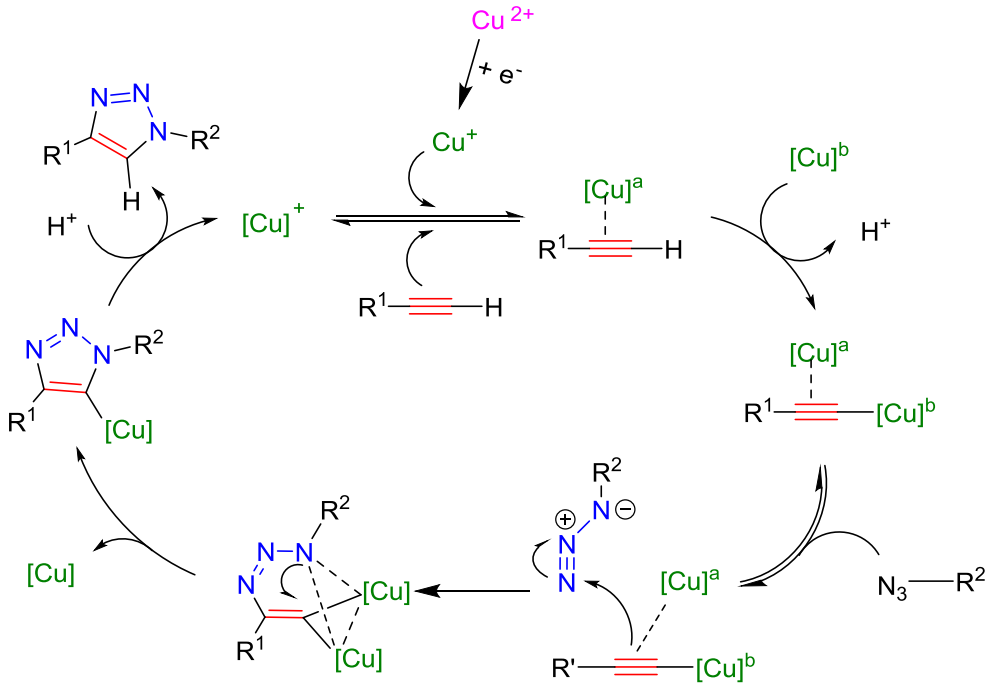

Scheme 1.2: Proposed mechanism for Cu(I) catalysed 1,2,3-triazole formation.

Organic azides potentially have explosive properties, especially if $(N_C+N_O)/N_N < 3$ and they are handled in dry conditions (where N_C, N_O and N_N are number of carbons, oxygen and nitrogen atoms in the molecule respectively).[80] Fokin *et al.*, developed an *in situ* azide generation method from the corresponding alkyl halide and NaN_3 in the presence of Cu(I). This revolutionist one-pot method makes the click reaction much safer and more useful. Furthermore, it has made this reaction microwave applicable with high yields of triazole moieties.[81] A copper-free click reaction has been developed as well, especially with a biorthogonal reaction to avoid copper *in vivo* toxicity.[82]

Triazole can play a role in lanthanide chemistry, it provides an adaptable coordination site, practically with 3 nitrogen atoms that can easily coordinate to the metal centre to procedure a stabile ligation. In addition, it can be employed as a linker between one/two Ln(III)-DO3A systems and a biomolecular/targeting agent, due to a rigid bridge that can be efficiently sensitised Eu/Tb(III). As depicted in Fig.

1.29, the triazole ring exhibits excellent sensitising bridge to transfer the T_1 energy to the DO3A metal centre.[83]

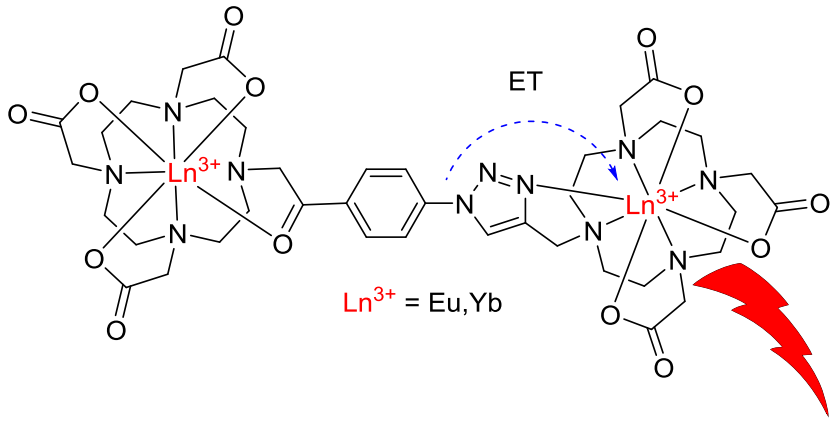

Figure 1.29: Eterometallic lanthanide complexes of azidophenacyl-DO3A.

Molloy *et al.*, investigated bis-lanthanide luminescent sensors synthesis by using copper catalysed 1,3-cycloaddition Scheme 1.3.[84] These probes possess higher order systems with observation of the infrequent $\Delta J = 0$ indicating generation of octa or heptadentate complex. Unfortunately, they failed to synthesise **Eu(17)** with acetamide arms *cf.* **Eu/Tb(18)** complexes that have *N*,*N*-dimethyl analogues, this is more likely related to the coordination between the primary amide and the copper catalyst Cu(I). The circular polarised (CPL) emission spectra shows that **Eu(19)** has polarised D_J = 2 and 4 intensities related to different coordination environment *S* and *R* isomers of the metal ion with the ligation arms. However, due to the water solubility and high energy excitation wavelength drawbacks, these polymetallic macrocyclic analogues high unlikely can be used as imaging probes.

Associating long lifetime emission of biomolecules with 1,2,3-triazole rings has shown a fast growing field of research for time-gated assay applications.[85] This approach has taken by O'Malley *et al.,* who linked Tb-DO3A that has pyridyl-alkyne appended with DEBP protein using click chemistry, see Scheme 1.4.[86] It was found that coordination of pyridyl-alkyne to a Tb(III) metal centre *cf*. pyridyl-carboxylate is preferable in terms of overall quantum yield, due to the efficiency to transfer the energy to the metal centre and close the T_1 of the pyridyl triazole (pyta) to the $^7D_0$ of the terbium.

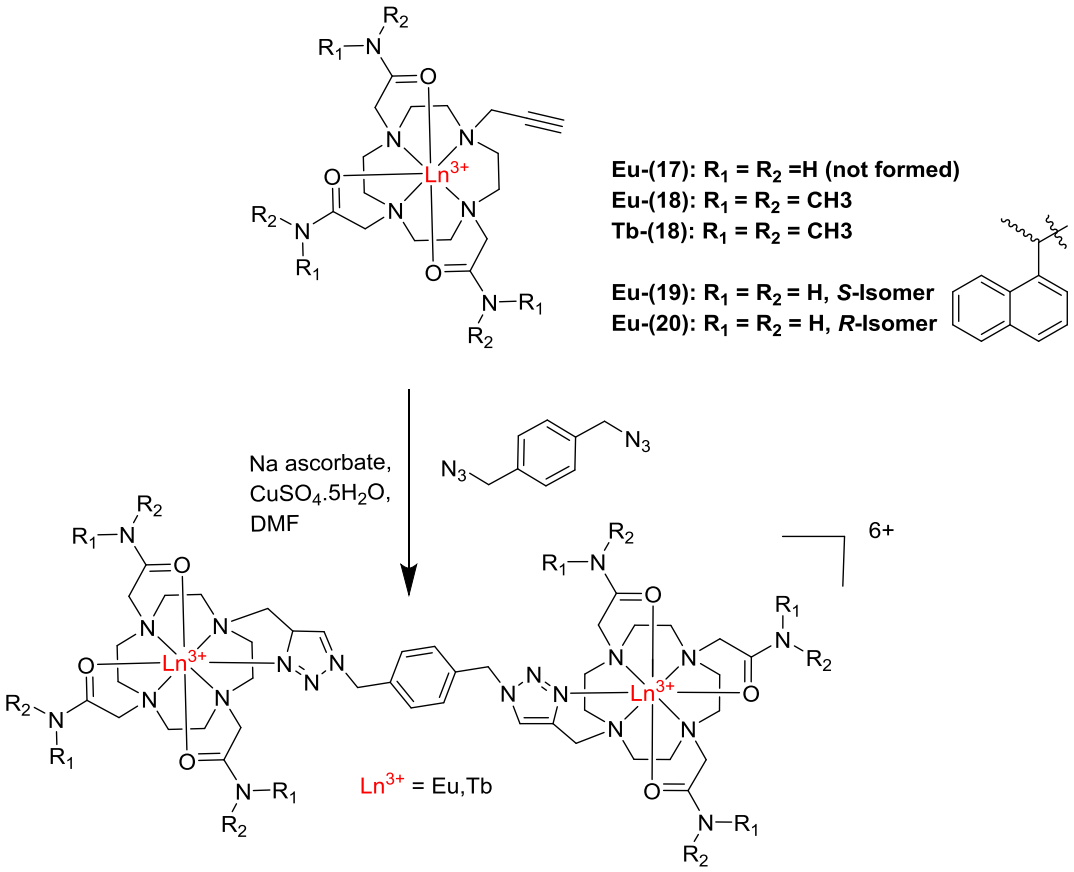

Scheme 1.3: Attempted synthesis of **Eu(17)**, and the synthesis of **Eu(18-19)** and **Tb(18)** using click chemistry.

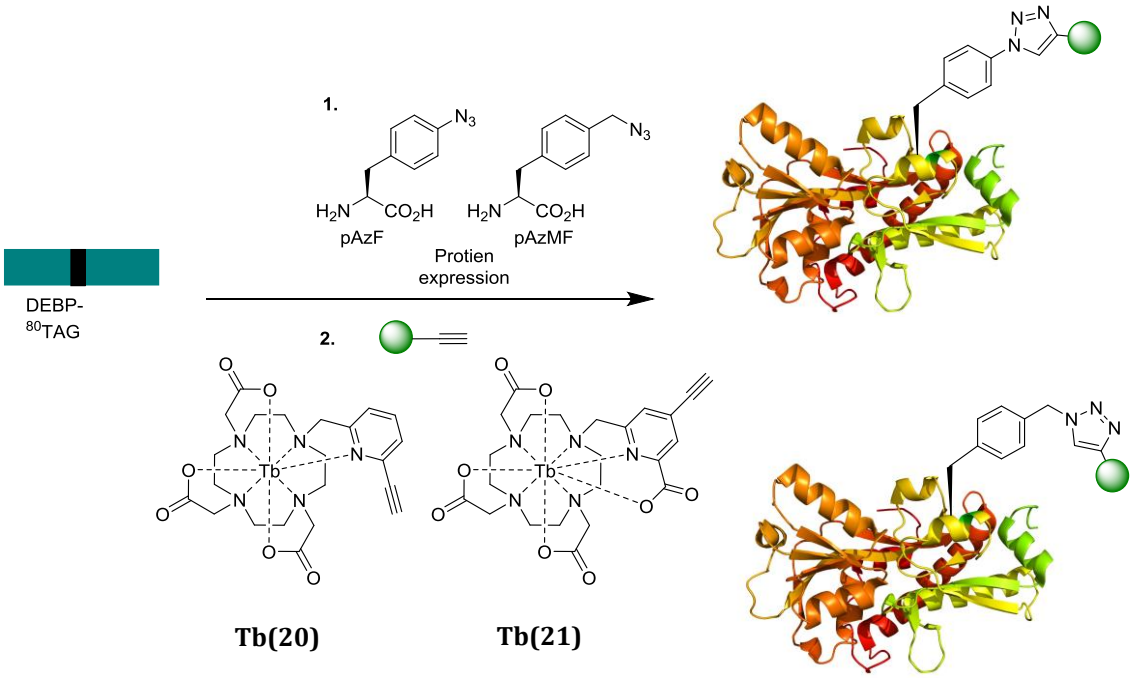

Scheme 1.4. Genetically encoded incorporation of **pAzF** or **pAzMF** into DEBP, and subsequent click ligation with **Tb(20)** and **Tb(21)**.

Generally, 2-pyridyl-1,2,3-triazole moiety derivatives introduce a variety of interesting properties especially in inorganic chemistry see Fig. 1.30.[87]

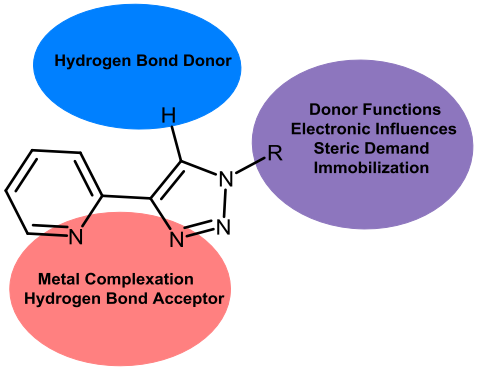

Figure 1.30: Functionality of 2-pyridyl 1,2,3-triazole (pyta) ligands.

1.7 Luminescent Transition Metal Complexes

1.7.1 *Background*

Organic fluorophores possess short fluorescence lifetimes, owing to π-conjugated ligands that originates from the spin allowed $S_1 \rightarrow S_0$ transitions. Furthermore, they have a small Stokes' shift and weak or no spin orbital coupling (SOC) which means lack of phosphoresce. On the other hand, the d^6 and d^8 second and third row transition metals ions [Re(I), Ru(II), Os(II), Ir(III), and Pt(II)] have significant features enabling them to occupy centre stage in biological imaging, as chemotherapeutic agents and other in biomedical applications. These are: large Stokes' shift (often > 5000 cm^{-1}), which can minimize self-quenching with high signal-to-noise ratio; a wide range of light emission usually in the visible region, due to the ability of tuning their emission; their complexes are well established and they display long-lived phosphorescence at room temperature (ns - 10 μs) allowing exclusion of background emissions; enabling them to be used in lifetime imaging microscopy. These heavy metals facilitate (SOC) pathways which enhance the population ($S_1 \rightarrow T_1$) that includes changing spin direction which depends on spin-orbital coupling constant, ξ, of the metal. Fortunately, relaxation from ($T_1 \rightarrow S_0$) is slower, due to $\Delta S \neq 0$ where S is the multiplicity. Nevertheless, even with these favourable properties, researchers face various obstacles related to TM emission, such as: quenching by O_2, variable complex solubility/stability and other quenching problems.[88,89]

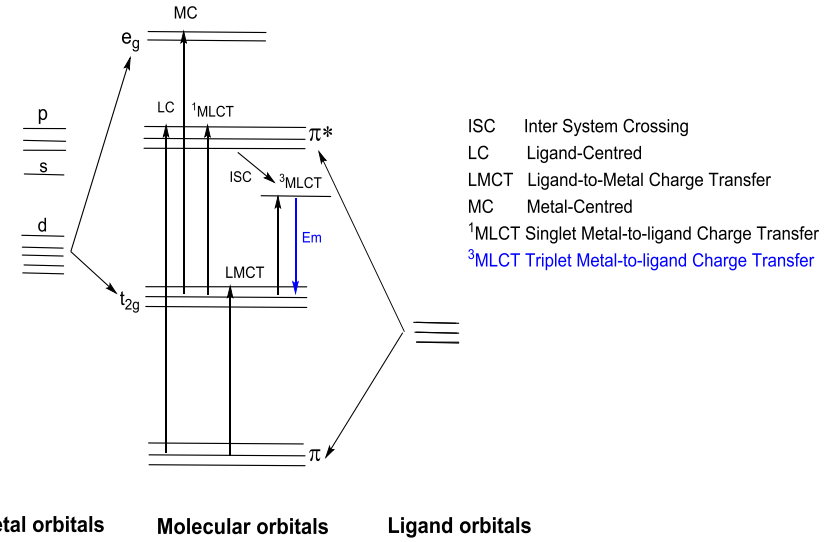

Figure 1.31: Simplified MO diagram of an octahedral MLC showing possible transitions.

Fig. 1.31 illustrates the origin of TM luminescence, which is generally promoted from the ^{3}MLCT excited state.[90] An electron from the mostly metal t_{2g} or ligand π Highest Occupied Molecular Orbital HOMO (electron donating) is promoted to the ligand-centred Lowest Unoccupied Molecular Orbital LUMO (electron accepting) which is typically the π* orbitals of the ligand. This generates a ^{1}MLCT excited state which is considered the singlet excited state (t_{2g}^5 π^{*1}). These transitions usually have higher absorptions coefficient in the visible region (ε = *ca.* 20,000 – 25,000 L mol^{-1} cm^{-1}). Then, depending on the efficiency of the ISC pathway, to ^{3}MLCT, the energy from this singlet excited state (^{1}MLCT) transfer can then relax to ground state (t_{2g}) with the energy lost as luminescence.[91, 92]

1.7.2 *Ir(III), Pt(II), Ru(II) and Re(I) Photophysical Properties*

The use of luminescent transition metal complexes for optical imaging has shown considerable growth over the last few decades, particularly with regards to delivering high resolution images to 1μm in the visible region.[93] In this field there are four transition metals that dominate in bioimaging: Ir(III), Ru(II), Pt(II) and Re(I) ions owing to formation of highly stabile, low-spin d^6 octahedral complexes (except square planer d^8 Pt (II)) with a large energy gap (Δ) making the potentially quenching the MC excited state higher energy in than the MLCT state. Trivalent iridium is the most used ion in bioanalysis, especially the heteroleptic-cyclometallated complexes, for example $[Ir(N^{\wedge}C)_2(N^{\wedge}N\text{-bpy})]^+$, due to its very solid

synthesis protocols, efficient ISC, long radiative rate decay and as well as the low net charge (+1) that is superior for cell membrane penetration. Divalent ruthenium however, is a strongly π-accepting metal which enhances ISC through preferable spin-orbital coupling. $[Ru(bpy)_3]^{2+}$ complex possesses high ^{3}MLCT emission in the visible region centring at ~610 nm, a large Stokes shift, high photostability with a long lifetime of around 500 ns. In the case of Re(I) the famous archetypal complex framework is $[Re(bpy)(CO_3)X]$ (X= ancillary ligand, such as halogen or pyridine). Due to the simplicity of the synthesis, the ease of linking to biomolecules and ease of tuning of the photophysical properties, these precursors grab great attention especially in Raman imaging microscopy. Re(I) tricarbonyl complexes with (*e.g.* pyta) show interesting photophysical properties such as low phototoxicity and stable light emission, promoting their use in confocal microscopy. Finally, d^8 Pt(II) 4-coordinate square planar geometry, especially cyclometallated complexes, have long lifetimes and unique characteristic emission in both their monomer and excimer form.[94-97]

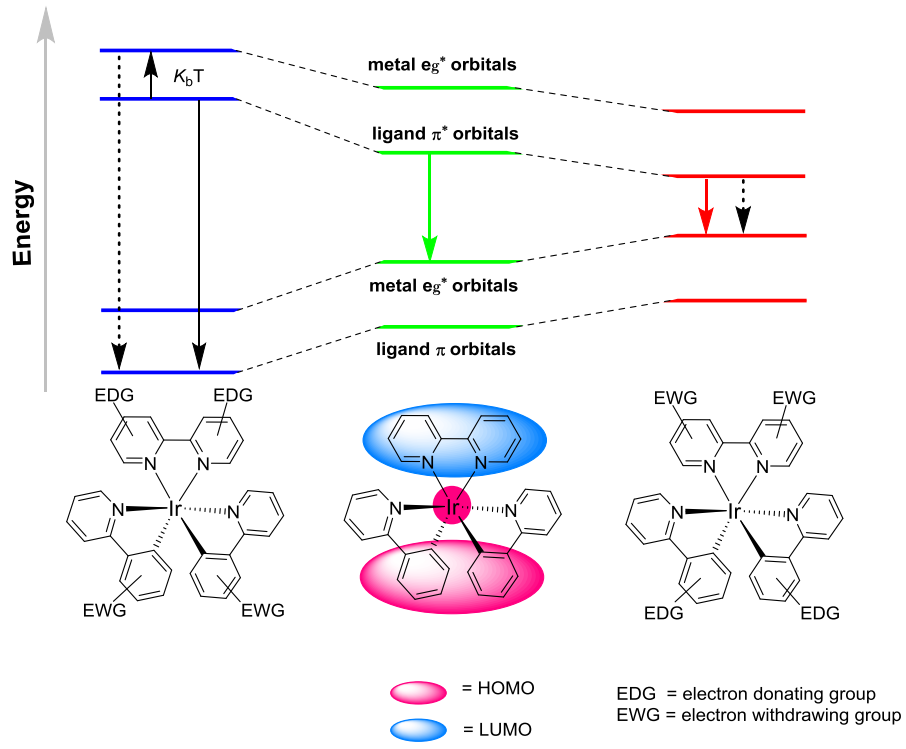

Figure 1.32: General scheme depicting strategy for colour tuning the emission of $[Ir(ppy)_2(bpy)]^+$, indicate an electron density distribution on the HOMO that is largely localised on the metal centre and the phenyl rings of the cyclometalating ligands, and on the LUMO that is largely localised on the bpy. This allows for tuning of the emission by appropriate functionalisation of the ligands. Dashed arrows indicate deactivation from the excited state via non-radiative decay.

The energy gap between HOMO and LUMO as well ligand design control the photophysical properties of TMs. For example, decreasing the separation between HOMO and LUMO will lead to a *Bathochromic shift*. It occurs by both rising the HOMO level (destabilising it) and/or lowering the LUMO (stabilise it), and *vice versa* as in Fig. 1.32.[98]

For instance, Donnelly *et al.*, recently worked on this by synthesising numerous $[Ir(C^{\wedge}N)_2(N^{\wedge}N)]BF_6$ complexes as in Fig. 1.33.[99] The absorption maxima of the MLCT band for complexes that contain 2-(2,4-difluorophenyl) pyridinato derivatives ($C^{\wedge}N$) show hypsochromic shifts (~20 nm) due to stabilising of the HOMO levels, while the complexes with 1-phenylisoquinolinto ($N^{\wedge}N$) demonstrate bathochromic shift in both ^{1}MLCT and ^{3}MLCT due to the greater increase of the

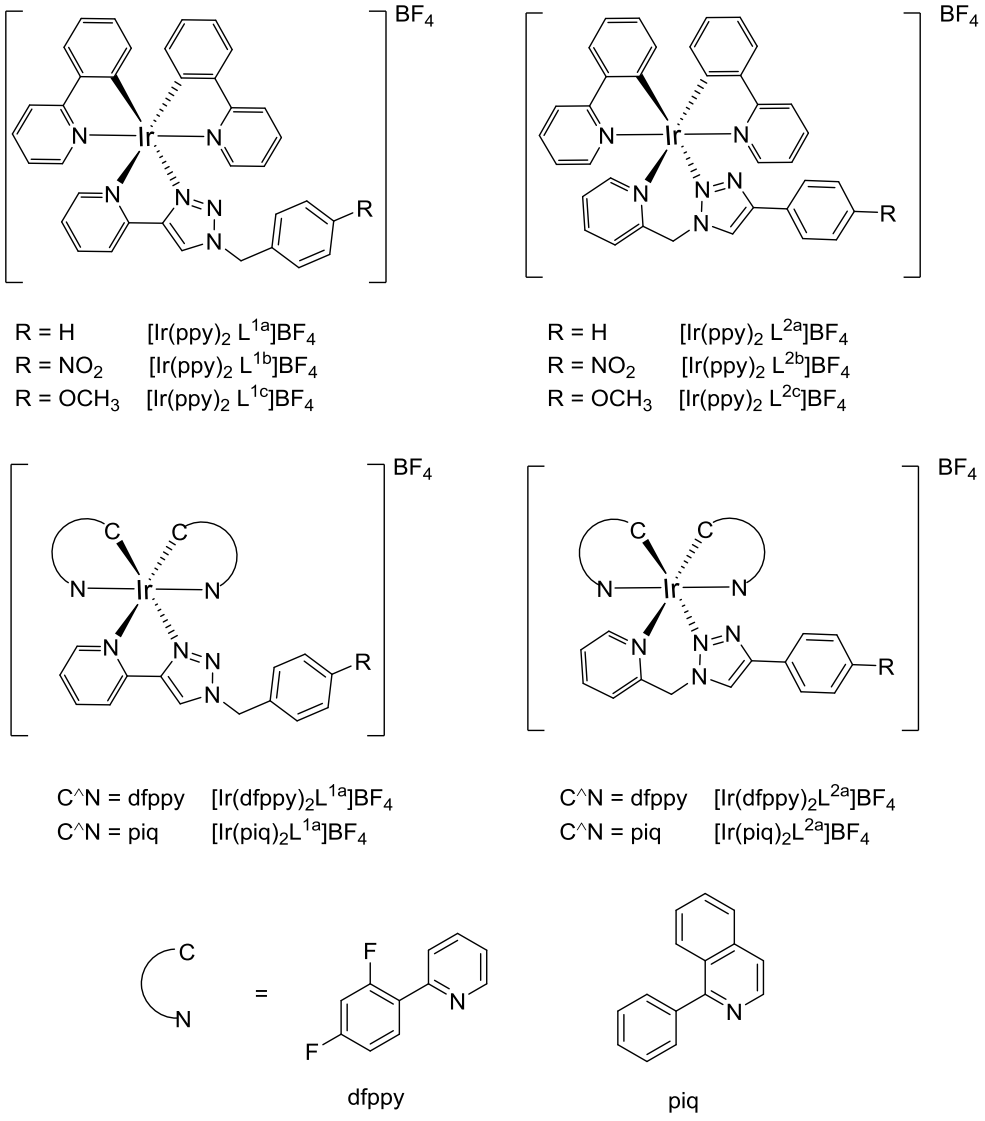

Figure 1.33: (ppy), (dfppy) and (piq) Ir(III) complexes with 1,2,3-triazole-containing ancillary ligands.

oxidation potential, leading to destabilising the HOMO. Generally, $[Ir(ppy)_2L^{1x}]BF_4$ has the best results in terms of stability in solution, quantum yield and lifetime, due to possessing a longer nonradative rate constant. Interestingly, complexes with L^{1x} in general show higher intensity emission and longer life-time *cf.* inverse L^{2x}, because of the flexibility of six membered ring with Ir(III) comparing with rigid five membered ring in L^{1x}. This pattern also appeared with Re(I) tricarbonyl complexes with L^{1x} and L^{2x}.

As mentioned before, TMs can be used for different medical applications such as biosensors, cellular probes and potential photodynamic therapy (PDT) of cancer. The latter depends on generating $^1O_2$ by quenching the triplet MLCT excited state indicated by enhancing the non-radiative characters, eventually low emission intensity from ^{3}MLCT and singlet oxygen is produced. The pattern of singlet oxygen formation increases alongside escalation emission lifetime, this production can be monitored in the near infrared region 1270 nm (O_2 emission).

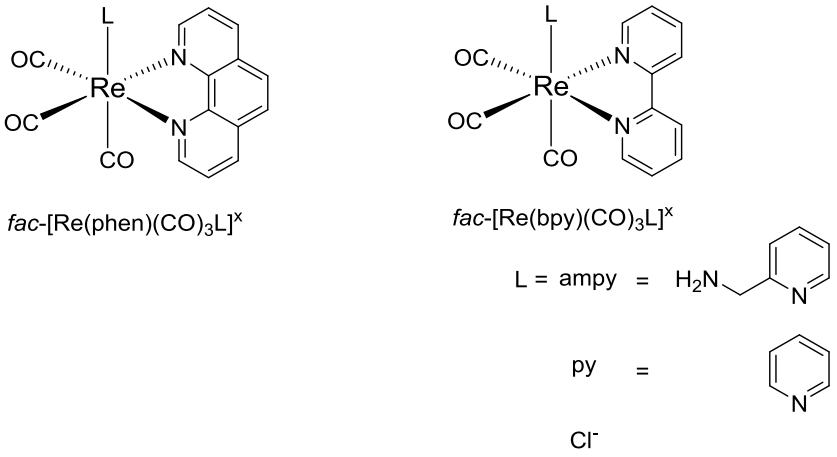

Figure 1.34: Chemical structure of rhenium polypyridyl complexes.

Following the same principle, Frin and co-worker synthesised rhenium polypyridyl analogues Fig. 1.34 and they found all the complexes can work as oxygen photosensitisers especially with a (phen) moiety, that exhibits a long lifetime with $k_r < k_{nr}$ as in Table 1.7. In terms of emission, Cl^- (σ donating) substitution with py (π acceptor) led to a hypsochromic shift due to destabilising the ^{3}MLCT. Whilst increasing the conjugation in N^N by using phen ligand led to a bathochromic shift

because of stabilisation of the ^{3}MLCT excited state (decreasing LUMO energy levels).[100]

	λ_{em} (nm)	τ(ns)	K_rx10^5 S^{-1}	K_{nr}x10^5 S^{-1}	Φ_Δ
[Re(ampy)(CO)$_3$(phen)]$^+$	560	560	1.63	16.20	0.55±0.05
Re(py)(CO)$_3$(phen)]$^+$	550	1300	1.38	6.32	0.59±0.02
[ReCl(CO)$_3$(phen)]	600	138	1.20	71.3	0.41±0.01
[Re(ampy)(CO)$_3$(bpy)]$^+$	568	100	2.40	97.6	0.38±0.01
[Re(py)(CO)$_3$(bpy)]$^+$	566	232	2.38	40.7	0.43±0.03
[ReCl(CO)$_3$(bpy)]	611	29	0.69	344	0.28±0.02

Table 1.7: Emission data and singlet oxygen quantum yield for Re(I) complexes in MeCN.

In summary, there are specific requirements for any imaging probe to be a best candidate for biomedical imaging:[94]

(i) A high absorption coefficient in the visible region.
(ii) A high emission quantum yield with reasonable emission lifetime.
(iii) Solublity in water.
(iv) Specificity.
(v) Penetration ability.
(vi) High thermodynamic stability and kinetic inertness.
(vii) High photostability, inducing high resistance to photobleaching.

1.8 Thesis Outline

There are numerous factors that can affect MRI CAs-Gd(III) effectiveness; the hydration state, q, number of Gd(III) chelates, water exchange rate, k_{ex}, and the rotational correlation time, τ_R. These elements can be manipulated in order to enhance relaxivity, r_1 and MR image intensity. Eu(III)/Tb(III) exhibit unique luminescent properties, similarly, transition metals such as Re(I), Pt(II) and Ir(III) are possessed of high quantum yields with long emission lifetimes and emit in the visible region that can be utilised for different bioimaging probes. The chapters in

this thesis will focus on various aspects and application of Ln(III) and Ln(III)-TM complexes.

Chapter 2 describes the chemistry of the synthesis of lanthanide chelates. Synthesis of the proligands and Eu(III)/Gd(III) precursors will be discussed. Numerous types of coupling, click reaction chemistry and metal complexation are involved in this section. These syntheses involve amongst other things, purification, and characterisation using different techniques such as: (RP) HPLC, NMR spectroscopy, and (HR) MS and the photoluminesence will be discussed.

Chapter 3 focuses on the synthesis of dual-mode magnetic resonance/optical imaging probes, by using Gd-DO3A analogues as CAs and taking advantage of Pt(II), Ru(II) and Ir(III) as luminescent transition metals. Pyridyl-triazole pendant derivatives are applied as ideal coordination sets for d^6/ d^8-block transition ions as well as phenyl-triazole and phenyl-pyridine which have been used in Ir(III) chelates.

Chapter 4 demonstrates the synthesis of a carbonate sensor, depending on the release of H_2O quenching water form Eu(III). Complexes containing both Re(I) and Eu(III) have been synthesised with different pyridyl-triazole pendant derivatives. The carbonate binding constant and the quantum yields were measured, as well as the relaxivity of the Gd(III) analogies to prove the substitution of H_2O with CO_3^{2-}.

Chapter 5 discusses synthesis and characterisation of metallated heteronuclear lanthanide complexes. Various Gd-ligands assemblies have been joined together using a pyridyl-triazole appendant with different transition metals such as Fe(II) and Co(III). The longitudinal relaxation time, T_1, was enhanced three fold compared with single Gd-DO3A analogous owing to increase the payload of Gd(III) chelates.

Chapter 6 covers the synthesis of smart MR contrast agents sensitive to pH changes. Gd-DO3A with 2-[(methanesulfonyl)amino]ethyl moiety exhibits a promising T_1 sensitivity over the physiological pH range. In addition, different MR phantom images at different pH levels were observed, as well as preliminary *in vivo* studies

Chapter 7 establishes all the conclusions and future direction.

Chapter 8 describes the experimental part.

Chapter 2

Synthesis of Ligands and Mono Ln(III) Complexes

2.1 Project Outline and Objectives of the work

As introduced earlier, the aim of this work was to develop a range of dual mode multimetallic complexes with two functional parts: a transition metal-centred complex, generally showing a framework with high chemical stability and interesting photophysical properties such as a long-lived ^{3}MLCT excited state for optical imaging and a Gd-DO3A unit to use as contrast agent in MRI, as shown in Fig. 2.1.

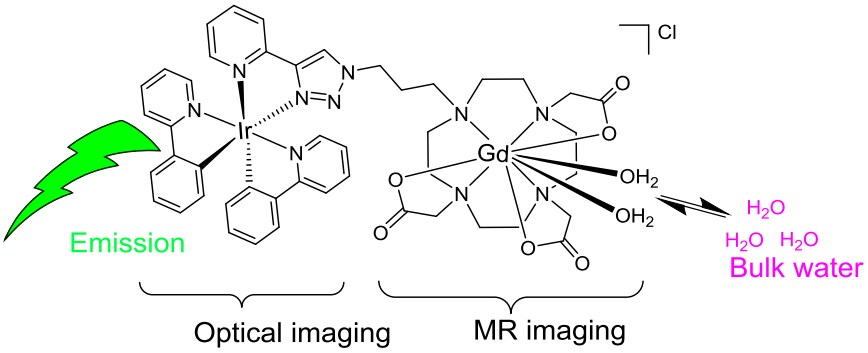

Figure 2.1: Schematic representation of the assembly of the dual mode MRI/OI probe.

With suitable design of diimine ligands or ancillary ligands in Pt(II) and Ir(I) complexes, their photophysical and photochemical properties can be readily tuned and modified. A number of TMs were investigated by taking the advantage of pyta analogues to synthesise a range of dual-mode MRI/optical imaging probes with varying numbers of pendent Gd-DO3A units. Variation of the cyclometallated and ancillary ligands was explored with Ir(III)/Pt(II) to adjust the excitation/emission wavelength for specific fluorescence microscopy applications.

In addition, the ligand system can be used in the design of a luminescent multimetallic Re(I)/Eu(III) complexes as carbonate sensors that depend on the on/off switching of Eu(III) emission. These heteronuclear complexes use Re(I) photoluminescence as an internal reference for monitoring carbonate binding related to variation of Eu(III) emission intensity, as depicted in Fig. 2.2. In this

context, this work aims to improve the luminescent properties of charge-neutral rhenium(I) diimine complexes and explore their possible applications.

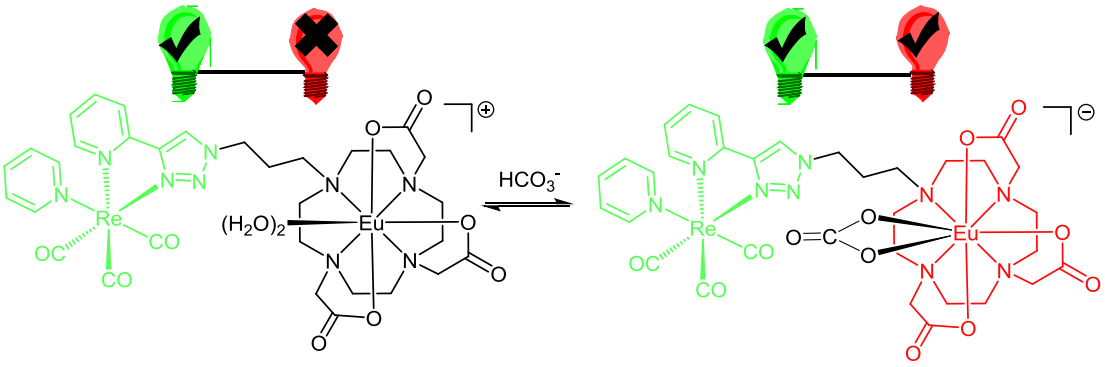

Figure 2.2: Mechanism of a carbonate sensor imaging probe mechanism.

To have a better understanding and future exploitation of the intrinsic Re-Eu heteronuclear complexes as a biological carbonate sensor, a series of luminescent Re(I) and Eu(III) complexes have also been prepared. The photoluminescence properties of Re(I)-pyta functional were investigated by modifying the pyridyl moiety with an electron donating / electron withdrawing groups. The photophysical properties for these analogues govern their potential use in confocal microscopy.

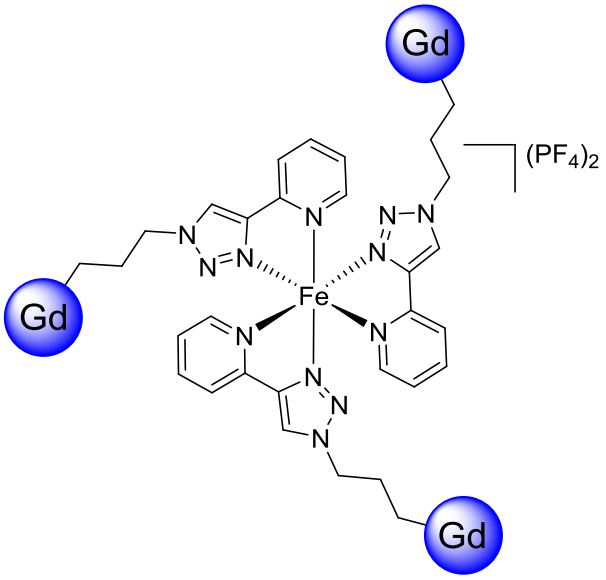

Figure 2.3: High molecular weight MRI CA.

Furthermore, high molecular weight heteronuclear complexes (Fig. 2.3) that can potentially offer higher relaxation were synthesised. These complexes consist of a diamagnetic low spin d^6 Fe(II)/Co(III) core with numerous pendant Gd-DO3A

units. The aim was to lower T_1 due to incorporation of a number of q = 2 contrast agent arms and an increase in the rotational correlation time.

The synthesis of the ligands in this woke involved various organometallic catalytic reactions, even so, this work obtained promising reaction yields that can be used as a reference in DO3A ligands/ Ln(III) complex synthesis. Ultimately, water soluble probes were produced that can be used for biological applications. A further target was the synthesis of an MRI contrast agent which contains a pendant sulfonamide, capable of responding to changes in pH within the physiological range, by changing its hydration number (Fig. 2.4).

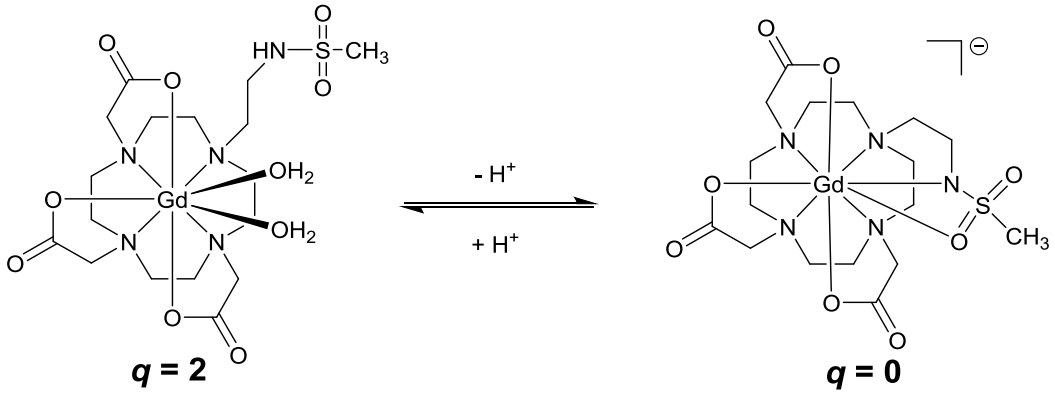

Figure 2.4: Mode of action of a contrast agent that responds to changes in pH.

The pH-responsive MRI contrast agents were design to detect changes in the pH of the brain after stroke. The pH sensitive MRI contrast agent can penetrate the BBB which is disturbed after a stroke. The relaxivity enhancement in acidic environments can be used to report on the changing in pH. The sulfonamide pendant can coordinate to the Gd(III) metal centre at normal physiological pH (pKa = 6.1) leading to a drop in the r_1 due to lack of water ligation and *vice versa*. The function of this probe was tested in a stroke model in a biological system, to explore the localisation, dose and permeability.

A key aspect of this chapter is discussion of the synthesis of pro-ligands and the monolanthanide chelators, which are used for further complexations in chapters 3-5. The ligands were synthesised following various carbon-carbon coupling with numerous S_N2 reactions. Both the pro-ligands and Ln(III)-complexes were characterised using different spectroscopy methods of analysis such as NMR, MS and fluorescence spectroscopy.

2.2 Synthesis of Pro-ligands

This work focuses on synthesis of DO3A with various pyridyl-triazole (pyta) pendants. These pendants were synthesised first *via* Sonogashira cross-coupling to install an alkyne moiety onto the pyridine precursor before undergoing Copper-catalyzed Alkyne–Azide Cycloaddition (CuAAC) to reach the desired bidentate pyta ligand. These bidentate (N^N') pendants are designed to coordinate with various transition metals, whilst acting as an antenna for Eu(III) ion excitation. Pyridyl-1,2,3-triazole (regular) produces high stabilise complexes with similar photophysical properties to bipyridine in octahedral complexes.[101,102] The chapter begins with a series of palladium-catalysed cross-coupling reactions.

2.2.1 *Cross-Coupling Reactions*

2.2.1.1 Sonogashira Cross-Coupling Reaction

In order to synthesise pyta ligands bearing electron withdrawing groups, first the 4/5 CF_3-substuted 2-ethynylpyridine was synthesised.

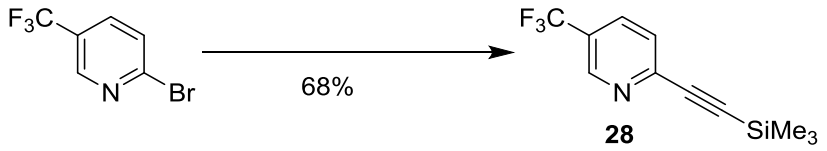

Scheme 2.1: **Reagents and conditions:** TMS-acetylene, $Pd(PPh_3)Cl_2$ (2 mol%), Et_3N:THF (1:1), CuI (4 mol%), rt 20 h.

The palladium-catalyzed sp^2-sp coupling reaction was used to link the pyridyl ring with trimethylsilyl acetylene, as seen in Scheme 2.1 to prepare **28**. These reactants were used in a 1:2 equivalency with of TMS-acetylene, in order to push the reaction forward and account for some loss of the volatile TMS-acetylene in excess. This carbon-carbon coupling reaction is catalytic and proceeds as per the catalytic cycle as in Scheme 2.2. Notably, in this reaction addition of a dry solvent such as THF (strong base), alongside the base, increases the yield by about (26%) compared with the same reaction without THF.[103] Despite these conditions, an amount of homocoupling is still observed, both by TLC and in the crude ^1H NMR spectrum as result of the presence of oxygen.[104, 105]

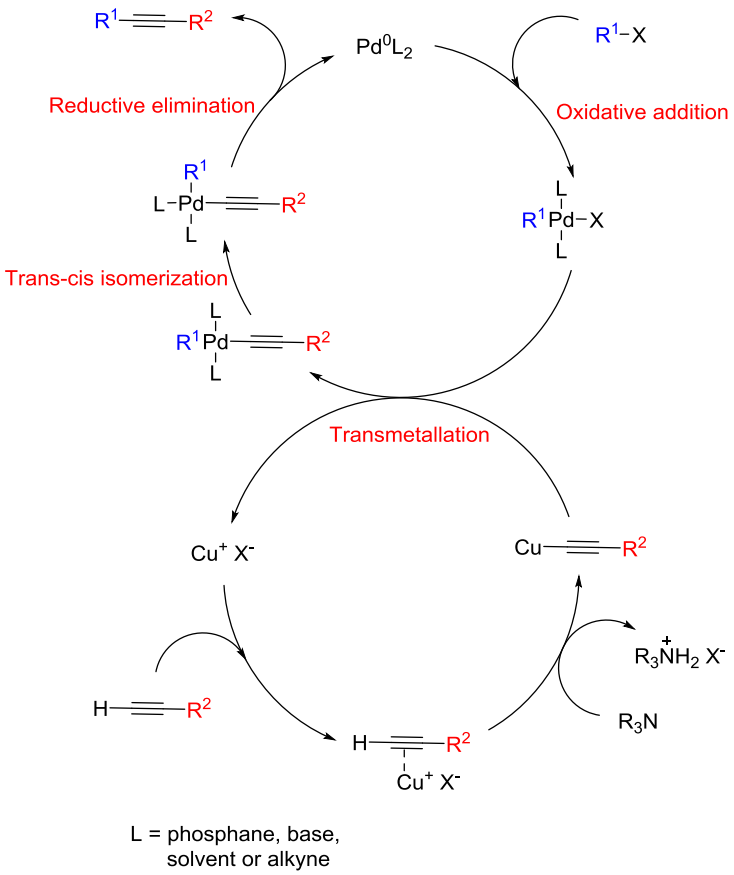

Scheme 2.2: Catalytic cycle for the Sonogashira reaction.[106]

The formation of the desired product was indicated by MS (ESI) with a peak at *m/z* 244 $[M+H]^+$ and ^1H NMR spectroscopy with the appearance of a characteristic singlet peak at 0.28 ppm related to $(CH_3)_3$ with 9H integration. The 4-CF_3 derived ethynyl pyridine **29** was also synthesised using Sonogashira cross-coupling reaction, as shown in scheme 2.3; however, this used the less reactive 2-chloro-4-(trifluoromethyl)pyridine *cf.* 2-bromo-4-(trifluoromethyl)pyridine used to synthesise **29**.

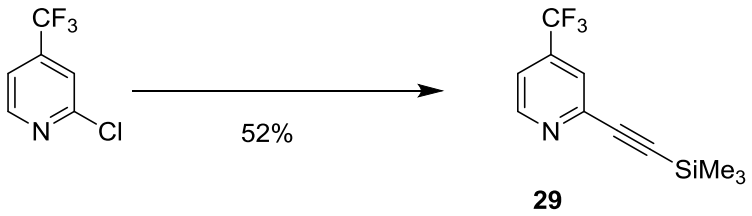

Scheme 2.3: **Reagents and conditions:** TMS-acetylene, $Pd(PPh_3)_2Cl_2$(5 mol%), CuI (5 mol%), PPh_3, Et_3N:THF (1:1), 90 °C.

It was important to add triphenylphosphine to facilitate generation and stabilisation of the active species Pd(0) catalyst. This synthesis gave a 52% yield with characteristic ^{1}H NMR spectrum peak at δ = 0.28 ppm (9H) and the expected changes to the chemical shifts of the pyridyl CF_3 resonance.[107] As a result of using the less active 2-chloropyridyl derivative, a high temperature was employed to increase the conversion compared with the room temperature reaction for the 2-bromopyridine derivatives.[106] Noticeably, alkylpyridinium species undergo spontaneous photopolymerisation with time to form ionic polyacetylenes which are brown in colour;[108] therefore, it is important to use them shortly after synthesis, and if this not possible, to store at low temperature or in the desiccator.

Synthesis of the bis-ethynylated compound **30** utilised alternative reaction conditions for the Sonogashira coupling (Scheme 2.4). Here $Pd(PPh_3)_4$ in toluene was used, with diisopropylamine as the base.[109] These conditions gave a higher yield 70% with **30**; more likely because of the use of $Pd(PPh_3)_4$ as catalyst and the presence of electron donating group bromide in both 2 and 6 positions on the pyridine ring, which leads to increase the electron density (good nucleophile).[110, 111]

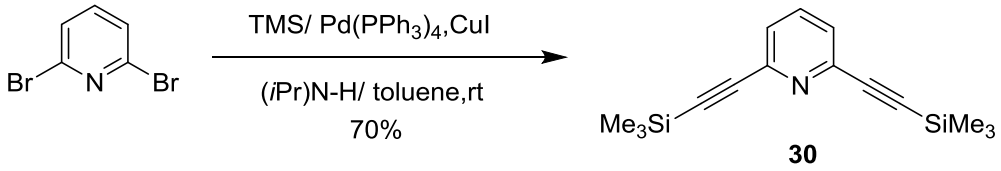

Scheme 2.4: Synthesis route of **30**.

It has been found that cross-coupling is facilitated with pyridines that contains an electron withdrawing group (CF_3) *cf.* electron realising group (OMe), due to the fact that electron donating groups can increase the halide bond strength ultimately, making it hard to break. Therefore DMF as solvent and high temperatures were used in synthesise **(31)** as shown in Scheme 2.5.

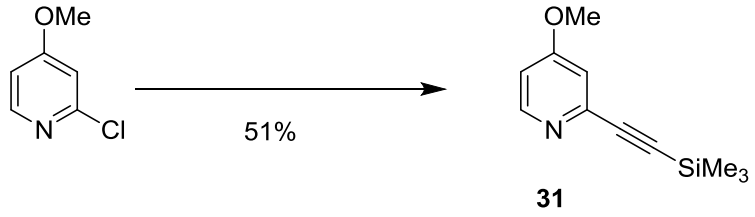

Scheme 2.5: **Reagents and conditions:** TMS-acetylene, $Pd(PPh_3)_2Cl_2$, CuI, NEt_3:DMF (3:1), 120 °C for 24 h.

2.2.1.2 Stille Coupling

Synthesis of the phenylpyridine **(26)** used in this thesis employed another palladium catalysed cross-coupling reaction, the Stille coupling. Although tri-*n*-butyltin is toxic, Stille coupling is considered an effective cross-coupling mechanism for C(sp^2)-C(sp^2) bond formation.[112] This reaction of an organohalide with an organostannane analogue uses a palladium catalyst and proceeds *via* similar steps to the Sonogashira coupling, through oxidative addition, transmetallation, trans/cis isomerization and reductive elimination processes.[113]

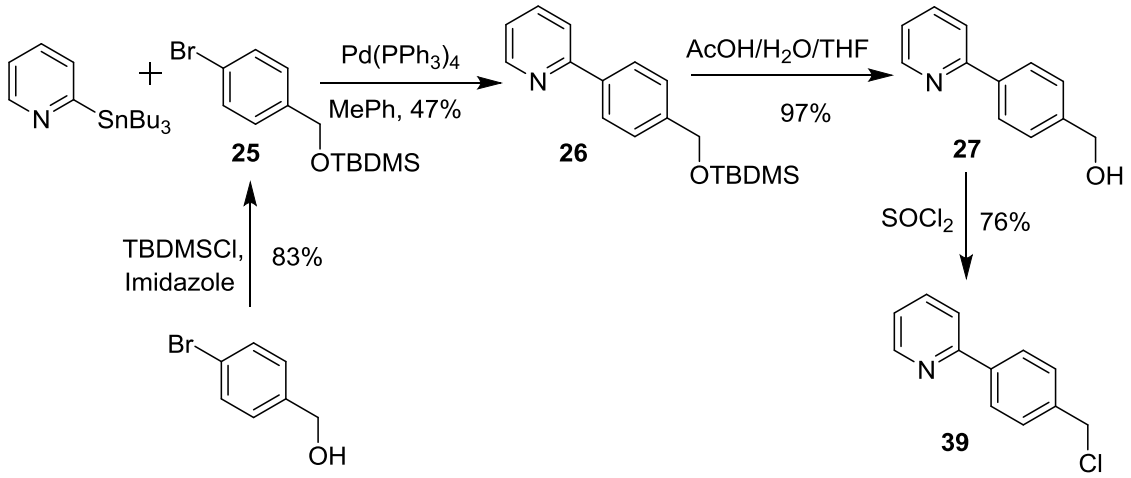

Scheme 2.6: Synthesis route of **39**.

The first step in the synthesis of **39** (Scheme 2.6) uses on organolithium reagent, reacting *n*-BuLi with 2-bromo pyridine in THF at -78 °C. The residue then undergoes an S_N2 reaction with tributyltin chloride to give 2-(tributylstannyl)pyridine. The purity of the product was determined by comparison of ^{1}H NMR resonance integrals of the pyridyl and tributyl protons which gives a yield of 98% over the two steps. The ^{t}Bu(CH_3)$_2$Si (TBDMS) protecting group is employed here as the Stille coupling reaction does not proceed when the hydroxyl moiety is unprotected It is most likely that the hydroxyl moiety perturbs the coordination of Pd(II) in the precatalyst activation.[114] When the hydroxyl group was protected with TBDMS, the coupling step goes to completion to give **26** in a 46% yield. Formation was verified by MS (ESI) 300 $[M+H]^+$ and ^{1}H-NMR spectroscopy with 5 resonances integrating for 8 H in the region δ = 8.69-7.09 ppm. Treatment of **26** with a solution of tetra-*n*-butylammonium fluoride (TBAF), to deprotect the OH did not go to the completion, due to the relative stability of TBDMS over fluoride compounds TMS <

TES < TIPS < TBDMS.[115] Deprotection with an acidic solution of (60% AcOH: 20% H_2O: 20% THF) showed full conversion to **27** by TLC (SiO_2, 2.5 % EtOAc in hexane) with yield 97%. The ^1H NMR spectrum shows the disappearance of the two singlet peaks of TBDMS (δ = 0.96 and 0.12 ppm) and appearance of a broad singlet OH peak at δ = 2.97 ppm. $SOCl_2$ was then used to chlorinate **27** and conversion monitored by TLC (SiO_2, 10% EtOAc in hexane). The product **39** was confirmed by ^1H NMR spectrum which shows the disappearance of a broad singlet OH peak at δ = 2.97 ppm, the MS (ESI) *m/z* 204, 206 $[M+H]^+$ also indicates the presence of chlorine, shown by the characteristic stable isotope pattern of ^{35}Cl, ^{37}Cl.

2.2.1.3 Negishi Coupling

A third palladium-catalysed cross-coupling reaction was employed in the synthesis of tridentate ligand 1,3-bis(2-pyridinyl)benzene (N^C^N) **(A)**. The 1,3-Bis(2-pyridinyl)benzene **(A)** (scheme 2.7) was prepared by palladium-catalyzed Negishi coupling; this reaction typically couples organic halides with organozinc species. The N^C^N ligand was synthesised following literature methods with some modifications.[116] *n*-Butyl lithium was added dropwise to 2-bromopyridine to avoid temperature elevation due to the exothermic nature of the reaction. Anhydrous $ZnCl_2$ was added to THF under an inert atmosphere and stirred until it had fully dissolved; this was then added to the reaction mixture. After stirring overnight at room temperature, $Pd(PPh_3)_4$ dissolved in THF was added to the solution and the mixture heated at 50 °C for 72 h. It was found that following this procedure increased the yield to > 50% , compared to the room temperature conditions used for the final step in the literature, affording the product as a yellow oil **(A)** as well as the by-product 1-bromo-3-(2-pyridinyl)benzene **(B)** in a 20 % yield.

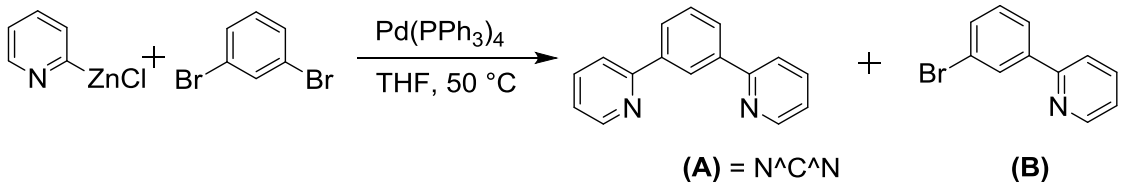

Scheme 2.7: Synthetic route of N^C^N and by-product.

2.2.2 *Click Chemistry*

Having synthesised the alkynylpyridines **28** - **31** by Sonogashira coupling, the next step in the synthesis of **32-36** (Scheme 2.8) is the click reaction to form a 1,2,3-triazole moiety. $CuSO_4$ (10 mol%) was used as a catalyst source with *in situ* reduction to Cu(I) by sodium ascorbate in MeOH:H_2O (3:1), giving yields of 73-87% (adapted from Sharpless *et al.*[76]). The one pot azide formation,[117] was monitored by TLC using first PPh_3 to reduce the azide to an amine, followed by the ninhydrin stain to detect the primary amines. Organic azides are potentially unstable with respect to explosive decomposition, especially compounds containing multiple azides. As a rule of thumb, compounds containing azides are considered explosive if $(N_C + N_O)/N_N \leq 3$. In all of these examples the azide was not isolated, but was generated *in situ* and reacted further.

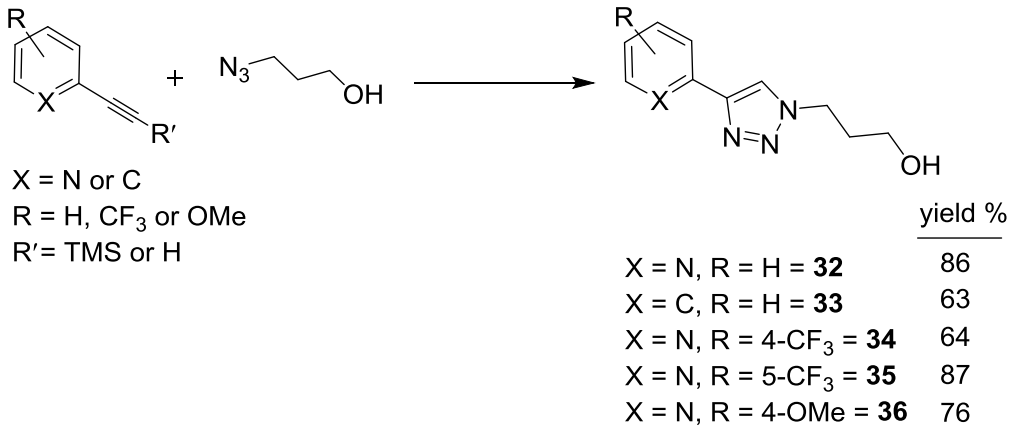

Scheme 2.8: **Reagents and conditions:** $CuSO_4.5H_2O$, Na Ascorbate, MeOH:H_2O, heating.

After EDTA addition to destroy any copper acetylide and scavenge the Cu(II), pyta compounds were extracted with EtOAc. The precursors **32-36** were purified by flash column chromatography (1:1 EtOAc:hexane). The MS (ESI) for example showed a peak at *m/z* 205 $[M+H]^+$ for **32** and the ^1H NMR spectrum exhibits a sharp singlet at 8.22 ppm integrating to 1H, indicative of the triazole ring proton, and characteristic triplet at 4.59 ppm of the CH_2 protons adjacent to the triazole ring indicating the formation of the desired products.

2-pyridine (1,2,3-triazole-1-yl) is an 'inverse' triazole. The first step in the synthesis of inverse triazoles **(37)** is preparation of 2-azidopyridine under microwave heating, which gives a good yield of 73%. In the following step of the

CuAAC reaction, a reducing agent such as sodium ascorbate was not employed due to the action of the terminal alkyne as a reducing agent.[118] Preparation of the inverse 2-pyridyl-1,2,3-triazole proceeded with a low yield using the previously developed microwave reactor method. This is most likely due to the presence the 2-azidopyridine in both tetrazole and azide forms (Scheme 2.9). In order for the reaction to go to completion, longer times at high temperature are required. To achieve this practically, the reaction was carried out in a Young's tube for 72 h.[119]

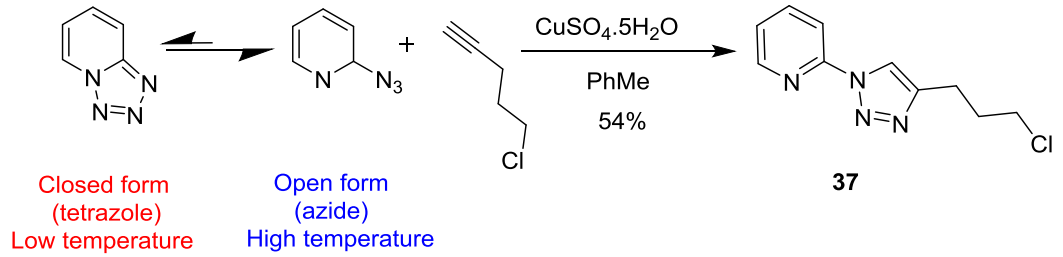

Scheme 2.9: 2-azidopyridine tautomerism and **37** synthesis.

The bis-triazole **38** was prepared from **30** in excellent yield (92%) using K_2CO_3 as an in situ TMS cleavage reagent. Purification was achieved by alumina chromatography (1% NH_4OH: 19% MeOH: 80% DCM) due to the high polarity of the product. The mass spectrum showed a peak at *m/z* 330 $[M+H]^+$ and ^1H NMR singlet at δ = 7.8 ppm with 2H integration related to the two triazole moieties indicating **38** was formed as depicted in Scheme 2.10.

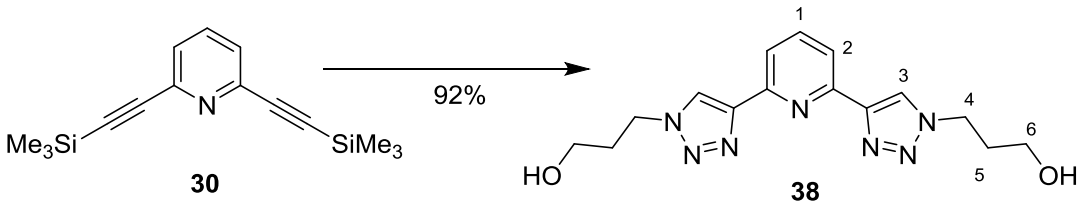

Scheme 2.10: **Reagents and conditions:** 3-azidopropan-1-ol, $CuSO_4.5H_2O$, Na ascorbate, K_2CO_3, 70 °C, 18 h.

2.2.3 *Halogenation of Alcohol Precursors*

Nucleophilic substitution of the hydroxyl moiety of the precursors **39–45** was carried out using thionyl chloride in DCM as a polar aprotic solvent. Using a high molar excess of thionyl chloride was sufficient to substitute the terminal OH with Cl; this excess was then removed by 2 M Na_2CO_3 to give a yields between 90-96%, as shown in Scheme 2.11. The conversion was monitored by TLC and characterised by

both MS (ESI) and ^{1}H NMR spectrum which shows the absence of the OH peak at ~ δ = 3 ppm, and a change in chemical shift of the CH_2 adjacent to the Cl.

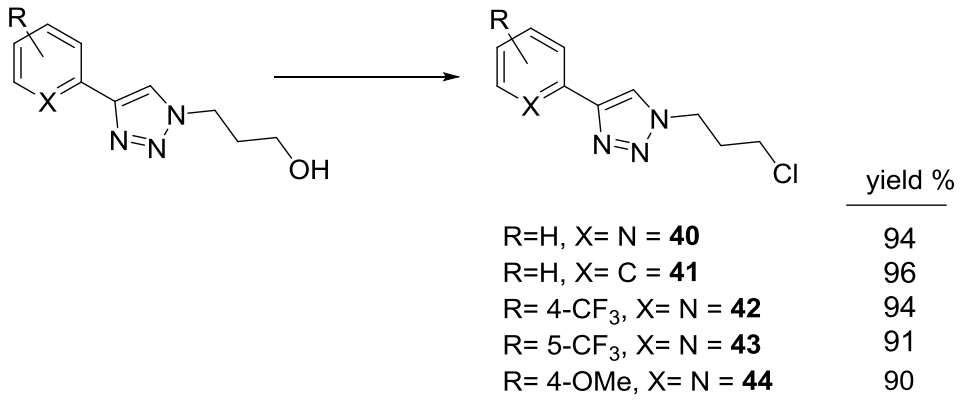

	yield %
R=H, X= N = **40**	94
R=H, X= C = **41**	96
R= 4-CF_3, X= N = **42**	94
R= 5-CF_3, X= N = **43**	91
R= 4-OMe, X= N = **44**	90

Scheme 2.11: **Reagents and conditions:** $SOCl_2$ (20 equiv.), DCM, 0 °C 3h to rt 18 h.

Attempts to halogenate **46** directly did not work, most likely the starting material goes through a dimerise transesterification as depicted in Scheme 2.12.[120, 121] Therefore an alternative method was employed by first reacting **46** with TsCl (Scheme 2.13). The formation of the tosyl product was indicated by ^{1}H NMR which shows two characteristic doublets at δ = 7.7 and 7.3 ppm that belong to the phenyl ring of the tosyl group with singlet at δ = 2.4 ppm that belongs to CH_3.

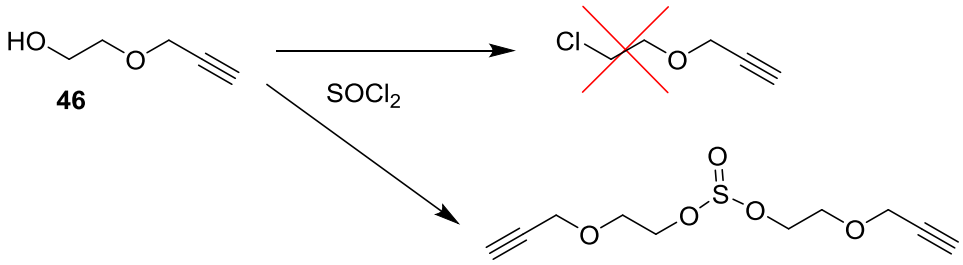

Scheme 2.12: Failed method for chlorination of **46** and likely dimerisation product.

The tosyl protected compound was reacted with KI in acetone as in Scheme 2.9 to give the iodo-alkyne compound **48** which is confirmed by MS (ESI) 211 $[M+H]^+$ and ^{1}H NMR spectrum that indicates the disappearance of tosyl moiety and a slight change in the ^{1}H chemical shift of the final compound.

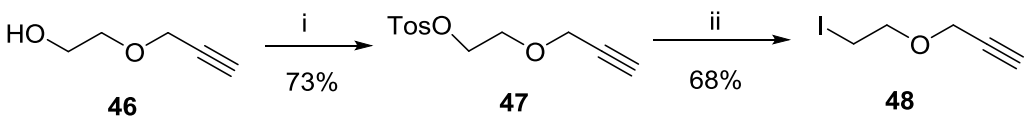

Scheme 2.13: **Reagents and conditions:** i) TsCl, KOH, Et_2O, 0 °C; ii) KI, acetone, 69% 70 °C.

2.2.4 *Nucleophilic Substitution (ᵗBuDO3A addition)*

Amines are good nucleophiles, they attacks halogenoalkanes to produce secondary or tertiary amines in presence of base. **ᵗBuDO3A** can be associated to different substituents through S_N2 in present of K_2CO_3. The macrocyclic proligands bearing pendant pyridyl/ phenyl triazoles were all synthesised using this method.

For instance 1.2 equiv. of **40** was reacted with a **ᵗBuDO3A** in the presence of K_2CO_3 (~8 equiv.) in MeCN at 90 °C give **49** in good yield 76%. KI was added to substitute the chloride with iodide as the iodide is a better leaving group S_N2 (Scheme 2.14). Due to HX liberation during the nucleophilic substitution and deprotonation of the tertiary amine in **ᵗBuDO3A**, an excess of inorganic base is required to ensure that the reaction remains under basic conditions. After 48 h reaction, the mass spectrum indicated that the reaction had gone to completion to form **49**. The latter was indicated by the appearance of the product peak in MS (ESI) at *m/z* 702 $[M+H]^+$; this was then isolated on silica using (90% DCM: 9% MeOH: 1% NH_4OH) as the eluent. The ^1H NMR spectrum shows resonances of (5H) multiplicity corresponding to the characteristic region of pyta in (8.5-7.1 ppm) and the cyclen ring peaks are seen at lower frequencies δ = 3.4 - 2.1 ppm as well as δ =1.4 ppm 27H that related to the ᵗBu groups. While the proligand **58** which contains two macrocyclic ligands showed integrations corresponding to 32H between 3.7-2.5 ppm and 54 H for ᵗBu groups with *m/z* 663 $[M+2H]^{2+}$ in the MS indicating formation of the product (Scheme 2.15).

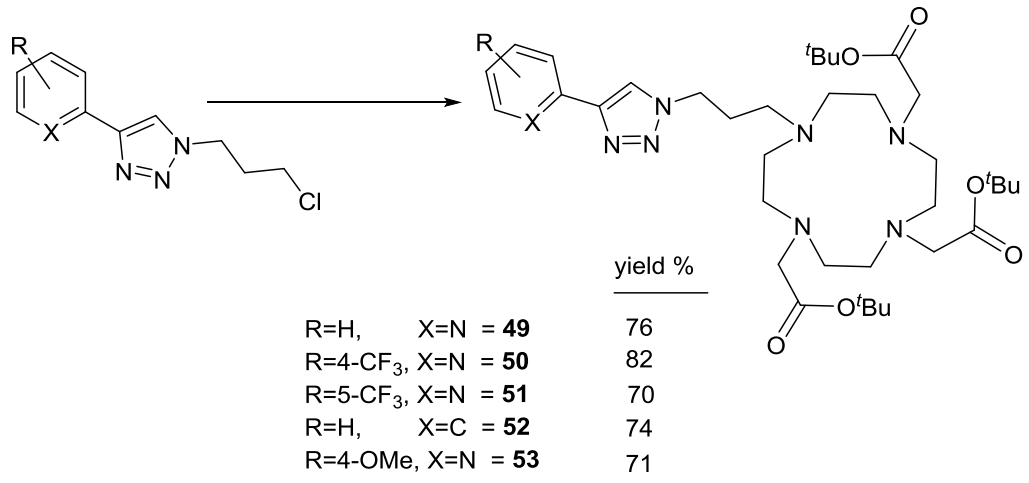

Scheme 2.14: Synthesis **49** – **53**, **ᵗBuDO3A**, K_2CO_3, KI, MeCN, 48 hr, 90 °C.

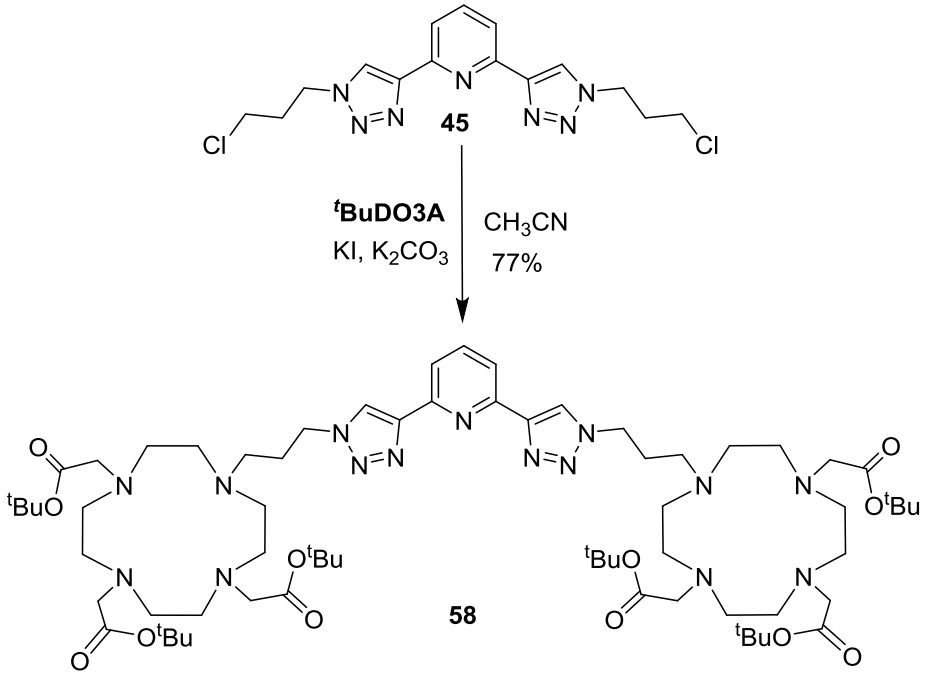

Scheme 2.15: Synthesis method of **58**.

This standard alkylation methodology failed in attempts to synthesise **57** (Scheme 2.16) by direct reaction of 4-bromo-1-butyne with **^{t}BuDO3A**. It is suggested that due to the basicity of the nucleophile and the configuration of 4-bromo-1-butyne, the proton at the β-position is extractable making the competing *E*2 elimination pathway preferable to produce vinyl acetylene over the desired S_N2 pathway. Furthermore, the vinyl acetylene product is volatile (b.p. 0-6 °C) so it cannot proceed with the standard alkylation pathway.

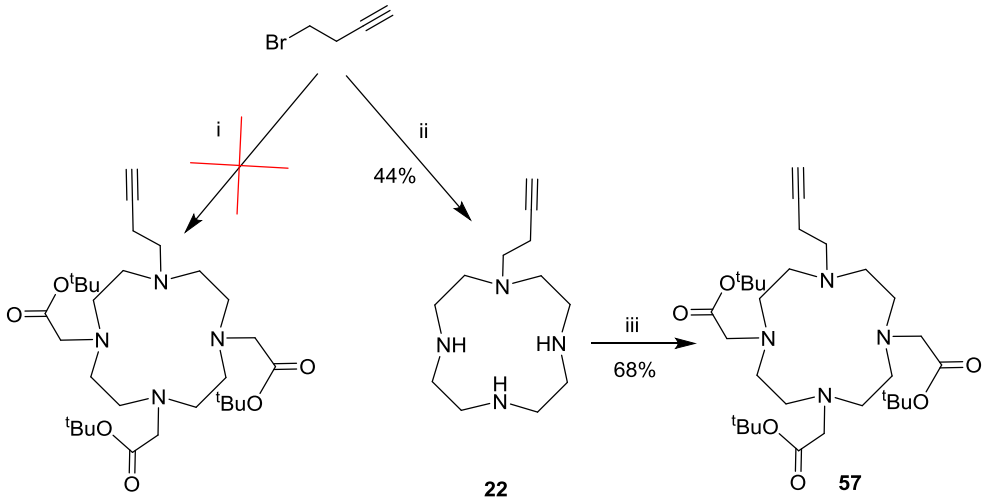

Scheme 2.16: **Reagents and conditions:** i) K_2CO_3, **^{t}BuDO3A**, MeCN; ii) Et_3N, $CHCl_3$, cyclen; iii) K_2CO_3, tert-butyl bromoacetate

Another route to synthesise **57** was required; first reacting 4-bromo-1-butyne with 1,4,7,10-tetraazacyclododecane (cyclen), then tert-butyl bromoacetate was added as in Scheme 2.12.[122] Albeit a (1:4) ratio of haloalkane: cyclen were used, cyclen can be recovered by neutralising the residue with 1 M HCl. After heating at reflux in chloroform for 20 h using Et_3N as base, **22** was confirmed by MS (ESI) which shows a peak at *m/z* 226 $[M+H]^+$. The ^1H NMR spectrum shows multiple peaks between 2.74 - 2.46 ppm belonging to the CH_2 of cyclen with 16H integration, and a triplet δ = 1.9 ppm is indicative of the alkyne CH and triplet of doublets at 2.27 ppm related to aliphatic CH_2. The product **22** was reacted with tert-butyl bromoacetate (3 eq) in the presence of K_2CO_3 to give **57** with a good yield 67%, which was characterised by (ESI) mass spectrum at *m/z* 568 $[M+H]^+$ as well as ^1H NMR which indicates the addition of three the acetate arms δ = 1.4 ppm 27H that belong to ^{t}Bu.

2.2.5 *Cleavage of Tert-butyl Esters*

The tert-butyl esters of the macrocyclic ligand precursors were hydrolysed with trifluoroacetic acid in DCM to give the desired pro-ligands. During the reaction, tert-butyl cations are formed, which can be converted to volatile tert-butanol as in Scheme 2.17. These precursors were obtained in good yield after purification by RP-HPLC. The hydrolysis requires adventitious water, thus the reactions were carried out in an open vessel. The produced pro-ligands are shown in Fig. 2.5.

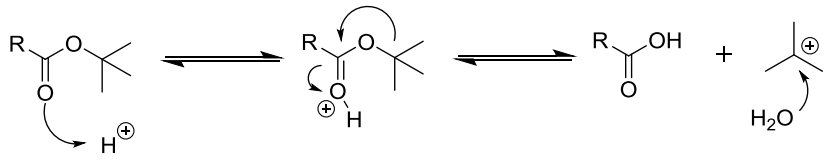

Scheme 2.17: Mechanism for acid catalysed hydrolysis.

In this step of ligand purification using HPLC, method A (Method A (A = 0.1% TFA in H_2O, B = 0.1% TFA in MeCN) 5% B for 5 min, 5-50% B over 30 min, 100% B for 5 min, 100-5% B for 2 min, 5% B for 5 min.) was used detecting absorbance wavelength at 280 nm except **H_3L9 and H_3L11** (due to lack of the chromophore).

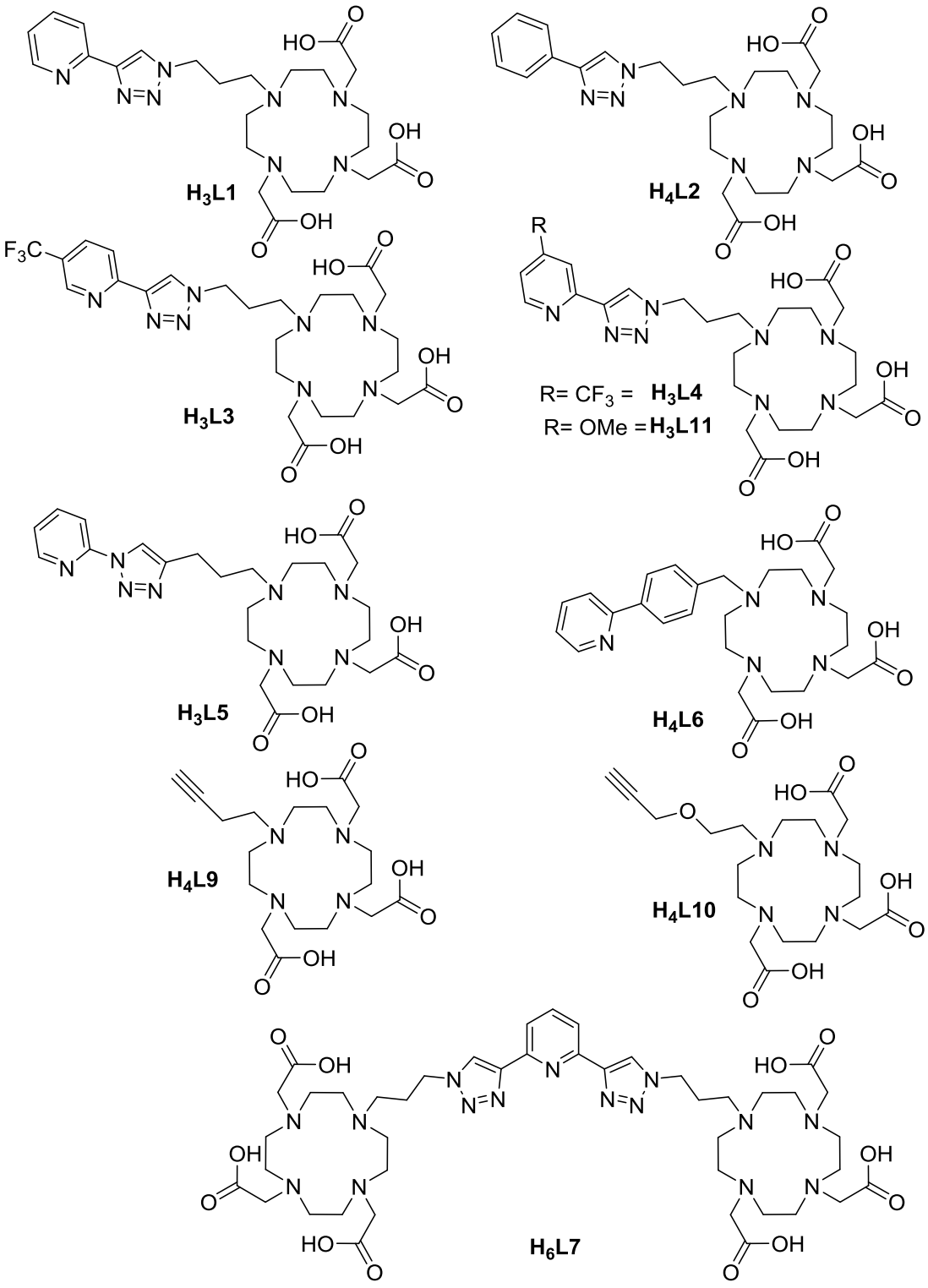

Figure 2.5: The synthesised proligands (N.b: **L2**, **L6** and **L9** are shwn as **H_4Ln** as a carbon becomes deprotonated in subseaent coordination reactions).

The desired compounds were characterised by MS (ESI) and ^{1}H NMR spectroscopy, for example **H_3L1** gives m/z 702 $[M+H]^+$, with a similar ^{1}H NMR spectrum pattern to **49** with disappearing the ^{t}Bu groups at δ = 1.4 ppm.

The ^{1}H NMR spectra at room temperature for these precursors are not very informative.[123] They show a remarkable broadening belonging to the several ethylene signals due to unrigidity by nitrogen inversion, C-C rotation and the movement of acetate arms.[124, 125] This perennial problem can be facilitated by either adjusting the temperature or increasing the rigidity by complexation; in this context, **H_3L1** ^{1}H NMR spectrum was recorded at a range of temperatures to increase the resolution of the methylene signals by reducing the line broadening, allowing signals to be separated and resolved.

Lowering the temperature of the NMR solution was unsuccessful to decrease protons exchange and restrict the rotation around the amine groups, as shown in (Appendix, Fig. 10.9). Comparison of the ^{1}H NMR spectrum at (-2 °C to -50 °C) showed that pyta hydrogen signals more second order reappeared due to the interaction with electron pairs of nitrogen atoms.[126]

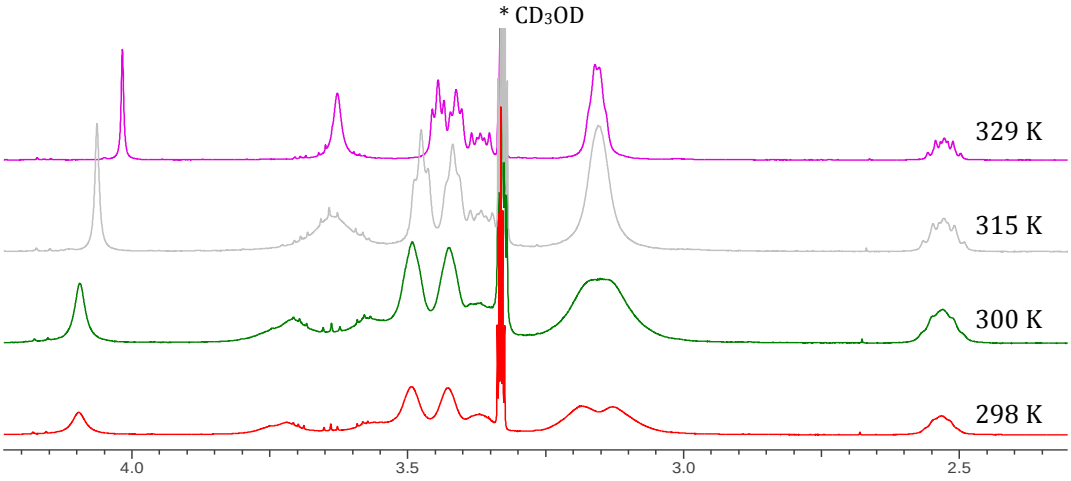

Figure 2.6: Partial ^{1}H-NMR spectrum of **H_3L1** in CD_3OD. The signals resolve with increasing temperature.

While recording the ^{1}H NMR spectra at higher temperatures (25 °C to 56 °C) showed acceleration in exchange rate that leads to enhancing the peak separation and broadness, especially with DO3A moiety, as shown in Fig. 2.6.[127] However, it is still not possible to identify clearly all CH_2 of macrocyclic resonances.

The ^{1}H NMR spectra were also recorded at different pH for **H_3L1** to investigate the changes in chemical shifts. It was found as the pH is lowered the ligand structure becomes more rigid with slight shifting in the resonances to higher frequency area

as seen in Fig. 2.7. These shifts are a consequence of protonation amine, acetate groups and the pyridine.[128, 129]

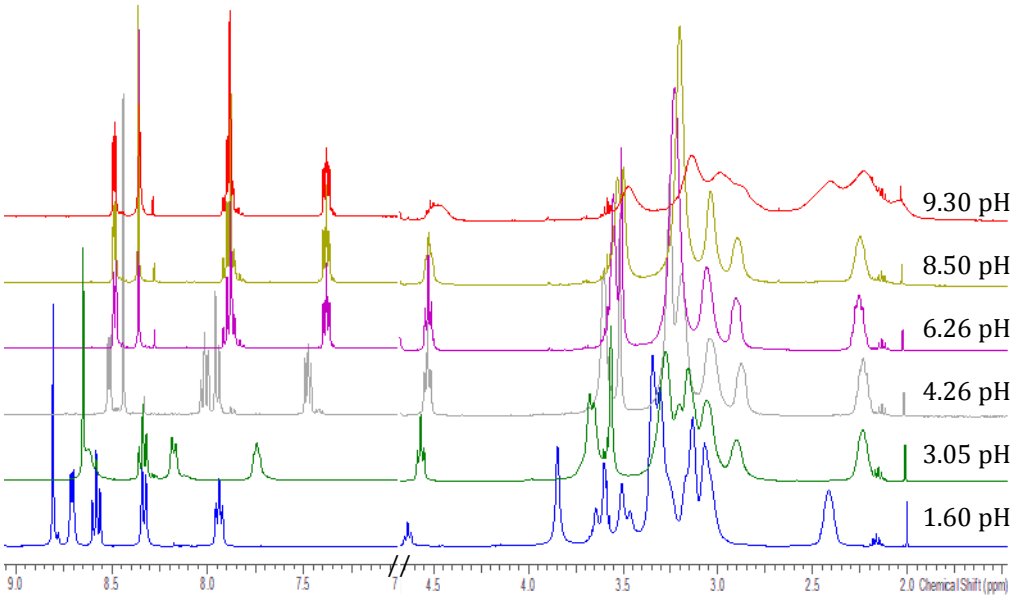

Figure 2.7: ^{1}H NMR spectrum of **H_3L1** in D_2O at different pH at 25 °C.

The pro-ligands were isolated as $[NH]^+CF_3CO_2^-$ salts, this ligation due to the presence of protonated amines with 3 or more $CF_3CO_2^-$ as counterions. This was confirmed by ^{19}F-NMR. The latter shows the presence ≃ 3 $CF_3CO_2^-$ molecules equivalent to one DO3A unit. This can be calculated by *cf.* the ratio of fluorine integration for both TFA and the F_3C group in **H_3L3** / **H_3L4** in the same spectrum as it seen in Fig. 2.8**,** or by adding a stock solution of 2,2,2-Trifluoroethanol (TFE) with the ligands that do not contain fluorines in their structure.

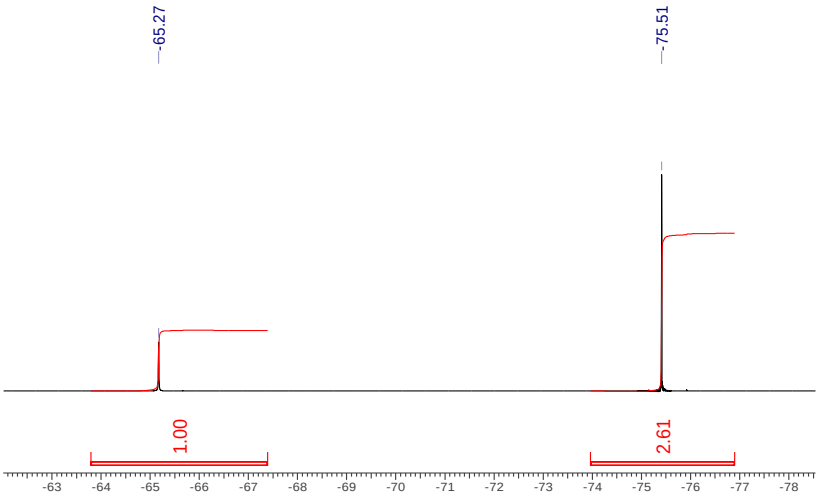

Figure 2.8: ^{19}F-NMR spectrum (400 MHz, D_2O) of **H_3L4**.$(TFA)_3$.

2.3 Synthesis and Characterisation Ln(III)DO3A complexes

All lanthanide complexes were synthesised *via* the same route, using the synthesised pro-ligands with $LnCl_3.6H_2O$ in H_2O at pH ~ 6 (Scheme 2.18). The reaction is carried out above pH 4, to ensure all CO_2H were converted to CO_2^-. While at pH above 7 the lanthanide starts to precipitate as hydroxide, therefore control of pH is vital to the reaction. The reactions were monitored by MS (ESI). Any unreacted lanthanide salts were removed using a celite® plug after precipitating as insoluble $Ln(OH)_3$ by increasing the pH to ~ 10. The solutions were tested for the presence of uncomplexed lanthanide ions using urotropine buffered solutions of xylenol orange at pH 5. If the solutions remained orange no free lanthanide ions were left in the solution.[130]

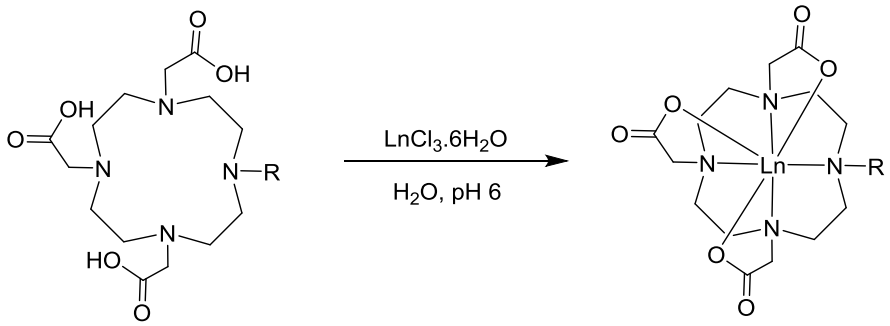

Scheme 2.18: General Ln(III) coordination conditions, for substituted DO3A ligands.

Complexes, especially those of gadolinium were purified by RP-HPLC to ensure no free Gd(III) ions are present, otherwise, relaxivity measurements will be inaccurate and *in vivo* studies will be compromised. In the purification process it is necessary to avoid using any low pH eluent, due to the possibility of decomplexation pH < 3. In addition, using HPLC, a buffered mobile phase containing phosphate, acetate and carbonate ions are high likely to coordinate with Ln(III) metal centre instead of inner sphere water, so were avoided.[131]

The MS (ESI) show characteristic patterns for each Ln(III), for example **EuL1** and **GdL1** exhibited patterns as in Fig.2.9. **EuL1** for example is a seven coordinate complex, the ^1H NMR spectrum is consistent with those observed for unsymmetrically substituted cyclen derivatives, in which all protons are non-equivalent.[132] The resonances only began to be partially resolved at low

temperature (~278K). These signals are broad even at this temperature due to the paramagnetisem of Eu(III) ion, implying a relatively low barrier to arm rotation in the complex that would allow fast exchange between the complex diastereoisomers.

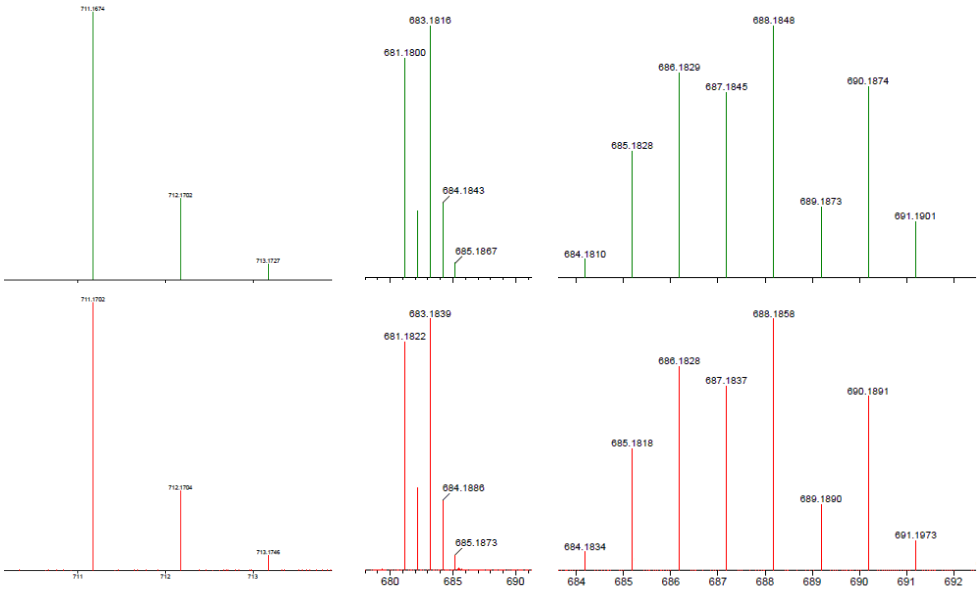

Figure 2.9: Simulation (top) and accurate mass specta (bottom) for **TbL1** (left), **EuL1** (middle) and **GdL1** (right).

Coordination of these ligands to diamagnetic yttrium(III) ion show clear and useful ^{1}H NMR spectra to prove that the pyta moiety does not coordinate to the metal centre. The metallic radii of the trivalent metal Y(III) is the ~same size as Ho(III) and is closer in size to Gd(III)/Eu(III) than diamagnetic La(III) and Lu(III). Due to the remarkably long electronic relaxation time of Gd(III) ions, has the effect of broadening lines to such extent that NMR spectra of Gd(III) complexes may not recorded.[133]

The ^{1}H NMR spectrum of **YL3** (Fig. 2.10) shown that the pyta resonances have been slightly shifted to the lower frequency region of the spectrum, with more resolved peaks compared with initial ligand **H_3L3** and broadened resonances for the corresponding Eu(III) complex. However, the shielded region which includes the coordinated polyaminocarboxylate unit with Y(III), becomes more poorly resolved than the ligand, due to the variable isomers (the square antiprismatic (SAP) and twisted-square antiprismatic isomers (TSAP)) that formed, alongside with rotation of the pendant arms or inversion of the cyclen chelate rings.[134]

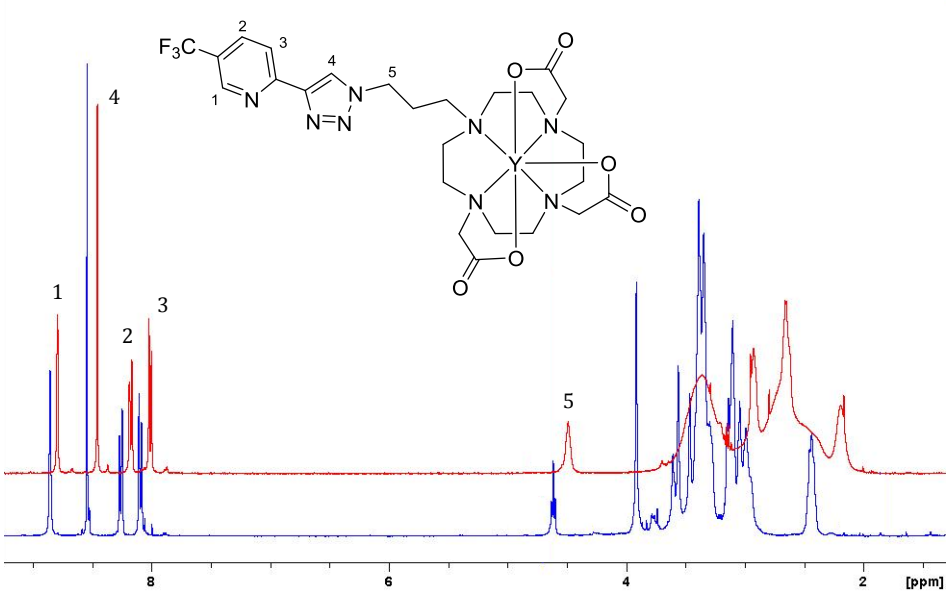

Figure 2.10: **YL3** (red) and **H_3L5** (blue) ^{1}H NMR spectrum, 400 MHz, in D_2O at 298 K.

2.3.1 *EuL1 Photoluminescence and Excited State Lifetime*

The absorption spectrum shows that **EuL1** can be excited at λ = 280 nm to give an emission spectrum as shown in Fig. 2.11. The pyta moiety works as an antenna to the Eu(III) ion, when the pyta was excited at 280 nm, energy of the triplet state T_1 transfers to the excited state of the europium ion ^{5}D.

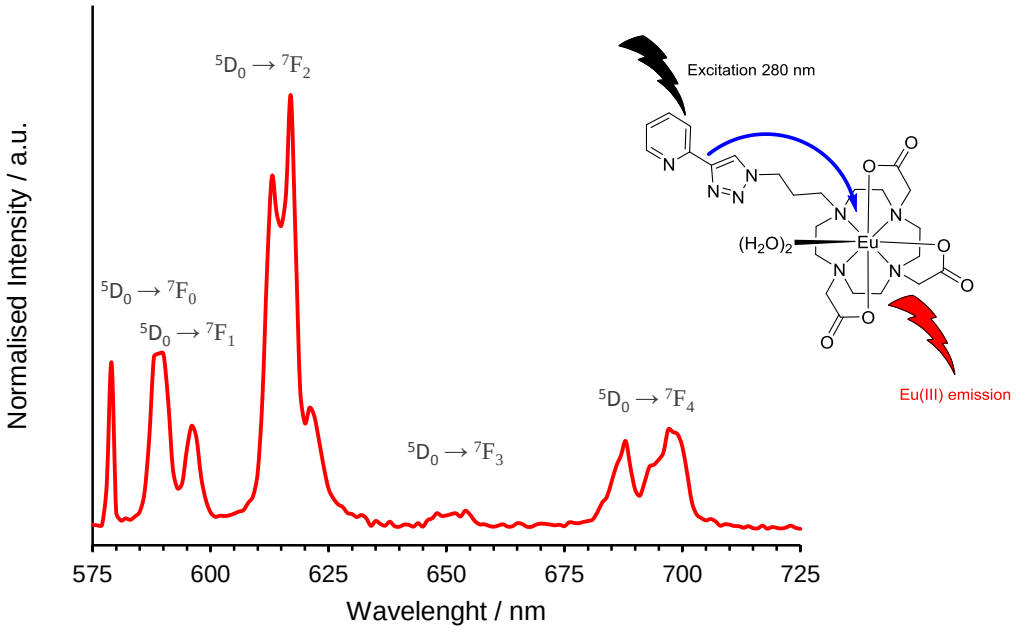

Figure 2.11: **EuL1** Emission spectrum (λ_{ex} = 280 nm, H_2O, 298K, pH 6).

Typical emission of Eu(III) at the red region with various $^5D_0$ to ^7F_J transitions were seen between (550 - 720 nm). The spectra show variation between the intense hypersensitive $\Delta J = 2$ transition ($^5D_0$ to $^7F_2$), *cf.* that of the $\Delta J = 1$ transition. This is a typical emission spectrum for a seven-coordinate complex with $q = 2$. This lanthanide complex can bind with bi-dentate anions such as carbonate; this results in an increased $\Delta J = 2$ transition; however, as the pH of the solution is ~ 6 the binding of carbonate is ruled out. Excited state lifetime measurements (Fig. 2.12) confirm that two inner-sphere waters are present. The $\Delta J = 2$ transition, at 616 nm is the wavelength that was monitored during lifetime studies in H_2O/D_2O to determine k_{H_2O} and k_{D_2O} in order to calculate q (Equ. 23). Plots of luminescence intensity *vs.* time are shown in Fig. 2.12. The rate of decay is faster in H_2O than in D_2O, this is due to the O-H oscillators quenching the excited state of the Eu(III) ion far more efficiently than the O-D oscillators of D_2O. From the lifetime studies, it was found that as expected, **EuL1** is $q = 2$ Table 2.1. It shows that **EuL1** is seven-coordinate, with respect to the ligand, with two inner-sphere water molecules, giving a coordination number of 9.

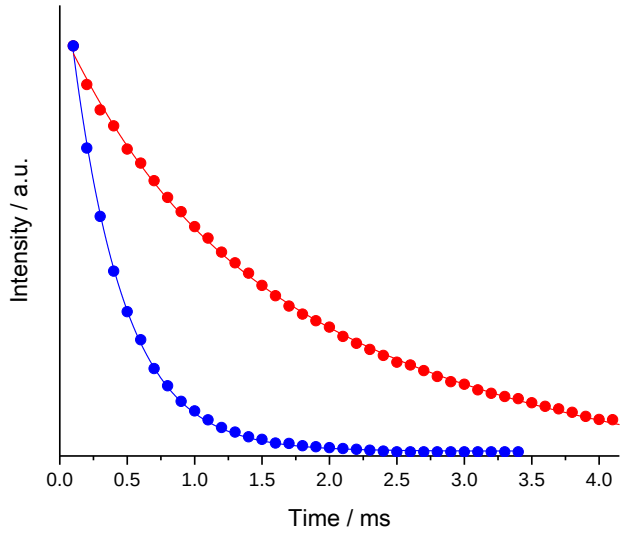

Figure 2.12: luminescence intensity vs. time in excited state life time studies for **EuL1** at 298 K, pH 6, λ_{ex} = 280 nm, λ_{em} = 616 nm. Blue = H_2O, Red = D_2O.

2.3.2 *TbL1 Photoluminescence and Lifetime*

TbL1 is expected to be similar to the structure of **EuL1**, These metals appear either side of gadolinium in the periodic table. Two waters bound at the metal centre

would be expected; the hydration state *q*, of the complex was determined (Equ. 24) and its luminescent properties investigated. The emission spectrum (Fig. 2.13) was recorded following excitation at λ_{ex} = 280 nm, this spectrum is typical for Tb(III) emission showing the various $^5D_4$ to ^7F_J transitions alongside with pyta emission maxima at 324 nm. The form of a Tb(III) emission spectrum is not as sensitive to water coordination environment as Eu(III), as the excited state of Tb(III) is of higher energy and therefore, less effected by quenching from the O-H oscillators. The excitation spectrum monitors the emission at λ = 544 nm, ΔJ = 1 ($^5D_4$ – $^7F_5$) transition. The Tb(III) excitation does not completely correlate with the Eu(III), this is due to the excited state of Tb(III) is being higher an energy than that of Eu(III), which leads to be less quenched by the water molecules, so, it is expected that the quantum yield for the Tb(III) is higher than Eu(III).

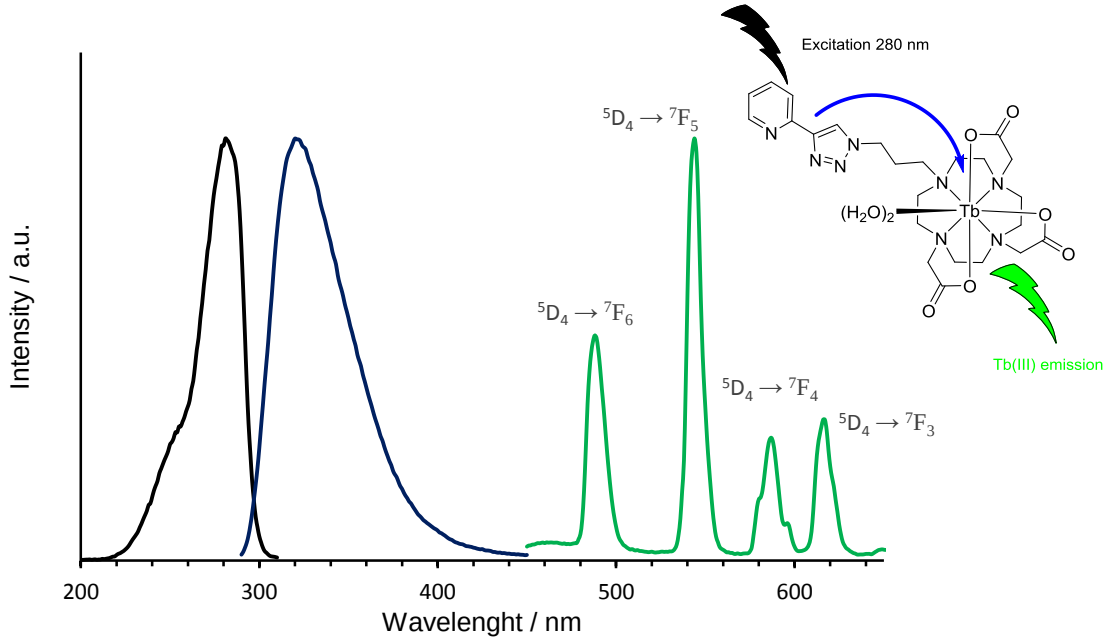

Figure 2.13: Excitation (black), pyta emission (blue), and Tb(III) emission spectra (green) of **TbL1**, (λ_{ex} = 280 nm, H_2O, 298K, pH 6). Excitation spectrum recorded by monitoring the emission at 544 nm.

The ΔJ = 1 transition at 544 nm, is the wavelength that was monitored during lifetime studies. The excited state lifetimes for **TbL1** are considerably longer than that of **EuL1**, as there is less efficient quenching from O-H oscillators as overlaps with the $^5D_4$ excited state of Tb(III) occurs *via* the less populated *v* = 5 vibrational levels of water (Franck–Condon principle, see Section 1.5.4). The results from the lifetime study confirms that **TbL1** is heptadentate chelate and will bind two waters.

Table 2.1 presents selected excited lifetime measurements and q number of Eu/Tb complexes that presents in Fig. 1.14.

Complex	λ_{em} / nm	λ_{ex} / nm	k_{H_2O}/ms^{-1}	k_{D_2O}/ms^{-1}	q (± 0.2)
EuL1	280	616	2.57	0.59	2.0
TbL1	280	544	1.16	0.74	1.8
EuHL2	280	616	2.39	0.59	1.9
EuHL6	280	616	2.51	0.61	2.0
EuL7	280	616	2.35	0.56	1.8
EuHL10	395	616	1.78	0.55	1.1

Table 2.1: Rate constants, k, for depopulation of the excited state and derived hydration states, q, for the decay of selective Eu and Tb complexes.

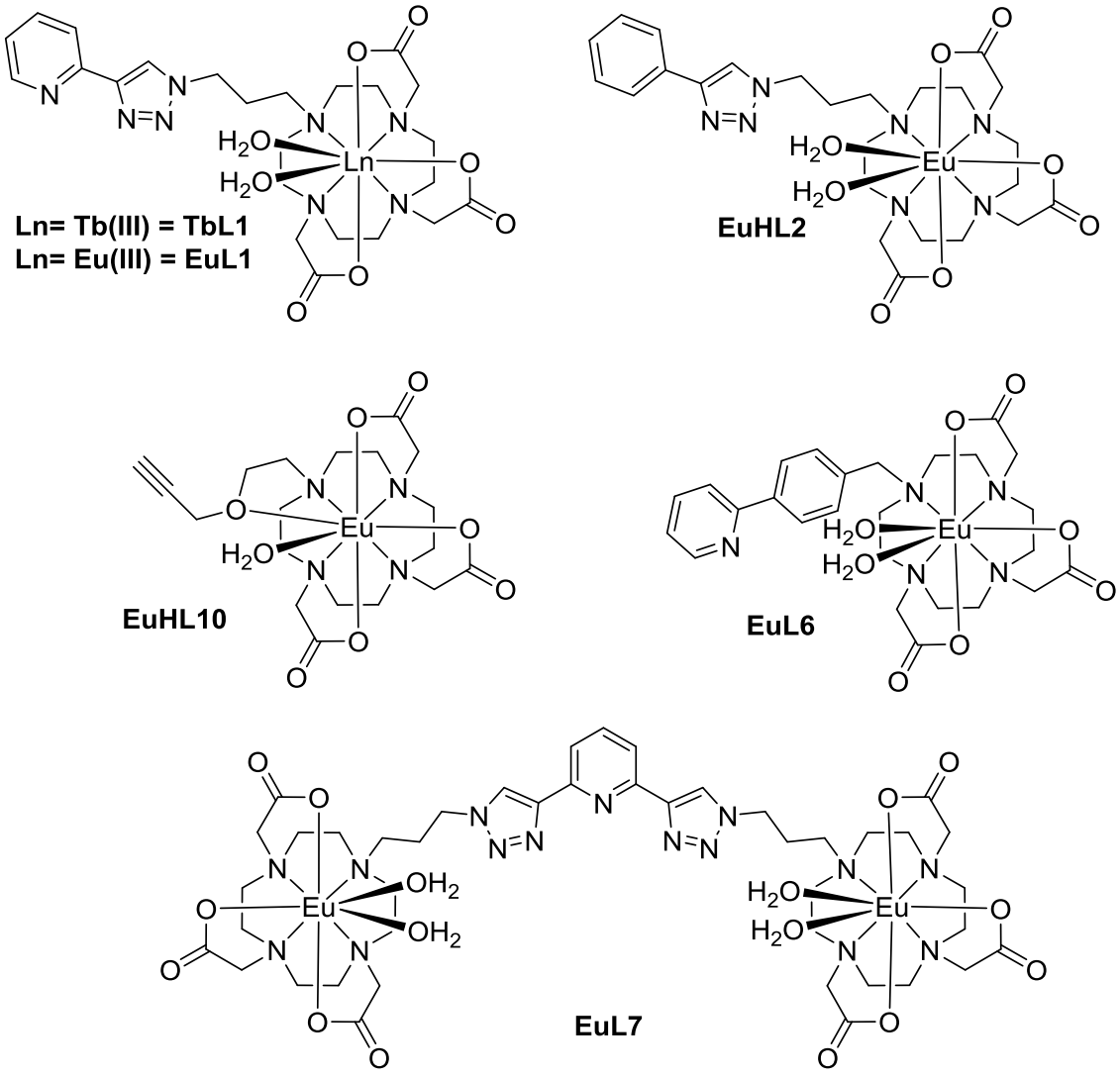

Figure 2.14: Selective Eu/Tb complexes.

2.4 Summary and Conclusions

In conclusion, the chemistry has been developed to allow the site-specific incorporation of pyta analogues into the DO3A pincers. Owing to the mild conditions, this paradigm can be used to establish a library of macrocyclic ligands. Regarding the Sonogashira coupling, it has been demonstrated that the chloride pyridine precursor is less productive than bromide analogues for synthesis of 2-ethynylpyridines derivatives. In addition, different reagents and conditions have been applied to increase the yield of 2-ethynylpyridines formation and obtaining better conversion.

Additionally, pyta ligands have been synthesised form organic azides in good yield using a one pot reaction. These ligands prove it can be used as antenna for sensitising the excited states of Eu(III) and Tb(III). In the next chapters the possibility of using it as coordination sites with different TMs will be explored with the ability to tune the emission.

Furthermore, it has been shown that the DO3A is not rigid/exchangeable unite in both before and after coordination with Ln(III). The synthesised ligands and mono lanthanide complexes show higher purity after being subjected to HPLC. The excited state lifetime measurements for Eu/Tb complexes, indicate that these complexes with $q = 2$, meaning the pyta is not coordinated to the Ln(III) ions.

Chapter 3

Dual-mode MR / Optical Imaging Contrast Agents

3.1 Introduction

MRI attracts a great deal of attention because it provides an efficient three-dimensional visualization, high spatial resolution in the 0.1 mm range, and harmful ionizing radiation is not required. On the other hand, it has certain sensitivity and time-processing limitations. Fluorescence microscopy using fluorescent probes is a popular imaging technique in medical diagnostics, in addition it can be used for image-guided surgery.[135] It is characterised by high imaging sensitivity and excellent spatial resolution, but it has limited depth penetration. Therefore, the integration of optical imaging and MRI techniques within one platform is an ideal approach to bridge gaps in sensitivity, spatial resolution, and penetration depth into tissue and might also allow for better theranostic performance.[136, 137] There have been a number of previous studies into joining CAs with organic imaging probes; Parac-Vogt and co-workers, for instance, synthesised **60** with dual-modality, as shown in Fig. 3.1.[138] Boron-dipyrromethene shows reasonable luminescence properties (λ_{exc}= 503 nm, λ_{em} = 560 nm), water solubility and stability in solution. Nevertheless, non-organometallic dyes generally exhibit short emission lifetimes from their singlet excited states (S_1), and inefficient intersystem crossing (ISC) between the singlet and triplet excited states that eventually gives low-intensity phosphorescence with high signal-to-noise ratios. Additionally, the overlapping (low Stokes shift) between the excitation and emission spectra leads to increased self-quenching.

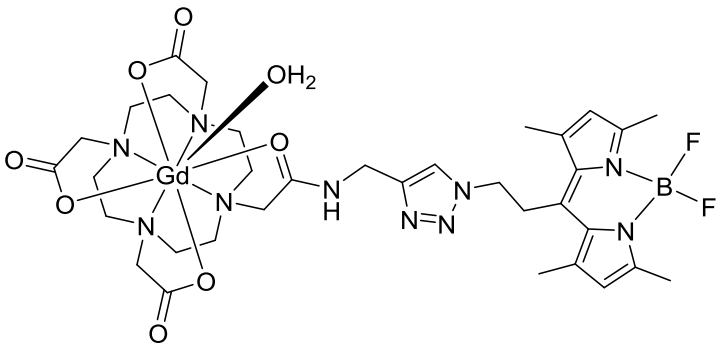

Figure 3.1: The **60** analogue.

In contrast, the heteropolymetallic dual-mode agents with d^6/d^8 luminescent transition metals show high intensity, a long emission lifetimes > 5 μs and a large Stokes shift with high photobleaching resistance.[36] In 2008, Faulkner *et al.*, synthesised a bimetallic complex, **61**, that contains a luminescent rhenium(I) chromophore with a gadolinium(III) ion (Fig. 3.2).[139] This complex displays a high relaxivity, r_1, and long emission lifetime > 20 ns in aqueous solution. However, because of its micromolar solubility, an MRI image was difficult to obtain. Furthermore, the latter shows high steric hindrance around the macrocycle and a low water exchange rate in terms of its inner water sphere. One possible way to circumvent these difficulties is to develop a multimetallic CA that can provide high chemical stability with numerous Gd(III)-units which can overcome the solubility, exchange rate and hydration state issues. Later, Helm and coworkers presented the Ru(II) complex (**62**) with linear pincers, which shows a r_1 = 15.8 s^{-1} mM^{-1} at 4.7 T, 200 MHz, 37 ◦C and modest quantum yield in aqueous solution for the $Ru(bpy)_3$ core that lies in the range Φ = 0.001- 0.1. It was found that the photophysical properties of this complex depend heavily on the environment, pH, temperature and the formation of singlet oxygen.[140]

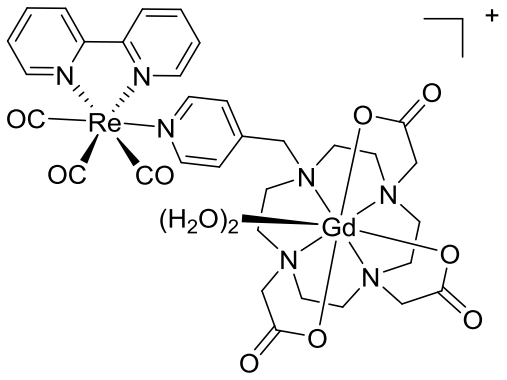

Figure 3.2: **61** complex.

The structure and design of the pincer that coordinates to the paramagnetic ion can also have a critical effect on the relaxivity of dual-mode contrast agents through aspects such as steric hindrance, molecular tumbling and the hydrophobicity of the complex shell. Para-Vogt and coworkers developed **63** as depicted in Fig. 3.3.[141] It is a multinuclear complex, a $Ru(bpy)_3$ core with 6 Gd units, which exhibits the low water exchange lifetime between the Gd(III) ion and the bulk water molecules that induces better relaxivity. It was determined at 20 MHz/310 K

that this complex has an r_1 = 12.0 mM^{-1} s^{-1} per Gd(III) unit with q = 2 in each arm, which is an approximately seven-fold higher relaxivity than Gd-DTPA (Magnevist). This enhancement is related to the rotational correlation time and fast IS H_2O exchange; nevertheless it exhibits a less than expected relaxivity, due to the flexibility of the methyl linker between the core centre and the polydentate ligand. The rotational correlation time of the Ru(II) core is still slower than for the pincers, which leads to quenching of the relaxivity of the Gd(III) ions. The HOMO-LUMO energy gap for the Ru(II) bipyridine (bpy) complex results in bright red luminescence centred at 610-620 nm with a quantum yield of 0.048.

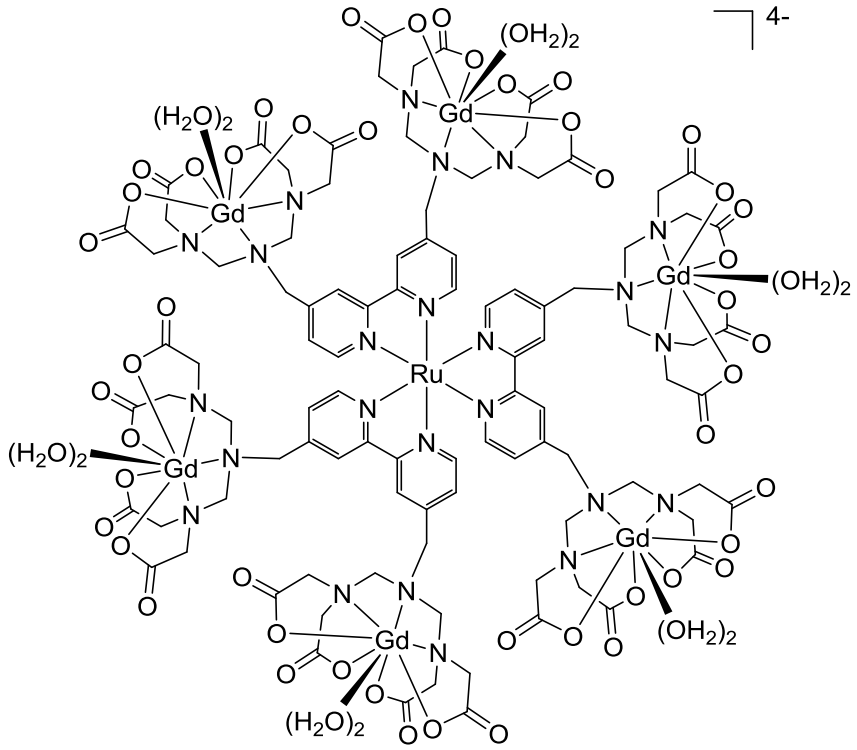

Figure 3.3: **63** complex chemical structure.

Recently, S. Yang and coworkers synthesised a **64** cyclometallated Ir(III) complex that contains one Gd(III).[142] This dual-mode complex shows a promising emission maximum at 560 nm with an excitation wavelength of 405 nm. However, it been found that the lifetime is quenched to 0.2 μs i.e. 66% *cf.* degassed media, due to singlet oxygen formation; the quantum yield (Φ) was similarly quenched in the aerated solution. Φ was found to be 0.014 in the N_2 bubbled aqueous solution, furthermore the relaxivity = 3.36 mM^{-1} s^{-1} at 3T, which is expected from this typical

amide arm that gives slower water exchanging rate, ultimately lower relaxivity than DOTA like complex. This *d-f* heteronuclear system shows selective mitochondria staining and high spleen, lung and liver co-localisation, but it also exhibits decomplexation in the same organs due to macrophage ingestion.

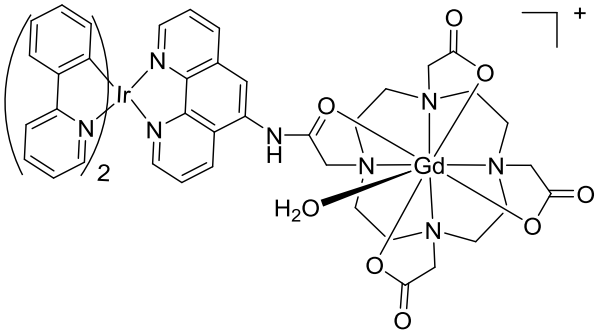

Figure 3.4: **64** complex.

Relaxation values and photophysical details of the discussed dual-mode MRI contrast agents are summarized in Table 3.1.

complexes	Relaxometric Ln(III)	Luminescent metal ion	r_1[a] ($mM^{-1}s^{-1}$)	λ_{ex} (nm)	Quantum yield Φ[b] (%)
60	Gd(III)	Organic dye	3.9	503	83
61	Gd(III)	Re(I)	8.6 (500 MHz)	337	-
62	Gd(III)	Ru(II)	7.0	440	4.7
63	Gd(III)	Ru(II)	23.0	293	0.1
64	Gd(III)	Ir(III)	3.36 (128 MHz)	405	26 (degassed) 7.6 (aerated)

Table 3.1: Relaxometric and photophysical key data of *f–d* heteropolymetallic complexes. [a] Relaxivity r_1 per millimolar Gd(III) at 20 MHz and 310 K unless stated otherwise. [b] Quantum yield relative to a standard solution.

3.2 Target Optical imaging dual-mode Multimeric / Oligomeric MRI Contrast Agents

The aim of the work presented in this chapter was to design d^6 and d^8 transition metal ion cores of Ru(II), Ir(III) and Pt(II). These act as luminescence probes attached to one or more Gd-DO3A units per molecule to act as MRI CAs. These heteronuclear complexes can potentially be used in image-guided surgery

and biological studies.[143] A possible use of these complexes is that of giving the surgeon the ability to locate a tumour and identify its size via MRI before surgery. During the operation, by using a light source for excitation, the tumor mass can be indicated. In addition, to avoid vital healthy tissues, such as blood vessels and nerves. This can be established, by linking these agents with targeting agents such as peptides, antibodies and polyamines, the surgeon can differentiate between the healthy and malignant tissue in tumour excision.[5] Another advantage of these agents is to overcome the sensitivity of the MRI technique, which can be improved by using contrast agents that focus on 'increasing the payload', *i.e.*, by delivering multiple Gd(III) chelates.[2] In addition to the resultant T_1 relaxivity enhancement, these multinuclear CAs with higher molecular weights will allow for a longer lifetime inside the body and an associated lower intake dose.[144]

3.3 Chemistry

The target dual-mode complexes in this chapter are shown in Fig. 3.5.

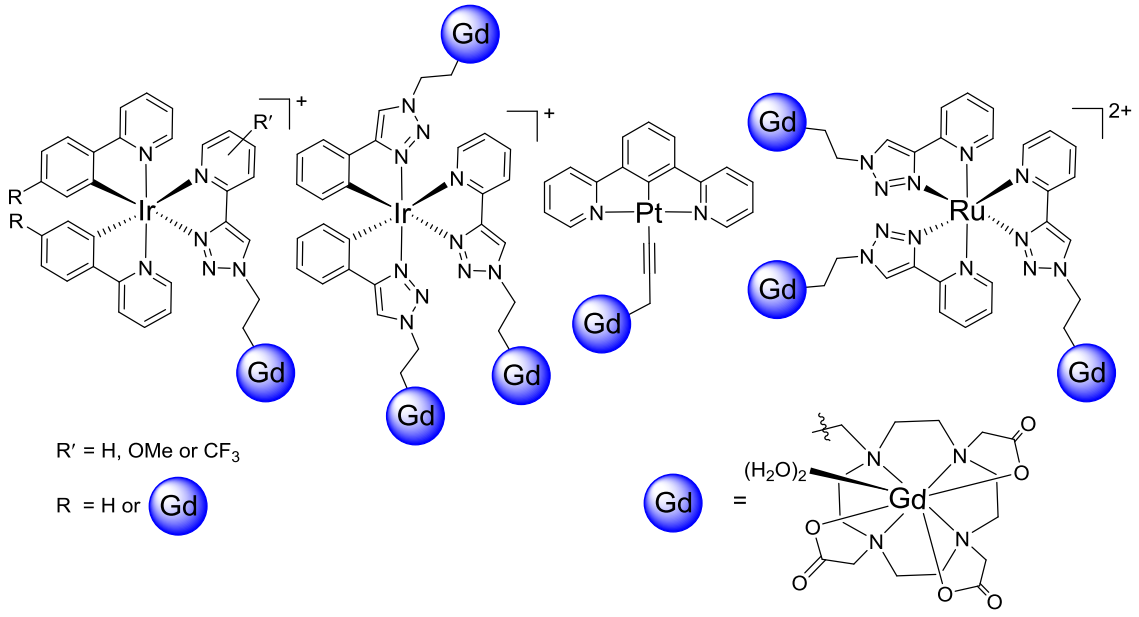

Figure 3.5: The target dual-mode probes.

3.3.1 *Iridium(III) Conjugates*

Retrosynthetic analysis for cyclometallated iridium probes is shown in scheme 3.1.

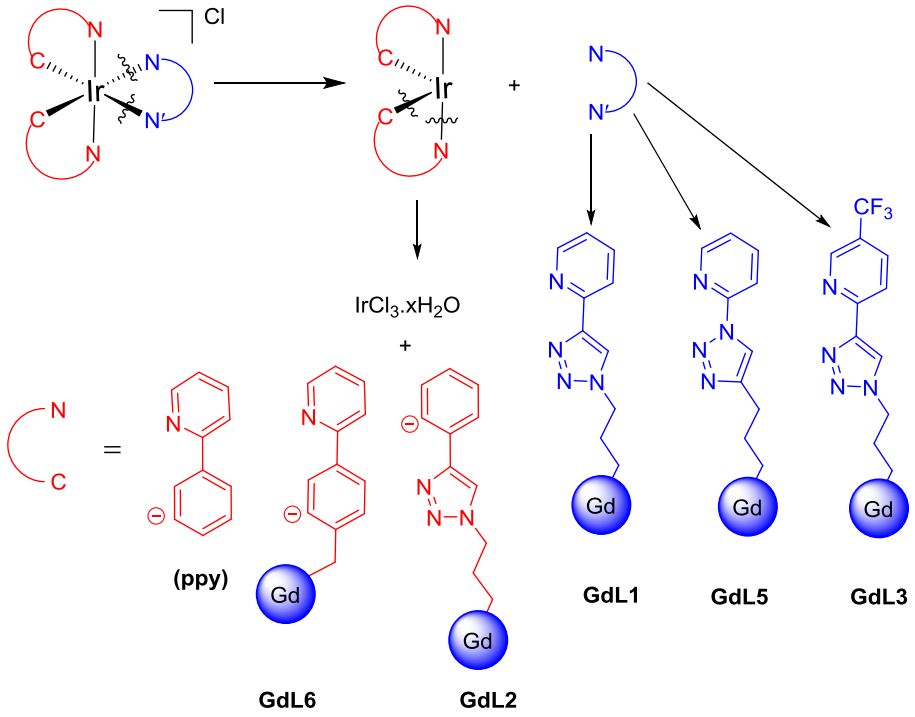

Scheme 3.1: Retrosynthetic analysis planning synthesis of Ir(III) cyclometallated precursors.

The Ir(III) complexes were synthesised in two steps: first, the synthesis of cyclometallated (Ir(C^N)$_2$)-chloride bridged dimers. These are then cleaved with (N^N') ligands to produce the final complexes, as depicted in Scheme 3.2 for synthesising **{Ir(ppy)$_2$Cl}$_2$** dimer and its final mono-lanthanide complexes.[145] The dimer **{Ir(ppy)$_2$Cl}$_2$** was reacted with **EuL1, GdL1**and **GdL5** to give **Ir(ppy)$_2$EuL1** and **Ir(ppy)$_2$GdL1**, **Ir(ppy)$_2$GdL5** and **Ir(ppy)$_2$EuL11** complexes, respectively, and purified via HPLC to give yellow solids with yields of approximates 50-53%. The use of a microwave reactor greatly reduced the reaction times and the use of RP-HPLC during purification allowed conjugates to be obtained in high purity. The formation of the final yellow solid Ir(III) complexes for mono gadolinium was indicated by MS (ESI) with peaks centred at *m/z* = 1188 $[M]^+$ and 1181 $[M]^+$ for **Ir(ppy)$_2$GdL1** and **Ir(ppy)$_2$EuL1**, respectively, the purity was confirmed by analytical-HPLC (Appendix, Fig. 10.15).

The phenyl triazole (plta) dimers **IrGdL2** and **IrEuL2** were synthesised from **GdHL2** or **EuHL2** and $IrCl_3.xH_2O$ following the same conditions using microwave heating (Scheme 3.3). The same conditions were also applied to synthesise the **IrGdL6** and **IrEuL6** dimers which are produced from **GdHL6** and **EuHL6**, respectively with yields in the range 47-48% as seen in Scheme 3.4.

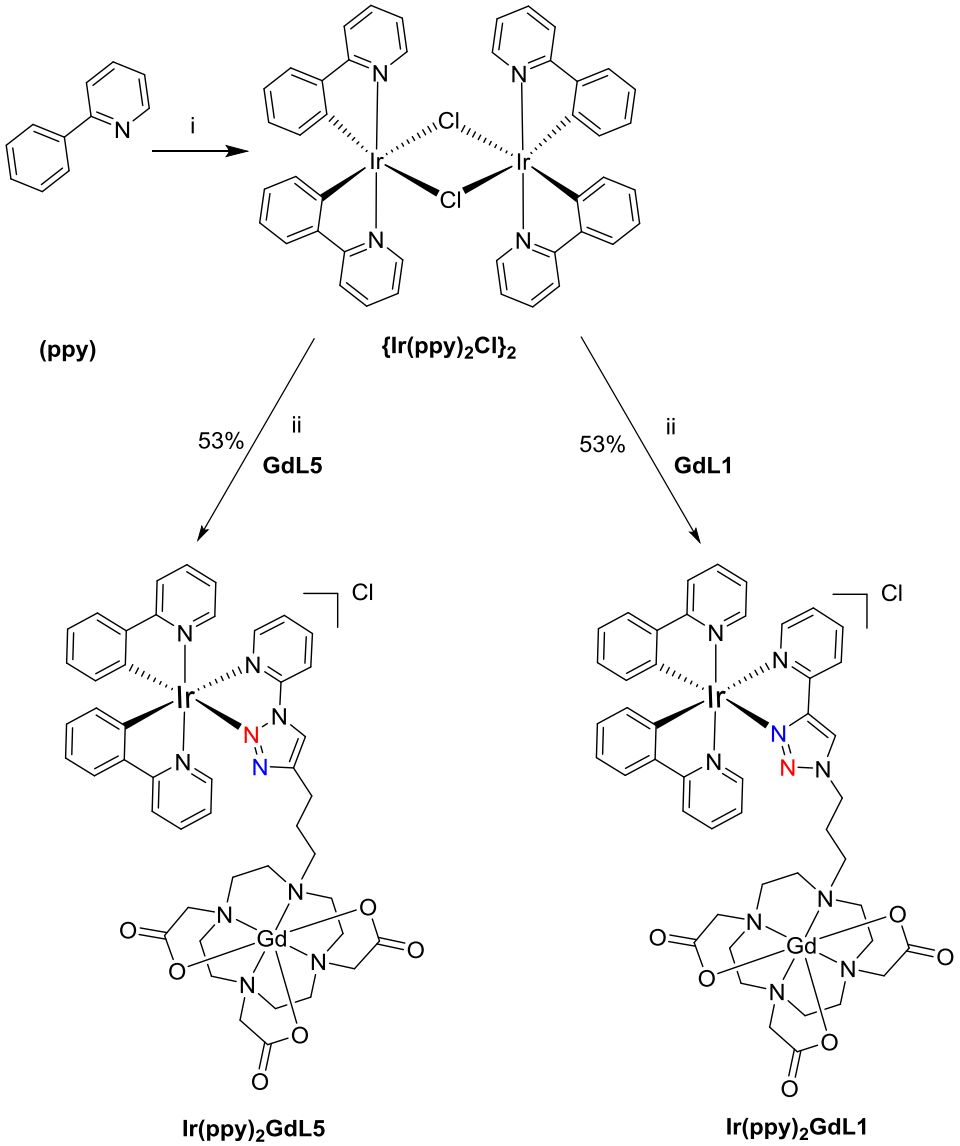

Scheme 3.2: **Reagents and conditions synthesis of** $\{Ir(ppy)_2Cl\}_2$, **$Ir(ppy)_2GdL1$** and **$Ir(ppy)_2GdL5$**: i) $IrCl_3.xH_2O$, H_2O/iPrOH, MW 110 °C, 120 min; ii) MeOH, heating at 90 °C for 18 h.

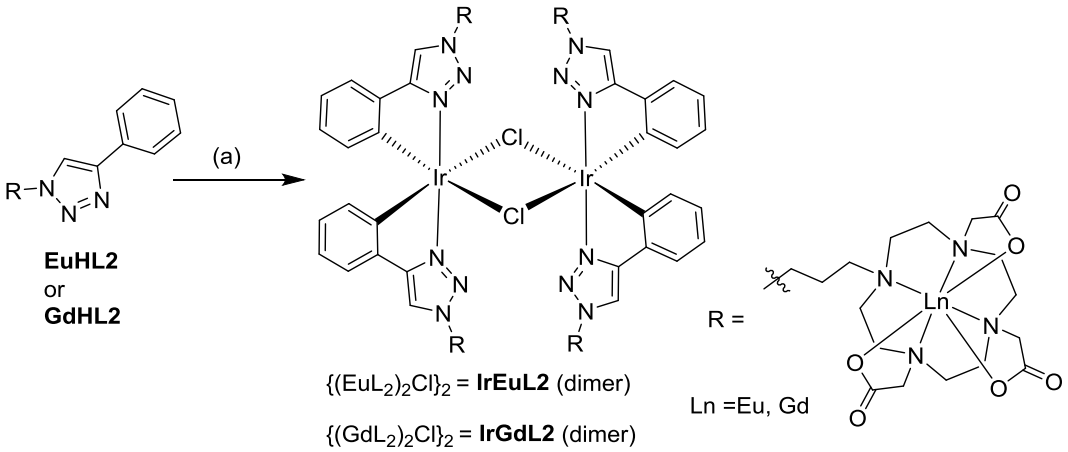

Scheme 3.3 **Reagents and conditions to synthesis IrGdL2** or **IrEuL2**: (a) $IrCl_3.xH_2O$, H_2O/iPrOH, MW 110 °C, 120 min.

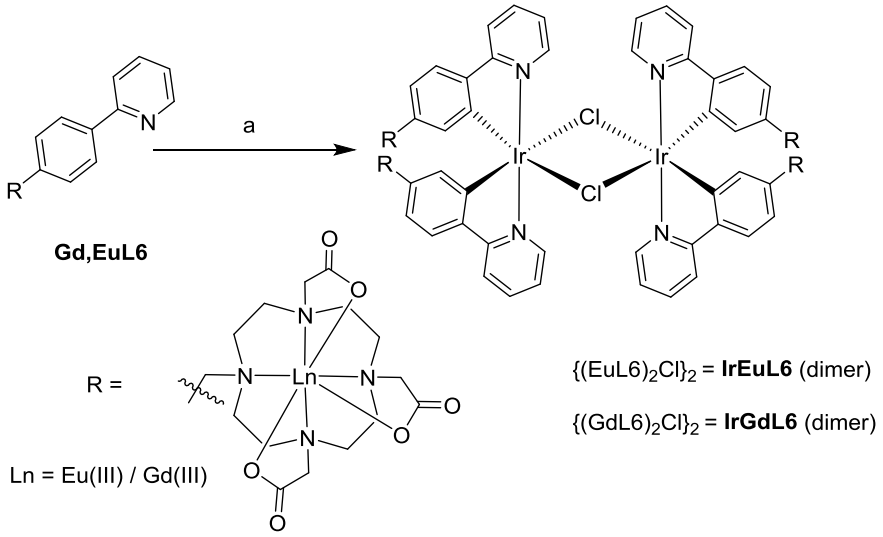

Scheme 3.4: **Reagents and conditions to synthesis IrGdL6 or IrEuL6**: (a) $IrCl_3.xH_2O$, H_2O/iPrOH, MW 110 °C, 90 or 120 min.

The dimers were purified by RP-HPLC, their formation being inferred through MALDI-TOF mass spectrometry due to difficulties ionizing these species using electrospray ionisation. For example, **IrEuL6** and **IrGdL6** dimers give a multiple peaks in MALDI (TOF) spectra centred at *m/z* 1515.2593 and 1526.0975 $[(dimer/2)\text{-}Cl]^+$, respectively. In the same manner **IrEuL2** and **IrGdL2** were detected via MALDI-TOF at *m/z* 1551.4646 and 1560.9862 respectively (Appendix, Fig. 10.6 and 10.7), showing an Eu(III) splitting pattern, and a Gd(III) splitting pattern, $[(dimer/2)\text{-}Cl]^+$. Fig. 3.6 shows the isotopic patterns observed are for **IrGdL6** (MALDI-TOF) and **IrEuL6** HRMS (ESI).

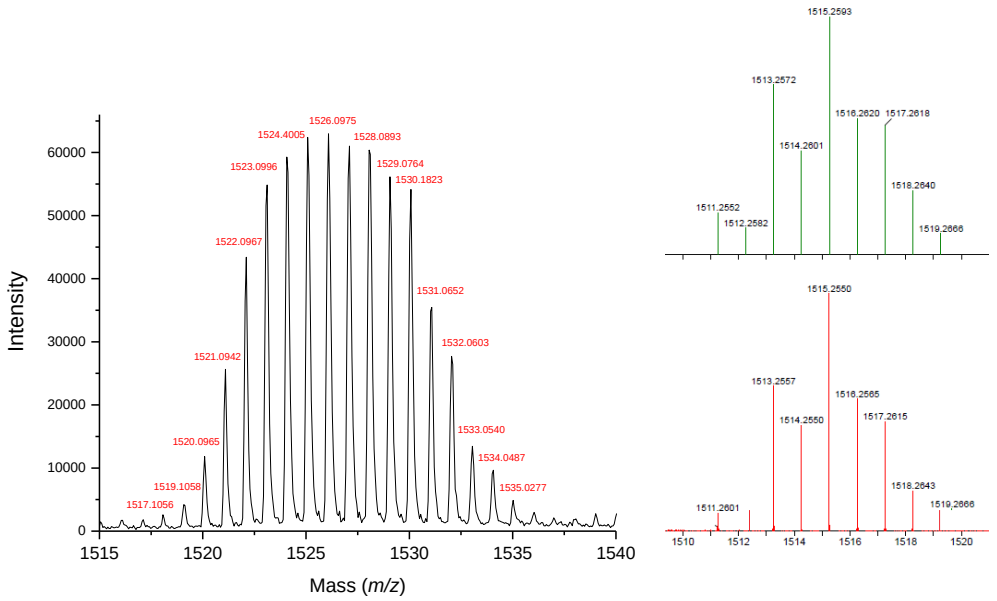

Figure 3.6: MALDI (TOF) of **IrGdL6** (left) and HRMS (ESI) of **IrEuL6** (top right simulation, lower right the observed).

Then **IrGdL2** or **IrGdL6** dimers were then cleaved with **L1** and **L3** lanthanide complexes to form strongly emissive cationic conjugates, such as **IrGdL2L1**, **IrGdL6L1** and **IrGdL6L3** as per general Scheme 3.5.

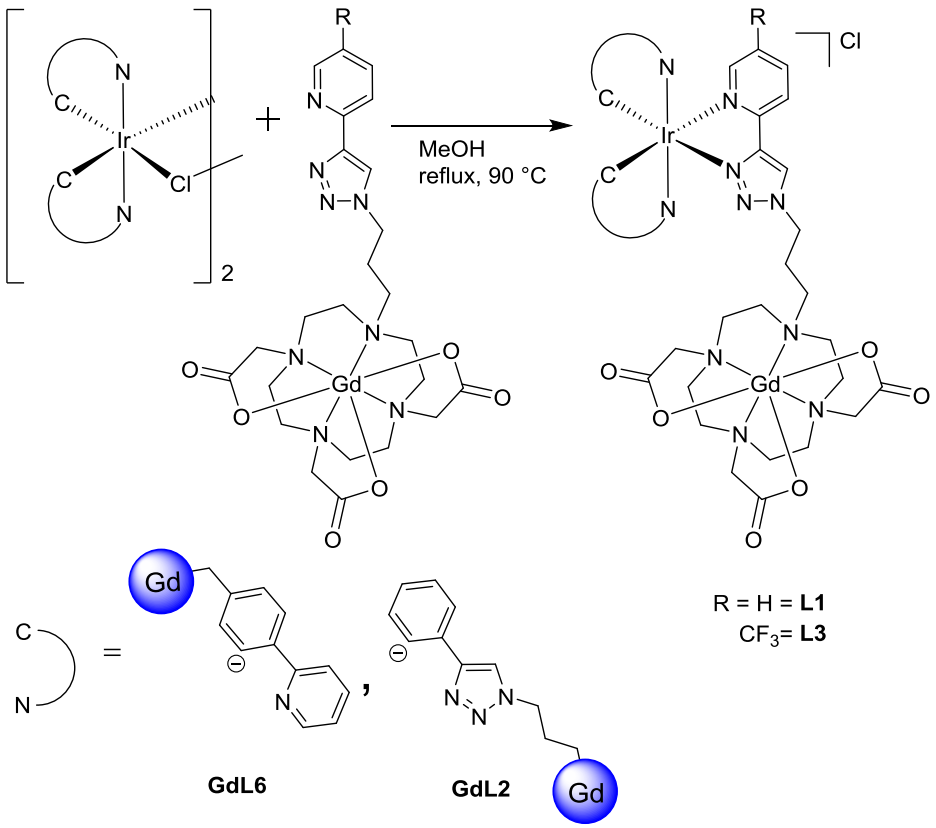

Scheme 3.5: Reagents and conditions for the synthesis of Ir-multigadolinium complexes.

For cyclometallated Ir(III) complexes it has been found that the more hydrophilic the counterion, the more water soluble the complex. For this reason, this work employed Cl^- as a counterion. The trend in hydrophilicity of the counterions typically used is depicted in Fig. 3.7.[146]

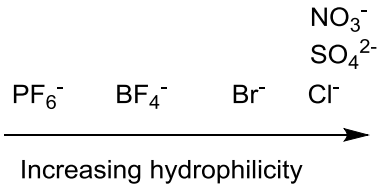

Figure 3.7: the trend in hydrophilicity of counterions.

For the multigadolinium complexes, MALDI (TOF) was used to prove the formation of the final complexes, and the purity was indecated by analytical HPLC (Appendix, Fig. 10.15). For example, **IrGdL6L1** gives a 42% yield, with the mass spectrum as shown in Fig. 3.8 showing multiple peaks at *m/z* 2212 $[M]^+$ *cf.* the mono **Ir(ppy)$_2$GdL1**. The final Ir(III) complexes are shown in Fig. 3.9.

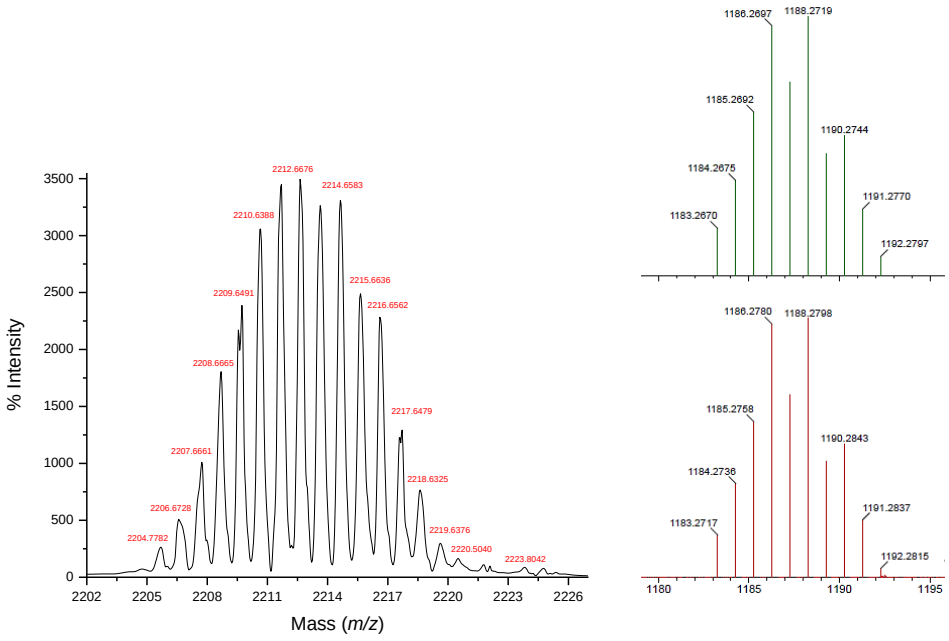

Figure 3.8: MALDI (TOF) of **IrGdL6L1** (left) and HRMS (ESI) **Ir(ppy)$_2$GdL1** (top right simulation, lower right the observed).

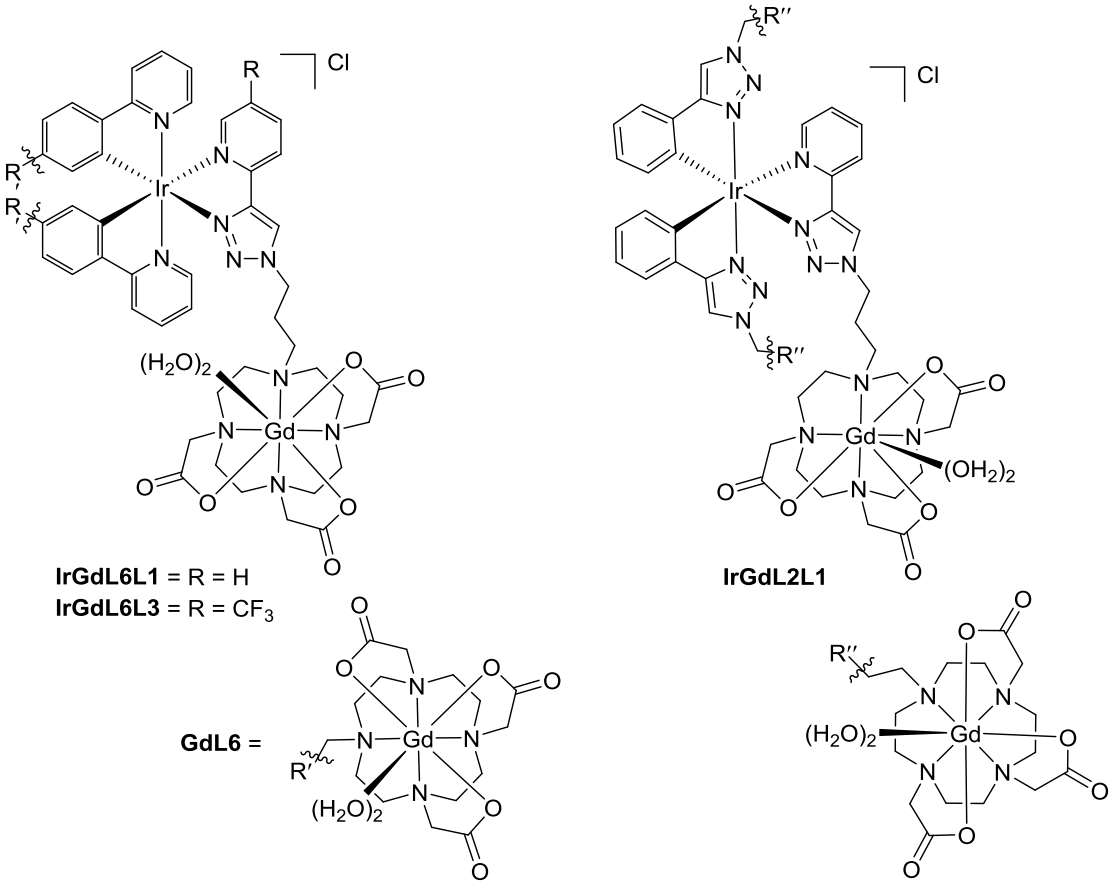

Figure 3.9: iridium-multigadolinium complexes.

3.3.2 *Synthesis of Water-Soluble Pt-Gd Conjugates*

Cyclometallated platinum(II) complexes **Pt(N^C^N)Cl** with a 1,3-di(2-pyridyl)benzene (dpyb) ligand have a high quantum yield, Φ_{lum}, of 0.6 with long-lived photoluminescence in the visible region, of 7.2 and 0.5 ns in degassed and air-equilibrated DCM, respectively.[147] The square planar Pt(N^N^C)Cl shows a distorted structure, which leads to a longer Pt–C bond compared to Pt(N^C^N)Cl. Williams *et al*. reported that the Pt(N^C^N)Cl complexes have a Pt–C bond length of around 1.90 Å, which is about 0.14 Å shorter than those in Pt(N^N^C)Cl.[148] This shortness is expected to deactivate the *d-d* states by raising their energy, making them thermally inaccessible and thus reducing non-radiative decay pathways, eventually resulting in bright luminescence in solution at rt. The platinum(II) complexes with an σ-alkynyl moiety exhibit high chemical and structural stabilities in aqueous solution,[149] as well as better photophysical properties. Therefore synthesis of a

water-soluble Pt-Gd complex with a strong field acetylide moiety containing a polydentate gadolinium pendant is recommended.

Pt(N^C^N)Cl was synthesised using a literature method.[150] While **Pt(N^C^N)I** was produced by reacting **Pt(N^C^N)Cl** with KI. **PtGdL9** was synthesised by reacting **GdHL9** with **Pt(N^C^N)Cl** in the presence of CuI and a base suspension in DCM:DMF. This metal-carbon ligation was characterized by MS (ESI) to give m/z = 1018 $[M+K]^+$ with moderate yield (47%) as a brown-coloured solid. The neutral complex **PtGdL9** shows high solubility in methanol compared to the dichloromethane solubility of the Pt(N^C^N)Cl starting material; however, this solubility is not sufficient for biological use, especially as MRI contrast agents require high water solubility.[139] For this reason, another alkyne gadolinium pendant was introduced, **GdHL10**, with a more polar extension, by introducing an extra oxygen atom into the acetylide arm. The final complex formula had four nitrogen and seven oxygen atoms. Indeed, **PtGdL10** exhibits optimum water solubility with a 46% reaction yield as brown-coloured solid with m/z = 1030 $[M+K]^+$ showing a complex Pt and Gd isotope pattern (Appendix Fig. 10.8). Scheme 3.6 depicts the synthesis of **PtGdL9** and **PtGdL10**. Due to the lability of Pt–C bond in the alkyne side and the possibility of ligand exchange with MeCN, determination of the complex purity by HPLC was unreliable.[151] The hydration number of the **PtGdL10** complex was deduced from **EuHL10** and **PtEuL10** by measuring the lifetime for these analogues. It was found that q = 1 for both **EuHL10** and **PtEuL10**, highly likely due to the coordination of the oxygen in the alkyne appendant to the metal centre to form five a membered stable ring. This was supported by measuring the relaxivity for the **PtGdL10**, which shows it has r_1 = 4.1 mM^{-1} s^{-1} (400 MHz, 298 K) similar to analogous Gd(III) complexes with q = 1 at higher magnetic field.[152] It has been found that using different Pt complex ancillary ligands such as I rather than Cl will increase the yield of the reaction, reduce the impurities, change the solubility and make it less inert atmosphere is needed.

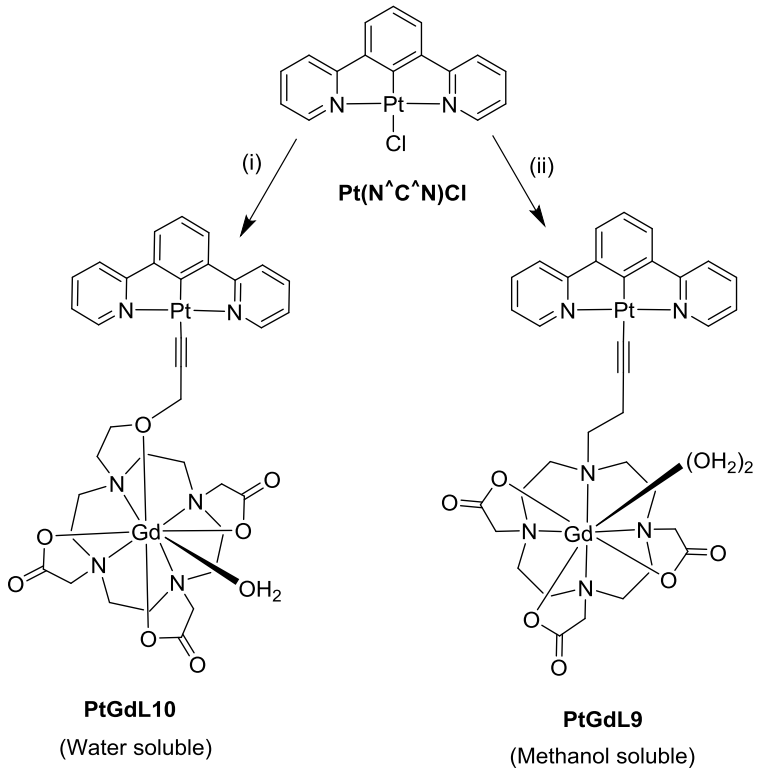

Scheme 3.6: **Reagents and conditions**: i) **GdL10**, CuI, Et_3N, KOH, DCM:DMF; ii) **GdL9**, CuI, DIPA, DCM.

3.3.3 *Ruthenium(II) Conjugates*

Another TM ion that can be used to synthesise emissive complexes of trimeric dual-mode CAs is Ru(II), it is well known to have long lived emission in the NIR region.[153] The cationic dual-mode CAs with ruthenium(II) as a core metal centre were synthesised by reacting anhydrous $RuCl_3$ (in EtOH) with three equivalents of **GdL1**/**EuL1**/**YL3** that bear a pendant pyridiyl-1,2,3-triazole ligand (N^N'). The formation was confirmed by HRMS (ESI) which gives *m/z* = 1073, 1080 and 1183 showing Ru/Ln isotope patterns $[M]^{2+}$ for **RuEuL1**, **RuGdL1** and **RuYL3**, respectively as dark green solid. The 2+ ion formation was confirmed by the spacing of the isotopes peaks in the spectrum with a separation of m/2 = 0.5 (Fig. 3.10). The Ru(II) complexes synthesis is shown in Scheme 3.7.

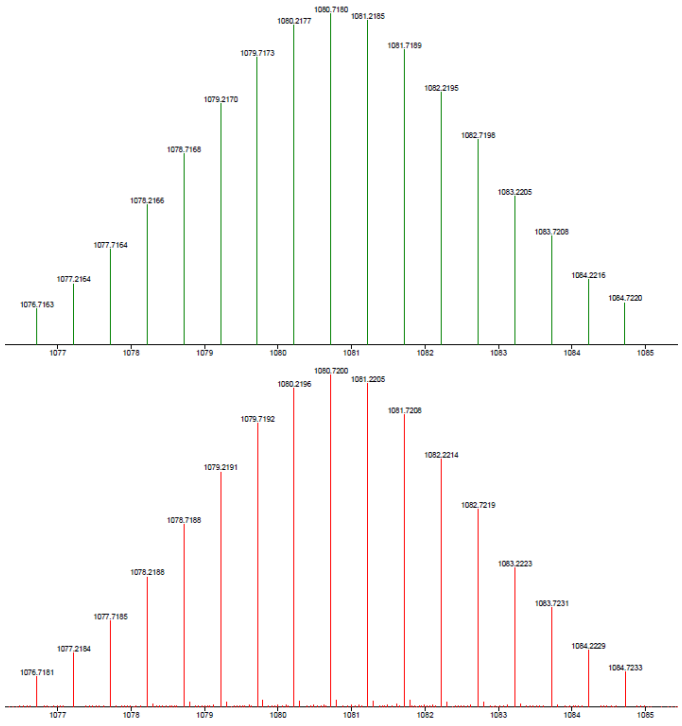

Figure 3.10: HRMS (ESI) for **RuGdL3** (top right simulation, lower right the observed).

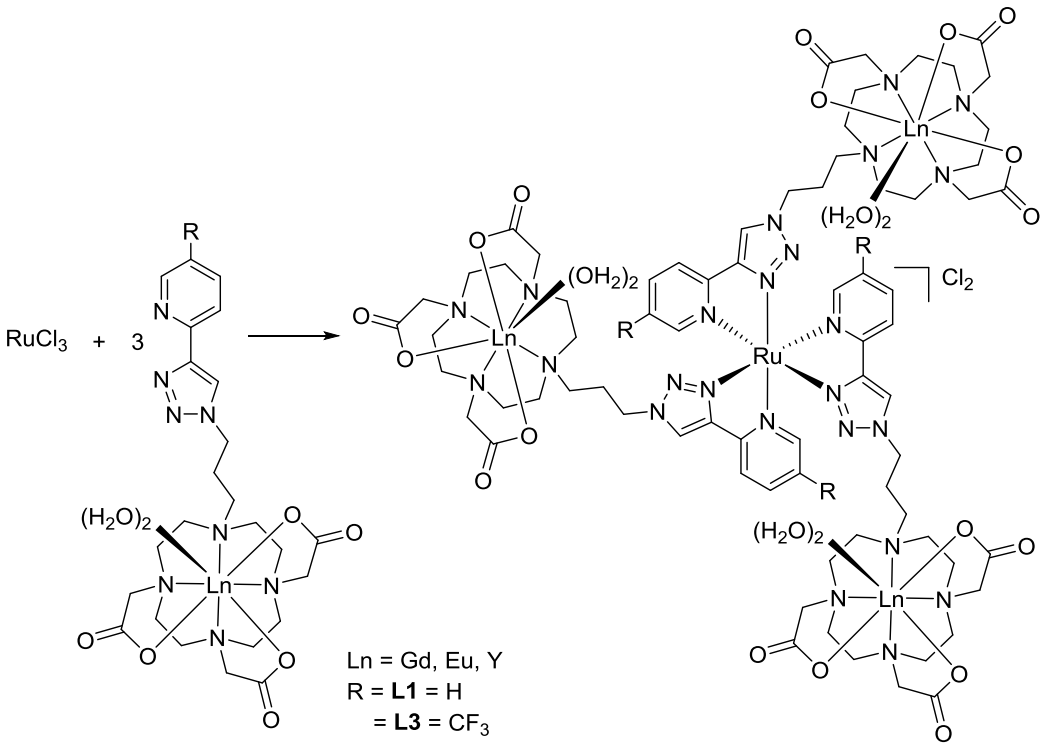

Scheme 3.7: Synthesis and the chemical structure of ruthenium complexes.

3.4 Photophysical Properties

3.4.1 *Eu(III) Lifetime Measurements*

Since the hydration number plays a vital role in CA relaxivity, determining q is necessary. It can be achieved by measuring the lifetime of Eu/Tb(III) analogues in H_2O and D_2O solvents. This work will focus on using the Eu(III) ion to monitor excited state lifetimes. For this reason, each dual-mode complex has been synthesised with Gd(III) replaced by Eu(III) analogue (Section 1.5.3).

One obstacle was faced in measuring the lifetimes for these agents with Eu(III) using this approach, namely the overlap between the transition metals and the Eu(III) emission at a wavelength of 616 nm. Coordinated d^6 and d^8 metals emit in the visible range which covers 616 nm, the wavelength at which the lifetime is monitored; this in turn perturbs the recording of the rate constant for the depopulation of the Eu(III) exited state. One possible solution to overcome this challenge is based on the long lifetime of the lanthanides (1 ms) compared to TMs (~1 μs). The use of a longer measuring time delay (0.1 ms) ensures the collection of Eu(III) photoluminescence only, and ultimately an accurate value for q. **IrEuL6L1** gives q = 1.6 for each Eu(III) ion, which is considerably less than the initial complexes of **EuL1** and **EuHL6** (q = 2). Presumably, this is due to the sterics around the metal centre as a result of aggregation or folding due to the hydrophobic nature of the complex, allowing less than two waters molecules to interact, it could be related to long Eu–OH_2 distances or there is mixture of q = 1 and q = 2 complexes.[154]

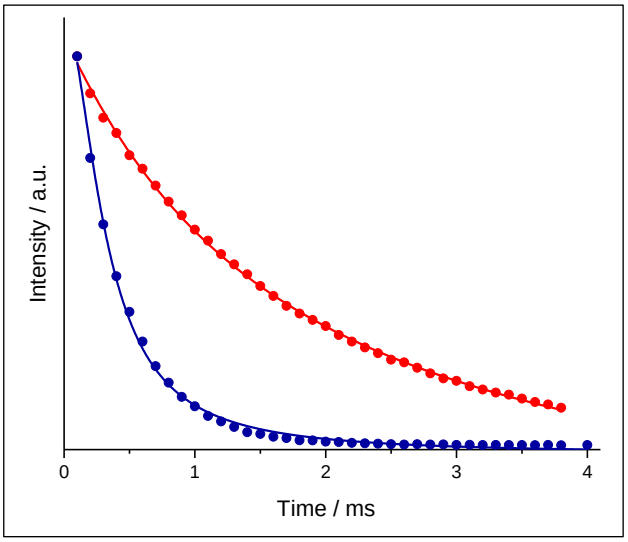

Figure 3.11 : Excited state life time studies fo
IrEuL6L1 at 298 K, pH 6, λ_{ex} = 280 nm, λ_{em} = 616 nm. Blue = H_2O, Red = D_2O.

Fig. 3.11 shows a long decay lifetime for **IrEuL6L1** in H_2O and D_2O. This process was followed to determine *q* for the remaining complexes (as reported in Table 3.2).[155]

Complex	λ_{ex} / nm	λ_{em} / nm	k_{H_2O}/ms^{-1}	k_{D_2O}/ms^{-1}	*q* (± 0.2)
EuL1	280	616	2.57	0.59	2.07
EuHL2	280	616	2.39	0.59	1.9
EuHL10	392	616	1.81	0.55	1.2
EuHL6	280	616	2.51	0.61	2.0
IrEuL2L1	320	615	2.1	0.71	1.4
IrEuL6L1	400	616	2.18	0.61	1.6
IrEuL6L3	400	616	2.18	0.59	1.6
RuEuL1	300	615	2.20	0.65	1.56
PtEuL10	395	611	1.84	0.71	1.0

Table 3.2: Rate constants, *k*, for depopulation of the excited state and derived hydration states, *q*.

3.4.2 *Ir(III)-Gd Dual-Mode CAs*

Cyclometallated iridium(III) complexes generally exhibit long-lived photoluminescence, τ, ~ 0.7 μs (aerated MeCN) with high quantum yields, Φ, ~ 0.3 at room temperature in various solvents.[156] The presence of this heavy metal, gives a strong spin-orbit coupling, leading to efficient ISC.[157] The excited state for these cationic complexes arises from: 1) metal-to-ligand charge transfer (MLCT) in which electrons are promoted from $5d_{xy}$- HOMO orbitals to the π*-antibonding LUMO orbitals that are localised on the ancillary ligand. 2) ligand-centred (LC) transitions which are promoted between the π orbitals of the ligands. As discussed in Section (1.6), pyta is considered an excellent ancillary ligand (N^N') for the synthesis of cationic iridium(III) complexes for use in generating organic light-emitting devices (OLEDs).[158] Clearly, a 1,2,3-triazole moiety can be incorporated into both bis-cyclometallated or/and ancillary ligands synthesis. Indeed, in the cyclometallated Ir(III) complexes, phenyl-(1,2,3)-triazole (phta) and pyta increase the band gap between the HOMO and LUMO levels via their electron-rich triazole moiety with its low π-acceptor characteristic.[159] The suitable highest excitation energy that can be

reasonably used in single photon excitation confocal microscopy is 405 nm, so it is important to design an imaging probe that shows an excitation maximum close to this wavelength.[160] However, Ir(III) complexes can also be excited at longer wavelengths in two-photon excitation microscopy (TPE). TPE has received considerable attention in the bioimaging field due to the reduced excitation energy used, giving deeper penetration, reduce specimen photodamage, less scattering in the tissue, ultimately highly resolved spatial 3D images that can be collected.[161]

Fig. 3.12 shows the photophysical properties of **IrGdL2L1**; the strong absorption in the UV region (200-260 nm) is attributed to the π-π* ligand-centred transitions (^{1}LC) of both pyta and phta ligands. The shoulder bands in the 275-360 nm range belong to both ^{1}LC/^{1}MLCT transitions with contributions from both the C^N and N^N ligands. The transitions responsible for the low intensity shoulder that tapers off at around 400 nm are mixed ^{1}LLCT/^{1}MLCT transitions. The emission of this complex can be best described as resulting from a mixture of ^{3}MLCT/^{3}LLCT, sometimes referred to as metal–ligand-to-ligand charge transfer (MLLCT).[162]

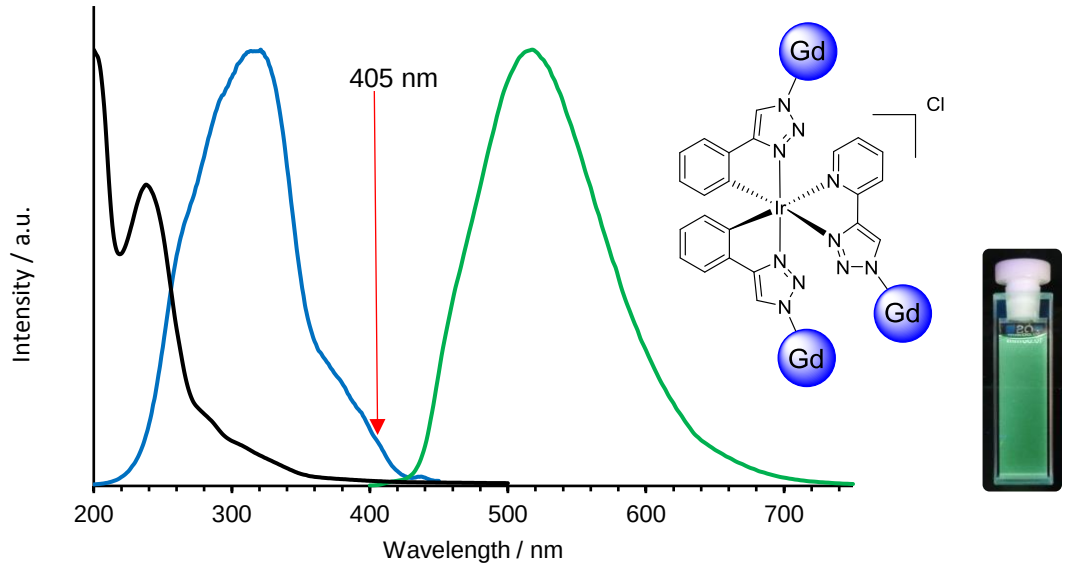

Figure 3.12: Normalised absorption (black), excitation (blue) and emission (green) spectra for **IrGdL2L1** λ_{ex} 513, λ_{em} 320, in aerated HEPES (50 mM, pH 7.4).

As seen in Fig. 3.12, de-population of the triplet excited states for **IrGdL2L1** gives a green emission maxima at 520 nm, with tail extends to lower energy at 750 nm. Noticeably, this π→π* in nature emission is more susceptible to oxygen quenching in aqueous solution, particularly when aerated.[163, 164]

This quenching behaviour can be described by the Stern-Volmer equation:

$$\frac{\tau_0}{\tau} = \frac{I_0}{I} = 1 + k_Q \tau_0 [O_2] \quad (25)$$

where τ_0 and I_0 are the excited-state lifetime and luminescence intensity in the absence of oxygen and τ and I are the same but in the presence of oxygen. $[O_2]$ is the partial oxygen pressure and concentration of oxygen and k_Q is the bimolecular quenching constant.[165]

Generally speaking d^6 / d^8 complexes with (1,2,3)-triazole ligands exhibit blue-shifts in both excitation and emission spectra due to the increased HOMO-LUMO energy gap *cf.* ppy ligands. This gap stems from the stabilisation of the HOMO relative to the LUMO.[156] This is related to receiving electron density in the π*-orbitals of the ligand-centred π-system *via* back-bonding, stabilising the occupied t_{2g} orbitals of the Ir(III).[158]

In terms of synthesising the imaging probe for use in single photon excitation microscopy, it was necessary to change the phta for a ppy ligand to shift the excitation spectrum further to the visible by destabilising the HOMO. First, changing the nature of the cyclometallated ligand is more successful than decorating the phenyl rings with electron donatng groups (EDG), because of the large emission shift (~80 nm) they exhibit with respect to the few nanometeres obtained with the addition of an EDG such as OMe.[166]

It is clear from Fig. 3.13, that **IrGdL6L1** exhibits a red shift in its excitation spectrum with respect to that for **IrGdL2L1** (Fig. 3.12). The absorption spectrum recorded for **IrGdL6L1** shows a perceptible 73 nm bathochromic shift, which is likely related to the lower energy of ppy compared to electron-rich nature of the pyta moiety, which leads to destabilising the HOMO levels, ultimately decreasing the HOMO-LUMO energy gap. The bands in the 250–300 nm region are then once again the allowed intraligand π–π* transitions of the phenyl-pyridine units and of the 2-pyridyl 1,2,3-triazole. The absorption spectra as well shows ^{1}MLCT transitions at energies lower than the ligand π–π* transitions, in the 350–450 nm region, partially overlapping with the spin-forbidden ^{3}MLCT transitions, which extend to 480 nm.

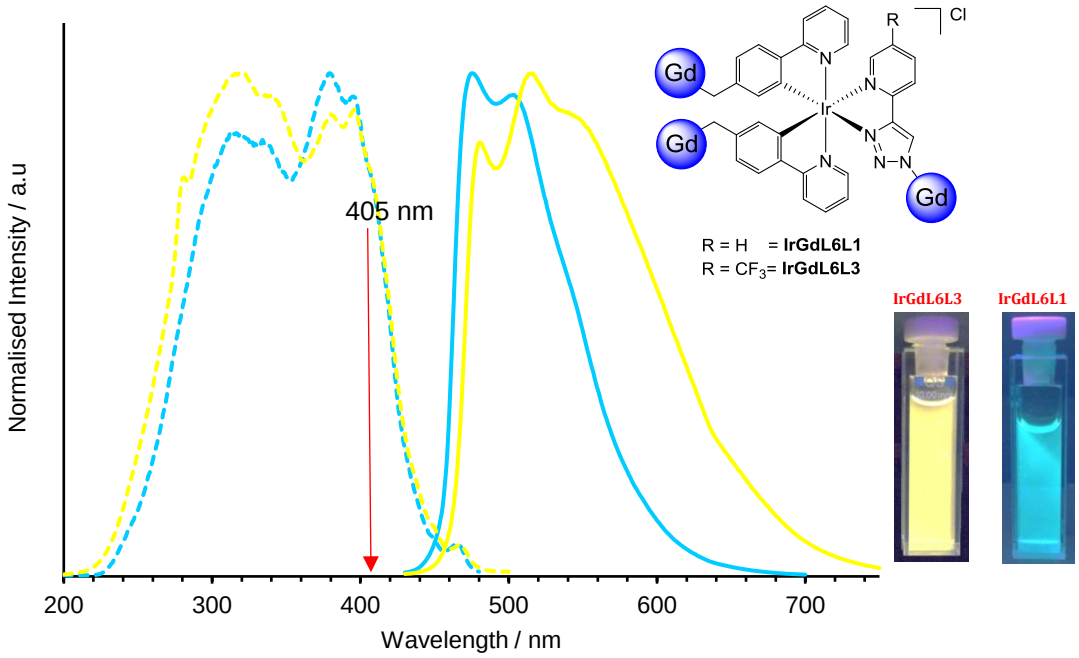

Figure 3.13: **IrGdL6L1** (sky-blue, λ_{ex} = 405 nm, λ_{em} = 505 nm) and **IrGdL6L3** (yellow, λ_{ex} = 405 nm, λ_{em} = 560 nm) excitation (dashed line) and emission (solid line) spectra in aerated HEPES (50 mM, pH 7.4).

IrGdL6L1 shows a narrower emission band with resolved vibronic structure emission maxima at 480 and 510 nm with a tail reaching to 700 nm, rather than a featureless spectrum of **IrGdL2L1** associated with MLLCT states (Fig. 3.14). The two strong shoulders in **IrGdL6L1** emission are ascribed to ^{3}ILCT characterized in the 480 nm region while the ^{3}MLCT transtions are in the 510 nm (Appendix, Fig. 10.10).

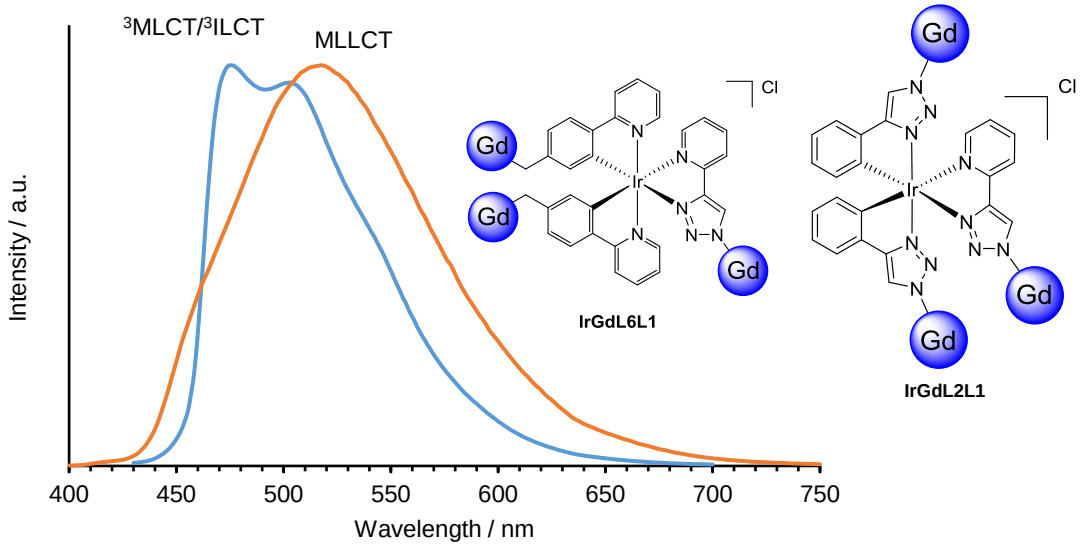

Figure 3.14: Normalised emission spectrum of **IrGdL2L1** (—), and **IrGdL6L1** (—), λ_{em} =320 and 405 nm respectively.

For optimum biological usage, investigation was carried out on **IrGdL6L1** to produce a probe that can be excited at 405 nm. A CF_3 group was substituted onto the pyridine C-5 atom in the ancillary ligand to produce **IrGdL6L3**. This substitution with an electron withdrawing group led to a stabilisation in the unoccupied pyta(π*) orbitals, consequently slightly reducing the HOMO-LUMO energy gap and appearance of new emission bands between 550-750 nm related to depopulation of excited pyta* as seen in Fig. 3.13.[156] Noteworthy, the excitation spectrum did not change or shifte when CF_3 group was added, this confirms that the main feature of the absorption of these complexes stems from ppy→ppy* or M→ppy*.[167]

The use of an inverted 1-(pyrid-2-yl)-1,2,3-triazole ligand (tapy) has gained some attention as a coordination site with TMs, in which it exhibits interesting photophysical properties that promote its use as a luminescent probe for imaging live cells.[157] The emission of tapy as an ancillary ligand in the cyclometallated Ir(III) complexes generally exhibit red-shifts, with high quantum yields and long-lived photoluminescence compared to "regular" pyta, suggesting a promising backbone for use in biomedical applications.[102, 168] Fig. 3.15 shows the differences in structure between inverse and regular 2-pyridyl-1,2,3-triazole moiety in the monogadolinium complexes **Ir(ppy)$_2$GdL5** and **Ir(ppy)$_2$GdL1**, respectively.

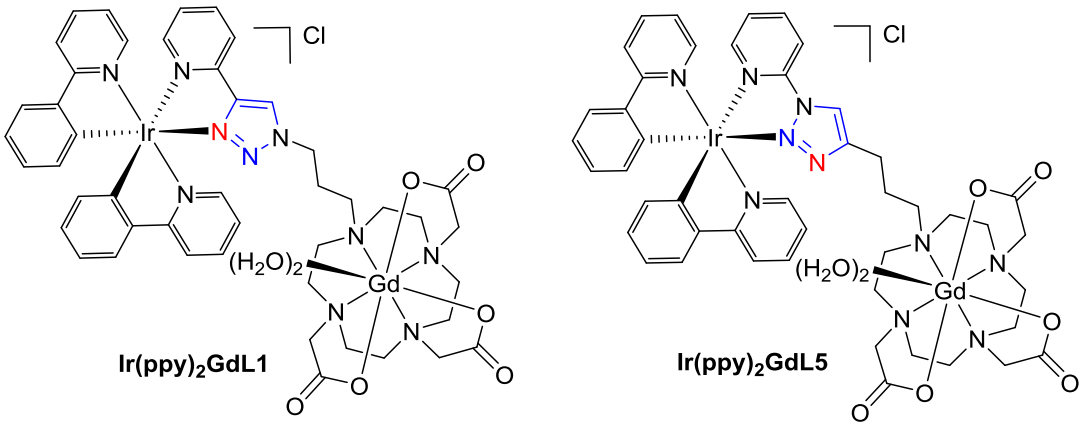

Figure 3.15: **Ir(ppy)$_2$GdL1** and **Ir(ppy)$_2$GdL5** structures, showing N(3) *cf.* N(2) coordination.

It has been found both complexes display comparable absorption spectra to each other with λ_{max} = 268 nm arising from π-π* transitions with weak shoulder transitions at < 350 nm due to MLCT.[99] The absorption spectrum of **Ir(ppy)$_2$GdL1** is shown in (Appendix Fig. 10.11). The emission maximum in **Ir(ppy)$_2$GdL5** is

shifted about 80 nm to the red compared to **Ir(ppy)$_2$GdL1**, which can be clearly can be seen in the change of the emission colour from sky-blue to yellow with maximum emission at 560 nm (Fig. 3.16). This is due to the coordination of Ir(III) to the less basic N(2) nitrogen molecule (less electron- rich) of the heterocyclic units (tapy); therefore, the metal–ligand interaction (ligation) is weak, ultimately reducing the HOMO-LUMO gap.[157]

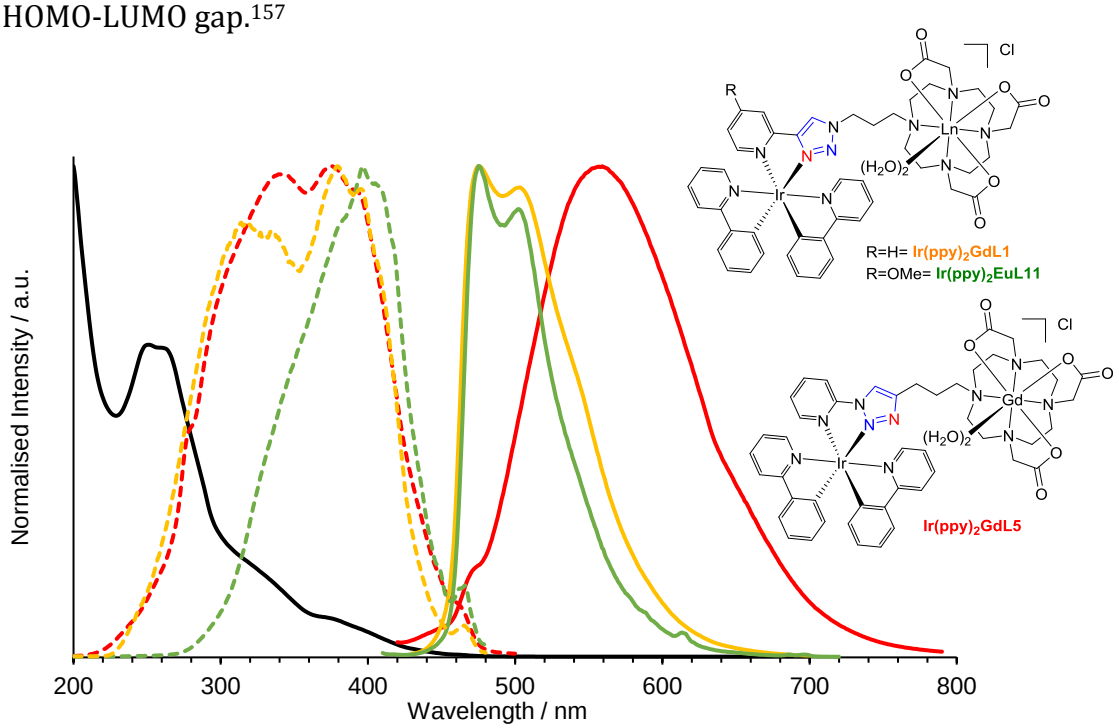

Figure 3.16: Normalised absorption (black), excitation (blue) and corrected emission spectra for **Ir(ppy)$_2$GdL5** (red) λ_{ex} 560 nm, λ_{em} 405 nm. **Ir(ppy)$_2$GdL1**(orange) λ_{ex} 480 nm, λ_{em} 405 nm, **Ir(ppy)$_2$EuL11**(green) λ_{ex} 500 nm, λ_{em} 410 nm (1 x 10^{-4} M) in aerated HEPES (0.1 M, pH 7.4).

In order to investigate the effect of substitution with electron donating group on the Ir(III) photophysical properties, **Ir(ppy)$_2$EuL11** was synthesised with OMe located in the pyta ancillary ligand. It was found that the 4-methoxy group leads to destabilise HOMO, which induces a large energy shift on π→π* transitions to higher wavelength led to disappear it in excitation spectrum with minor change on ^{1}MLCT *cf.* **Ir(ppy)$_2$GdL1** as seen in Fig. 3.16.[167] The latter as well demonstrates that the electron donating group has not effect on the LUMO orbitals ^{3}MLCT/^{3}ILCT-based emission at 478/504 nm respectively, this is might be related to LUMO orbitals are heavily localised on ppy (π*) rather than pyta.

3.4.3 *Pt(II)-Gd Dual-Mode CAs*

The HOMO of cyclometallated Pt(N^C^N) complexes is localized across the metal centre, the ancillary ligand, and partially, the phenyl ring. The LUMO is mainly located on the (N^C^N) ligand. The T_1 states are assigned as being a mixture of ^{3}MLCT/^{3}ILCT character.[92] Substitution of the chloride with monodentate ligands such as acetylide in Pt(N^C^N)Cl represents an indispensable method for modifying these complexes and tuning their emission. It has been found that acetylide motifs, compared to acetonitrile or pyridine derivatives, give more stable complexes with red-shifted emission.[169]

3.4.3.1 Pt(II) Monomer Photophysical Properties

The electronic absorption spectrum of **PtGdL10** in water is shown in Fig. 3.17. The low-energy band in the 400-500 nm range is ascribed to the ^{1}MLCT transition, while the high-energy absorption bands at 280-390 nm are assigned to the π→π*/n→π* transitions within the dipyridylbenzene ligand.[170]

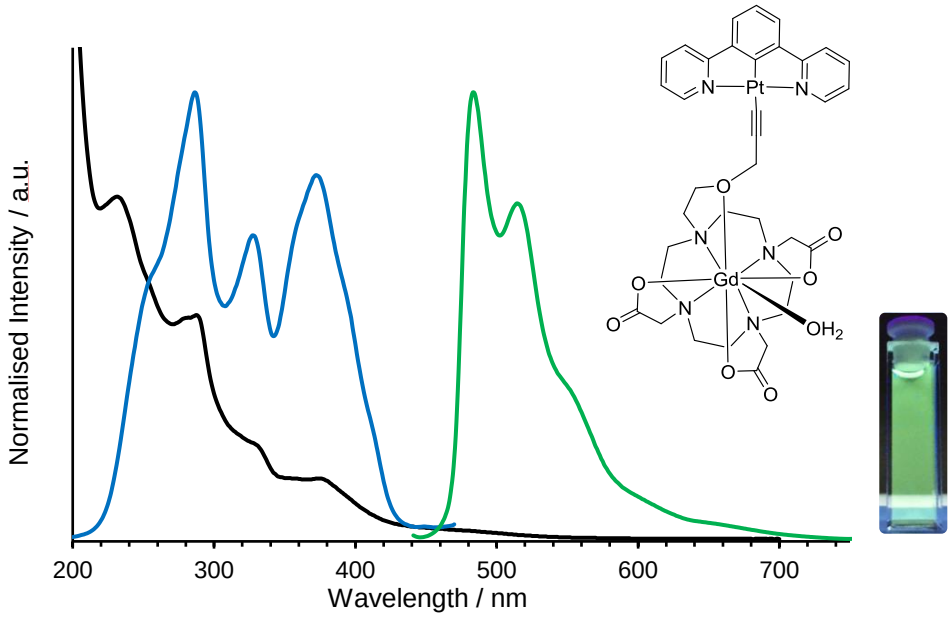

Figure 3.17: **PtGdL10** absorption (black), excitation (blue) and emission (green) in aerated 0.1 M HEPES (25 μM, pH 7.4). λ_{ex} 377 nm, λ_{em} 482 nm.

Complex **PtGdL10** is emissive at room temperature in aqueous solution. Fig. 3.18 shows its emission spectrum when excited at 377 nm. The high intensity peaks at 515 and 485 nm most likely originate from the ^{3}IL [π → π*- (L)] and ^{3}MLCT [dπ(Pt) → π*(L)] excited states respectively.[171] The sharp emission is related to the rigidity

of this complex, as is the large Stokes shifts of 112 nm, whilst lifetimes of around 0.9 μs suggest that the emission originates from a triplet state.[172]

PtGdL10 shows green emission at concentrations of around 25 μM. The cyclometallated platinum complexes usually show long lifetimes with high Φ, due to the small distortion of the excited state and the emission that has ^{3}MLCT character mixed with significant ligand character $^3\pi$–π^*.

It is well known that chloride substitution with a high field acetylide moiety in Pt(N^C^N)Cl tunes the photophysical properties of the complex.[170] To investigate this theory, both complexes (the initial halogenated ligand and **PtGdL10**) were dissolved in DMSO/H_2O (2/98 v/v) to compare their photoluminescence properties in aqueous media. Fig. 3.18 shows that there is a slight bathochromic shift in both the excitation and the emission spectrum of about 10 nm for **PtGdL10** *cf.* Pt(N^C^N)Cl. This is due to destabilisation of the HOMO energy in the **PtGdL10** complex because of the electron-rich acetylide ligand (π-donating group) metal–carbon bond.[173]

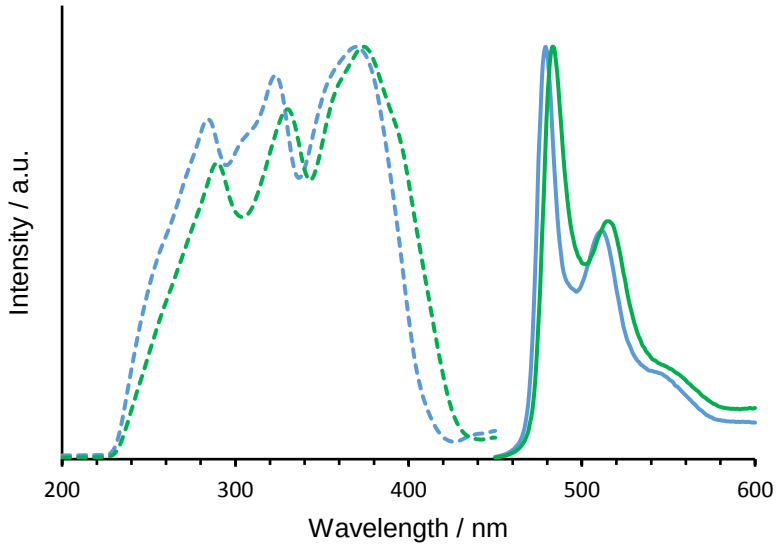

Figure 3.18: comparison between **PtGdL10** (green) and **Pt(NCN)Cl** (blue) in 2% DMSO at pH 7.4, 298 K

3.4.3.2 Pt(II) Dimer Emission

There has been considerable research into the synthesis imaging agents that emit in the 700-900 nm region of the electromagnetic spectrum, due to the relative transparency of the tissue to such wavelengths and low cytotoxicity.[174] Platinum(II) complexes with square planer geometries form flat architectures. This structure

introduces Pt–Pt aggregation at elevated concentrations, which leads to the production of emission at lower energies (λ_{max} 630 nm). The excimer emission is characterised by a low quantum yield and shorter lifetime, owing to forbidden *d-d* transitions.[175] As shown in Fig. 3.19, **PtGdL10** exhibits an inter-molecular excimer emission at 20 μM – 900 μM concentrations in the 700-900 nm region upon excitation at 377 nm. This is related to metal-metal-bond-to-ligand charge transfer (MMLCT) or $d\sigma^*(Pt_2) \rightarrow \pi^*(L)$ transitions. It may be noticed that the monomer luminescence of **PtGdL10** at 482 nm decreases at higher concentrations, the reason for which could be related to: 1) a large degree of aggregation that diminishes the amount of the monomer, or 2) significant self-absorption by the aggregates in the high-energy region.[175]

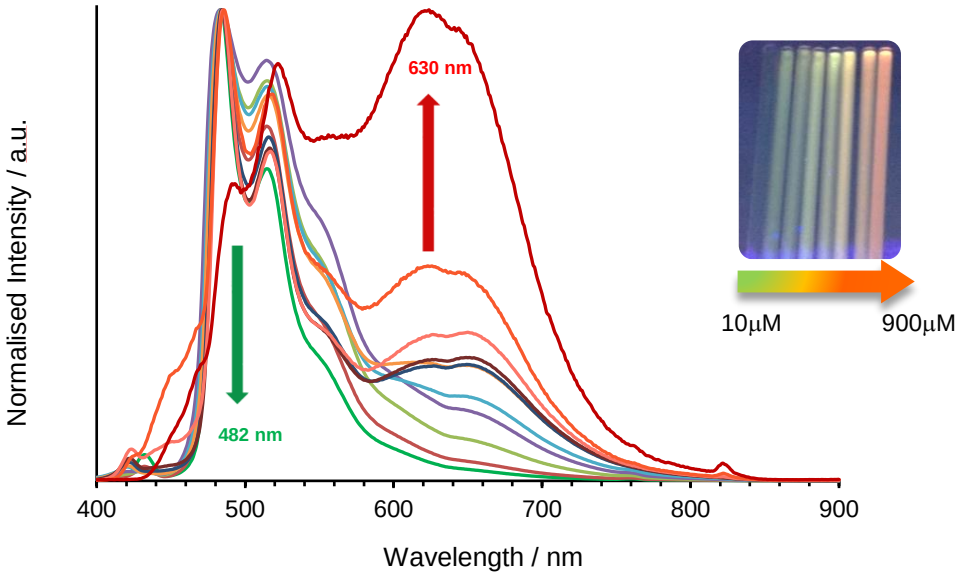

Figure 3.19: **PtGL10** excimer in H_2O over different concentrations. λ_{ex} = 377 nm at 298 K.

Fig. 3.20 shows the molecular orbital diagram of the monomer Pt(II) transitions and the ground-state aggregation of two platinum(II) metal atoms through the perpendicular d_{z^2} orbitals.[171] This aggregation will eventually lead to a decrease in the excited state energy level accompanied by a significant bathochromic shift of the emission maximum in comparison to the monomeric species.[171] The ratio of the increase the dimer emission at 630 nm regarded to decrease the mono at 482 nm could potentially be used to report on probe concentration.

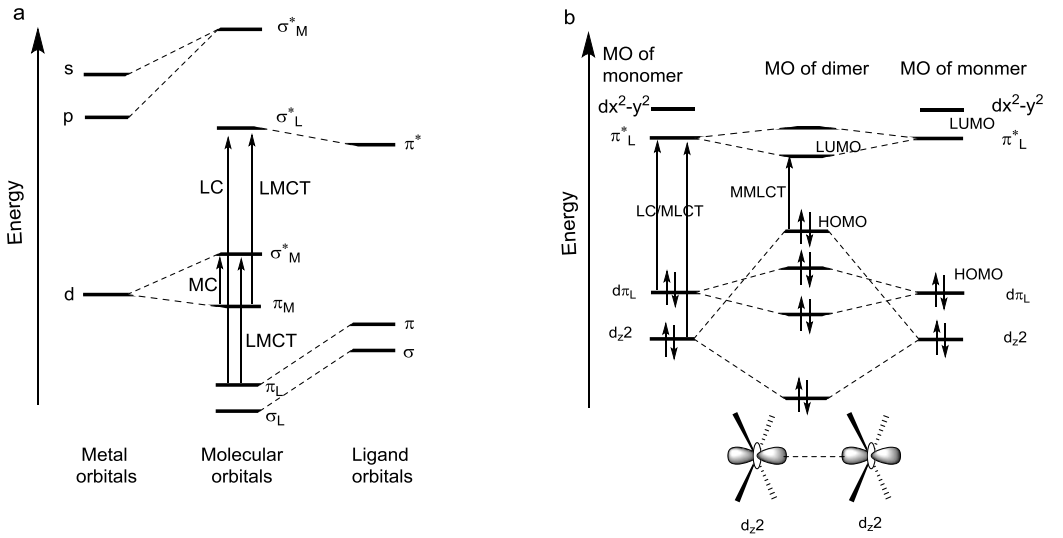

Figure 3.20: (a) Simplified MO diagram for a generic transition metal complex and relative spectroscopic excitation transitions. (b) Simplified MO diagram of two interacting square-planar platinum(II) complexes, showing the intermolecular dz^2 orbital overlap in the ground-state and its influence on the energy of the MO levels.

3.4.4 *Ru(II)-Gd Dual-Mode CAs*

The homoleptic $[Ru(bpy)_3]^{2+}$ complex displays outstanding photophysical properties, promoting its use in red-emitting bio-sensors. Such an emission in the visible region, with long-lived photoluminescence up to the microsecond timescale and large Stokes shift (>5000 cm^{-1}) with high photo- and chemical stabilities in aqueous media.[176] Similarly, Ru(II) with pyta moieties allows synthesis of homoleptic / heteroleptic complexes that can exhibit interesting photophysical properties and antimicrobial activities.[177] The emission of $[Ru(bpy)_3]^{3+}$ and its derivatives arises from ^{3}MLCT, nevertheless this emission is blue-shifted on pyta ligand substitution.[178]

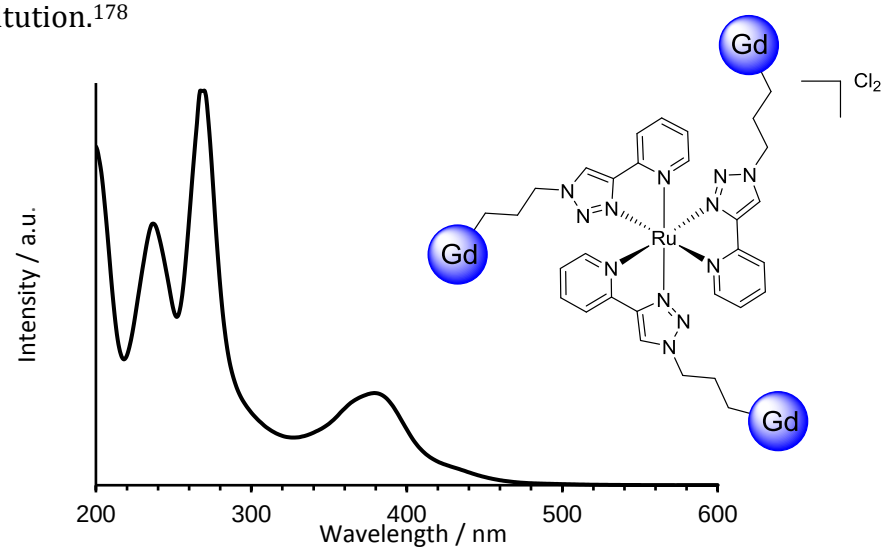

Figure 3.21: **RuGdL1** absorption (black) emission (blue) at λ_{ex} = 300 nm spectra in (50 mM HEPES, 273 K).

The UV-Vis absorption spectrum of **RuGdL1** is shown in Fig. 3.21. As expected, the complex shows a MLCT transition in the 324-473 nm region and LC (π→π*) between 324-250 nm, while the peaks at wavelength less than 250 nm may relate to metal centre MC transitions (*d-d*).[177] In terms of emission, **RuGdL1** exhibits a faint quenched emission in the blue region of the electromagnetic spectrum, unlike $Ru(bpy)_3$ that shows intense photoluminescence in the visible region (610 nm). Due to the reduced π-acceptor properties of pyta over bpy, the electron density was increased on the pyta ligands and consequential stabilisation of the LUMO relative to the HOMO.[179, 180] In addition the high energy of ^{3}MLCT leads to a decrease in the energy gap between it and ^{3}MC, facilitating non-radiative decay back to the ground state, as shown in Fig. 3.22.[181] Happ *et al.* stated that pyta acts as an efficient quencher in Ru(II) octahedral complexes, as well as enhancing the fast T_1 relaxation to S_0 through radiationless deactivation pathway.[178]

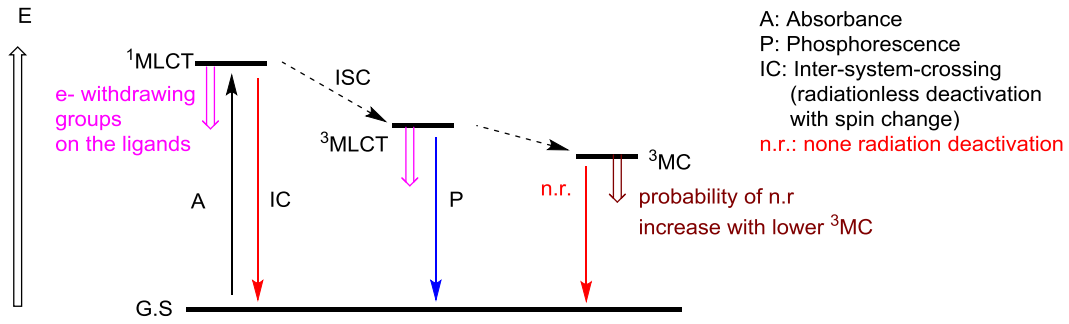

Figure 3.22: Jablonski diagram for the photophysical properties of **RuGdL1**.

An attempt to decrease the HOMO-LUMO energy gap was made by introducing an EWG to the pyridine ring. It can be argued that the EWG group could decrease the ^{3}MLCT excited state energy in order to obtain efficient emission in the low energy region, or at least produce dequenched emission.[182] Unfortunately, the same scenario was seen with **RuYL3**, as shown in Fig. 3.23.

Again Ru(II) exhibits a weaker luminescence intensity from ^{3}LC at 336 nm, indicating the enormous gap between the HOMO-LUMO levels with efficient energy transfer to the ^{3}MC level. The electron withdrawing group (CF_3) substitution of the pyridine unit at position 5 leads to the stabilization the π*-orbital (LUMO) levels, resulting in more rapprochement between the ^{3}MLCT and ^{3}MC levels. Albeit that no emission was seen with Ru(II) complexes, **RuGdL1** can nevertheless work as a multinuclear CA with efficient relaxivity and high kinetic stability.[176]

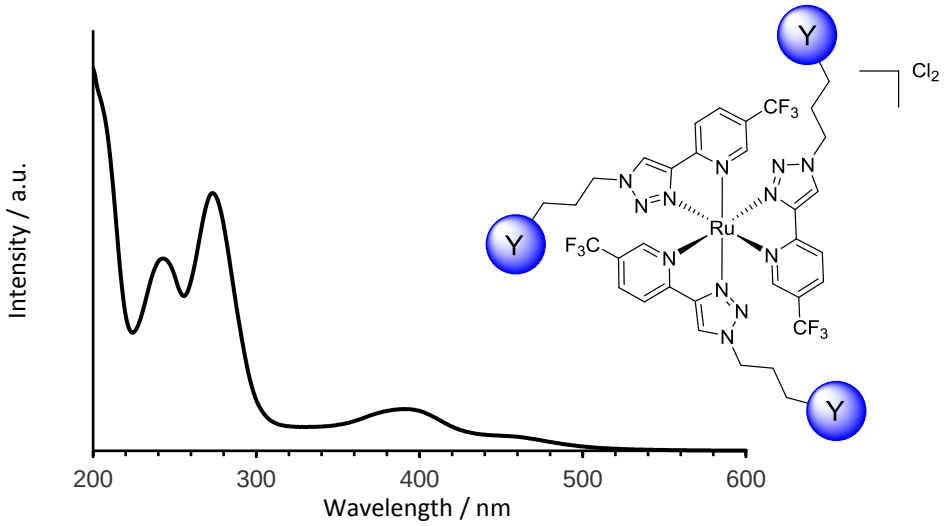

Figure 3.23: **RuYL3** absorption and emission (blue) at λ_{ex} = 280 nm spectra in (50 mM HEPES, 273 K).

The geometry of **RuYL3** was investigated by recording its ^{1}H NMR spectrum. This diamagnetic complex can be used to explore the structure of these complexes in solution. Yttrium has been chosen due to the similarity in its oxidation state, radial size and near identical chemical and structural properties to Gd(III).[183]

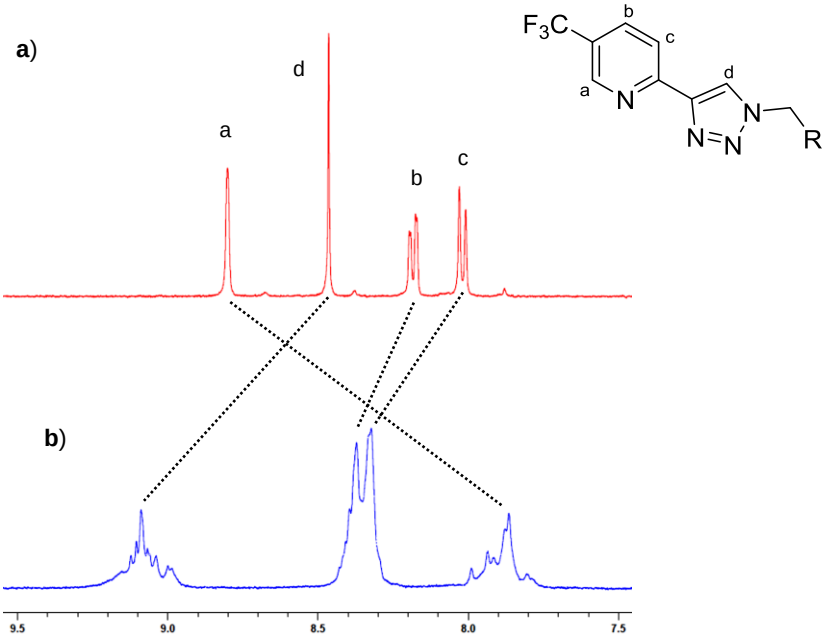

Figure 3.24: Partial ^{1}H-NMR spectrum (D_2O, 298 K, 400 MHz) stacked plot of the (a) **YL3** parent ligand (b) **RuYL3** (indicates that the " as-synthesised" material is mixture of mer- and fac-[**RuYL3**]$^{2+}$.

The ^{1}H NMR spectrum for **RuYL3** suggests there is a mixture of the *mer*- and *fac*-$[Ru(YL_3)_3]^{2+}$ in the solution as seen in Fig. 3.24. It has been reported that these

complexes usually display four triazole resonances (three corresponding to the *mer*-$[Ru(YL_3)_3]^{2+}$ diastereomers and the additional peak from the higher-symmetry *fac*-[**RuYL3**]$^{2+}$ diastereomers, as shown in Fig. 3.25.[177] The triazole proton H_d is shifted to the high frequency region, in contrast to H_a which is shifted to lower frequency after complexation with Ru(II).

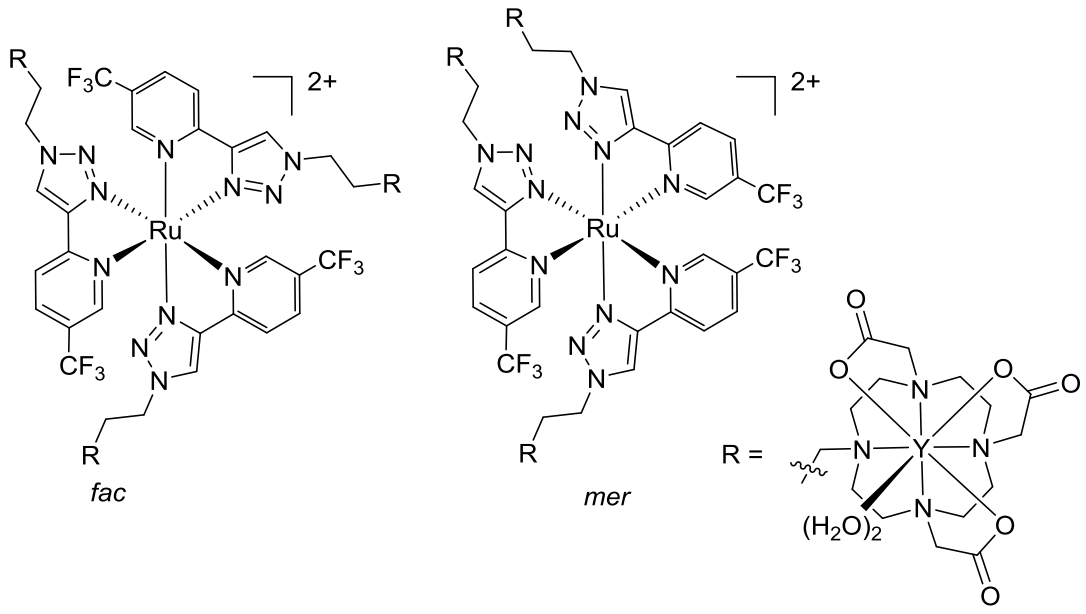

Figure 3.25: The geometric isomers at the core of **RuYL3** complex.

3.5 Lifetime and Quantum Yield of Emission

Another important criterion that requires discussion is the quantum yield and lifetime of emission which demonstrates the efficiency of the compound to emit any absorbed photons through fluorescence.

Highly emissive compounds show fluorescence quantum yields ≈1, meaning the number of the absorbed photons is equal to the number emitted. The quantum yield, Φ, can also be described by the relative radiative k_r and non-radiative k_{nr} rates that arise from the energy transfer, internal conversion, electron transfer and excimer formation relaxation pathways that relax the excited state.[184]

$$\Phi = \frac{K_r}{K_r + \sum K_{nr}} \tag{26}$$

It has been found that the complexes with NIR emission exhibit low quantum yields due to the increase in the interaction between the high excited states and the

ground state. In addition, the singlet oxygen formed can decrease the triplet state's energy by enhancing the non-radiative decay, eventually low quantum yield.[156]

The luminescent lifetime (τ) is the average time a fluorophore remains in the excited state before emitting a photon, which can be measured by monitoring the decay time of the fluorescence signal. The process is called time-correlated single photon counting (TCSPC). For this time-resolved measurement a pulsed light source is harnessed for excitation and is adjusted so that less than one photon is detected per pulse and the time between the pulse and the photon detection is measured. This provides a curve representing the decay of the fluorescence signal which can be fitted with an exponential decay rate using the equation:

$$I_t = I_o e^{\frac{-t}{\tau}} \tag{27}$$

Where I_t is the intensity at time = t, I_0 is the intensity at time t = 0 and τ is the lifetime. The lifetime decay for emissive dual-mode agents is shown in Fig. 3.26.

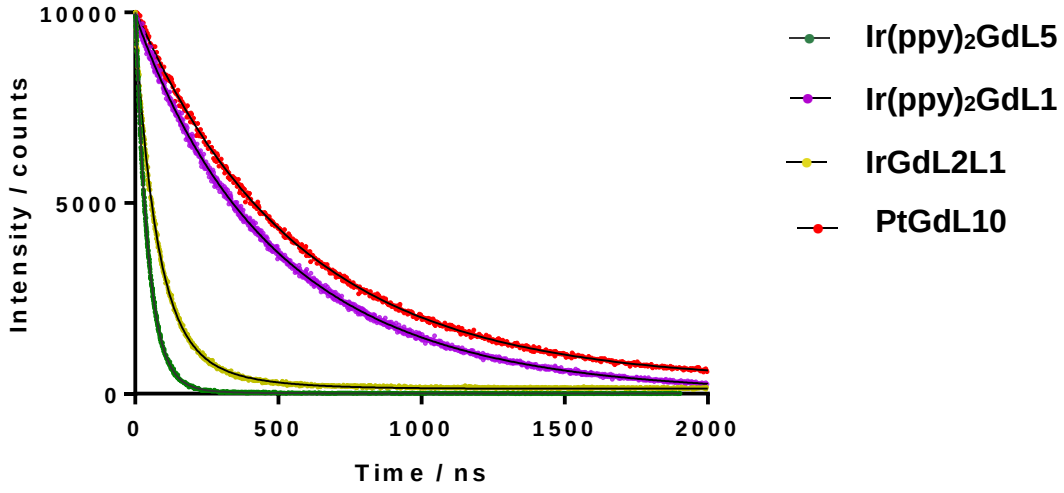

Figure 3.26: TCSPC luminescence exponential decay plot. c = 1 x 10^{-4} M, 0.1 M HEPES pH 7.4, λ_{ex} = 372 nm, λ_{em} = 540 nm, two exponential decay: **PtGdL10** R^2 = 0.9985; **Ir(ppy)$_2$GdL1**, R^2 = 0.9997; **Ir(ppy)$_2$GdL5** R^2 = 0.9986, **IrGdL2L1** R^2 = 0.9992.

The integrated emission and absorbance of these heteronuclear complexes were plotted against one another and the gradients used to calculate the quantum yields. The lifetime and the quantum yield were measured, and are summarised in Table 3.3.

	λ_{em}(nm)	Grad	τ (ns)	Φ
[Ru(bpy)$_3$]Cl$_2$		7.0629 ± 0.14 x 10^8	-	0.028
PtGdL10	482	2.6132 ± 0.17 x 10^8	907	0.075
IrGdL2L1	520	4.2179 ± 0.02 x 10^8	216	0.016
Ir(ppy)$_2$GdL1	500	3.8050 ± 0.16 x 10^9	556	0.150
Ir(ppy)$_2$GdL5	560	4.0281 ± 0.04 x 10^8	126	0.016
IrGdL6L3	500	1.0139 ± 0.04 x 10^9	614	0.040

Table 3.3: Quantum yields determined by the gradient comparison method using the gradients obtained in H_2O, lifetimes determnied via TCSPC.

It is clear from Table 3.3 that iridium complexes with ppy and pyta display typical excited state lifetimes in the microsecond range, with a high quantum yield in water. This is related to the less O_2 overlapping, less nonradiative decay and greater π→π* emission character *cf.* **IrGdL2L1** that shows characteristic ^{3}MLCT emission, similarly, [Ir(ppy)$_2$ptya-BCD]Cl shows τ = 690 ns and Φ = 0.14 in water.[185] However, **Ir(ppy)$_2$GdL5** which contains an inverse triazole ancillary ligand exhibits lower τ and Φ than regular **Ir(ppy)$_2$GdL1**, this is related to the increase in nonradiative decay pathways (most likely promoted by the increased flexibility of the **L5** ligand relative to their regular triazole ligands).[186] Correspondingly, iridium(III) inverse conjugate [Ir(ppy)$_2$L^{2a}]BF$_4$ has a lifetime of 0.20 μs and Φ = 0.02 in MeCN. **IrGdL6L3** gave long lifetime 0.61 μs, this is related to the CF_3 group that enhances oxidation/reduction between HOMO to LUMO which means efficient ISC to T_1.[166] Nevertheless, it exhibits low quantum yield 0.04 due to increase the radiationless deactivation pathway as energy gap low decrease between HOMO-LUMO. **PtGdL10** showed a lower lifetime (0.9 μs) in aerated water (Fig. 3.27), compared with Pt(N^C^N)Cl (7.2 μs) in CH_2Cl_2. This is possibly due to water polarity, as it has been found that Pt(II) emission is increasingly suppressed with increasing solvent polarity.[187] Aqueous media may as well lead to enhanced aggregation unlike chlorinated solvents; furthermore, polar solvents lead to reordering the T_1 excited states, thus less efficient ISC.[188]

3.6 Relaxivity

The relaxivity of these complexes has been measured at 400 MHz (9.4 T) at 298 K, which is given in Table 3.4. As relaxivity were measured at higher magnetic field

rather than 20 or 60 MHz, τ_R effect will not be significant. These complexes show typical relaxivities *cf.* similar complexes with multinuclear Gd(III) carrying two inner sphere water molecules.[189] Which can be rationalised to the payload and the rotational correlation. However, the slight lower r_1 could only be described by separating global and local motions. This is maybe because the $(CH_2)_3$ linker brings a certain flexibility to the molecules.[190] These relaxivities values confirm q number and Eu(III) luminescence data, for example **PtGdL10** displays q = 1 with r_1 4.0 mM^{-1} s^{-1} compatible with complexes that have same hydration number and similar molecular weight (3.6 - 4.8 mM^{-1} s^{-1}).

Complex	*q*	*Gd*	r_1 mM^{-1} s^{-1} per Gd (400MHz)
GdL1	2	1	8.0
GdL2	2	1	7.3
GdL3	2	1	7.7
Ir(ppy)$_2$GdL1	2	1	7.5
Ir(ppy)$_2$GdL5	2	1	7.1
IrGdL6L3	2	3	7.9
IrGdL6L1	2	3	7.8
PtGdL10	1	1	4.0
RuGdL1	2	3	8.2

Table 3.4: represent the relaxivity per Gd of selected Gd-complexes at 400 MHz, 9.4 T (298 K).

3.7 *In vitro* Imaging Studies for **Ir(ppy)$_2$GdL1**

Understanding brain function is key to developing our knowledge of its behaviour and the consequences of disturbances in its function. Developing bioimaging tools, such as **Ir(ppy)$_2$GdL1** with two-photon excitation ability at 850 nm, could play a critical role in exploring nervous system dysfunctions.[191] Traditional methods of studying brain function, in particular neurochemistry, tend to be invasive and focus only on one specific aspect, for example the functioning of a particular neurotransmitter.[192] Possible applications of "multimodal" imaging are monitoring the blood- brain-barrier's permeability (BBBP) and identifying changes in brain neurochemistry when brain physiology is perturbed. For instance, in the brain after a stroke, encephalitis, and tumours, the BBBP increases, leading to loss of BBBP selectivity via diffusion.[193] This gives the opportunity for non-invasive imaging techniques (such as MRI) to be used, taking advantage of the MRI contrast

agent. Then, confocal microscopy can be used, for example, to monitor the function of a particular synaptic transmission and investigate the co-localisation of this CA in brain slices. One of the most important questions that can be answered using MRI/OI contrast agents in brain MR imaging is the action of these dyes related to the accumulation, or the high relaxivity of these agents.[194] The presence of different functional groups in the **Ir(ppy)$_2$GdL1** structure, such as triazole, amines and aryl moieties, will confer the selectivity of this dual mode to work as a live neuron imaging biomarker.[191] The reliability of this probe that can be excited by multiphoton absorption, was tested with 300 μm live rat brain slices using a multiphoton microscope to obtain ultra-fine optical sections. Images were acquired by Dr Vincenzo Marra (Department of Neuroscience, Psychology and Behaviour) using a Zeiss LSM710 microscope with multiphoton excitation at λ_{ex} = 850 nm and a 500-550 nm emission filter using a 20x/NA1.0 objective. The low magnification image of layer 2/3 cortical slice as in Fig. 3.27, shows that cell bodies appear dark while neurites are bright green; this might relate to the lipophilicity of the complex. The lipophilicity leads to rapid interaction of this dye with neurite cell membranes.[195]

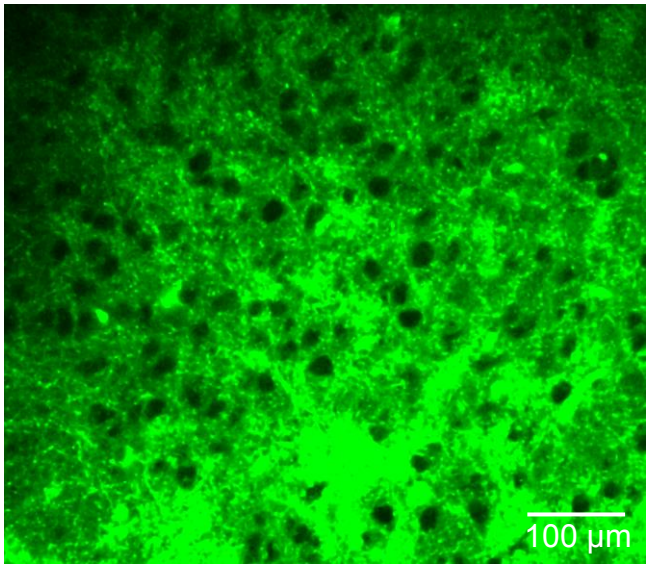

Figure 3.27: Low magnification image CM of rat cortical slice, 300 μm thick, cell bodies appear dark while neurites are in bright green incubated for ~1 minute with 10 μM **IrppyGdL1**.

Importantly, dying cells will also appear brighter as their cellular membrane collapses. The imaging probe also showed a promising selectivity for the imaging of cell death, as seen in Fig. 3.28. At high magnification, the cell bodies of healthy cells appeared dark while a dying cell appears bright green. This is highly likely related

to the triazole ring and due to a subtle balance of hydrophobicity and lipophobicity.[196] As well as, loss of a symmetric distribution of phosphatidyl-ethanolamine and phosphatidylserine during cell death leads to the transformation of the cell membrane from essentially charge-neutral to anionic.[197] Because of its positive charge, **Ir(ppy)$_2$GdL1** will exhibit electrostatic interactions with these cells in contrast with a neutral cell, therefore this probe could be used as an extracellular apoptosis biomarker.[198]

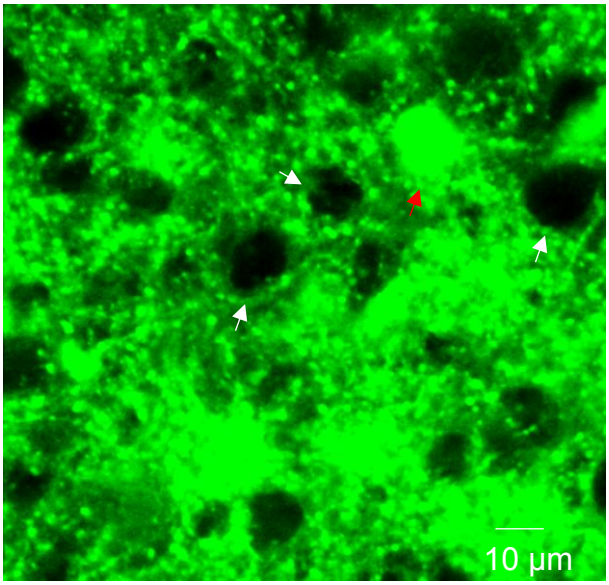

Figure 3.28: High magnification, cell bodies of healthy cells appear dark (white arrow) while a dying cell can be observed in bright green (red arrow).

Ir(ppy)$_2$GdL1 cannot cross the cell membrane and it accumulates in the extracellular space. For single optical sections this results in the dark appearance of cell bodies and large dendrites (Fig. 3.28, 3.29) and a brighter appearance of smaller compartments such as axonal varicosities (boutons) or spines. Taking the advantage of the high magnification, the confocal microscopy shows the organelle.

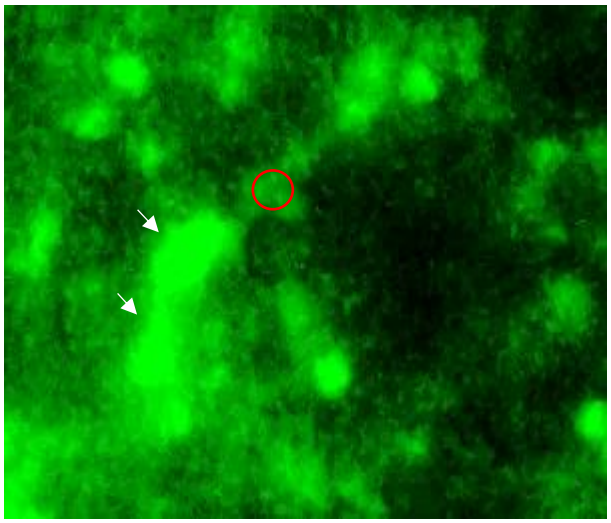

Figure 3.29: High magnification image of neurites, a spine on a dendrite branchlet in the red circle while white arrowheads indicate two putative presynaptic terminals on the same axon.

3.8 Summary and Conclusions:

A number of dual-mode optical/MR imaging probes of Ir(III) and Pt(II) as a luminescent core complex have been synthesised with single or multiple Ln-DO3A pendant units. The hydration number was measured by monitoring the excited life time for Eu(III) analogues in H_2O and D_2O solvents. The photophysical properties of the Gd(III)-containing agents were investigated in H_2O, and it has been found that **PtGdL10** complexes have the longer lifetimes (0.9 μs) with Φ = 0.07 and the excitation maxima near 405 nm, recommending its use in single photon and the potential for two-photon absorption to obtain emission at 482 nm. It was also shown that **PtGdL10** exhibits excimer emission in red region with increasing the concentration. In terms of Ru(III) emission, it has been demonstrated that ligation with pyta does not result in any emission, due to the higher ^{3}MLCT energy with a high possibility of the ^{3}ML transition that prefers a thermal relaxation pathway; however, it demonstrates high relaxivity due to high molecular weight. The mono-gadolinium **Ir(ppy)$_2$GdL1** showed r_1 = 7.5 s^{-1} mM^{-1} and quantum yield for emission Φ = 0.15 at 500 nm compared to **IrGdL2L1**, where Φ = 0.01 at 520 nm with r_1 = 23.7 s^{-1} mM^{-1}. These differences are related to cyclometallated phta that increased the HOMO-LUMO energy gap in **IrGdL2L1**, as well as, the latter exhibits higher relaxivity due to increase the Gd(III) payload and τ_R. **Ir(ppy)$_2$GdL1** can be excited at 405 and 850 nm as shown in *in vitro* neuron images. The most interesting results were seen with **IrGdL6L3**, which exhibits a bathochromic shift in its emission spectrum with 58 ns longer lifetime compared to **IrGdL6L1**. While **Ir(ppy)$_2$EuL11** exhibits rad shift in ^{1}LLCT absorption without effecting on MLCT excitation/emission, due to this transition is mainly located over the ancillary rather C^N ligand.

The *in vitro* optical imaging for rat brain slices using the **Ir(ppy)$_2$GdL1** agent showed that this probe is promising in use for molecular imaging due to its high stability, and intense green emission. The monopositive charge leads to increase the interaction between the dye and cell membrane.

It seem to be iridium complex with CF_3 substitution on the pyta is the best dual-mode MR/OI probe that can be recommended to use for further investigations, due to its superior water solubility, photophysical properties and reactions yield.

Chapter 4

Carbonate Responsive Luminescent Probes

4.1 Introduction

The carbonate ion is essential to life, as it plays a vital rule in pH regulation, numerous mammals' cellular processes, and kidney function.[63] On the other hand, carbonates / bicarbonates have a strong caustic effect on the gastro-intestinal tract which may cause severe abdominal pain, vomiting, diarrhoea, collapse and even death.[199] CO_3^{2-}efflux depends on the buffering capacity of the cell and on membrane-based ion exchangers, the Na^+/H^+ antiport, and Na^+-dependent HCO_3^-/CO_2 exchange mechanism.[200] It can proceed through different transporting proteins identified as bicarbonate transporters (CA2 and CA12), as shown in Fig 4.1, which have vital physiological roles; it also relies on the CO_2 concentration inside the cell resulting from mitochondrial respiratory oxidation processes and, indeed, the presence of cancer. The physiological cytosolic pH depends on the HCO_3^-/CO_2 primary buffer, so the balance between these two species most be controlled and monitored, especially when influenced by the pK_a of the media.[201] Mis-expression of carbonic anhydrase (CA) is associated with a variety of tumour types and CAII deficiency syndrome in humans which can give rise to renal tubular acidosis, osteoporosis and mental retardation.[202]

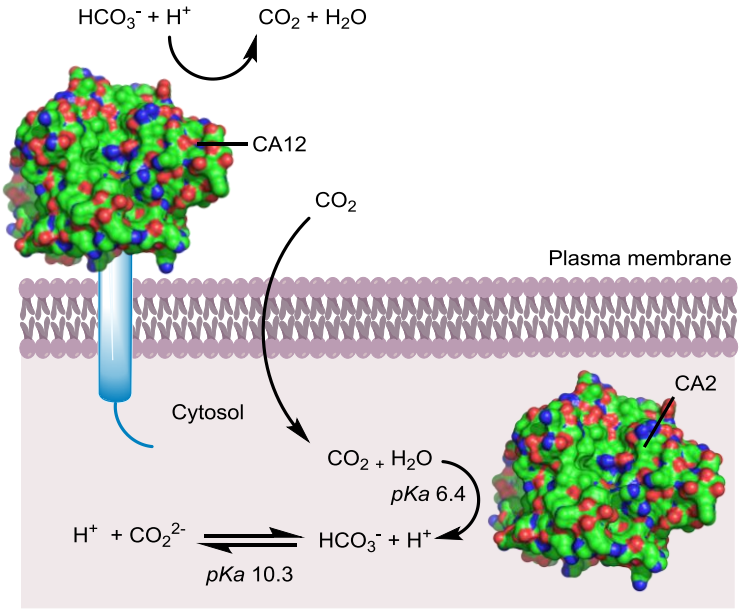

Figure 4.1: Eukaryotic cells constantly produce CO_2.[203]

4.2 Measuring [HCO_3^-]

The normal serum concentration range for bicarbonate is 22-30 mM, therefore a highly sensitive and selective bioprobe is required for its quantitative assessment. Carbonate can be qualitatively detected using a number of trivial inorganic reactions, such as: elevation of CO_2 levels or its participation as an insoluble carbonate salt. The latter is based on addition of water-soluble Ca^{2+} salts, and heating to produce $CaCO_3$ as a white precipitate with subsequent application of acid-base titration.

Nowadays, the majority of commercial or medical equipment used for the detection of carbonate/bicarbonate concentrations in the blood are based on ion-selective electrodes. The principle of quantification can be divided into two categories: analyte-specific potentiometric membranes, and enzyme electrodes.[204] The results obtained from these devices are not accurate; basically, there is no simple probe that exists which is able to measure direct changes in HCO_3^- activity, especially in a biological environment or in living organisms.[205] Moreover, they possess several drawbacks, such as pH dependence, and a lack of sensitivity and selectivity issues originating from interference due to the various other anions typically present (*e.g.* salicylate, lactate, chloride).[206] In summary, highly selective and sensitive bio sensors are needed to quantify carbonate ions at the extracellular level on the μM scale-without other ions interfering.

4.3 Carbonate Responsive Luminescent Sensors

The use of lanthanides in optical bioanalysis has gained a great deal of attention due to long excited-state lifetimes of up to a millisecond, high photo bleaching resistance and sharp emission spectra.[207] Eu(III)/Tb(III) with macrocyclic heptadentate DO3A chelators exhibit high carbonate selectivity and affinity compared with other polyaminocarboxylate ligands.[208] It is necessary for these biomarkers to be able to work in different pH environments, with high bio-ion selectivity and where the skeleton structure of these complexes possess high structural rigidity to prevent any metal centre liberation.[63, 209]

In general the mechanism of using Eu(III)/Tb(III) complexes as carbonate detectors is based on the displacement of quenching coordinated water(s) from the

metal centre by CO_3^{2-}. The binding affinity of biological bidentate ions toward DO3A follows the order CO_3^{2-} > oxalate^{2-} > picolinate^{-}> phthalate^{2-} ≈ citrate^{3-}.[202] Carbonate binding affinity depends on the total charge of the complex and the steric demand at the metal centre, as seen in Table 4.1 which relates to the complexes in Fig. 4.2.

Complex	Bicarbonate log *K*a
[64]$^{3+}$	2.81
[65]$^{3+}$	3.07
[66]$^{+}$	2.55
[67]$^{+}$	2.23
[68]$^{+}$	2.14
[69]$^{+}$	2.80
[70]$^{-}$	2.11
[71]$^{-}$	1.27
[72]$^{-}$	1.23

Table 4.1: Affinity constants for **64-72** in salt solution contains: 0.1 M NaCl, 4 mM KCl, 0.1 M HEPES and 0.9 mM NaH_2PO_4.[202]

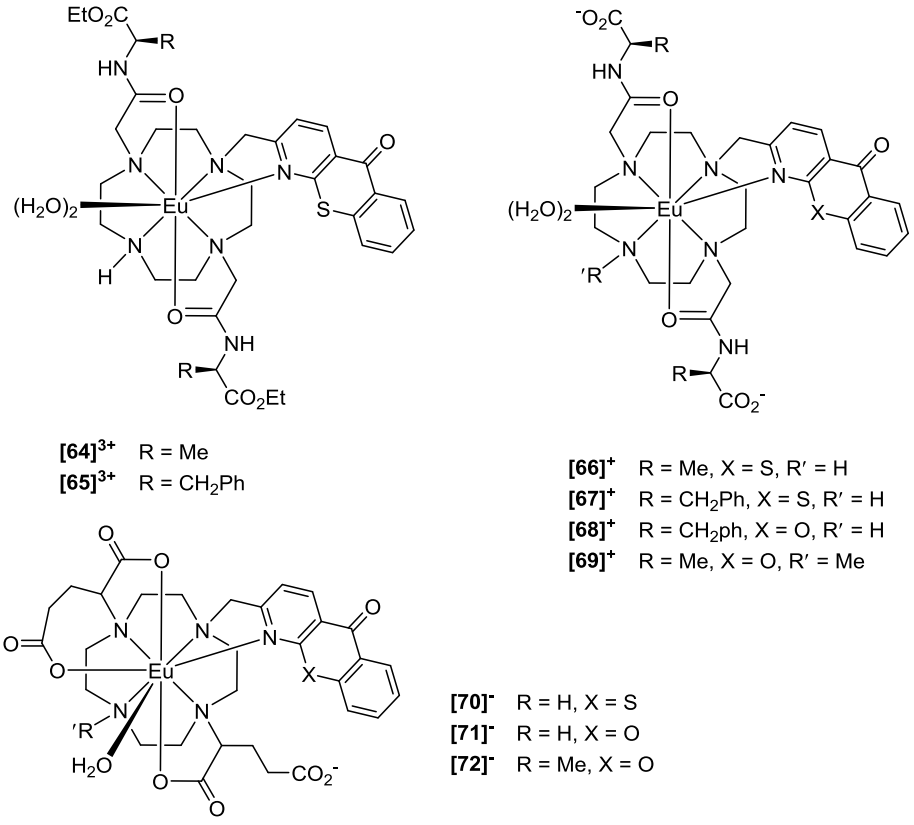

Figure 4.2: Complexes with different steric hindrance and total charges.

Additionally, Lowe and Giardiello, investigated the binding of carbonate with neutral and anionic DO3A complexes. It was found the binding percentage increased eight-fold with the neutral complex **73** compared to anionic **[74]**$^{3-}$ (Fig. 4.3).[210] This was due to the increase the electrostatic repulsion effects of the negatively charged complex with regarded to coordination of bicarbonate anion. Thus, it can be concluded the affinity of CO_3^{2-} toward Ln(III)-DO3A complexes follows the order: cationic > neutral > anionic.

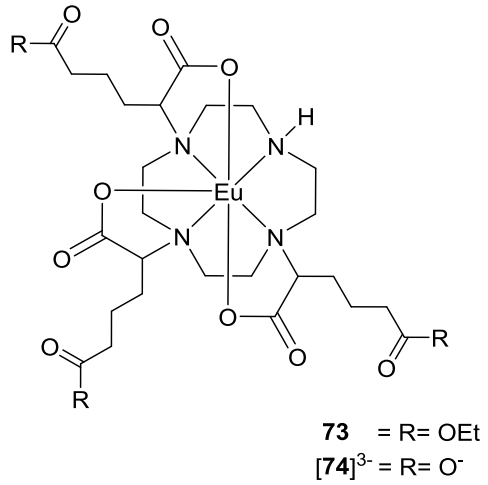

Figure 4.3: Lowe's **[74]**$^{3-}$ and **73** complexes.

In the same scenario, Ln(III) itself shows a different affinity to carbonate moieties because of its ionic radius and charge density, leading to the ordering: Tb^{3+} > Dy^{3+} > Eu^{3+} ≈ Sm^{3+}.[211] Exchanging the ligating water has two effects on Ln(III) emission(Fig. 4.4): it increases emission intensity and lifetime, which is beneficial to obtaining high resolution spectra, and can be used for time-gating measurements.[208]

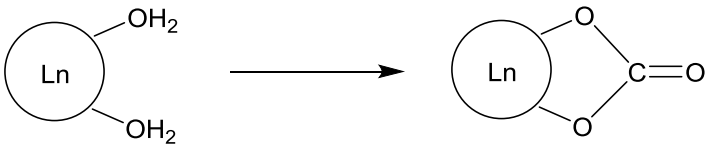

Figure 4.4: mechanisem of action carbonate lanthanide sensors.

Another sensitive strategy that can be followed to synthesise carbonate sensors that show a ratiometric responsive, is to replace the coordinated antenna by these analytes. This leads to a lack of emission sensitising, resulting in intensity quenching for Ln(III) emission, as shown in Fig. 4.5.[212] Comparing isoquinoline-3-carboxylic acid (IQCA) with picolinic acid (PA) sensitising, it was found the Eu(III)

emission with IQCA exhibits ~230-times higher intensity than PA, most likely as consequence of formation of a more thermodynamically stable complex where the metal centre is efficiently shielded from quenching. Even though this strategy demonstrates selectivity and sensitivity toward CO_3^{2-}, it also shows some of the obstacles regarding to the preparation of the probe. In addition, it was found that 5 mM is the maximum concentration of picolinic acid that can be added to the solution otherwise the Eu(III) emission will be quenched.

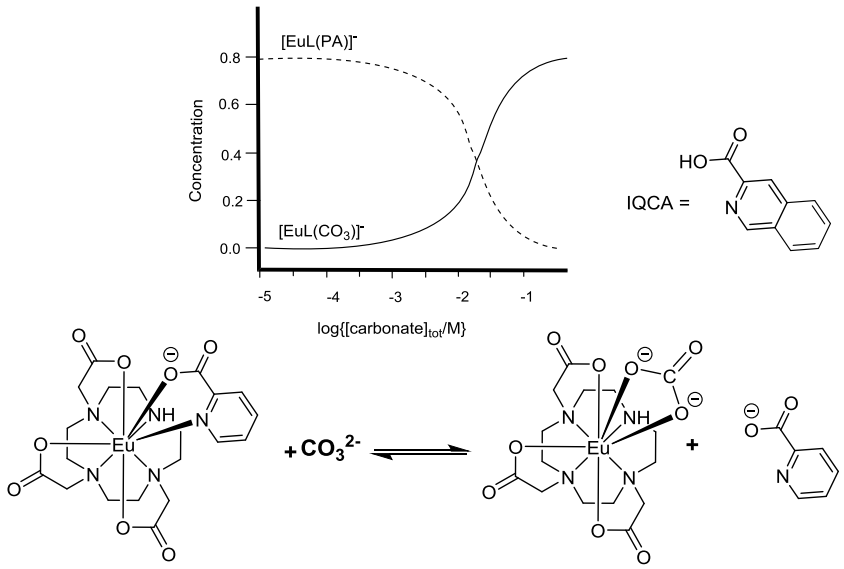

Figure 4.5: The mechanism action of Pc(DO3A) as a carbonate sensor.

Liu *et al.*, designed a luminescent lanthanide metal-organic framework LnMOF based on a benzophenone-3,3′,4,4′-tetracarboxylate thin film **(75)**; it was synthesised directly on an electrode surface via an electrochemical hydrolsis mechanism in a nitrate solution.[213] It shows a high selectivity toward carbonate ions in aqueous solution compared with other ions such as SO_4^{2-}, PO_4^{3-}, HPO_4^{2-}, ClO_4^-, BrO_3^-, and IO_3^-. These Eu-**75** based thin films show strong $^5D_0 \rightarrow {}^7F_J$ emission in aqueous solution at λ_{ex} = 317 nm with high HCO_3^- binding to the protonated carboxyl groups, affecting the rate of energy transfer to the europium ions, therefore resulting in higher luminescence intensities. Two drawbacks of this sensor have been found: long detection times that can extend to 1 hour, and higher ion concentrations are required.

Using two binuclear lanthanides can also be used to sense biologically relevant anions. Andolina and Morrow synthesised **76** and **77** (Fig. 4.5),[207] to test the binding

affinity and study Ln(III)–Ln(III) luminescence resonance energy transfer (LRET). It has been found that carbonate ions bind strongly to both complexes and the elevation in the binding affinity of Eu-**76** follows the series DEP < MP < PO_4^{3-} due to increasing negative charge (MP = Methylphosphate, DEP = Diethylphosphate). The two lanthanides sensitisation is effectively controlled by the distance between them via the *m*-xylyl, compared to the *o*-xylyl, linker. Although the $^7F_0 \rightarrow {}^5D_0$ transition would seem to allow for a promising means of ratiometric analysis for carbonate concentrations with two complexes, it has been found that the replacement of H_2O molecules is variable due to steric hindrance (bulky group) on the amido arms.

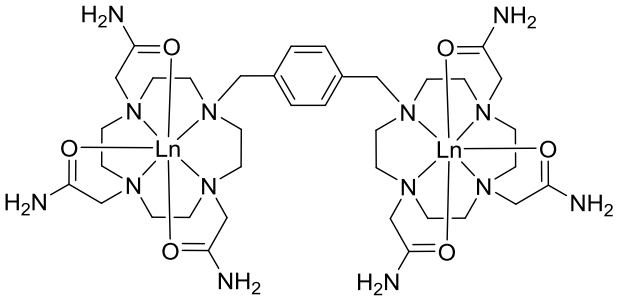

76 = Eu-Eu, Tb-Tb, Eu-Nd, Eu-Tb

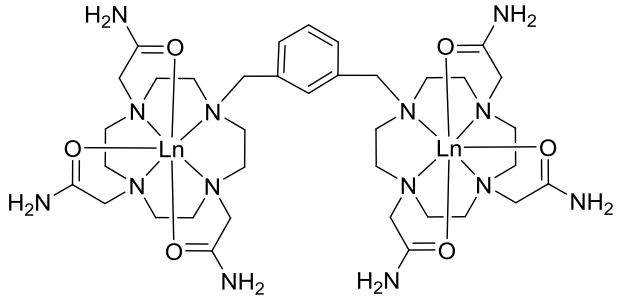

77 = Eu-Eu, Tb-Tb, Eu-Nd, Eu-Tb

Figure 4.6: dinuclear lanthanides probes.

A metal-based cellular probe must fulfil several requirements: (1) high selectivity for the target substrate; (2) reversible binding of the substrate for real-time measurements; (3) water solubility; (4) effectiveness in biologically relevant media; (5) high thermodynamic and kinetic stability of the metal-based sensor; (6) low biological toxicity; and (7) high cell permeability. Furthermore, for ease and accuracy of measurement, "turn-on" sensors, whose signals increase upon binding of the substrate, are preferred to "turn-off" sensors.[208] In this chapter, the synthesis Eu(III) probes as carbonate sensors linked to Re(I) as a means of internal reference

is established. Owing to the fact that Re(I) luminescence is unchangeable compared to the elevation of Eu(III) emission in the presence of HCO_3^-, responsive luminescent probes can be synthesised incorporating these two metals. Additionally, they can be used as carbonate indicators in aqueous solution by changing the colour of the solution under UV-light for biomedical and industrial applications. Photophysical properties have been tuned by adjusting the HOMO-LUMO energy gap of Re(I) complexes by changing the nature of the pyridyltriazole moiety (LUMO).

4.4 Preparation of Bimetallic Complexes

As shown in Chapter 3, pyta (N^N') constitutes an excellent coordinating ligand with different TMs. The model bimetallic Re-Ln complexes in this chapter can be synthesised by the reaction of $Re(CO)_5OTf$ with Eu(III), Gd(III) or Y(III) complexes in bearing a pendent pyta. $Re(CO)_5OTf$ was prepared from $Re(CO)_5Cl$ following a literature produce,[214] by reacting $Re(CO)_5Cl$ with silver triflate in dry DCM. This is to avoid Ag(I) complexation with the macrocycle and avoid subjecting the Ln(III) complexes to the harsh conditions needed to remove the chloride.[215] The complexation with Ln-complexes is achieved in MeOH followed by exchange the OTf moiety with pyridine as seen in scheme 4.1 for synthesis Re-Eu complexes.

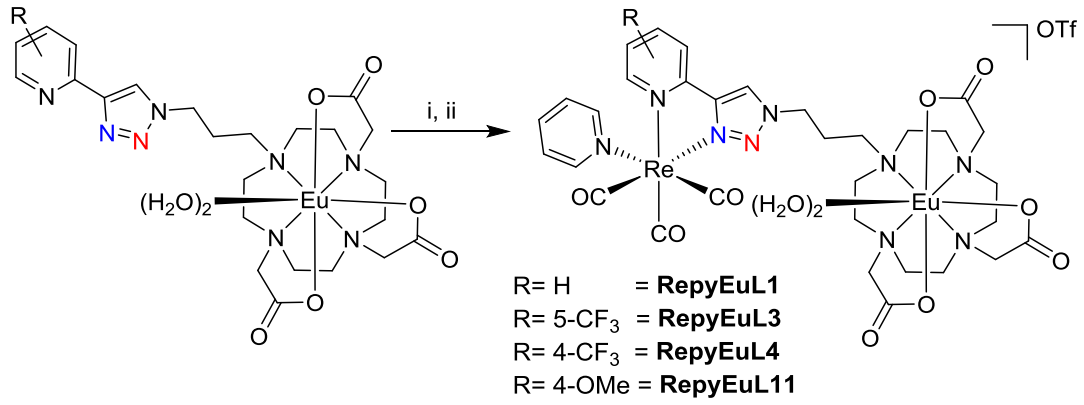

Scheme 4.1: **Reagents and conditions**: i) $Re(CO)_5OTf$, MeOH, reflux 80 °C; ii) pyridine, reflux 80 °C. Yield is 31-39% over two steps.

The coordination was monitored via ESI-MS, which shows the formation of the pre-complex after 18 h of reflux (Re-LnOTf). The final complex was obtained *in situ* by substitution of the OTf^- moiety with pyridine. The resulting complexes are then purified by RP-HPLC (method B). The mass spectrum of **RepyLnL1** is

presented in Fig. 4.7, whose synthesis saw a 31-39% final yield over the two steps and the purity was indicated by analytical HPLC (Appendix, Fig. 10.15).

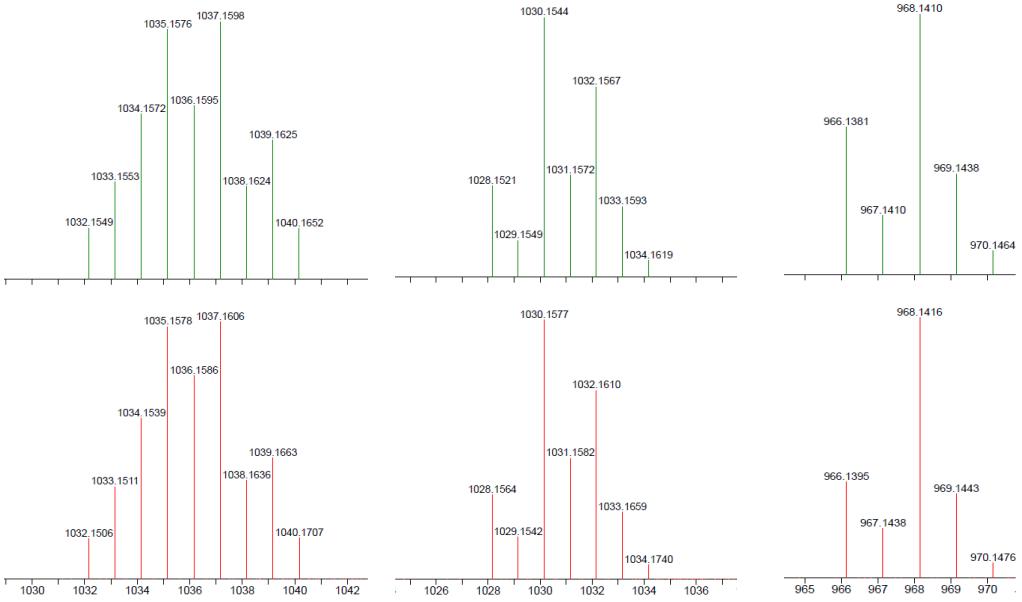

Figure 4.7: HRMS (ESI) of **RepyGdL1**, **RepyEuL1** and **RepyYL1** respectively, observed (bottom) simulation (top).

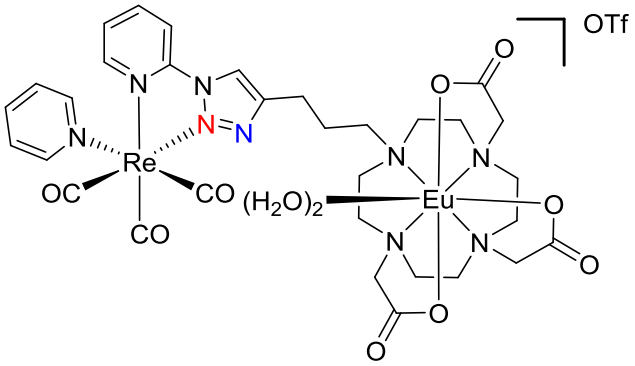

Figure 4.8: **RepyEuL5** complex.

Following the same procedure, **RepyEuL5**, as per Fig. 4.8, was synthesised from **EuL5** to give MS (ESI) showing Eu/Re isotopic patterns with m/z = 1029 $[M]^+$. Finally, a cyclometallated variant was synthesised **ReEuL2** (Fig. 4.9). This was prepared by heating **LnL2** with one equiv. of $Re(CO)_5Cl$ in methanol in a microwave reactor (MeOH, MW 90 °C, 1h) to give a 38% yield after purification and an MS (ESI) shows m/z = 952 $[M\text{-}CO+H]^+$, and which possessed the correct isotope pattern.

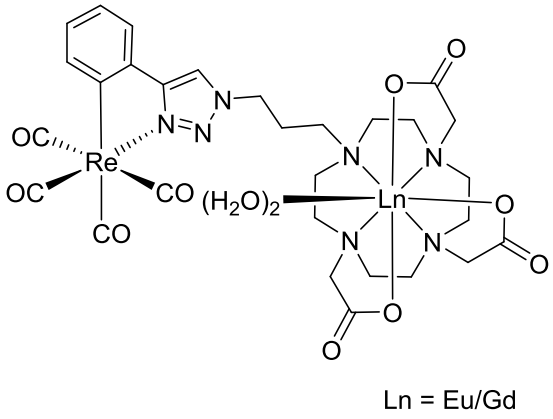

Figure 4.9: **ReLnL2** structure.

4.5 Luminescence Studies

Changing the intensity of Eu(III) emission in the presence of HCO_3^- allows ratiometric analyses to be undertaken. This is most appropriate in the analyses of europium emission spectra as the relative intensity of the magnetic-dipole-allowed $\Delta J = 1$ manifold is usually insensitive to any associated change in the coordination environment, while the intensities of the electric dipole-allowed $\Delta J = 2$ and $\Delta J = 4$ transitions change considerably, particularly if the 'hard' axial water molecule is displaced by a more polarisable charged donor.[216]

The HOMO in [Repy(CO)$_3$(N^N)] complexes predominantly localizes over the Re(I) and py atoms and originats from π and e$_2$g orbitals; by contrast, the LUMOs are essentially the π* orbital N^N ligands e.g. of the pyta and bpy.[217] Hence the electronic transition at the lowest energy region can clearly be assigned to the mixed metal–ligand-to-ligand charge transfer (MLLCT) in both complexes. Here, the fact that pyta shows a higher energy LUMO compared to bpy, explains the blue-shift of the MLLCT band of the former and the associated extended lifetime of the excited state.[218]

For better stability, photophysical properties and less toxicity of the Re(I) tricarbonyl complexes, chloride has been substituted with a pyridine moiety.[97] The halide ligand is potentially more readily exchanged than pyridine; furthermore, the former with rhenium exhibits low quantum yield, by up a factor of ten, and a short emission lifetime due to its higher non-radiative decay constant *cf.* replacement with pyridine.[218] **ReClEuL1** emission at 520 nm notoriously shows high intense Eu(III) spectra which dominates the Re(I) emission (Fig. 4.10). This maybe attributed to efficient energy transfer from the triplet excited state of Re(I) → $^5D_0$ of Eu(III)

leading to quenching of rhenium luminescence.[219, 220] This overlapping was examined using **ReClGdL1** complex at the same concentration when the energy transfer to Gd(III) is not possible, indeed this lead to retrieved Re(I) emission (Fig. 4.10). The low intensity of the Re(I) emission in these complexes is not reliable to use as a reference in carbonate responsive luminescent probe.

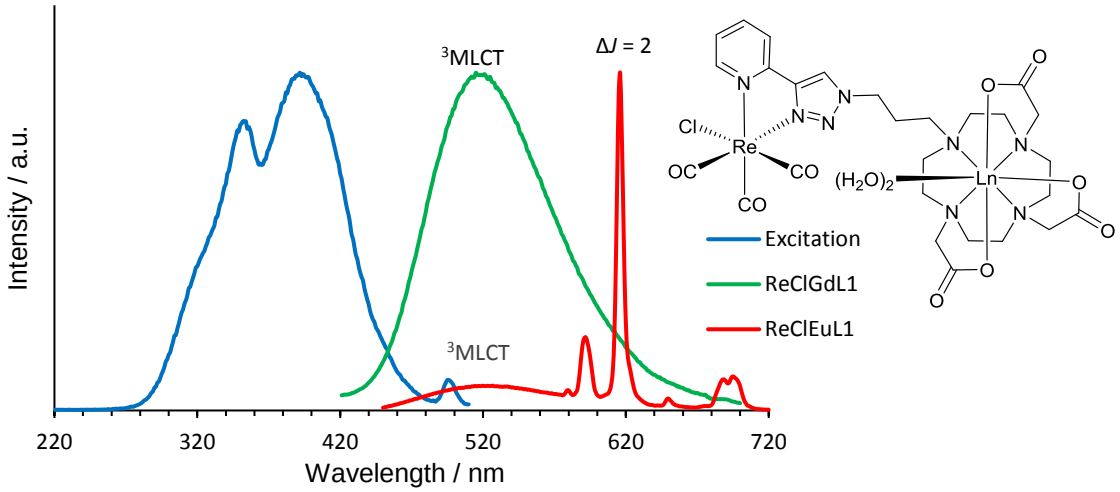

Figure 4.10:**ReClEuL1** and **ReClGdL1** excitation and emission spectra, λ_{ex} 420 nm, λ_{em} 520 nm in H_2O at 298 K.

To demonstrate Eu(III) emission sensitisation and the strong overlapping between Re(I) triplet state and excited states of Eu(III), **ReClEuL1** excitation spectra were obtained by monitoring various wavelengths such as 700 nm where Re does not emit *cf.* 520 and 616 nm.

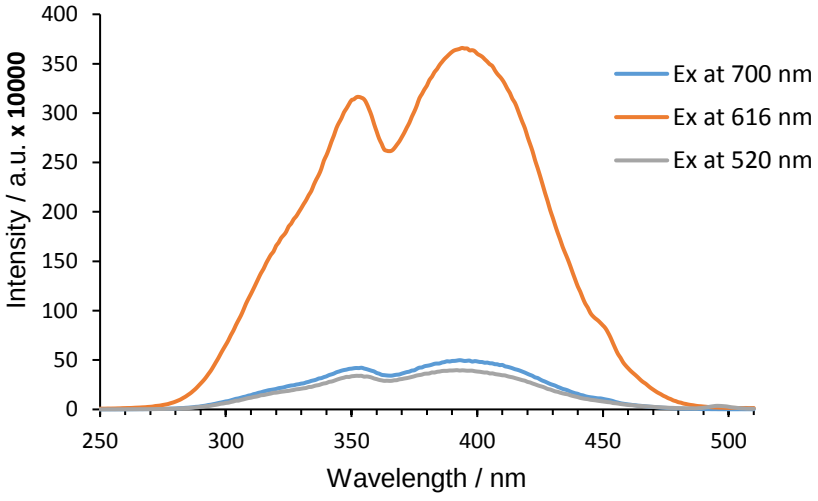

Figure 4.11: Extitation spectra for **ReClEuL1** monitring diffrent excitation wavelengths.

It is clear from Fig. 4.11 there is a strong association between T_1 of Re(I) and $^5D_0$ of Eu(III) especially at 616 nm, which proves the emission of europium is not from direct excitation, it originates from LUMO levels on π* of pyta.[220]

The **RepyEuL1** complex with pyridine in place of Cl gives the desired emission, which shows higher intensity ^{3}MLCT maxima compared to Eu(III) emission as seen in Fig. 4.12, by decreasing the energy transfer from the T_1 state of Re(I) to the Eu(III) excited state. This substation with py who leads to a shift in the excitation/emission spectra to higher energy *cf.* Cl ligand. The reason for this is the electron-withdrawing pyridine ligand (π-electron acceptor) decreasing the electron density on the Re(I) (stabilizes HOMO levels) that means great HOMO-LUMO gab, eventually blue shifted mission but higher τ and Φ.[100, 221] It is clear from Fig. 4.12 that the emission in the visible region is dominated by the Re(I) complex emission, with the Eu(III) emission seen as humps on the tail of the Re emission.

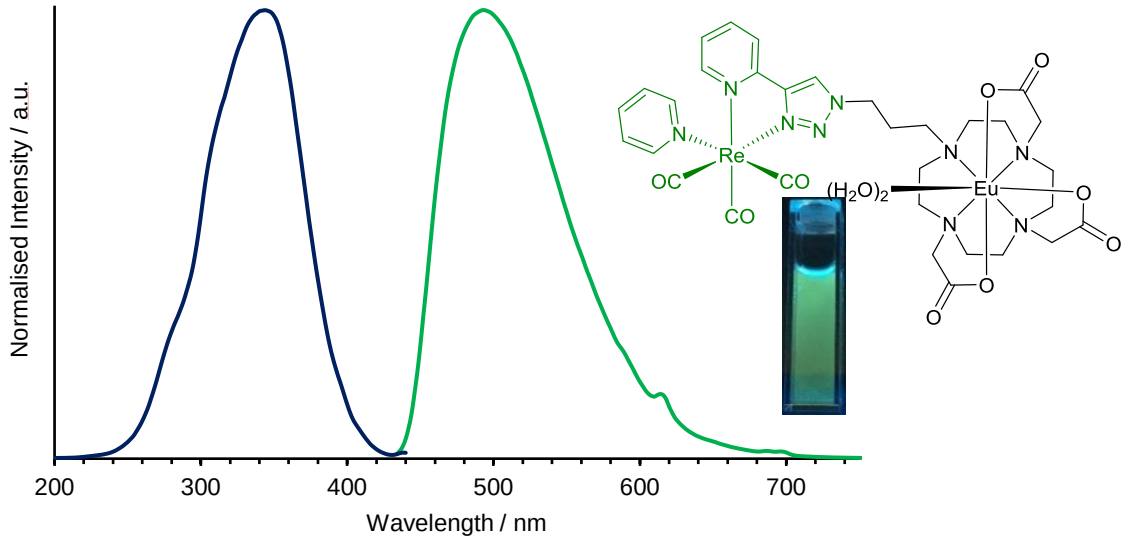

Figure 4.12: **RepyEuL1**, emission (—) and excitation (—) spectra λ_{ex} 355nm, λ_{em} 500 nm in H_2O at 298 K, 40mM HEPES. Inset: (0.1 mM) solution in cuvettes view under 365 nm illumination.

Fourier-transform infrared (FTIR) spectra of the **RepyEuL1** and **RepyEuL3** complexes show a typical profile for CO in the [Re(py)(CO)$_3$(N^N)] complex with the presence of intense bands around 2100–1900 cm^{-1} ascribed to the C–O stretching vibration characteristic of a facial coordination geometry (Appendix, Fig. 10.12, 10.13). These vibrations are in a higher frequency region than those with the axial chloride coordinated moiety. Additionally, bands in the 1800–700 cm^{-1} region were also observed and identified as ring vibrations of the coordinated pyta.[100]

4.6 Binuclear *d-f* Complex Binding to Carbonate

The sensitivity of the probe **RepyEuL1** to carbonate has been tested by addition of $NaHCO_3$ (0→ 33 mM) (Fig. 4.13). This shows an apparent elevation of electric dipole-allowed ΔJ = 2 peak, compared to the ^{3}MLCT emission from Re(I) to the ΔJ = 1 manifold, this is related to the hypersensitivity of the 616 nm band to CO_3^{2-}coordination and the displacement in inner-sphere waters.[222]

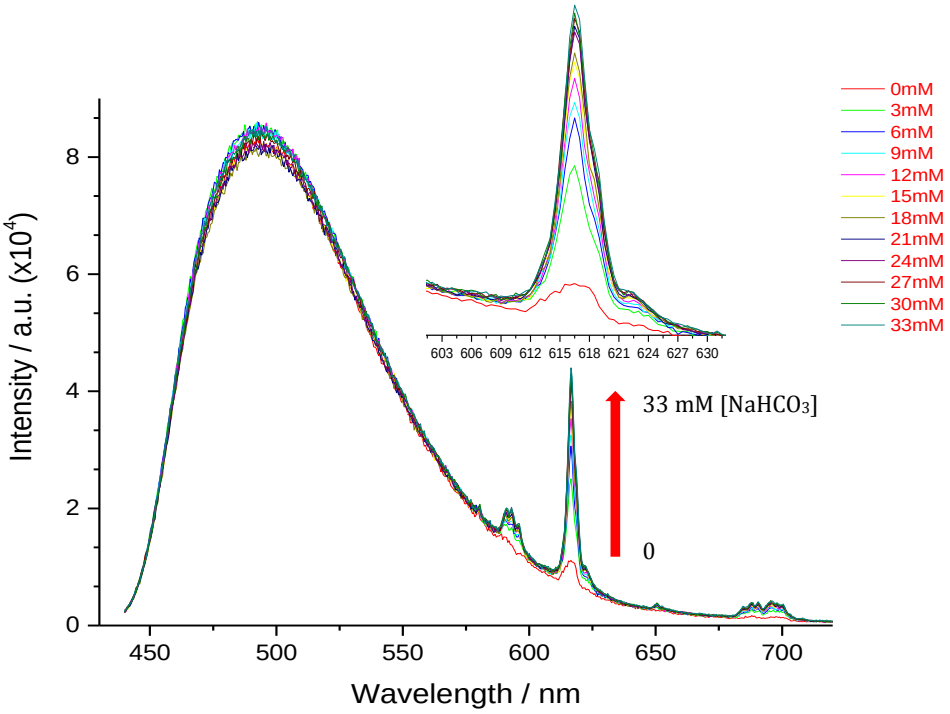

Figure 4.13: variation of emission intensity for **RepyEuL1** following addition of $NaHCO_3$ (0.1 mM **RepyEuL1**, 0.1 HEPES, pH 7.4, λ_{ex} = 355 nm).

The O–H oscillator from coordinated water can be excited from the ground vibrational levels, as a result of efficient Frank-Condon overlapping between v = 3 vibrational levels of H_2O with the $^5D_0$ excited state of Eu(III). This quenches the emission intensity of the Eu(III) in **RepyEuL1** complex.[223] When the two H_2O molecules exchange with carbonate, this leads to an increase in Eu(III) emission intensity by about 300% as seen in Fig. 4.13. As a result, the complex exhibits a colour change when illuminated at 365 nm from light green (Re(I) emission) to yellow emission after carbonate addition, due to the overlap between the green Re(I) and red Eu(III) emission (Fig. 4.14).

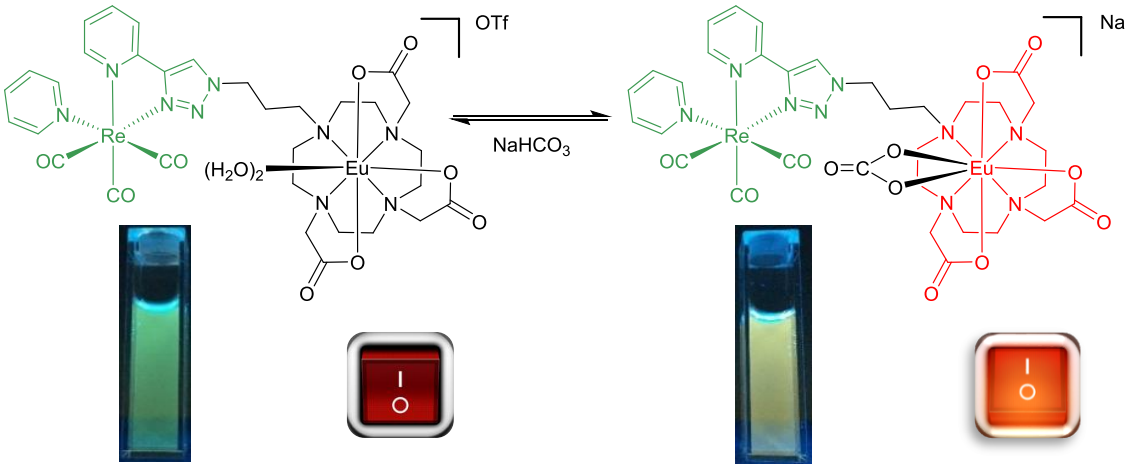

Figure 4.14: colour change for **ReEuL1** after 30 mM $NaHCO_3$ addition. Cuvettes illuminated with a 365 nm UV lamp. Inset: (0.1 mM) solution in cuvettes view under 365 nm illumination.

The hydration number of **RepyEuL1** was calculated and it found ~2, the luminescence decay measurements for Eu(III)(k_{H_2O} and k_{D_2O} were 2.31 ms^{-1} and 0.6 ms^{-1}, respectively). The hydration number Eu(III) and relaxivity Gd(III) were measured for **RepyEuL1/RepyGdL1** complexes before and after inner sphere water displacement by carbonate to investigate water exchange. The r_1 change for the Gd(III) complex is in agreement with the lifetime measurements on the Eu complexes. These indicate full substitution on addition of 30 mM $NaHCO_3$; the drop in relaxivity from 8.3 to 2.7 mM^{-1} s^{-1}, as reported in Table 4.2, due to a lack of exchange between inner-sphere and bulk water molecules.[224] The value 2.7 mM^{-1} s^{-1} is related to the action of the outer sphere of water.[32]

	RepyGdL1 r_1 mM^{-1} s^{-1} (400 MHz, 9.4 T at 298 K)	**RepyEuL1 q (± 0.2)**
No $NaHCO_3$	8.3	1.73
30 mM $NaHCO_3$	2.7	0.34

Table 4.2: q and r_1 for **RepyGdL1** and **RepyEuL1** in the absence and presence of $NaHCO_3$ (pH= 7.4).

4.7 Binding Strength and Stability

The apparent bicarbonate affinity constant for the ternary complex formation was measured by monitoring the variation of Eu(III) emission intensity (*e.g.,* at 617 nm) with the addition of $NaHCO_3$. A representative binding isotherm is given for the association with **RepyEuL1**, in which the curve shows the least squares-derived fit to the experimental data, based on a 1:1 stoichiometry (Fig. 4.15).[223]

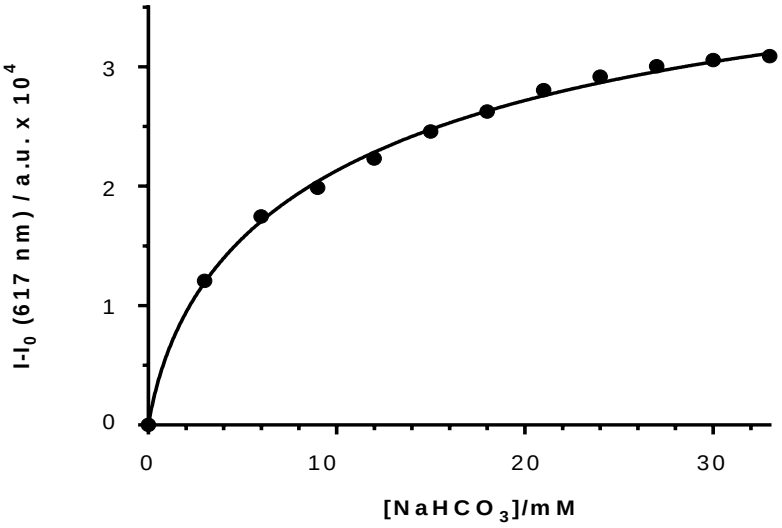

Figure 4.15: Variation of europium intensity (617 nm) of **RepyEuL1** complex as a function of added $NaHCO_3$ showing the fit (line) to the experimental data for 1:1 complexation (λ_{exc} 420 nm, 0.1 mM complex, HEPES 0.1 M, pH 7.4).

The binding constant, *K*, is given by $[LnLHCO_3^-]/[LnL^{3+}][HCO_3^-]$. The resultant binding isotherms were fitted to a 1:1 binding model by least-squares iterative analysis, log *K* for **RepyEuL1** has been found to be 2.33±0.03. Similar data, giving binding constants, within 10% were obtained by examining the intensity ratio at two emission wavelengths (e.g., 617/500 nm). Fig (4.16) proves monitoring I_{Eu}:I_{Re} emission ratio is able to be used to characterise the ternary complex formation. Comparing this value with Parker's results, it is similar to that of reported monopositive complexes based on DO3A (Table 4.3).

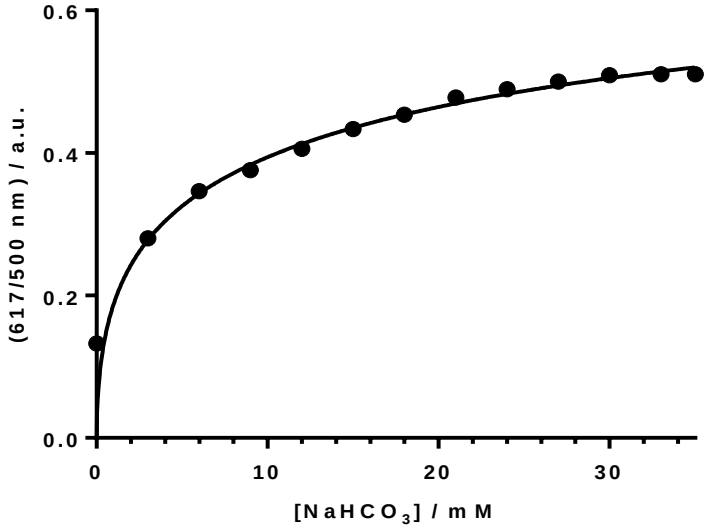

Figure 4.16:Variation of (617/500 nm) intensity of **RepyEuL1** complex as a function of added $NaHCO_3$ showing the fit (line) to the experimental data for 1:1 complexation (λ_{exc} 420 nm, 0.1 mM complex, HEPES 0.1 M, pH 7.4).

Complex	Bicarbonate log *K*	
RepyEuL1	2.33	Our work
[57]⁺	2.55	
[58]⁺	2.23	
[59]⁺	2.14	
[60]⁺	2.80	

Table 4.3: Comparsion between our work affinity constant to carbonate and Parker's complexes.[202]

Since this probe could be used in cellular imaging, the stability of **RepyEuL1** was studied via NMR spectroscopy by synthesis of the analogous **RepyYL1** complex, for which a number of ^{1}H-NMR spectra were then recorded. It is clear from Fig. 4.16 that **RepyYL1** exhibits excellent stability even after 24 h under light; the pyridine resonances remained unchanged without any obvious dissociation, unlike that recorded for Re chloride complexes.[225] This is thought to be related to the strong back-donation between the nitrogen of the pyridine(py → Re(I)) and the basicity of this moiety.[226, 227]

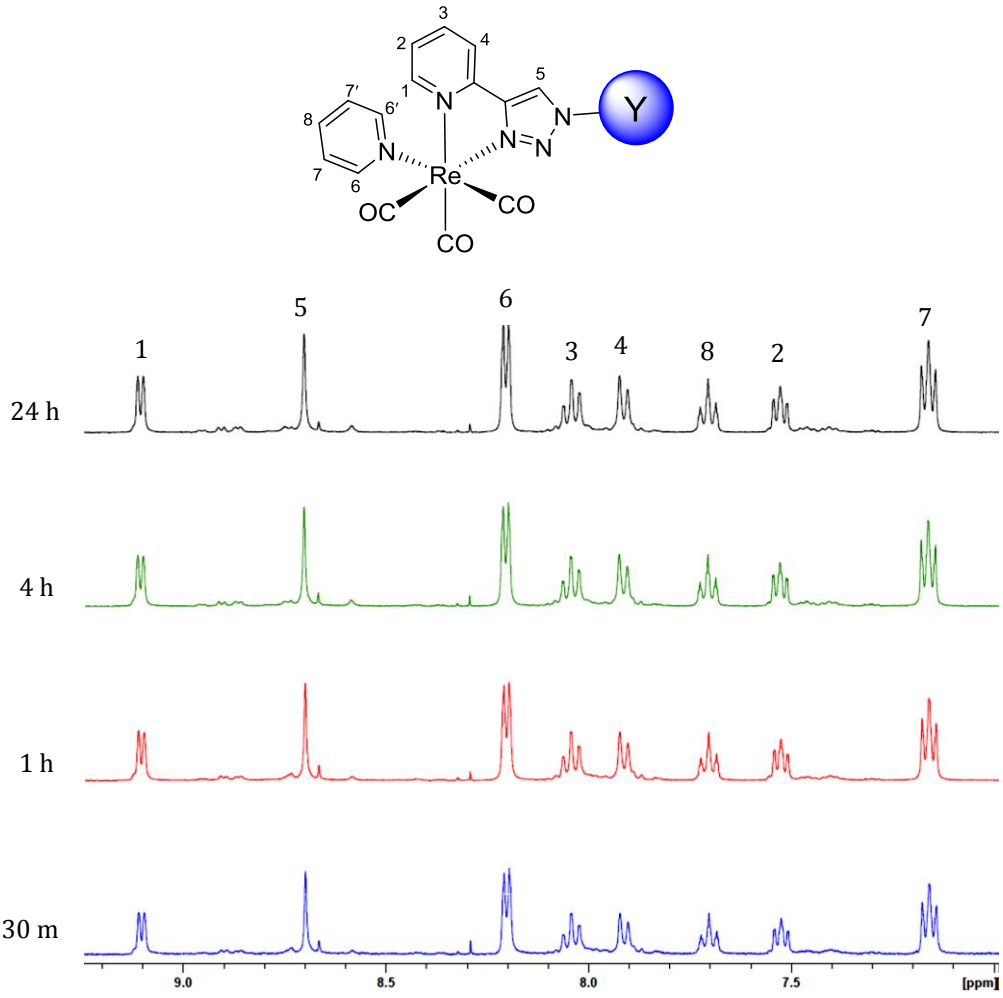

Figure 4.17: partial **RepyYL1** ^{1}H NMR spectra after addition 30 mM $NaHCO_3$ over a period of 24 h.

4.8 Tuning Rhenium Emission

The main advantages of transition metal complexes in the synthesis of bioimaging and biosensing reagents are their ability to tune their excitation/emission spectra (unlike lanthanides). In biology, using lower energies for excitation/emission is preferable to prevent photo-induced damage to cells and obtain maximum cell penetration. For this reason, the highest excitation energy that can generally be applied in confocal microscopy is 405 nm (violet), although in some cases where λ_{ex} < 405 nm multiphoton absorption can be used, which gives a low autofluorescence background and a high imaging contrast due to the low excitation energy required.[228] Due to **RepyEuL1** having high excitation energy, it is necessary to synthesise probes that have higher absorption at 405 nm (more to the visible region).

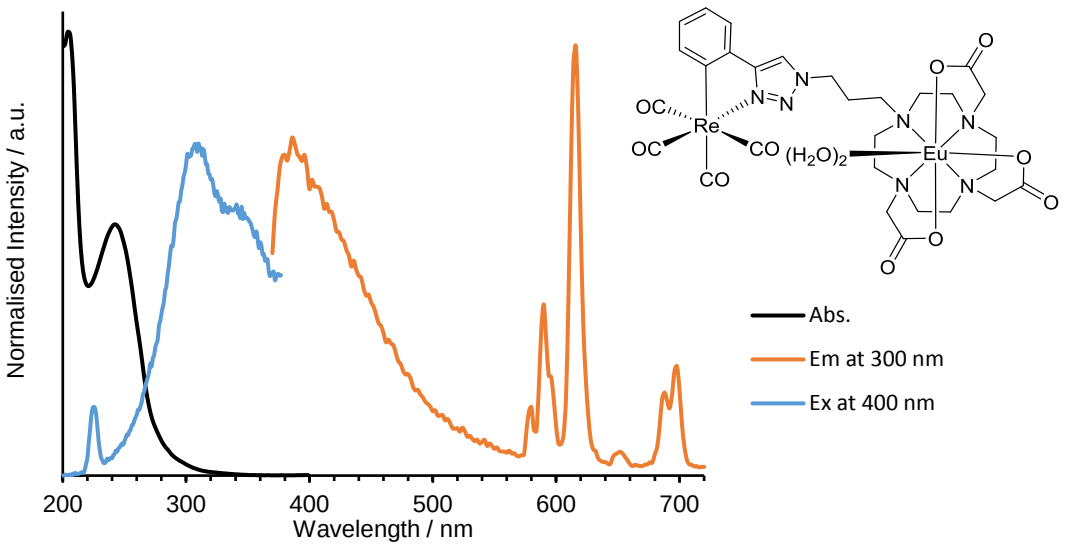

Figure 4.18: Normalised absorption, excitation and emission profile for **ReEuL2**, in aerated HEPES (0.1 M, pH 7.4), λ_{ex} = 400 nm, λ_{em}= 300 nm.

In terms of tuning the Re(I) emission, the cyclometallated **ReEuL2** shows an electronic absorption spectrum with two peaks: a strong peak at λ = 203 nm (π→π*) and a shoulder at λ = 245 nm corresponds to (n→π*). It has been found that the excitation at 300 nm gives a weak emission spectrum maximum at 400 nm related to Re(I) ^{1}MLCT and Eu(III) ^5D_J as shown in Fig.4.18. The weak and higher energy photoluminescence of Re complex related to the π→π* LC nature of the excited state leads to no electron density transfer from the metal centre or CO to the N^C part.[229] Therefore this complex cannot be use used as a carbonate sensor or even as an imaging probe.

Density functional theory (DFT) shows with *fac*-[Re(N^N)$(CO)_3$(L)]$^{n+}$ complexes the HOMO orbital is localized on the Re(I), $(CO)_3$ and (L) (L = pyridine , Cl, Br) while the LUMO is centred on the pyta. As pyta ligand is higher in energy compared to bpy, this explains the blue shift in the absorption as more energy is required to promote the electron to a higher energy level. However, this higher energy LUMO also suppresses the non-radiative decay, giving longer-lived and potentially brighter emission due to big energy gap between HOMO-LUMO.[218]

It has been assumed that substituting withdrawing groups onto the pyta (pyridyl ring) such as NO_2 or CN leads to a decrease in LUMO level, ultimately red-shifted emission bands compared with analogous donating groups.[230] It is important to strike the right balance between a favourable absorption and emission region; as the absorption is pushed further towards (or into) the visible spectrum and becomes near to the emission spectrum, the lifetime and emission intensity are potentially compromised. With the aforementioned in mind, one question that needs to be addressed in this section, is whether a withdrawing -CF_3 group in the 4 or 5-position or donating group 4-OMe on the pyridyl moiety will induce the same bathochromic shift and what the difference is between them in terms of lifetime and quantum yield.

For optimum biological usage, an investigation was carried out on **RepyEuL1** probe, Fig. 4.19 clearly shows an expected red shifted emission spectrum for both **RepyEuL3** and **RepyEuL4** complexes (5, 4-CF_3) respectively, that is related to the stabilization of the LUMO levels, resulting in a decreased HOMO-LUMO energy gap. This shift equates to about 52 nm for both complexes *cf*. **RepyEuL1** (500 nm), is likely to be related to red shift ^{3}MLCT transitions. The excitation spectra however, exhibit contradictory features, with a peak at 338 nm related to $\pi \rightarrow \pi^*$ and a shoulder at 308 nm stemmed from $d \rightarrow \pi^*$. This is high likely related to CF_3 which is known to have a strong stabilisation effect as well on the ligand-based HOMO.[167] Unfortunately, in **RepyEuL3** and **RepyEuL4** complexes Eu(III) emission is 'buried' under long wavelength Re(I) emission as it can be seen as a shoulder at 617 nm, therefore they are not applicable to use as carbonate sensor.

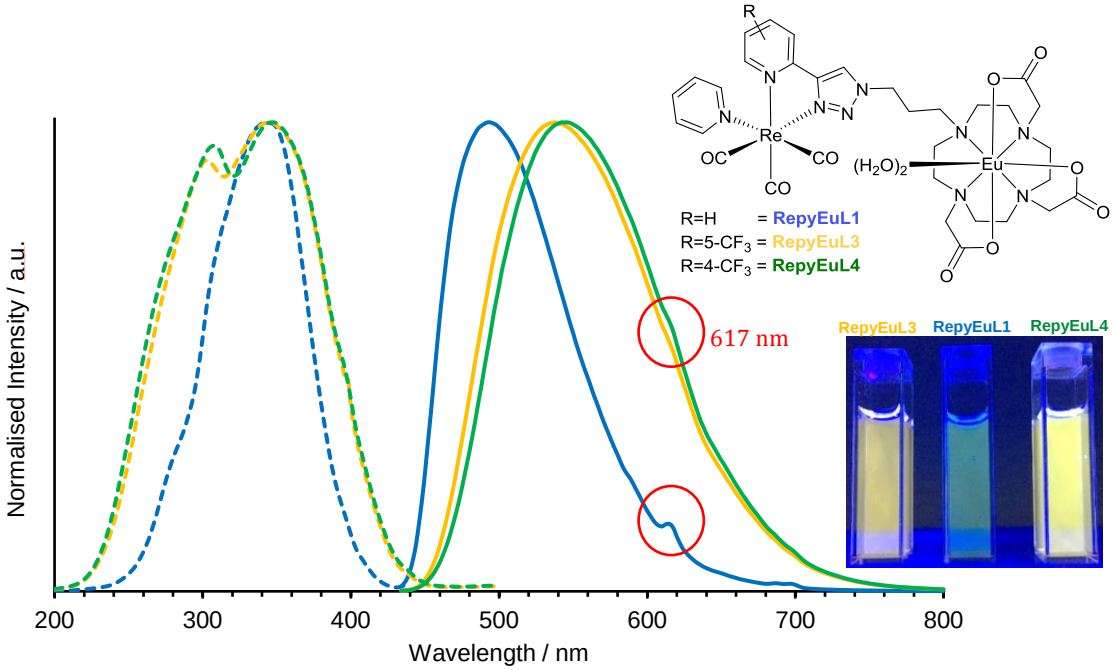

Figure 4.19: Normalised excitation (dashed) and emission (solid) spectra of **RepyEuL1** (—), **RepyEuL3** (—), **RepyEuL4** (—) in aerated HEPES (0.1 M, pH 7.4), λ_{ex} = 405 nm, λ_{em} = 500 for (—); 540 nm for (—) and (—). Inset: (0.1 mM) solution in cuvettes view under 365 nm illumination.

Additionally, changing the coordination of the nitrogen atom on the triazole ring (inverse click) leads to a change in the photophysical properties in comparison to the regular triazole complex. Fig. 4.20 proves that the inverted 1-(pyrid-2-yl)-1,2,3-triazole ligand (tapy) in **RepyEuL5** that coordinates to rhenium(I) through the less basic N(2) atom results in a bathochromic shift in the emission spectrum compared to that of **RepyEuL1**.[231]

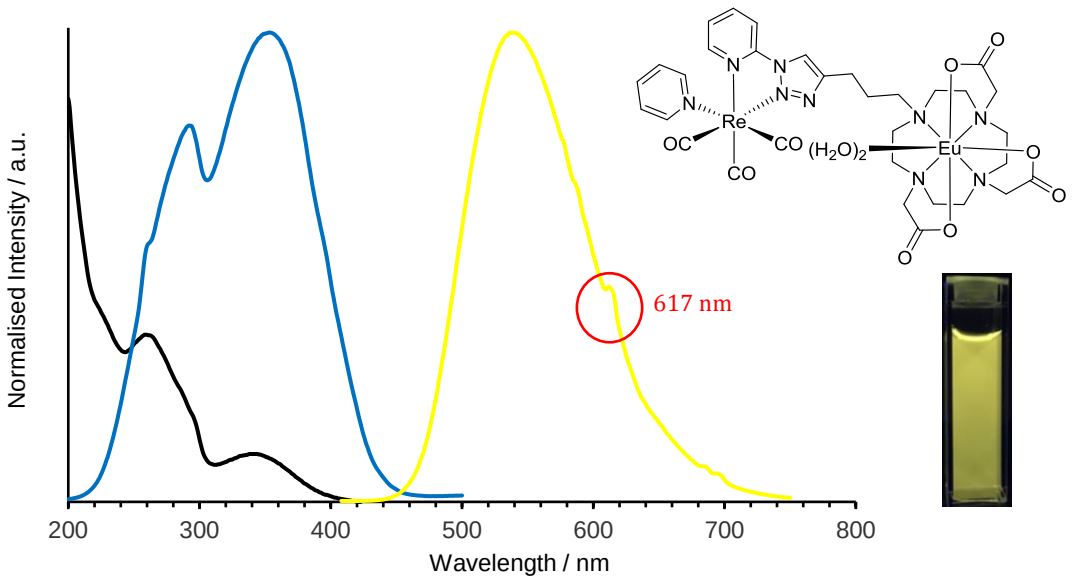

Figure 4.20: Normalised absorption (black), excitation (blue) and emission (yellow) spectra for **RepyEuL5**, in aerated HEPES (0.1 M, pH 7.4), λ_{ex} = 350 nm, λ_{em}= 540 nm. Inset: (0.1 mM) solution in cuvette view under 365 nm illumination.

A decrease in the energy of the ^{1}MLCT transition (LUMO) due to inverting the triazole bridge gives an emission maximum at 546 nm, which is red-shifted by 52 nm compared to **RepyEuL1** (λ_{em} = 494 nm). As well as, the absorption spectra at the lowest energy band (355 nm) associated with MLCT has been red-shifted 11 nm, with ILCT appearing at 294 nm. This complex shows the presence of intense bands in FTIR spectrum around 2041 and 1917 cm^{-1} ascribed to the C–O stretching vibration characteristic of a facial geometry. Similar results were obtained by Crowley and co-workers,[102] they found that emission from complexes formed with the regular pyta framework were more sensitive to their coordinating solvents and have short excited state lifetimes and low quantum yields compared to their inverse-pyta analogues. However, again Eu(III) emission was buried under Re(I) emission makes this complex not useful as carbonate sensor.

Until now all the attempts to shift Re(I) emission away from Eu(III) and excitation spectrum further to the red region were failed. **RepyEuL11** complex however, demonstrate a clear progression from broad ^{3}MLCT to narrower ^{3}IL phosphorescences on going from unsubstituted pyta to electron donating group 4-OMe, with less overlap with Eu(III) emission (Fig. 4.21).

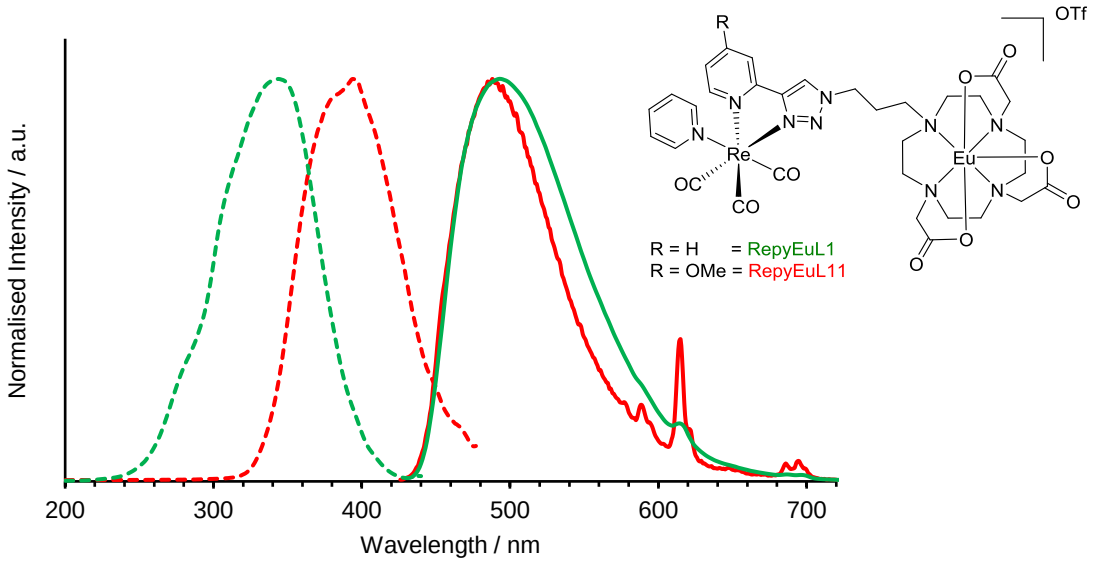

Figure 4.21: Normalised excitation (dashed) and emission (solid) spectra of **RepyEuL1** (—) λ_{ex} 500nm, λ_{em} 355 nm in H_2O and **RepyEuL11** (—) λ_{ex} 500nm, λ_{em} 400 nm in MeOH.

More importantly, the excitation maxima was shifted to lower energy ~60 nm *cf.* **RepyEuL1** 340 nm. This can be attributed to the electron donating group, it induces destabilization to the highest occupied energy level by injecting electron

density to the Re(I) ion with maintains LUMO energy level.[232] Unfortunately, it has been found **RepyEuL11** is not fully water soluble, so addition DMSO is needed to use as imaging agent or carbonate sensor.

In summary this section shows the ease of which the LUMO levels can be stabilized in rhenium tricarbonyl complexes, by adding electron withdrawing group onto the pyridyl moiety or via synthesising the inverse pyta, which leads to a bathochromic shift in the associated emission spectrum. While, by adding electron donating group will lead to destabilise the HOMO, eventually red shifted excitation spectrum.

4.9 Quantum Yield and Lifetime Measurements

The fluorescence quantum yield is a key parameter for measuring the efficiency of the conversion of absorbed light into emitted light, see Equ. (28), where $photons_{em}$ is number of emitted photons and $photons_{abs}$ is the number of absorbed photons.

$$\Phi = \frac{photons_{em}}{photons_{abs}} \tag{28}$$

The comparative method for determining Φ is a more accurate and reliable method than others; as introduced by Williams *et al.*,[233] it involves using well-characterised standard samples with known values of Φ. Ideally, the standard and the test sample should have approximate absorbances at the same excitation wavelength. Under identical conditions, a simple ratio of the integrated fluorescence intensities of the two solutions can be plotted, at which point Equ. (29) can be used to measure the Φ for the sample.

$$\Phi_x = \Phi_s \left(\frac{Grad_s}{Grad_x}\right)\left(\frac{\eta_s}{\eta_x}\right)^2 \tag{29}$$

Here, the subscripts x and s represent the analyte and the standard, respectively, *Grad* is the integrated fluorescence intensity (plot of integrated fluorescence vs. absorbance) and η is the refractive index of the solvent. All spectra were obtained in the same solvent, so the final term in this equation can be ignored. There are a wide range of standards that can be used in the comparative method, however for water solubility and similarity in absorbance and emission of Re(I)

complexes, a standard such as $[Ru(bpy)_3]^{2+}$ (Φ = 0.028) or quinine sulphate (Φ = 0.59) are preferable.

Generally TMs such as Ru(II) or Re(I) complexes, for example, have short excited state lifetime about 15 ± 10 fs for $[Ru(bpy)_3]^{2+}$ and 0.241 μs for $[Re(bpy)(CO)_3py]^{+}$ in deaerated MeCN because of partly or formally forbidden optical transitions and extremely fast ISC rates (10^{12} s^{-1}). Additionally, these emitters (on the order of several hundred ns up to a few ms) favour collisional luminescence quenching in oxygen and thus result in oxygen-dependent quantum yields.[234] To measure the lifetime decay and quantum yield, Gd(III) analogous were used, to eliminate any emission that could interfere from Eu(III) with Re(I) emission ultimately inaccurate results.

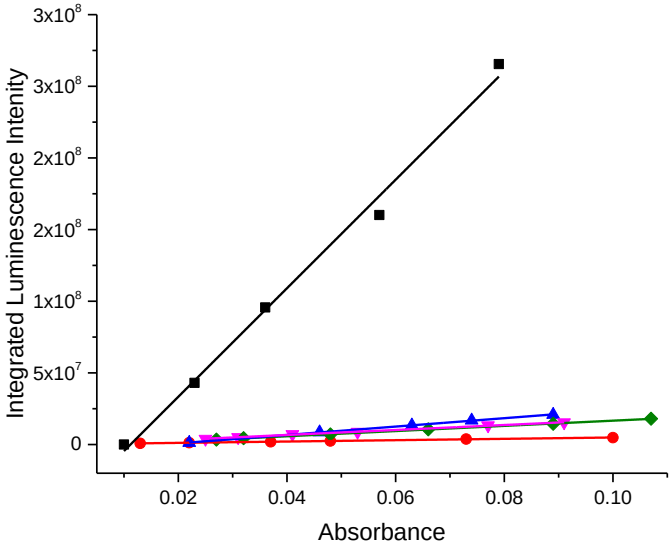

Figure 4.22: Integrated Fluorescence Intensity-Absorbance plot. Linear fit y = mx + c: quinine sulfate as reference (■), λ_{ex} = 342 nm, λ_{em} 400-700 nm in H_2O at 273 K. **RepyGdL1** (●), **RepyGdL3** (◆), **RepyGdL4** (▼), **RepyGdL5**(▲).

The integrated emission and absorbance of four of the hetero nuclear Re(I) complexes were plotted against each another (Fig. 4.22) and their gradients used to calculate the quantum yields. Fig. 4.23 shows the life time decay for **RepyGdL** complexes, the values obtained for the lifetimes and quantum yield are summarised in Table 4.4.

The solubility, relaxivity, stability and emission data for Re-Gd complexes promote it as a candidate to use as dual-mode optical / MR imaging agents.

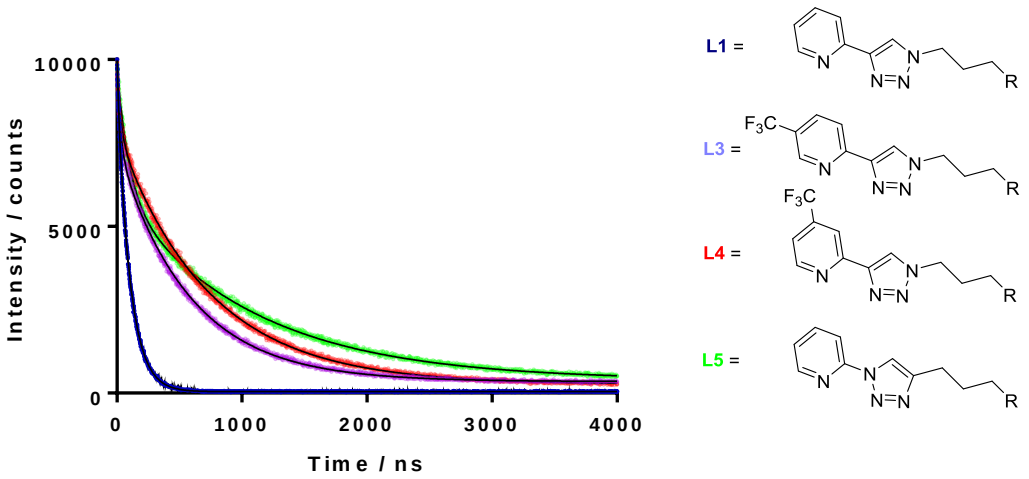

Figure 4.23: TCSPC luminescence exponential decay plot. c = 0.1 mM, 0.1 M HEPES pH 7.4, λ_{ex} = 372 nm, λ_{em} = 500 nm, two exponential decay gives: **RepyGdL1** (blue) R^2 = 0.9987; **RepyGdL3** (purple), R^2 = 0.9985; **RepyGdL4** (red) R^2 = 0.9983, **RepyGdL5** (green) R^2 = 0.9983.

	λ_{em}	Grad	τ(ns)	Φ
quinine sulphate		3.786 ± 0.17 x 10^9		0.59
RepyGdL1	500	4.688 ± 0.17 x 10^7	100	0.007
RepyGdL3	540	1.815 ± 0.07 x 10^8	570	0.028
RepyGdL4	540	1.584 ± 0.12 x 10^8	720	0.024
RepyGdL5	540	2.928 ± 0.04 x 10^8	1070	0.045

Table 4.4: Lifetime and quantum yields determined by the gradient comparison method using the gradients obtained in Fig. 4.21 the values were obtained in aerated water.

Generally speaking the emission energies, quantum yields and lifetimes of rhenium(I) tricarbonyl complexes decrease with increasing polarity of organic solvents.[235] The higher τ and Φ for the emissive Re(I) complexes *cf.* **RepyGdL1** could be explained by the difference in the degree of the electronic overlap between the emissive triplet excited and singlet state of the complexes and the purest ^{3}MLCT emitting state, ultimately larger radiative, k_n than nonradiative energy, k_{nr}.[236] Noticeably, **RepyEuL5** is very bright, about seven-fold more intense than **RepyEuL1**, and double the intensity of **RepyEuL3,4**. This is related to the *inv*-pyta ligand which has been found more resistant to the environment and easier to reduce than its *reg*-pyta counterparts; therefore, the Re(I) with *inv*-pyta displays a higher quantum yield in water than in organic solvents.[231,102] The two CF_3-substituted complexes show almost comparable values in terms of quantum yield, though

RepyEuL4 shows a longer lifetime by ~0.15 μs. These values are expected, since attaching the electron withdrawing group increases the resistance to quenching, especially in polar solvents.[237]

4.10 Summary and Conclusions

A series of bimetallic rhenium-lanthanide complexes have been synthesized, by heating at reflux a solution of $[Re(CO)_5OTf]$ in methanol with various pyta / tapy ligands with pendants of Eu(III)/Gd(III)-DO3A. The resulting hetero nuclear Re(I)–Ln(III) complexes were characterized by HRMS (ESI) and IR spectroscopy. **RepyLnL1** shows high water solubility, stability and excellent response upon HCO_3^- addition with a 300% increase in Eu(III) emission intensity. Furthermore, this complex exhibits a clear colour that changes on addition of 30 mM carbonate solution, making it a good candidate for a bicarbonate sensor. It has been found that substituting the 4- or 5-positions on pyridine pyta with CF_3 leads to a red shift in emission spectra due to stabilization of the LUMO level. Additionally, **RepyEuL3** and **RepyEuL5** show higher lifetime and quantum yield values, related to the high resistance of the molecular orbitals and the excited states to solvent quenching. This makes the probes more promising from a confocal microscopy viewpoint, but they are unsuitable to report on carbonate concentration as their Re(I) based complexes emission overlaps with the Eu(III) emission.

RepyEuL5 also shows interesting photophysical properties with a lifetime of up to 1 μs and a quantum yield of 0.045 in aerated water, making it an excellent candidate for cell-imaging, although not good with respect to carbonate sensing. This is likely to be related to the 1-(pyrid-2-yl)-1,2,3-triazole ligand being easier to reduce compared to *reg*-pyta, which is analogous with a low HOMO-LUMO energy gap. Re(I)–Gd(III) analogues could be used as dual-mode optical/MR imaging agents, since they demonstrate promising Re(I) emission with high relaxivities, even in the presence of high carbonate concentrations.

Finally, **RepyEuL11** exhibits lack of water solubility but significant bathochromic shifting in ^{1}MLCT absorption, due to destabilising the energy level of HOMO orbitals without effecting on LUMO orbitals in comparison with that of **RepyEuL1**.

Chapter 5

Multimetallic Contrast Agents

5.1 Introduction

MRI is a vital non-invasive clinical diagnostic technique that shows deep tissue penetration through which highly spatially resolved anatomical images can be obtained. However, the slow relaxation of tissue water protons often requires the introduction of paramagnetic contrast agents to enhance image quality. The relaxivity of a GdBCA is mainly determined by the following parameters: the hydration number (q), rotational correlation time (τ_R), the residence time of the coordinated water molecules (τ_m) and the electronic spin relaxation time (T_{1e}).[36] Optimization of these parameters will increase the relaxivity of the contrast agents. Synthesis of multiple lanthanide CAs with q > 1 are highly beneficial in terms of enhancing the total relaxivity and decreasing the intake dose, ultimately allowing low toxicity, detection of low-concentration targets and demonstrating low clearance rates from biological systems due to high molecular weight (slow to go through nephrons). In addition, building a highly rigid skeleton for the polymetallic macrocyclic analogues can lead to reduced rotational motion, eventually doubling relaxivity improvements (Section 1.4.2).[238]

High magnetic field scanners of up to 7 T have become widely available in modern clinics. There is a strong argument for their use, because of the numerous advantages relative to lower field strengths including: high signal-to-noise ratios, high spatial resolution, short acquisition times and the ability to image low sensitivity nuclei other than ^{1}H (including ^{19}F, ^{13}C, ^{23}Na and ^{31}P).[239] At low magnetic field strength (1.5–3.0 T) the relaxivity of GdBCA is limited by its fast rotational correlation time,τ_R, where optimal relaxivity is achieved when the correlation time, τ_{c1}, of the contrast agent is equal to the inverse of the Larmor frequency ($1/\omega_I$) of the proton.[240] As seen in Equ. (30) this correlation time can be optimised by slowing down the three processes, namely rotational correlation time,τ_R, water residence lifetime, τ_m, and electronic relaxation time, T_{1e}.

$$\tau_{c1}^{opt} = \frac{1}{\omega_I}; \frac{1}{\tau_{c1}} = \frac{1}{\tau_R} + \frac{1}{\tau_m} + \frac{1}{T_{1e}} \quad (30)$$

Therefore, the dipole–dipole relaxation of the GdBCA at low field strengths can be modulated by attaching a small molecule CA to a macromolecule (*e.g.*, protein, polymer, and nanoparticle) or the synthesis of rigid multimeric agents. In this instance, the resulting molecule will show a reduction in tumbling, resulting in a longer τ_R /T_{1e} and a subsequent increase in relaxivity.[31]

It is well known that the relaxivity of GdBCA decreases dramatically with increasing magnetic field strength ≤ 3T due to the decrease in the optimal value of τ_R; for example, Caravan and Aime reported that the rotational correlation time dropped from ~ 20 ns to ~ 0.5 ns for high field magnets ≥ 1.5 T.[38] Hence, τ_R and τ_m dominate the relaxivity at B_0 ≤ 3T, and while T_{1e} does not contribute significantly, it does increase with increasing magnetic field strength, unlike at low field which is dominated by all three parameters.

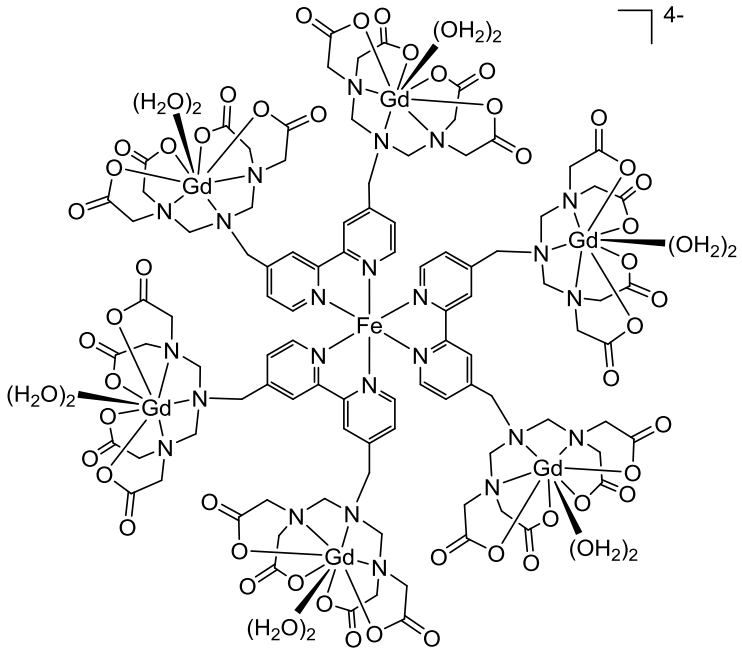

Figure 5.1: Multimetallic complex **78**.

Rational approaches are being applied that seek to optimize the relaxivity of CAs depending on the systematic modification of these previous parameters.[31] For example, Tóth and co-workers synthesized the metallostar system **78,** as seen in Fig. 5.1. This system with six Gd(III) units each with q = 2, showed an impressive total relaxivity of 33.2 mM^{-1} s^{-1} (60 MHz, 25 °C) as compared with the 30 mM^{-1} s^{-1} for the PAMAM [poly(amidoamine)] dendrimer system functionalized with Gd(DOTA) units, and of much greater mass.[241, 242]

Replacement of the iron(II) metal centre with more kinetically inert ruthenium(II) ion in a tetranuclear Gd(III) complex showed a relaxivity enhancement of almost double at 310 K in a 20 MHz field strength.[176] This is mainly attributed to the fast water-exchange rate (τ_M^{310K} = 77.5 s) and slow tumbling rate (τ_R^{310K} =∼ 240 ps). The Fe(bpy)$_3$ core of **78** exhibits higher rigidity than the Gd(III) arms alone, and has been found to tumble five times slower than the motion of the entire complex, due to a methylene spacer between the Gd(III) unit and the 2,2-bipyridine groups.[243]

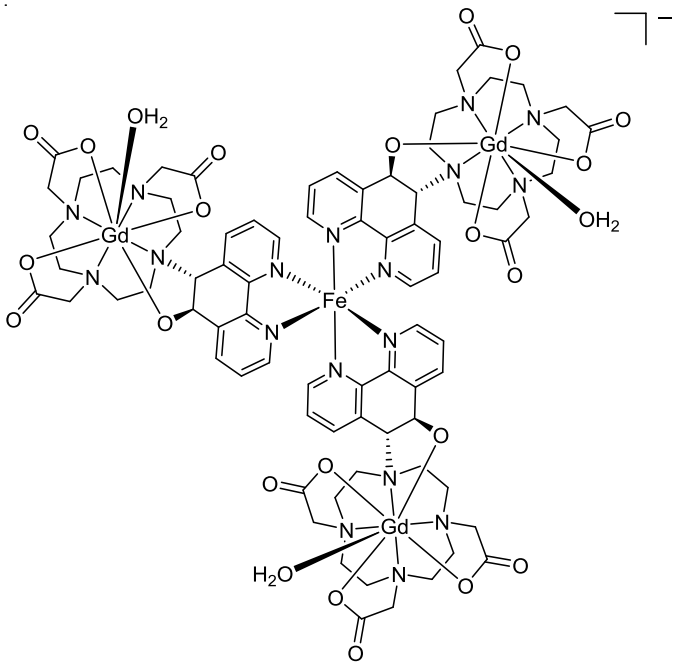

Figure 5.2: **79** structure.

Along the same lines, Tóth and co-workers synthesized the **79** complex with *q* = 1, as per Fig. 5.2, which shows a relaxivity 200% higher and four times slower rotation (τ_R^0 = 398 ps) than the monomeric unit due to its the internal rigidity.[241] **79** exhibits higher rigidity compared to **78** due to the hydroxyl units attached to the phenanthroline moiety which force the rotation of the whole complex as single entity. However, this multimetallic complex showed a slow water exchange rate because of the phenanthroline alcohol group.

Multi-gadolinium / high molecular weight CAs can also be synthesised without introducing *d*-block metals as ligation centres.[244, 245] However, these GdBCA complexes do not exhibit high relative relaxivities compared to complexes that have a TM core, for instance **80** in Fig. 5.3 which shows an r_1 = 6.1 $mM^{-1}s^{-1}$ at 20 MHz per

molecule which means relaxivity per Gd = ~2 mM^{-1} s^{-1}. This is due to the flexibility and dipolar interaction between the three Gd(III) ions leading to greater electronic quenching than that for dinuclear complexes.[238]

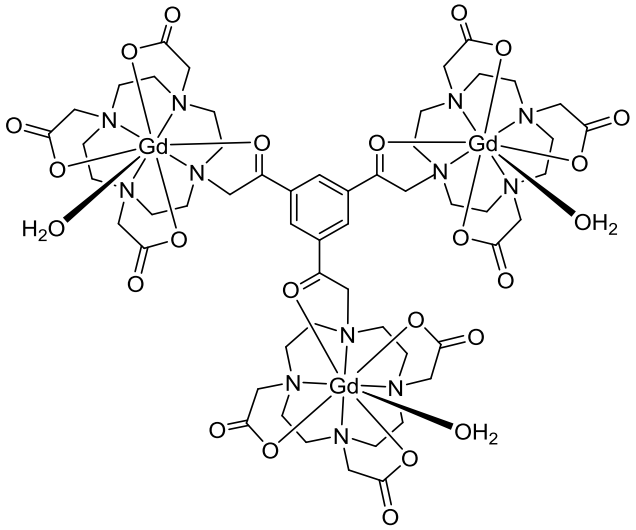

Figure 5.3: **80** structure.

80 with Fe(II) is obviously unlike the complex **81** core (Fig. 5.4), which exhibits a total relaxivity of 7.56 mM^{-1} s^{-1} (400 MHz, 9.4 T, 25 °C).[246] This slight elevated in relaxivity is related to the higher magnetic field, rigidity and the efficient spacer between the Gd(III) ions that helps prevent the dipolar Gd^{3+}–Gd^{3+} interactions that could otherwise accelerate electronic relaxation. In addition, this self-assembly gadolinium complex shows a 1.15-times increase in relaxivity after addition of HSA, which is likely to be due to the non-covalent binding to this protein.

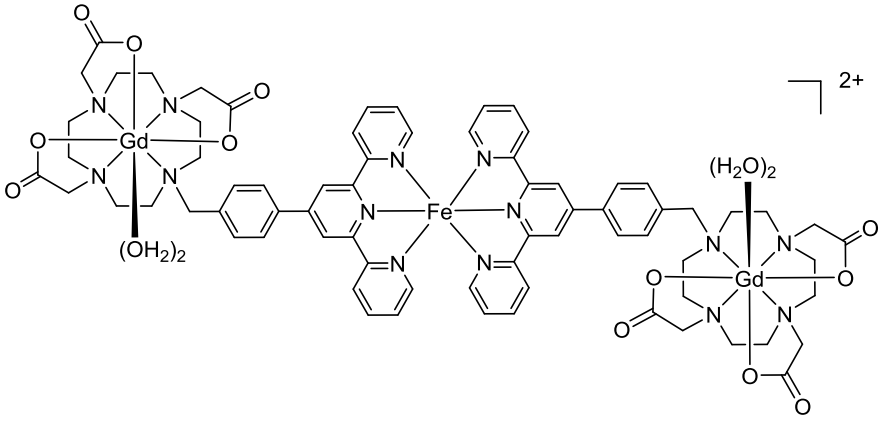

Figure 5.4: complex **81**.

SBM theory states that at proton Larmor frequencies higher than 200 MHz the relaxivity increases with the inverse of the rotational correlation time, $1/\tau_R$, while at lower frequencies it is proportional to τ_R (Fig. 5.5). Therefore, in higher magnetic fields, rigid molecules of intermediate size are favoured over large very slowly tumbling species.[244] In summary, at higher magnetic fields ≥ 1.5 the relaxivity is expected to be lower than that observed at 0.5-1.5 T. The synthesis of small, rapidly tumbling molecules with *intermediate* magnitudes of τ_R ranging between 0.5 and 4 ns, a hydration number > 2 and rigid multimeric Gd(III) units are a prerequisite to a good contrast agent for improving r_1 at ultra-high field strengths.[38, 240]

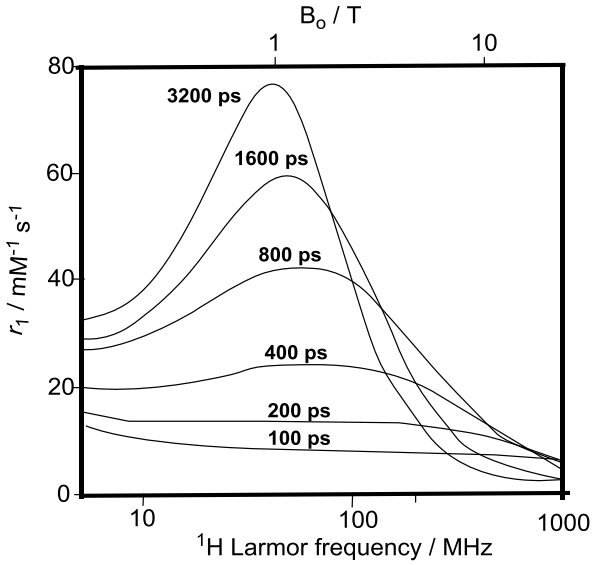

Figure 5.5: Inner sphere proton relaxivities for q = 2 complexes calculated using the Solomon–Bloembergen–Morgan theory for various values of the rotational correlation time, τ_R, as a function of the magnetic field (upper x-axis) or the proton Larmor frequency (lower x-axis).[244]

In this chapter, high molecular weight CAs have been synthesized to obtain longer rotational correlation times (τ_R) / slower molecular tumbling, and ultimately higher relaxation. This can be achieved by fusing several small-molecule agents together with the help of pyta moieties. Heteronuclear complexes were synthesised from various monomeric-Ln(III) units, and joined together by octahedral coordination of Fe(II) and Co(III) to form 6-coordinate octahedral complexes containing three Ln(III) units. In addition, a complex of two Gd(III) ions attached to a tridentate ligand was synthesised; this CA is expected to give a higher r_1 than the mono-Gd(III) complex at low field strengths.

5.2 Complex Syntheses

FeGdL1 was prepared by heating at reflux $Fe(BF_4)_2.6H_2O$ with three eq. of **GdL1** in EtOH (5 mL). The coordination of **FeGdL1** is shown in Fig. 5.6 which is obtained with a good yield of 48% after RP-HPLC t_R = 8.20. The studies prove these complexes with iron(II) can be exist as *fac* and *mer* isomers in solution depending on the temperature, however this diastereoselectivity is more labile than these related compounds.[247] The MS (ESI) exhibits an characteristic isotopic pattern for ^{56}Fe and ^{158}Gd centred at *m/z* = 1080.7200 $[M]^{2+}$.

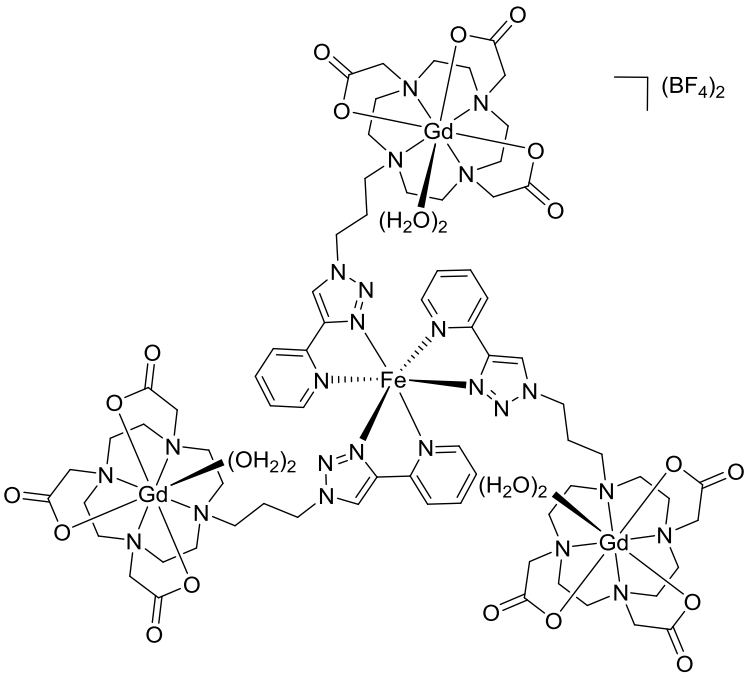

Figure 5.6: *fac*-**FeGdL1** structure.

The cobalt complexes were prepared following the same conditions by heating at reflux $CoCl_2.6H_2O$ with three eq. of **LnL1** to obtain the final product as a red solid; the HRMS (ESI) for **CoEuL1** showed the isotopic pattern for ^{59}Co and ^{153}Eu centred at *m/z* = 1051 $[M]^{2+}$, as seen in Fig. 5.7, while **CoGdL1** gave the isotopic pattern for ^{59}Co and ^{158}Gd centred at *m/z* = 1059 $[M]^{2+}$. The analogous Co(III) complexes of these ligands exist as a 1:1 mixture of the *mer* and *fac* isomers in solution.[248] Interestingly, the Ln(III) (Ln = Gd and Eu) complexes showed similar RP-HPLC retention times, suggesting that the Ln(III) ions share the same coordination sphere in these metallostar architectures.[249]

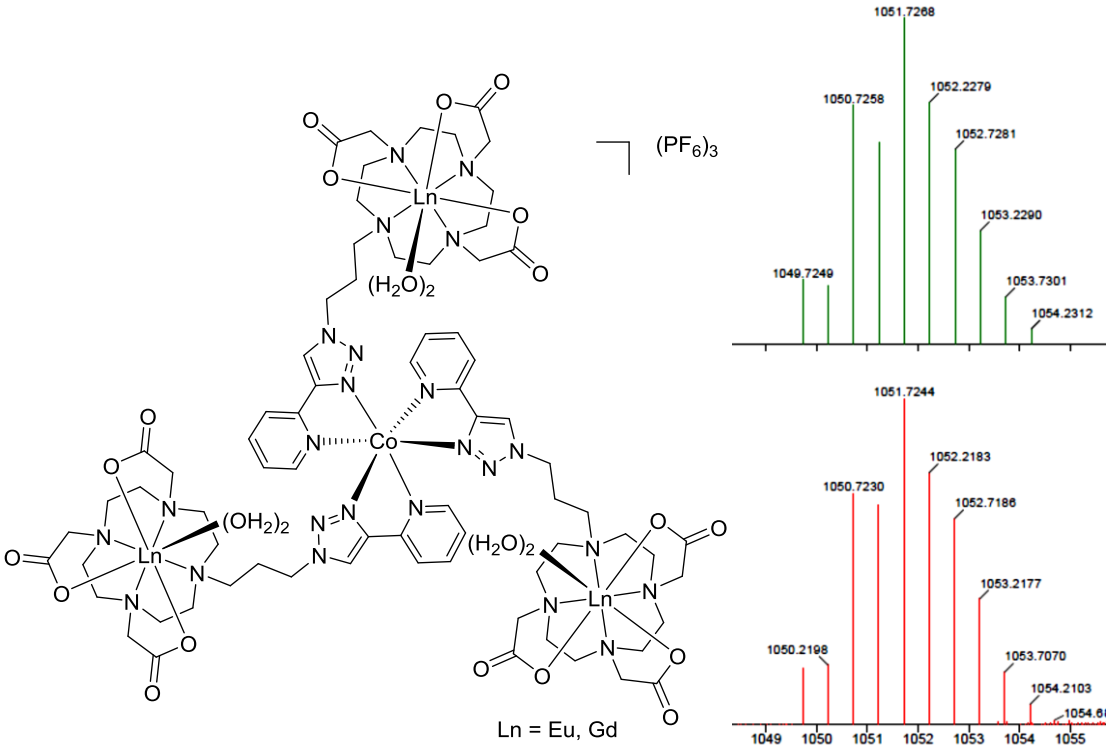

Figure 5.7: Chemical structure of *fac*-**CoLnL1** and observed (lower) and simulated (upper) isotope distributions for the doubly charged ion obtained by fragmentation of **CoEuL1** complex.

The third CA, which possesses two Ln(III) complexes, was prepared by complexing $LnCl_3.6H_2O$ with the ligand **H_6L7** to give **LnL7** (Fig. 5.8) with a good yield after purification by HPLC t_R = 7.51 min. The MS (ESI) for **GdL7** shows *m/z* = 1296 $[M+H]^+$, while **EuL7** shows *m/z* = 1285 $[M+H]^+$ and 643 $[M+H+Na]^{2+}$.

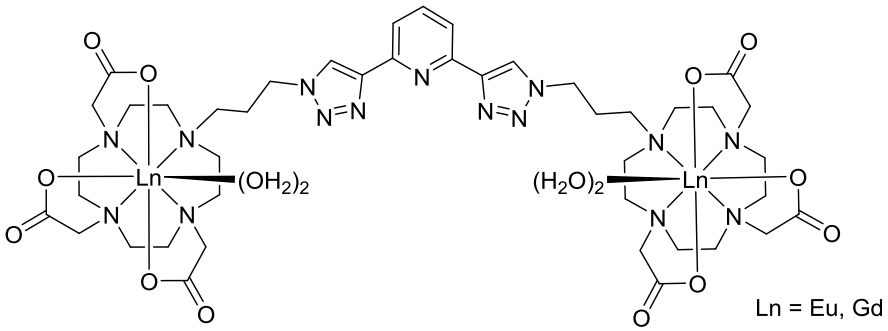

Figure 5.8: **LnL7** chemical structure.

5.3 Photophysical Studies

EuL7 shows characteristic Eu(III) photoluminescence ($^5D_0 \rightarrow {}^7F_J$ transition) at excitation wavelength = 300 nm as seen in Fig. 5.9, indicating that the pyridyl bis triazole works as a good antenna for both Eu(III) ions . The hydration state *q* of the europium component in the **EuL7** and **CoEuL1** complexes was evaluated by comparison of the luminescence lifetimes of the europium-centred emission in H_2O

and D_2O solutions, after which the empirical equation (see Section 1.5.4) was applied. At 298 K, k_{H_2O} (2.32 ms^{-1}) and k_{D_2O} (0.56 ms^{-1}) point to the presence of two metal-bound water molecules per Eu(III) ion (q = 1.8), as per Table 5.1. **EuL7** showed q = 1.9 for per DO3A unit.

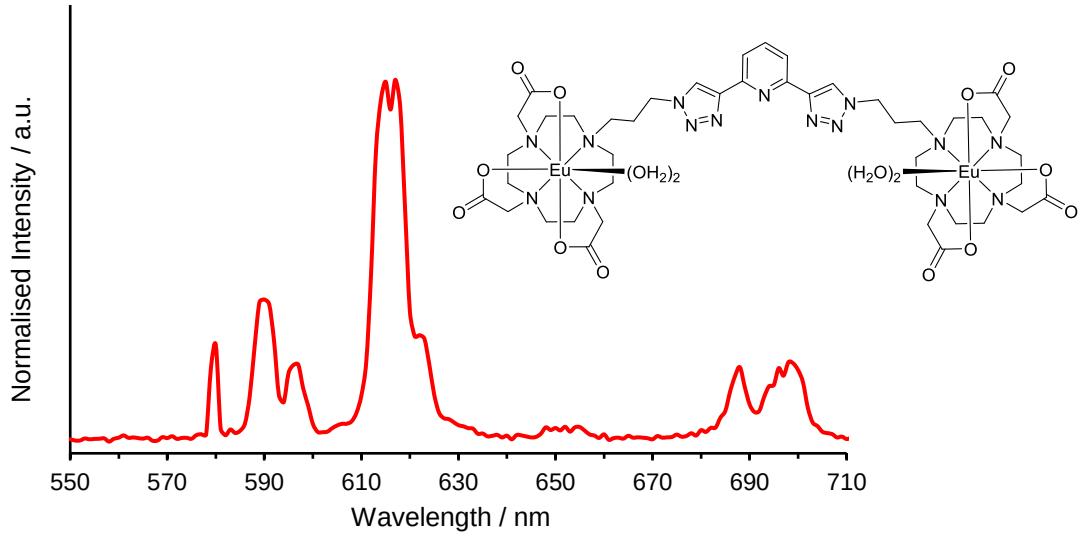

Figure 5.9: **EuL7** emission excited at 300 nm.

	k_{H_2O}/ms^{-1}	k_{D_2O}/ms^{-1}	q ±0.2
EuL1	2.57	0.59	2.0
CoEuL1	2.32	0.56	1.8
EuL7	2.45	0.59	1.9

Table 5.1: Selected photophysical data for the complexes in the aqueous solutions. (pH 7.4, 298 K, λ_{ex} = 280 nm, λ_{em} = 616 nm).

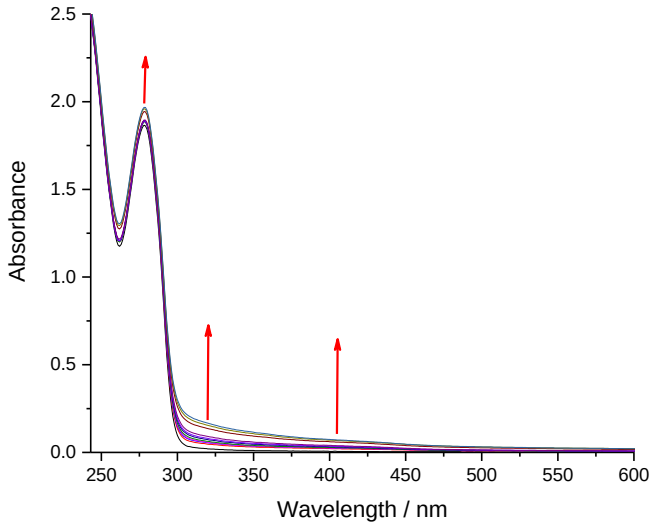

Figure 5.10: Absorption spectra of **GdL1** (30 μM) upon titration with Fe^{2+} (0-1 equiv.) in 50 mM HEPES buffer solution at 25 °C and pH 7.2.

The complex structure of **FeGdL1** was as well implicit from the change in the photophysical properties. After addition of Fe(II) ions, the pyta ligand starts to coordinate with the Fe(II) forming a low spin octahedral complex. It can be seen that there is a new absorption bands are generated assign to MLCT as seen in Fig. 5. 10 in the visible region of the spectrum (300–450 nm).[250]

When the complex forms the pyta emission, weaker which can be monitored to investigate the coordination metal:ligand ratio. In this case, the ratio of Fe(II) to **GdL1** was predicted by monitoring the reduction in pyta fluorescence intensity at 320 nm. This is related to the formation Fe(II) octahedral complex that quenches the S_1 excited state via non-radiative pathways through the ^{3}MC transition, so that eventually the fluorescence intensity will be decreased. Indeed, iron complexes are not emissive, which can be attributed to the forbidden *d-d* state being closer to the ground state than the emissive state MLCT, as in Ru(II) complexes.[251] The ratio of Fe(II) to **GdL1** was determined by using 30(μM) of **GdL1** with serial addition of Fe(II) in a 0 → 0.3 eq., as per Fig. 5.11.[252] The emission spectra show that the Fe^{2+} binds completely in a 3:1 ratio in aqueous solution, which minimises the intensity of the 320 nm emission.

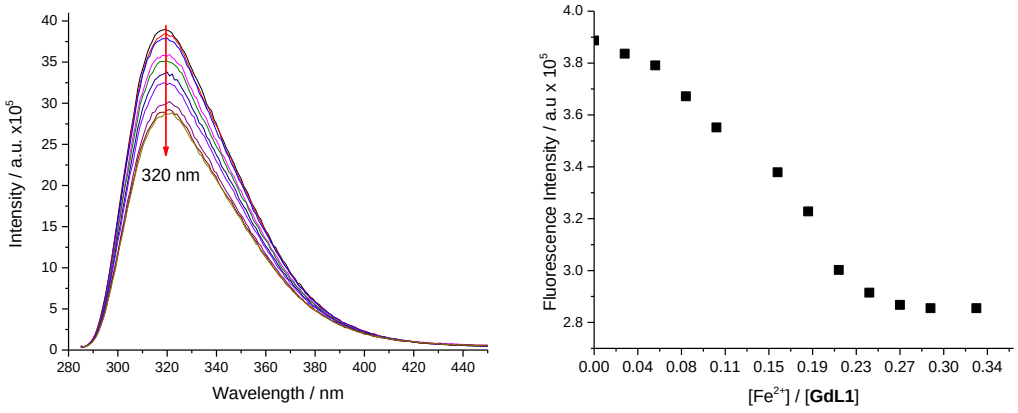

Figure 5.11: Changing in the emission spectrum of **GdL1** (30 μM) following the addition of Fe^{2+} ([Fe^{2+}] = 0, 1, 2, 4, 6, 8, 10 and 11 μM) in 50 mM HEPES buffer solution at 25 °C and pH 7.2 (λ_{ex} = 280 nm)(left), the data at (λ_{em} = 320 nm) (right).

Similarly, d^6 cobalt(III) forms high energy ^{3}MLCT triplet state fails to emit because the low OSC and the forbidden ^{3}*d-d* state is too low in energy to emit even at 77 K, as demonstrated in Fig. 5.12.

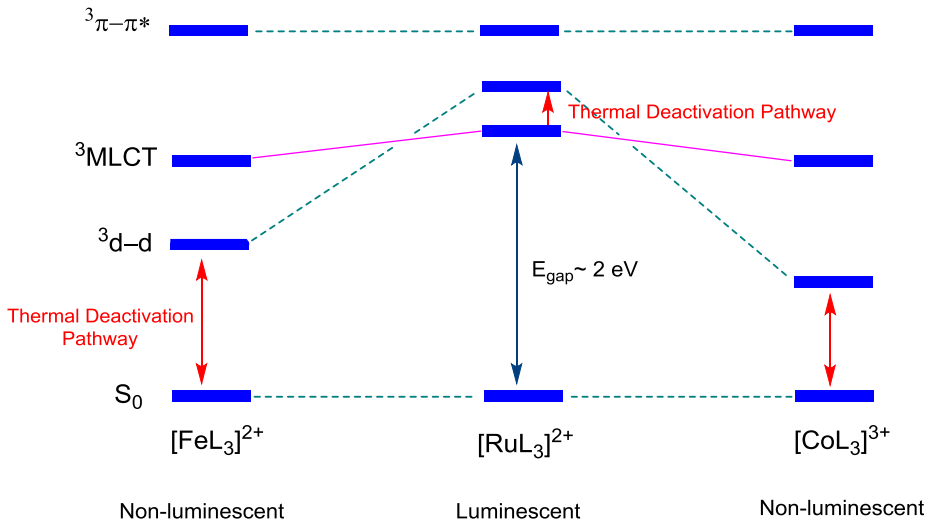

Figure 5.12: Lowest energy triplet states for complexes Fe(II), Ru(II) or Co(III) metals with bpy ligands.

5.4 Relaxometric Studies

The longitudinal relaxation times (T_1) of the Gd complexes were measured using an inversion-recovery pulse sequence (400 MHz, 9.4 T at 25 °C). The relaxation time was derived from the plots of inversion recovery versus time. Using the Evans method, the concentration of the paramagnetic complex can be calculated by measuring the shift of the *tert*-Butyl alcohol (TBA) resonance, as seen in Fig. 5.13.[253] Equ. (31) can be applied to calculate the concentration after measuring Δ_x.

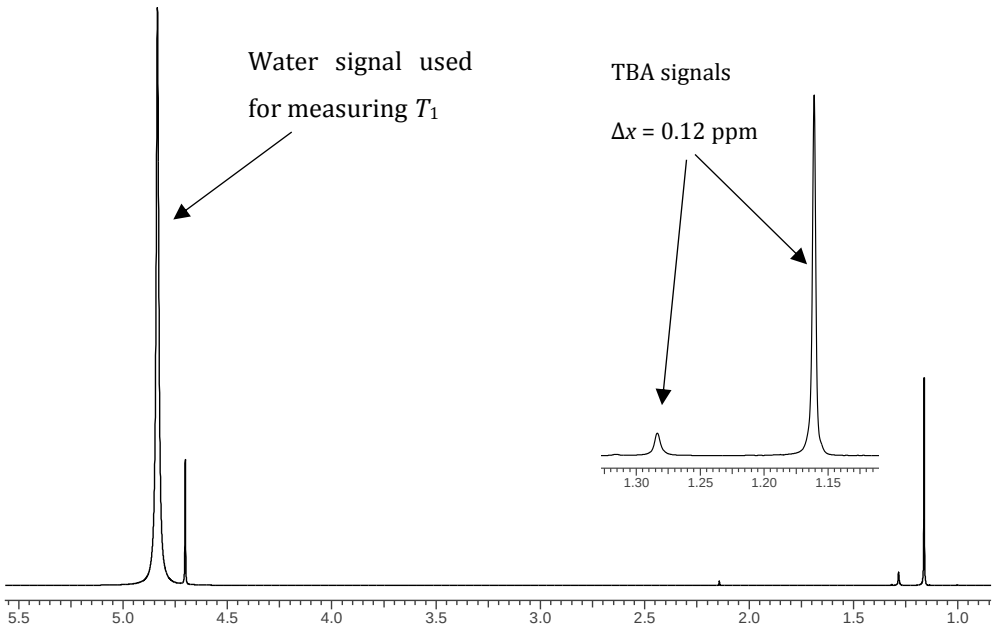

Figure 5.13: ^{1}H-NMR spectrum of **FeGdL1** and 10% TBA in H_2O with a D_2O inset containing TBA as a refrence (400 MHz, 298 K).

$$\Delta_x = \frac{4\pi cs}{T}\left(\frac{\mu_{eff}}{2.48}\right)^2 X\ 10^3 \quad (31)$$

Where Δ_x, is the shift in the TBA resonance in ppm, c is the concentration in mol dm^{-3}, s is the position of the sample in the magnetic field (s = 1/3 for vertical NMR), T is the temperature, and μ_{eff} is the effective magnetic moment.

Complex	r_1 mM^{-1} s^{-1} per Gd (400 MHz, 298 K)	*Total relaxivity*
GdL1	7.96	7.96
FeGdL1	7.26	21.78
GdL7	7.24	14.48
CoGdL1	7.35	22.05

Table 5.2: relaxivity data for the complexes at 400 MHz, 9.4 T, 298 K.

It is clear from Table 5.2 that at higher magnetic fields B_o = 400 MHz, these multigadolinium complexes showed promising r_1 results per Gd, due to hydration numbers of 2. Surprisingly, **GdL1** exhibits 20% higher relaxivity at high magnetic field more than other q = 2 mono-Gd complexes with similar MW.[239] Namely, as the SBM theory predicts, at proton Larmor frequencies above 200 MHz r_1 increases with the inverse rotational correlation time $1/\tau_R$. Thus at high frequencies, intermediate-size, rigid molecules are favored over large ones, with an optimal τ_R of 0.5-1.5 ns range at 400 MHz is effective, therefore high molecular CAs **FeGdL1** and **CoGdL1** with could have slow intermediate correlation time exhibit slight lower relaxivity per Gd *cf.* low molecular weight **GdL1** complex at 9.4 T.[254] However, these trinuclear Gd(III) chelates **FeGdL1** and **CoGdL1** still give high r_1 values (21.78 and 22.05 mM^{-1} s^{-1} respectively) *cf.* other work with trimer or metallostar-structured systems,[189] which indicates the actual relaxivities at low field strengths would likely be higher for each Gd(III) analogue than at high field strength.[244] This means that they could potentially be used specifically for low-field MRI (10-70 MHz). **GdL7**, with its intermediate molecular weight, means that this binuclear pincer can be used in an ultra-high field scanner due to its promising relaxivity at higher magnetic fields of 14.48 mM^{-1} s^{-1}. **GdL7** could be modified by e.g. adding targeting agents attached to the pyridine ring, e.g. to bind to HSA and enhance r_1.

5.5 Summary and Conclusions

A number of hetero metallic complexes containing multiple Ln(III) chelates have been synthesized, and these precursors have the potential for use as MRI contrast agents at low field (10-70 MHz). These multigadolinium agents have the ability to enhance water proton relaxivity to a greater extent than agents with a single gadolinium unit. **FeGdL1** and **CoGdL1** exhibit $q \simeq 2$ per unit and higher molecular weights lead to show higher relaxivity than initial complexes. Therefore, they furnish reasonable r_1 values even per Gd when tested at higher magnetic fields of 7.26 $mM^{-1}s^{-1}$ and 7.35 $mM^{-1}s^{-1}$ for **FeGdL1** and **CoGdL1**, respectively. Similarly, the final complex, **GdL7** could be suitable for use in high magnetic field MRI ≥ 3T, whose relaxivity value at 400 MHz and 9.4 T is 7.24 $mM^{-1}s^{-1}$.

Chapter 6

pH responsive MRI contrast agent

6.1 Introduction

Over the past decades, the use of MRI in medicine has received considerable attention due to its highly spatially resolved, non-invasive images and its ability to diagnose various deep-tissue abnormalities. The use of CAs is essential to enhancing the abundant ^{1}H tissue relaxivity in order to gain high-resolution anatomical images. Since the first CA was approved in 1988, scientists have been interested in developing smart CAs that show response for different biological ions, pH and enzymes variance.[255] pH-responsive contrast agents are considered a promising strategy by which to visualise and study the early stages of various cancers, ischemia and brain stroke.[43] The vascular perfusion, regional hypoxia and increased flow of bicarbonate ions leads to an increase in the extracellular acidity in solid tumours. Additionally, the rise in production of protons (H^+) and lactic acid (LA) in cancer cells related to anaerobic glycosis leads to an increase in intracellular acidity. Brain ischemia stroke is accompanied by high intracellular acidosis in nervous cells due to the associated increase in LA production and HCO_3^- flux. It has been found that the level of LA escalates by 20-fold, leading to a decrease in brain pH to 6.10 – 6.20.[256] With regards to the above discussion, it is vital to develop a smart CA that can detect the critical pH extracellular / intracellular drop from pH 7.2 to 6.2 in carcinoma or brain stroke.[257]

There have been several attempts in the last few decades to synthesise pH-responsive agents, that exhibit a sensitive response to pH changes in the cells in the range ~5 – 7, with high blood brain barrier penetration (BBBP) in brain stroke.[258] There are several methods for mapping the physiological proton concentration using lanthanides as a metal centre. The first is *in vitro* via optical methods, depending on Tb(III)/Eu(III) emission. The photoluminescence intensity of these metals can change depending on the acidity of the environment as a consequence of suppressing the energy transfer from T_1 of the antenna to the Ln(III). For instance, the phenanthridine pendant in **82** can sensitise Eu(III) emission at low pH.[63] On the contrary, at higher pH the chromophore triplet state energy drops dramatically as a

consequence of phenanthridine-NH-protonation effectively blocking energy transfer, as per Fig. 6.1 which shows **82** emission vs. pH.

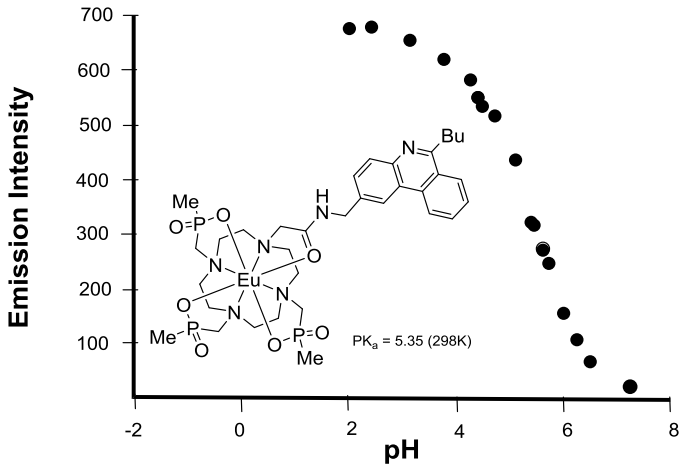

Figure 6.1: Emission intensity vs. pH for **82** (λ_{em} = 616).[63]

A second approach that has been used to synthesise a responsive luminescent Ln(III) probe is via replacing H_2O oscillators which quench Tb(III) / Eu(III) emission intensity (see Section 1.5.4). For instance Lowe and Parker synthesised intramolecular pH ratiometric probes with an arylsulfonamide group pendant.[259] They found that at higher pH the sulfonamide arm coordinates to the metal centre, enhancing the Eu(III) emission. Furthermore, the variation in the sulfonyl nitrogen basicity can be controlled using different *p*-substituents, thus the *p*-CF_3 europium complex gave a pK_a of 5.7 while the *p*-Me/*p*-OMe analogues offered values of 6.4 and 6.7 respectively (Fig. 6.2). The Eu(III) luminescence, especially the hypersensitive transition $\Delta J = 2$ (wavelength at ~ 616 nm), can give mirror titration curve results to Gd(III) relaxivity using the same ligand under the same conditions.[260]

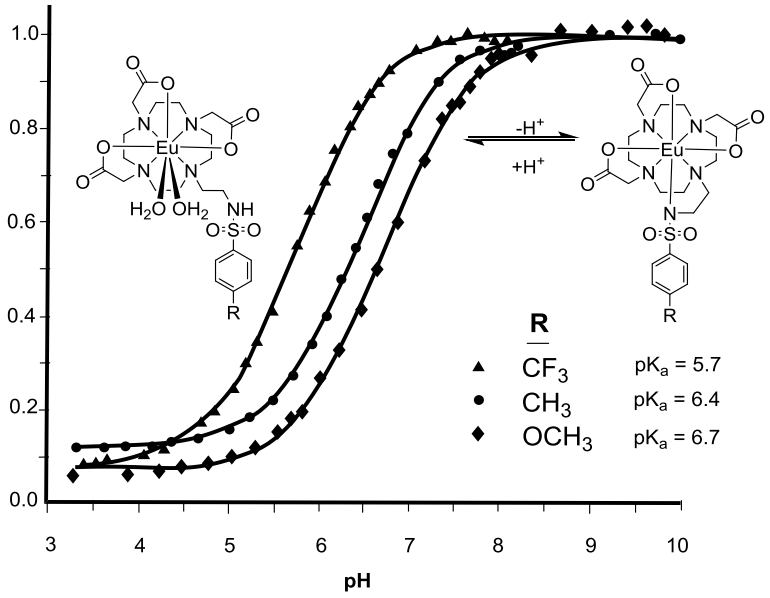

Figure 6.2: Eu(III) (I/I_o) emission intensities vs. pH for para-substuated aryl sulfonamide complexes.[259]

In vivo, via MRI methods, using low molecular weight (550−600 Da) GdBCAs, such as DO3A or DTPA-BMA that show high BBBP, can play a vital role in monitoring the physiological pH.[261] The specifications for pH-ratiometric agents, are similar to those of first generation contrast agents, they have to be nontoxic, kinetically stable, relatively cheap and should exhibit reversible detection when environmental conditions change from being acidic to basic, and vice versa; in addition, it needs to exhibit particularly high $[H]^+$ sensitivity, with pK_a values in the acidic range.[260]

Sulfonamides are used in the synthesis of a wide range of pharmaceutical compounds, especially in antibacterial and diuretic drugs.[262] They have variable nitrogen protonation ranges depending on the substituent, such as electron withdrawing groups, heteroatoms and groups with resonance; for example, $F_3CSO_2NH_2$ and $H_3CSO_2NH_2$ have pK_a values for the amine proton of 6.3 and 17.5, respectively, in H_2O.[263]

In terms of a pH-dependent alkylsulfonamide moiety, Parker and Pal investigated this pendant with different macrocycle ligands under various conditions.[264, 265] They synthesised three ligands **83**, **84** and **85** (Fig. 6.3), followed by coordination with various lanthanides.

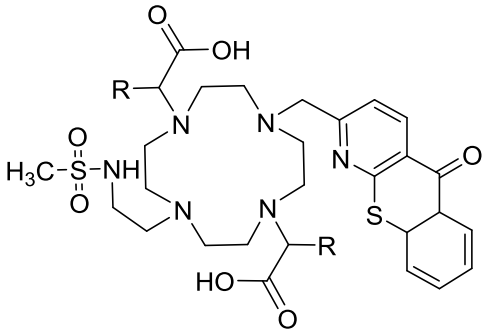

83 = R= H
84= R = $CH_2CH_2CO_2H$
85 = R = $CH_2CH_2CH_2CO_2H$

Figure 6.3: N-sulfonamide ligands.

It has been found these complexes display different pK_a values with high affinities to biological ions, even with **Eu(84)** and **Eu(85)** that possess negative charge at higher pH values. This is due to the low free energy of hydration and the complexes' hydrophilicity, as shown in Table 6.1.

Complex	Log *K* Lactate pH 5.5	Log *K* Citrate pH 7.4	Log *K* Bicarbonate pH = 7.4	pK_a
Eu(83)	3.50(0.06)	4.59(0.05)	1.97(0.03)	6.1
Eu(84)	3.86(0.02)	<1	2.15(0.02)	7.6
Eu(85)	4.09(0.08)	<1	2.75(0.02)	6.2

Table 6.1: Summary of log anion binding affinity constants and pK_a values for Eu**83**-**85**, at the stated pH (0.1 M NaCl, 295 K).

Europium complexes with **(84)** and **(85)** show no citrate affinity due to both electrostatic repulsion and the steric hindrance around the Eu(III) ion. Fig. 6.4 shows an **Eu(85)** titration *vs.* pH to calculate the pk_a by converting the complex from q = 1 at low pH to q = 0 at pH > 7. Additionally, **Eu(83)** exhibits a protein affinity (HSA) with a binding constant of log K = 4.46, with 1:1 binding at pH 7.4. This higher affinity is related to the interaction of the aryl groups with binding IIa site in the protein.

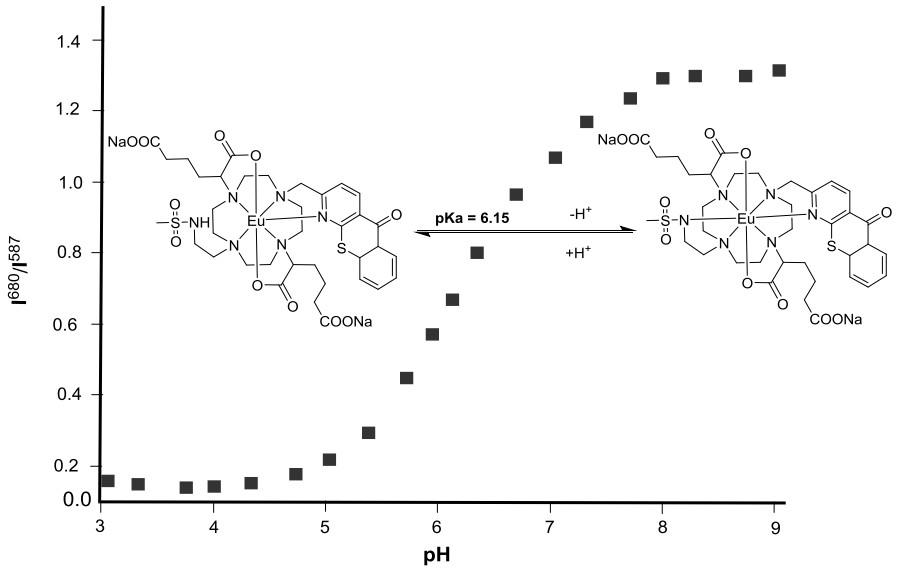

Figure 6.4: Reverse intensity ration vs. pH plot of **Eu(85)**.[264]

Herein, the interest was in the synthesis of a reversible responsive CA towards biological pH, by using an N-sulfonamide pendant to DO3A. This agent has been synthesised with Eu(III) / Gd(III) ions, purified by RP-HPLC and characterized by MS, NMR spectroscopy and fluorescence spectroscopy, the molecular weight of the probe was made as low as possible to encourage permeability of the disrupted BBB . The pK_a values for these complexes have been measured by mapping the europium emission and r_1 relaxivity in gadolinium complexes *vs.* pH. Phantom imaging to map T_1 at different pH values was undertaken for eight **GdL8** samples. Additionally, **GdL8** was tested *in vivo* by simulating cerebral stroke conditions in rat brains to ensure the BBBP, localisation and the action of this agent.

6.2 Synthesis of Ligand and Complexes

The preparation of the initial target ligand, **H_3L8**, was proceeded by reacting aziridine **24** with ^{t}BuDO3A as shown in Scheme 6.1. The aziridine was synthesized following the work of Chen *et al.*[266] Due to low m.p. of **24,** it can be easily decomposed, therefore it is cautiously isolated and concentrated to give a yellow solid with an 88% yield. It was characterized by ^{1}H NMR spectroscopy and shows a singlet at δ = 2.3 related to CH_3 and a broad singlet at δ = 2.2 related to two carbon atoms with an integration of 4H. Additionally, X-ray crystallography gives the compound formation and the structure (see Appendix, Fig. 10.14). Then **24** was

reacted in a 1:1.2 ratio with **^{t}BuDO3A** to give the protected ligand **56**. The latter was hydrolysed by TFA to give the pro-ligand **H_3L8** as a white solid with 47% yield after RP-HPLC using method A, detecting at wavelength 214 nm. **H_3L8** was characterized by NMR spectroscopy which gives characteristic ^{1}H NMR singlet peak for the CH_3 group at 3.78 ppm and MS (ESI) a peak *m/z* = of 468 $[M+H]^{+}$. The Eu(III)/Gd(III) complexes were obtained by reacting **H_3L8** with the appropriate $LnCl_3.6H_2O$ at pH = 5.5 (Scheme 6.1) to give MS (ESI) showing *m/z* = 618 $[M+H]^{+}$, 616 $[M-H]^{-}$ for ^{153}**EuL8** and 642 $[M+H]^{+}$, 643 $[M-H]^{-}$ for ^{158}**GdL8** with characteristic isotope patterns. The final complexes were purified by RP-HPLC to ensure the absence of free Ln(III) using method B, Xylenol orange tests were also used to conform this.

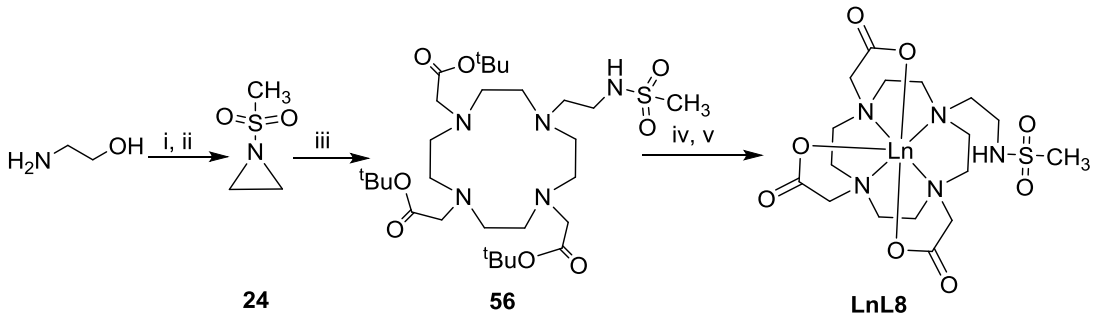

Scheme 6.1: **Reagents and conditions:** i) MsCl, Py, 0 °C; ii) K_2CO_3, MeCN, rt; iii) ^{t}BuDO3A, K_2CO_3, MeCN; iv) DCM: TFA; v) $Ln(III)Cl_3.6H_2O$.

6.3 pH Dependence of ^{1}H NMR Relaxometry Gd(III) and Emission Eu(III) of **LnL8**.

The pK_a of **L8** depends on coordination of N-sulfonamide pendant to Ln(III) metal centre as seen in Fig. 6.5, which was derived from both **EuL8** emission and r_1 measurements of **GdL8** over a series of pH values.

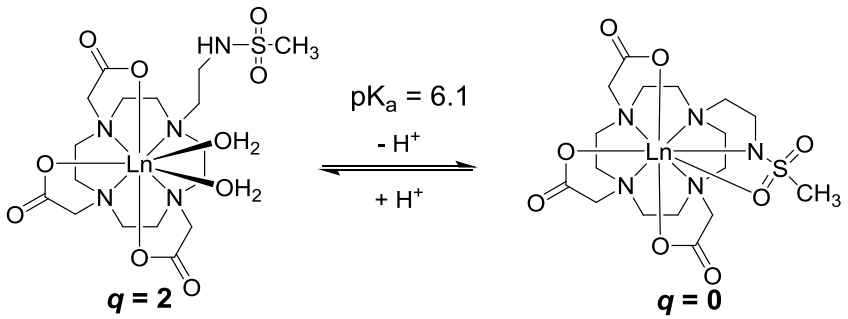

Figure 6.5: changing the coordination régime of **LnL8** in acidic and base condition.

Profound changes in the form and intensity of the Eu emission spectra in **EuL8** were seen when moving from a basic to an acidic environment, especially with the hypersensitive Δ J = 2 and Δ J = 4 transitions (Fig. 6.6). This is related to the coordination of the ligand **L8** being transformed from being heptadentate at low pH to a deprotonated nonadentate regime at higher pH.[267]

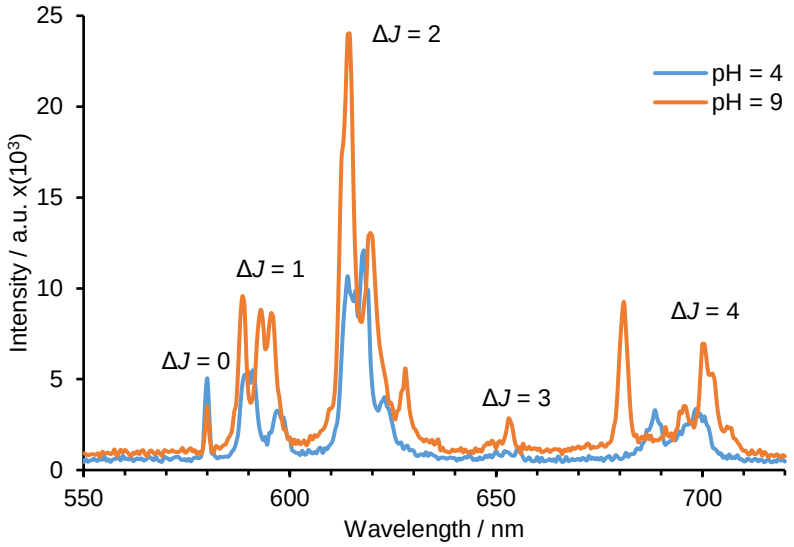

Figure 6.6: **EuL8** emission spectra at pH 4 and 9 (λ_{ex} = 395 nm, 298 K, H_2O, I = 0.1 M NaCl).

The peak Δ J = 2 at 614 nm was monitored from pH 3 → 9 and fit to a pKa ~ 6.1 as depicted in Fig. 6.7. This is promising with respect to operating in the pH range of the ischemic brain. Independent measurements of the excited state lifetime for **EuL8** were evaluated. The hydration number at pH 9 and 3 (λ_{exc} = 395, λ_{em} 615; 298 K) are reported in Table 6.2. The results of the titration and the lifetime measurements are consistent with the hypothesis that the complex has a hydration state q = 2.0 at pH 4 while q = 0.1 at pH 8. This suggests that at higher pH the *N*-sulfonamide moiety is deprotonated and coordinated to the metal centre while at low pH decomplexation was occurred leads to recoordinate the Ln(III) with two water molecules as depicted in Fig. 6.5.

	pH/pD 4			*pH/pD 8*		
	k_{H_2O}/ms^{-1}	k_{D_2O}/ms^{-1}	$q(\pm 0.2)$	k_{H_2O}/ms^{-1}	k_{D_2O}/ms^{-1}	$q(\pm 0.2)$
EuL8	2.52	0.55	2.0	1.11	0.72	0.1

Table 6.2: Rate constants k and hydration states q, for decay of **EuL8** at limiting pH values (λ_{ex} = 392 nm and λ_{em} = 615 nm (295 *K*, I = 0.1 M NaCl).

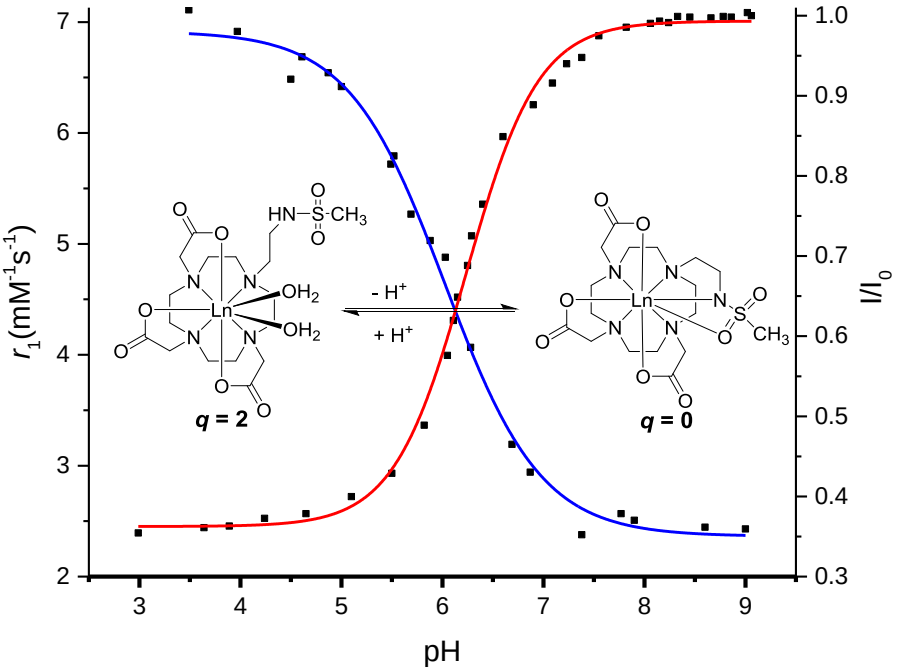

Figure 6.7: Correlation of the pH-dependent relaxivity of **GdL8** (blue line) [1 mM complex, 400 MHz, 40 mM HEPES, 0.1 NaCl, 298 K] and **EuL8** luminescence (red line) [0.1 M NaCl, 0.1 M PIPES, 30 mM $NaHCO_3$, 2.3 mM Na lactate, 0.13 mM Na citrate, 0.9 mM NaH_2PO_4; λ_{exc} = 392 nm, λ_{em} = 614 nm 295K].

In emission assessment, it was necessary to add positive and negative charged ions to the solution such as Na, Cl^-, HCO_3^- and PO_4^{3-} to create an electrically neutral solution that mimics extracellular concentrations. In measuring Gd(III) relaxivity carbonate and citrate must be avoided due to high affinity of these negative ions to coordinate to Gd(III) ion at high pH. However, r_1 was measured in presence of HCO_3^- to show no interference can be observed at pH < 7.0.

In addition the relaxivity of 0.1 mM **GdL8** complex was recorded (400 MHz, 9.4 T, 298 K) *vs.* pH in over the range 3.5 → 9. At lower pH, the limiting relaxivity was of the order of 7 mM^{-1}s^{-1}, falling to a value of 2.4 mM^{-1}s^{-1} at pH 9 as shown in Fig. 6.7. These relaxivity values are typical of a q = 2 and q = 0 Gd(III) complexes at 400 MHz.[239] This reveals that the complexes **EuL8** and **GdL8** show mirror behaviour with respect to the pH dependence of emission intensity (Eu) and relaxivity (Gd), with a comparable pK_a of 6.1. When the sulfonamide is coordinated and q≃ 0, Eu(III) emission is enhanced by the absence of quenching waters, whereas this lack of inner-sphere water leads to a low relaxivity for the Gd complex. On protonation of the sulfonamide, coordination of two waters quenches the Eu(III) luminescence, but 'switches on' the Gd relaxivity. These results strongly suggest that the mechanism

of action of **LnL8** is as depicted in Fig 6.5. This pK_a value is promising in terms of detecting pH change in the brain after stroke as this would be expected to happen somewhere in this critical range, *i.e.* Fig. 6.7 shows a significant change in r_1 53% between pH 7.4 and 6.1, (2.01 mM^{-1} s^{-1} and 4.26 mM^{-1} s^{-1} respectively) the range between healthy and ischaemic brain tissue.

Unlike the complex reported by Amie (DO3A-NHTosyl),[267] this work deals with an aliphatic N-sulfonamide appendant (DO3A-NHMesyl), which means greater stability, due to the nitrogen of the aliphatic sulfonamide having higher basicity than nitrogen of the aromatic one, therefore **L8** has stronger metal-ligand interaction (*i.e.*, when the deprotonated N^- donor atom is coordinated).[268] Additionally, lower molecular weight and reduced affinity for binding with HSA.[269] Furthermore, **GdL8** exhibits large increases in r_1 values of about 50% from 7.0 → 6.0 pH, this will give the opportunity to detect cell acidity with great contrast performance.

An MRI phantom investigation upon **GdL8** was performed using a 9.4 T (400 MHz) MRI scanner, in callboration with Dr Mike Kelly (university of Leicester Core Biotechnology Services). The phantom images are T_1 maps with each voxel colour reflecting variation in the relaxation time of samples. As the pH of vessels that contain **GdL8** increased, there was a prominent increase in the MR signals as revealed by the increasing brightness. The T_1 map in Fig. 6.8 shows longer T_1 values with brighter colours while shorter T_1 values have darker colours. This is the opposite to how we normally visualise images, *i.e.* it is providing a T_1 map *cf.* an intensity map.

The linearity between T_1 *vs.* pH implies that **GdL8** complex has the predicted T_1 response over the expected ischaemic stroke pH range which could be used later to measure the pH of the brain *in vivo* after stroke. Eight pH phantoms were constructed over the expected ischaemic stroke pH range (6.0 to 7.4 in steps of 0.2) using PIPES buffer 0.1 M with a 1mM concentration as seen in Fig. 6.8-A, T_1 maps for the eight phantoms are inlaid to give a visual representation. T_1 and pH were found to be highly correlated ($R^2 = 0.942$) and absolute T_1 values (Fig. 6.8-B) were in good agreement with r_1 values in Fig. 6.7, as measured by ^1H NMR spectroscopy (400 MHz, 9.4 T). Control samples were scanned (pH buffer topped up with water instead

of contrast agent) concomitantly with sample vessels to prove the functionality of **GdL8** and to quantify pH change.

The pH values of these samples were measured again after seven days to ensure that the pH had remained stable in each eppendorf vessel during and after the phantom imaging, and was in the same range for all samples. Additionally, these specimens were tested with xylenol orange to ensure no "free" Gd(III) was present. These tests demonstrated the stability of the complex at different pH values, and the values of T_1 be seen to be related to pH.

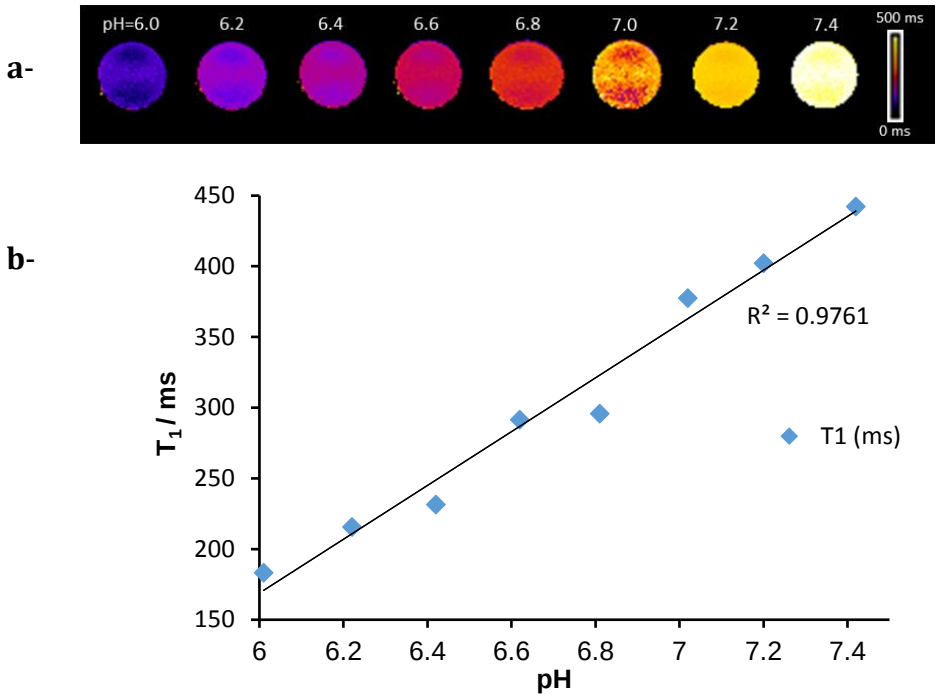

Figure 6.8: T_1-weighted image of eight microfuge tubes filled with **GdL8** samples at different pH (0.1 mM, 400 MHz, 9.4 T, 298 K).

At the conclusion of the MR protocol, Fig 6.8 shows promising results in terms of detecting the change in T_1 *vs* pH in the range 6.0 - 7.4, from which it can be interpreted that **GdL8** can detect changes over a biologically relevant pH range. For instance, the relaxation time reduces form 442.2 ms to 231.5 ms when the pH decreases from 7.42 to 6.42 that means 92% enhancing in relaxation rate, R_1 over one pH unit change.

6.4 Preclinical Studies

The following experiment was designed to test the reliability of **GdL8** for use in detecting the change in the brain pH based upon a change in relaxation time after ischemic stroke. The study was conducted using three rats out of four (one had a brain haemorrhage) that had being given an induced stroke, 0.5 M **GdL8** in PBS was injected via an intravenous (IV) route after 4 hours.[270] T_1 maps of the brains were measured for all before, and four hours post stroke. Contrast agent was injected after 4 hours in an attempt to exploit the permeability of the BBB post stroke. Animal models of focal cerebral ischemia in which middle cerebral artery occlusion (MCAO) is used can reproduce the pattern of ischemic brain damage observed in many human ischemic stroke patients. In this regard, rat MCAO has been used since 1975 due to the similarity to the human clinical setting.[271] Therefore, for preliminary data, *in vivo* assays are needed to examine the toxicity, CA efficacy and biodistribution.

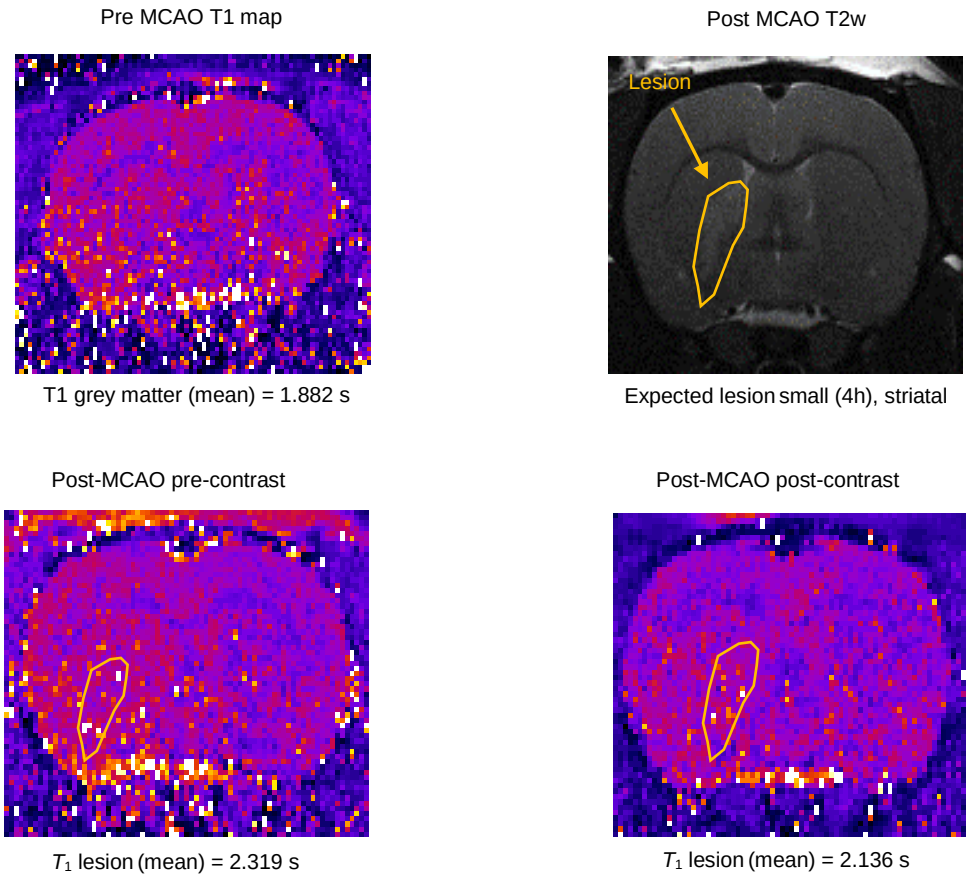

Figure 6.9: MR T_1 mapping and T2W of rat brain before and after 3.5 and 4.0 h MCA occlucsion (400 MHz, 9.4 T, 298 K).

The histochemical mapping of T_1 and T_2-weighted spin-echo images reveal that after injecting 0.5 M (0.2 mmol kg^{-1}) of the pH sensor, it penetrates to the brain with good BBBP. The localization and function of the dye was confirmed by comparing the results of T_1 between the four rats pre and post-MCAO which shows that **GdL8** has been diffused and localised in grey matter (Fig. 6.9). The response of the contrast agent was very promising as seen in Fig. 6.10, where it can be seen that there was a noticeable change in T_1 of the brain after 4 hours due to the presence of **GdL8** and presumably a significant propotion of q = 2 form is shaped from the increase in acidity after stroke. The T_1 mapping after 3.5 h post-MCA occlusion (without **GdL8**) indicates a lowering of the brain pH was occurred, more than 23% reduction in relaxation rate was seen (Fig. 6.9), this indicates that the brain is recovering and LA is declining. [272]

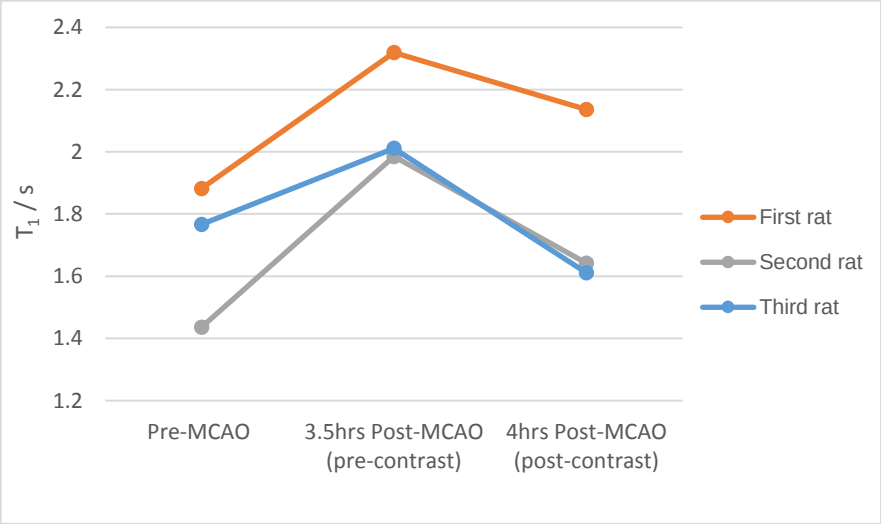

Figure 6.10: monitring T_1 before and after the stroke.

While after 4 h post-MCA occlusion (with **GdL8**), the T_1 for the contralateral MCA territory is less than that obtained in the absence of contrast agent, this is related to the action of the CA (high r_1 at low pH). These data indicate that **GdL8** accurately reflects pathophysiologic changes induced by acute cerebral ischemia with efficient BBBP and warrants further an investigation and optimisation.

6.5 Summary and Conclusions:

Macrocyclic Eu(III) and Gd(III) complexes based on DO3A have been prepared showing apparent protonation constant, log K_a, of 6.1 in which the intermolecular ligation of a methylsulfonamide nitrogen is rendered pH-dependent, giving rise to a change in the hydration state at the lanthanide centre. For **GdL8** it has been observed that the amplification of the relaxivity is approximately doubled between pH 7.4 and 6.1 at 298 K, 400 MHz over a pH range of 3-9, consistent with the mapping of T_1 at same pH values in the MR scanner during phantom imaging (400 MHz, 9.4 T). Pre-clinical experimentation proceeded with three rats given induced ischemic stroke, where it was found that **GdL8** has promising BBBP properties with an excellent T_1 changes with variations in brain pH after acute cerebral ischemia.

Chapter 7
Conclusions and Future Direction

7.1 General Conclusions

This thesis reported the research into the synthesis of dual modality imaging agents that have the potential to act as both MRI and optical contrast agents, and could also target cellular function. It was accomplished by synthesising compounds that have the capability to encapsulate a lanthanide metal ion and have further functionality for the attachment of optical dyes. The physical properties and localisation *in vitro* were then investigated for the resulting multi-modality imaging agents. Additionally, a pH responsive MRI CA has been synthesised and investigated *in vivo*.

Chapter 2 discussed the preparation of a series of ligands based on DO3A chelators appended with phenyl triazole, phenylpyridine, acetylide or pyridyl triazole derivative. These edifices were used to synthesise Ln(III)-complexes, the resulting monometallic complexes were characterised by HRMS (ESI), NMR and FTIR spectroscopy. The use of THF solvent in Sonogashira cross coupling increased the reaction yield; it was also found that pyridines substituted with electron releasing groups need higher temperature in this reaction *cf.* electron withdrawing groups. The synthesis of pyta and phta arms were successfully synthesised using (1:3) ratio (H_2O:MeOH, 1:3) solvent system. Reacting DO3A with 4-bromo-1-butyne does not form the desired molecule, an alternative method involved first reacting cyclen with 4-bromo-1-butyne, then the product treated with three equiv. of tert-butyl bromoacetate to give **(57)**. RP-HPLC was shown to be an efficient technique for purifying the pro-ligands and complexes.

Chapter 3 presented the synthesis of the dual-modality imaging agents, where optical dyes consist of Ir(III) and Pt(II) linked with mono or mulit-Gd-DO3A chelator derivatives as CA. These heterometallic architecture were investigated by luminescence and relaxivity measurements. In terms of photophysical properties, cyclometallated **PtGdL10** showed ~ double the mission lifetime (907 ns) *cf.* iridium complexes in aerated aqueous solution due to the rigidity of the square plainer architecture. While **Ir(ppy)$_2$GdL1** exhibits better chemical stability and double the

quantum yield value with Φ = 0.15 *cf*. **PtGdL10**. Ir(III) complexes with phenyl pyridine showed red shifted excitation and emission spectra *cf.* phenyl triazole analogues. Grafting the ancillary ligands with a CF_3 moiety led to a shift in the excitation spectrum of 73 nm to the red region, on the other hand, OMe just led to narrowing of the excitation spectrum. A Ru(II) complexes were not emissive with pyta ligands even with tuning ^{3}MLCT energy levels, because of the depopulation of the excited state from radiationless ^{3}MC transition level. **Ir(ppy)$_2$GdL1** showed the ability to be excited by two photon absorption in confocal microscopy within λ_{ex} 850 nm used to image acute cerebral brain slices.

Chapter 4 discussed the preparation of fluorescent dyes based on specific heterometallic Re(I)-Eu(III) architecture as carbonate responsive luminescent probes as a result of changeable Eu(III) emission intensity. Development of Re-Eu optical dyes can be used as carbonate responsive agents which indicate the level of carbonates via elevation of Eu(III) emission intensity at 616 nm. The **RepyEuL1** showed high HCO_3^- binding affinity log K = 2.33, in addition, modifying the pyta ligand with CF_3 moieties lead to a red shift in Re(I) emission and significant increasing in τ and Φ, while with OMe just shifting in the excitation spectrum was occurred.

Chapter 5 reported the synthesis of complexes with multiple-Ln(III) chelators linked by either Fe(II) or Co(III). These homomultimeric complexes with q = 2 were intended to an increase in relaxation rate, for instance trimer-gadolinium complexes **FeGdL1** and **CoGdL1** showed almost three folds higher r_1 *cf.* mono-gadolinium analogue **GdL1**.

Chapter 6 demonstrated the ability of DO3A based chelators to work as pH responsive agents after incorporation of a N-sulfonamide arm. The response for [H^+] was examined by emission, relaxivity and phantom imaging at 400 MHz (9.4 T, 298 K); the localisation/enhancement of contrast in the brain was also investigated *in vivo*. The emission and the relaxation time were recorded for the Eu(III) and Gd(III) complexes of **L8** at a range of pH, both values showed pK_a = 6.1. **GdL8** demonstrated *in vivo*, the ability to penetrate through BBB after brain stroke and the relaxation rate increased as result of acidic conditions.

7.2 Future direction

7.2.1 *Modification of the pyta Ligand for Rhenium(I)*

The synthetic route to the core structure has been established, so it remains to build around the core to investigate the effects of altering or adding to the pyta ligand since it is more stable than tapy. The major drawback of the pyta ligand system is that because of the higher energy of the LUMO, the MLCT absorption is blue-shifted in comparison with complexes of the bipyridine (bpy) ligand, so it cannot be excited at longer wavelengths as efficiently. Another problem with pyta is its high sensitivity to aqueous solvent, which quenches Re(I) photoluminescence (gives a low quantum yield).

Hence, it is important to synthesise Re(I) complexes with excitation maxima at 405 nm (a common light source for confocal microscopy). It is clear that the pyta precursors in this work have excellent emission profiles in the visible region; however, the excitation was to slightly higher energy than is otherwise acceptable in confocal microscopy. Therefore, future work should focus on shifting the excitation further to longer wavelength. This can be achieved by adding aromatic substituents to the pyridine pyta. Quinolinyl triazole (quinta) ligands can shift the MLCT band to the red with regards to excitation wavelength, and show a higher quantum yield compared to analogous pyta ligands.[153] This can be accomplished by reacting 2-haloquinolines with trimethylsilylacetylene through Sonogashira cross coupling followed click chemistry (Azide-Alkyne Cycloaddition) to synthesise the functional diimine ligands of this type (Scheme 7.1).

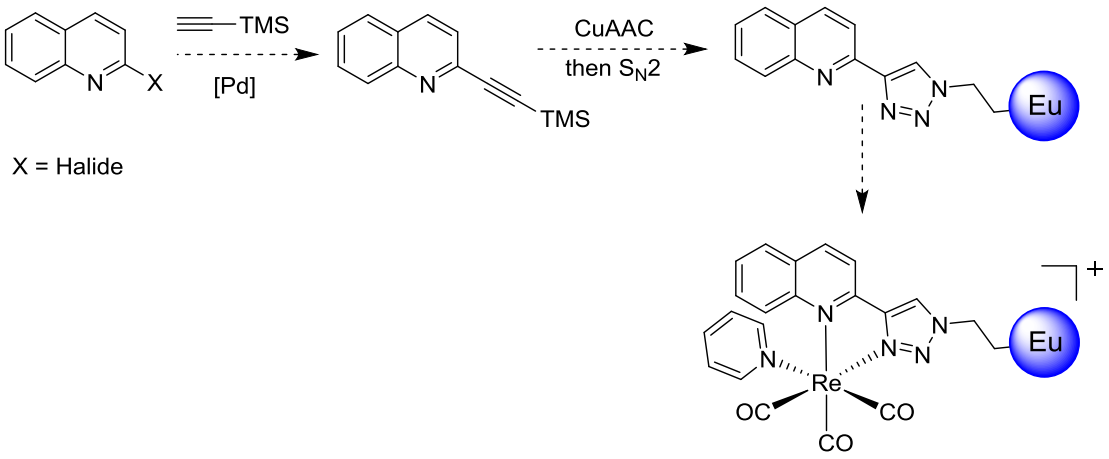

Figure 7.1: Potential synthetic routes to the quinta ligand and its Re(I)-Eu(III) complex.

A recent study showed that the substitution of pyta with triphenylamine-substituted 2-pyridyl-1,2,3-triazole (TPA-pytri) gives a red-shifted MLCT absorption band and brighter emission for analogous complexes.[273] These new 2-pyridyl-1,2,3-triazole (TPA-pytri) ligands could be easily synthesised from 4-(Diphenylamino)phenylboronic acid and 5-bromopyridin-TMS followed by palladium(0)-catalysed Suzuki cross coupling. Finally, The TPA-pytri ligand was generated one-pot in situ azide formation-click conditions (Scheme 7.2).

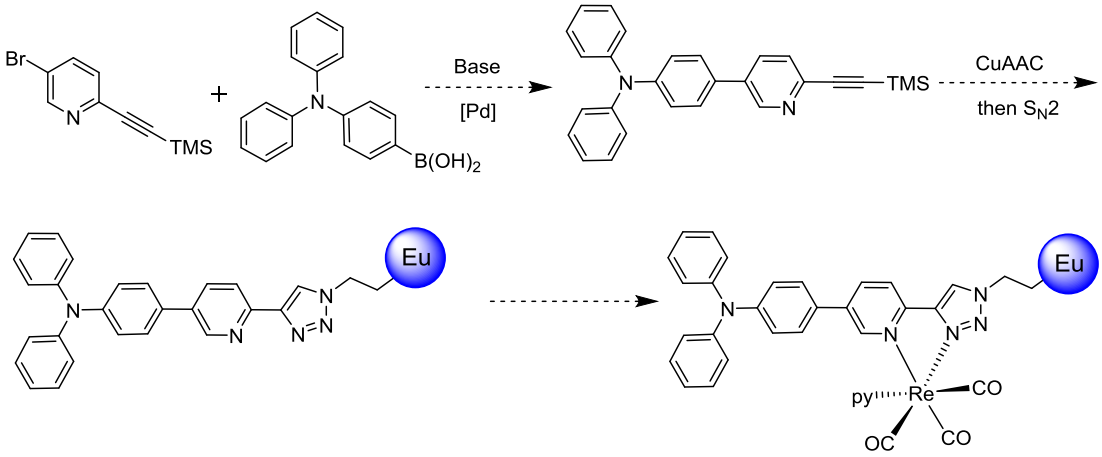

Figure 7.2: Potential route to triphenylamine-substituted 2-pyridyl-1,2,3-triazole Re(I)-Eu(III) complex.

In terms of investigating the ancillary ligand in $[Re(CO)_3(N^N)L]$ architectures, the substitution of a halide (Cl, Br) with an alkynyl ligand can result in bathochromic shifting in both the emission and the excitation spectrum.[274] For example, the carboxaldehyde alkynyl moiety will raise the energies of the metal-centred *d–d* states, thus improving the ability to populate the emissive MLCT state. The electron-withdrawing carboxaldehyde group will, in a practical sense, lead to a red-shifted emission spectrum *cf.* the same complex with electron-rich trialkoxyphenylalkynyls,[275] suggestive of a degree of mixing of alkynyl-to-diimine ligand-to-ligand charge transfer LLCT [π(C≡CR)→π*/(diimine)] character in the structureless emission band (Scheme 7.3).

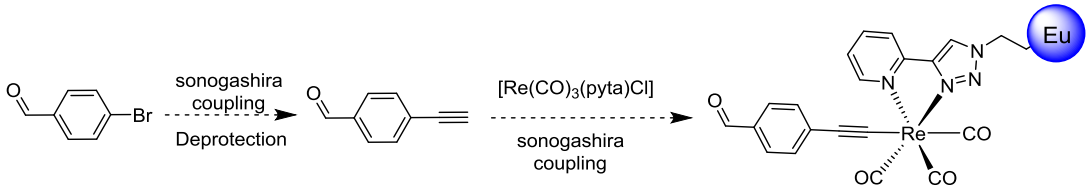

Figure 7.3: Potential route to carboxaldehyde alkynyl-substituted pyta ligand.

Another route can be followed by using DO3A with a 1-butyne pendant; in this instance different Re(I) polyamine ligands (N^N) can be used, for example bpy, tapy and phen (Scheme 7.4). This substitution gives the opportunity to use ligands other than pyta, especially as the latter induces a blue shift in both the excitation and emission spectrum and is further characterised by a short lifetime and low quantum yield.

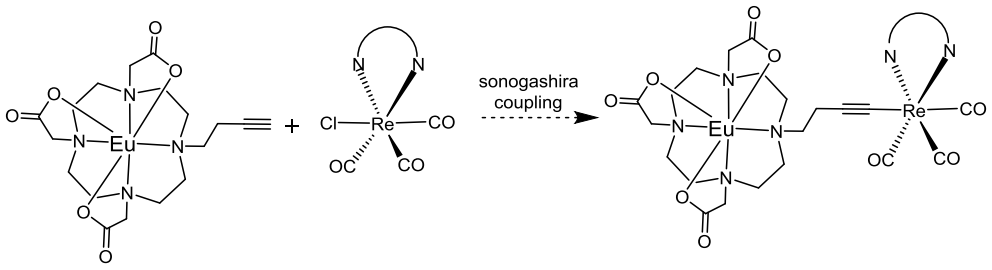

Figure 7.4: potential route to DO3A alkynyl-substituted N^N ligands.

7.2.2 *Iridium(III) and Platinum(II)*

It is also possible to tune the electronic absorbance of iridium(III) complexes by altering the substituents on the cyclometallated ligands (C^N) or the ancillary ligand (N^N) in order to shift the emission.[276] At a fundamental level, it would be interesting to establish the effects of substitution of various electron-withdrawing groups around the pyta ligand to optimise the Ir(III) photoluminesence, such as with SO_3H, COCl, and C≡N. The substitution of electron-releasing groups, such as OMe, CH_3, and $C(CH_3)_3$ onto the phenyl pyridine ligand would be expected to shift the excitation to the red by at least 50 nm so as to be suitable for single photon excitation and two-photon excitation (Fig. 7.5).

Neutral iridium hetroleptic complexes can be synthesised by breaking the Ir(III) phta dimer with ppy ligand. It has been found that *fac*-Ir(III) with two cyclometallated phta ligands with one ppy ligand shows interesting photophysical properties in the NIR region.[277] In these complexes, the HOMO is localised on the Ir(III) and phenyl ring of ppy while the LUMO is localised on the ppy itself. Therefore, the MLCT and LLCT emission/absorption can be tuned by substituting an EDG onto the phenyl of ppy. A high-pressure mercury lamp (200 W) can be used for the photoisomerisation of the *mer* to the *fac* isomers (Scheme 7.1).

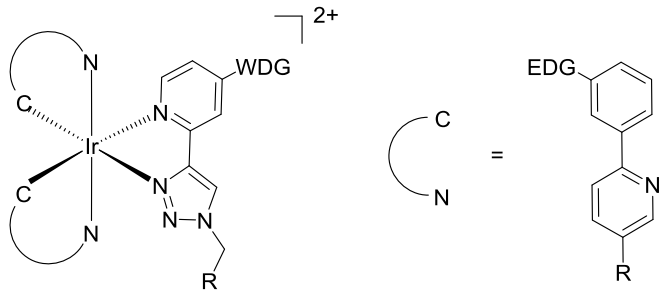

Figure 7.5: the route for substitution In Ir(III) complexes.

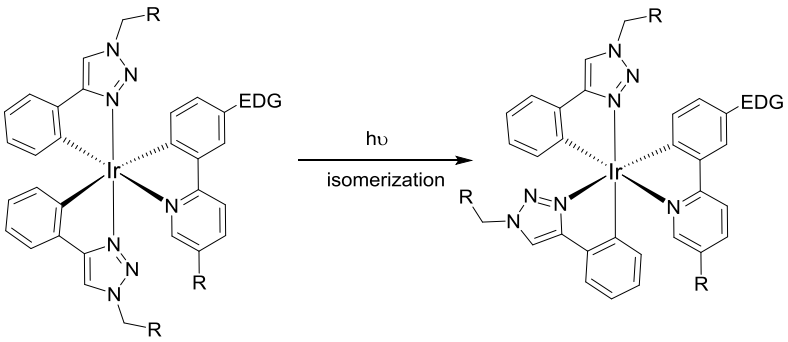

Scheme 7.1: The proposed *fac*-Ir(III) complexes.

These neutral Ir(III) complexes seem to be vital in terms of Ln(III) toxicity, because of their inefficient cellular internalisation.[278] Since these complexes are more suitable in use as extracellular imaging probes, they would be more reliable in use as extracellular dual-mode agents.

The Pt(N^C^N) complex is generally used in two-photon absorption microscopy due to the large energies required to achieve photoexcitation. Since the HOMO in this complex has about 48% (N^C^N) character, tuning the absorption by substituting electron-donating groups into the phenyl ring has a considerable impact on the resultant excitation spectra. Thus, introducing groups such as OMe, NH_2, CH_2CH_2Cl and $C(CH_3)_3$ may result in bathochromic shifting in the absorption, with an increase in the lifetime of the emission (Fig 7.6).[279, 280]

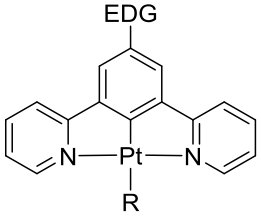

Figure 7.6: the platinum complex structure with electron-releasing group.

7.2.3 *Cell Receptor-Targeted Imaging Probes*

The key issues are those of enhancing the selectivity and accumulation of these imaging agents in *e.g.* tumorous tissue. Enhancements include decreasing both the amount of drug that needs to be administered and the reduction in potential toxicity to normal tissue. The cancerous tissue can be addressed by attaching cancer-cell delivery vehicles to the imaging probes such as polyamine, the tetraethylammonium cation and glutathione (GSH). It is well established that an increase in intracellular polyamine concentration, correlates with increased cell proliferation and tumourigenesis.[281] Glutathione (GSH) is an important natural antioxidant compound that consists of the three amino acids L-cysteine, L-glutamic acid, and glycine. It has been found that GSH levels are significantly higher in tumour cells, for instance in bone marrow, breast, colon, larynx and lung cancers than in normal cells.[282] Finally, the amphiphilic cationic moieties can target the low-density lipoprotein cancer cell membrane, which have the potential to represent a milestone in bio-imaging. The triphenylphosphonium unit has a higher affinity for mitochondria, and therefore can target both normal and cancerous cells.[283] Based on the above mentioned, synthesis of specific biological imaging agents requires targeting agents that are able to cross the mitochondrial, cell membrane or accumulate within the cancer matrix. For instance, these targeting agents can be attached to pyta or pyridine ligands in Re(I) complexes or to the phenyl ring in Pt(II) complex (Fig. 7.7).

7.2.4 *MRI pH Sensor*

In terms of investigating the coordination and the role of the N-sulfonamide arm as pH sensor in **GdL8** complex, a control probe can be synthesised by substation the proton on the N-sulfonamide by methyl group (Fig. 7.8). This will prove the functionality and sensitivity of amide proton for ligation with Gd(III) metal centre at various pH values. Because, in the presence of the methylated nitrogen there will be no coordination to the metal centre, ultimately the complex lucks pH responsive functionality.

Another modification can be made, by exchange of the methyl with CF_3 group as seen in Fig. 7.9. This substitution on the sulfonyl group will lead to shift the pK_a of

N-sulfonamide further to the acidic region, in this case it can be used to monitor/image low extracellular pH abnormalities.[284] It will be expected this be unresponsive in the range pH 6.1–7.4.

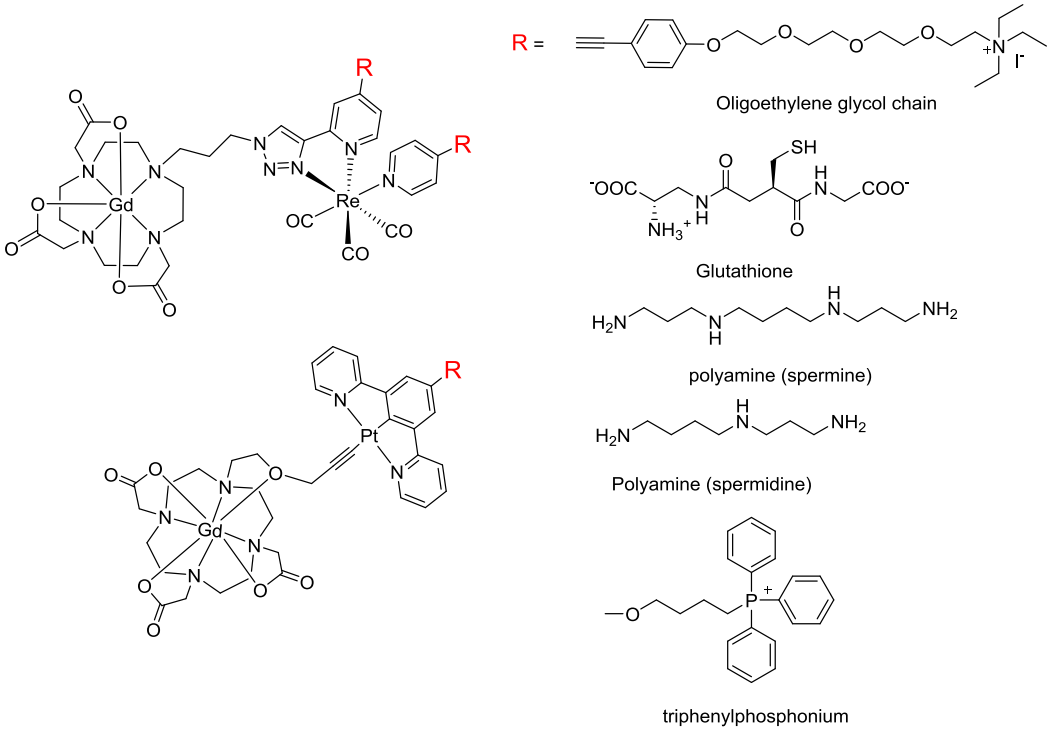

Figure 7.7: proposed targeting agents.

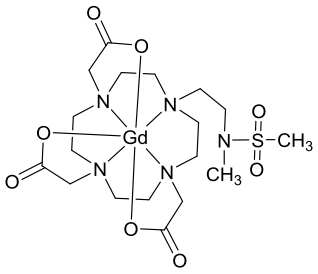

Figure 7.8: Control MRI pH sensor.

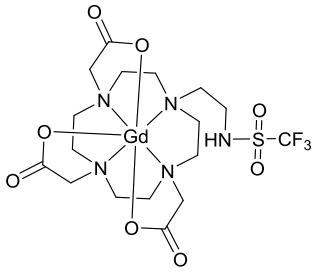

Figure 7.9: MRI pH sensor with CF_3.

Chapter 8

Experimental

8.1 Materials and Methods

8.1.1 *Reagents*

All reagents and solvents were obtained commercially and used without further purification with the exception of: triethylamine, which was distilled over potassium hydroxide and stored over potassium hydroxide pellets, tetrahydrofuran was dried and distilled over sodium benzophenone. Acetonitrile was dried using an Innovative Technology inc. PureSolv solvent purification system.

8.1.2 *Chromatography*

Analytical TLC was run on aluminium-backed silica or neutral alumina plates with a fluorescence indicator at 254 nm, preparative flash column chromatography was performed with silica gel 60 (230-400 mesh) or neutral activated Brockmann I grade alumina (150 mesh).

Analytical and preparative HPLC was performed on a ThermoFisher Ultimate 3000 system with Chromeleon software on Phenomenex Luna C18 column. Methods employed are as follows: Method A (A = 0.1% TFA in H_2O, B = 0.1% TFA in MeCN) 5% B for 5 min, 5-50% B over 30 min, 100% B for 5 min, 100-5% B for 2 min, 5% B for 5 min. Method B (A = H_2O, B = MeCN) 5% B for 5 min, 5-50% B over 30 min, 50-100% B for 5 min, 100-5% B for 2 min, 5% B for 5 min.

8.1.3 *Spectroscopy*

Mass spectra were recorded on a Micromass Quatro LC spectrometer (electrospray), a Kratos Concept 1H spectrometer (FAB, 3-nitrobenzyl alcohol was used as the matrix), high resolution mass spectrometry was performed on a Water Acquity XEVO Q ToF machine and are measured in *m/z*. Electronic absorption spectra were recorded on a Shimadzu UV 180 spectrometer using 10 × 10 mm quartz Hellma cuvettes with spectra recorded 1 nm resolution.

MALD-TOF spectra were recorded following this procedure. The sample was mixed 1:1 with a 10 mg/ml solution of α-cyano-4-hydroxycinnamic acid or 2′,4′,6′-

trihydroxyacetophenone monohydrate and 0.5 μL spotted onto a stainless steel target plate. Analysis of complexes was carried out on a Voyager DE-STR MALDI-TOF mass spectrometer (Applied Biosystems, university of Leicester, UK) in positive ion reflection mode.

Luminescence Spectroscopy

Luminescence data was recorded using a Jobin Yvon Horiba FluoroMax-P spectrometer (using DataMax for Windows v2.2). Samples were held in a 10 x 10 mm quartz Hellma cuvette and a cut-off filter (typically 450 nm) was used to avoid second-order diffraction effects. Excitation and emission slits were typically 5:1 nm for Eu(III) emission spectra. Excitation and emission slits for transition metals were 3:3 nm with a 1.0 s integration time.

Quantum yield was measured following comparative methods.[233] Quinine sulfate 0.1M H_2SO_4 or $Ru(bpy)_3Cl_2$ were used as standards for photoluminescence quantum yield. Five dilute solutions from both the standard and the sample were prepared depending on the absorbance wavelengths (0.1, 0.08, 0.06, 0.04, 0.02). After determining the integrated fluorescence intensity at the same λ_{ex} and solvent for all solvents, a graph of the integrated fluorescence intensity *vs*. absorbance was plotted. The quantum yield was found according to Equ. (32) after calculating the gradient of the graphs.

$$\Phi_X = \Phi_{ST}\left(\frac{Grad_X}{Grad_{ST}}\right) \quad (32)$$

Lifetimes were measured using a Jobin Yvon Horiba FluoroLog 3 exciting at 372 nm monitoring the emission at 500 nm or 550 nm with a bandwidth of 10 nm (Re) or 1.5 nm (Ir). The bandwidth of the excitation laser was determined by Rayleigh scattered light from a suspension of Ludox. The data was binned into channels of 0.59 ns.

Dye loading into rat brain cells was achieved by incubating the desired concentration of conjugate for the desired time in F12-K media and excited using a UV laser diode at 850 nm (50 mW). Images were taken using an Olympus Scan^R/Cell^R widefield microscope at 20x or 60x magnification or an Olympus FV1000 laser scanning

confocal microscope using a 430/25 emission filter. This was in collaboration with Dr Vincenzo Marra (Department of Neuroscience, Psychology and Behaviour).

8.1.4 *Hydration State, q, Determination*

Excited state lifetimes of Eu(III) complexes were measured by excitation at different wavelengths (as stated), or 395 nm direct excitation of the Eu(III) complex has no antenna using a Jobin Yvon Horiba FluoroMax-P spectrometer in a 10 × 10 mm quartz Hellma cuvette. A short 40 ms pulse of light (500 pulses per point) is followed by monitoring the integrated intensity of light (ΔJ = 2) emitted during a fixed gate time of 0.1 ms, at a delay time later. Delay times were set at 0.1 ms intervals, covering 4 or more lifetimes. Excitation and emission slits were set to 5:1 nm. The data was then applied to the standard first order decay Equ. 33, minimised in terms of k by iterative least-square fitting operation in Graphpad prism 7, where I_{obs} is the observed intensity, I_o is the initial intensity of the excited state Eu(III) and t is the time (ms).[285]

$$I_{obs} = I_o e^{-kt} + offset \tag{33}$$

8.1.5 *T_1 Relaxation and Concentration Determination*

The calculation of Gd relaxivity was determined using Evans' method.[286] The observed longitudinal water proton relaxation times (T_{1p}) were measured on a Bruker AV 400 NMR spectrometer operating at 400 MHz at 298 K. An inner co-axial capillary tube containing 1mM of the paramagnetic compound dissolved in H_2O was placed in a 5mm NMR sample tube containing D_2O. Both the D_2O solution and insert contained 10% *tert*-butyl alcohol. A standard inversion-recovery for 16 experiments sequence was used. The paramagnetic water proton relaxation rate, R_{1p} and relaxivity, r_1 were determined using Eqns 34 - 37 where 0.38 is the diamagnetic contribution of the bulk water molecules.

$$M_z = M_o\left(1 - 2Ae^{(-t/T_1)}\right) \tag{34}$$

$$R_1 = \frac{1}{T_1} \tag{35}$$

$$R_{1p} = R_1 - 0.38 \tag{36}$$

$$r_{1p} = \frac{R_{1p}}{[Gd]} \tag{37}$$

8.1.6 *pH Titrations*

pH measurements were recorded using a Jenway 3510 pH meter with a BDH probe, model 309-1025-02 calibrated at pH 4, 7 and 10. Both luminescence and relaxivity pH titrations were carried out in a background of constant ionic strength (I = 0.1 NaCl, 298 K). Aqueous solutions were made basic by addition of 1 M or 0.1 M NaOH and titrated to acid pH by addition of small aliquots of 1 M or 0.1 M HCl.

8.1.7 *Xylenol Orange*

Xylenol orange is used as a metal ion indicator for the lanthanides. Metal ion coordination occurs through both the iminodiacetic moiety and the phenolic hydroxyl group, resulting in its deprotonation. The presence of metal ions has, therefore, the same resulting colour change effects as variation of pH. When the solutions are buffered to pH 5, colour changes to purple can be entirely attributed to the presence of free lanthanides in solution.

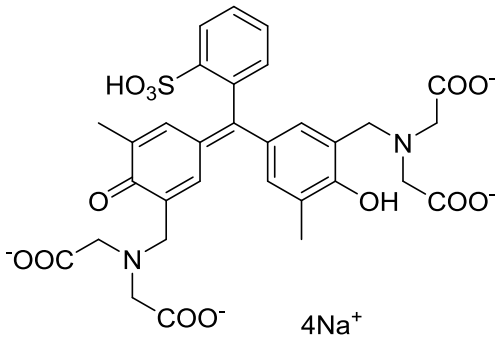

Xylenol Orange

8.1.8 *MRI Phantom Studies at 9.4 T MRI Scanner*

MRI phantom experiments were performed using a 9.4 T (400 MHz) MRI scanner by Dr Mike Kelly (Core Biotechnology Servies). Samples were measured in a 1.6 mL eppendorf vessel at eight different pH values with a final concentration of **GdL8** of 1 mM using 0.1 M PIPES as buffer solution. Water was used as a control.

8.1.9 *The methodology for preparing the eppendorf tubes for phantom imaging*

Each eppendorf was prepared by adding 80 µL of **GdL8** at a concentration of 20 mM to 1.52 mL of 0.1 M PIPES giving a final volume of 1.6 mL and a 1 mM concentration of the complex. While, the blank (control) solutions were prepared by the addition of 80 µL water to 1.52 mL of the buffer solution (Table 8.1).

pH	0.1M PIPES (blanks).	GdL8 (1 mM) in 0.1M PIPES	pH of the samples (GdL8) after 1 week
6.01	1A	1B	5.63
6.22	2A	2B	5.26
6.42	3A	3B	6.45
6.62	4A	4B	6.68
6.81	5A	5B	6.86
7.02	6A	6B	7.08
7.20	7A	7B	7.25
7.42	8A	8B	7.47

Table 8.1: The pH of phantoms samples.

8.2 Synthesis of Macrocyclic Compounds

8.2.1 *1,4,7-Tris(tertbutoxycarbonylmethyl)-1,4,7,10 tetraazacyclododecane. Hydrobromide (^{t}BuDO3A.HBr)*[287]

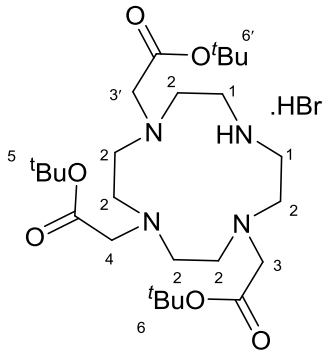

Tert-Butylbromo acetate (7.00 g, 35.89 mmol) in N,N-dimethylacetamide (20 mL) was added dropwise over 30 m to a stirred suspension of 1,4,7,10-tetraazacyclododecane (cyclen) (2.00 g, 11.61 mmol) and sodium acetate (3.00 g,

36.57 mmol) in N,N-dimethylacetamide (20 mL) at ~ 0 °C. After the last addition the reaction was allowed to warm to rt. After stirring for 5 d, the white slurry was poured out in warm aq. solution ~ 60 °C (200 mL) containing KBr (1.3 g, 11.6 mmol) to give a clear yellow solution. **(^{t}BuDO3A)** starts to precipitate at pH 9 by addition aq. $NaHCO_3$. After stirring for 4 h at room the title compound was afford as a white powder (5.32 g, 77%), m.p. 189-190 ^{o}C (lit[288] m.p. 190-191 °C) which was used without further purification. NMR δ_H (500 MHz, $CDCl_3$, Me_4Si) 9.99 (s br, 2H, HBr, NH), 3.35 (s, 4H, 3-CH_2), 3.27 (s, 2H, 4-CH_2), 3.08 (s br, 4H, 1-CH_2), 2.8- 3.03 (m, 12H, 2-CH_2), 1.44 (s, 18H, 6-CH_3), 1.43 (s, 9H, 5-CH_3); NMR δ_C (125 MHz, $CDCl_3$, Me_4Si) 170.5, 169.6 (C=O), 81.8, 81.6 (C_q), 58.1(3-C), 51.3, 51.2, 49.1, 47.5 (CH_2), 48.7 (4-C), 28.1, 28.2 (CH_3); IR (neat)ν_{max}/cm^{-1} 3478 (N-H), 2937 (C-H), 1718 (C=O); MS (ESI) 515 $[M+H]^+$; HRMS (ESI) $C_{26}H_{51}N_4O_6$ $[M+H]^+$ requires 515.3823 found 515.3809.

8.2.2 *1-(But-3-yn-1-yl)-1,4,7,10-tetraazacyclododecane (22)*

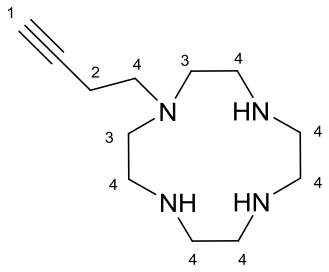

Cyclen (0.518 g, 3.00 mmol), 4-Bromo-1-butyne (0.100 g, 0.75 mmol) and Et_3N (417 µL, 3.0 mmol) were suspended in dry $CHCl_3$ (15 mL) and heated at reflux for 20 h. The mixture was washed with 1 N NaOH (3 x 10 mL), then with water (10 mL). The organic layer was dried over $MgSO_4$, filtered and concentrated to afford the product as a colourless oil (74 mg, 44%). The aqueous layer was neutralised with 1 M HCl and extracted with EtOAc to recover the excess of cyclen. NMR δ_H (400 MHz, $CDCl_3$, Me_4Si) 3.00 (s br, 3H, NH), 2.74-2.67 (br m, 4H, 3-CH_2), 2.63-2.46 (m, 14H, 4-CH_2), 2.27 (td, 2H, ^3J = 6.9, ^4J = 2.5, 2-CH_2), 1.91 (t, 1H, J = 2.5, 1-CH); NMR δ_C (100 MHz, $CDCl_3$, Me_4Si) 68.1 (1-C), 51.7, 51.1, 46.6, 44.7 (CH_2), 16.4 (2-C); MS (ESI) 226 $[M+H]^+$; HRMS (ESI) $C_{12}H_{25}N_4$ $[M+H]^+$ requires 225.2079 found 225.2083.

8.3 Synthesis of Aziridine

8.3.1 *2-[(methanesulfonyl)amino]ethyl methanesulfonate (23)*[266]

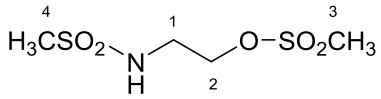

Ethanolamine (4.96 mL, 82.0 mmol) in pyridine (10 mL) was added dropwise over 20 min to methanesulfonyl chloride (13.3 mL, 164 mmol) in pyridine (20 mL) at ~ 0 °C and left to stir for 3 h. The reaction mixture was extracted with (brine: 10% citric acid 2:1) (2 x 50 mL). The aqueous layers were combined and extracted with EtOAc (6 x 50 mL). The organic layers were combined and washed with brine (50 mL), dried over ($MgSO_4$), filtered and concentrated to afford the title compound as a white solid (15.3 g, 86%), m.p. 49-50 °C. NMR δ_H (400 MHz, $CDCl_3$, Me_4Si) 5.29 (t, 1H, *J* = 5.9, NH), 4.34 (t, 2H, *J* = 5.0, 2-CH_2), 3.48 (q, 2H, *J* = 5.0, 1-CH_2), 3.08 (s, 3H, 3-CH_3), 3.01 (s, 3H, 4-CH_3); NMR δ_C (100 MHz, $CDCl_3$, Me_4Si) 68.8 (2-C), 42.3 (1-C), 40.8, 37.5 (CH_3); MS (ESI) 240 $[M+Na]^+$; HRMS (ESI) $C_4H_{12}NO_5S_2$ $[M+H]^+$ requires 218.0157 found 218.0161, $C_4H_{11}NO_5S_2Na$ $[M+Na]^+$ requires 239.9976 found 239.9980.

8.3.2 *Synthesis 1-(methylsulfonyl)aziridine (24)*[266]

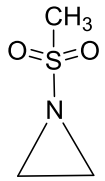

(23) (0.62 g, 2.86 mmol) and K_2CO_3 (0.6 g, 4.32 mmol) were suspended in MeCN (15 mL) and stirred for 20 h at rt, after which the reaction mixture was filtered through Celite®, washed with EtOAc then left to dry under pressure to give the title compound as a yellow solid (0.3 g, 87%). NMR δ_H (500 MHz, $CDCl_3$) 2.94 (s, 3H, CH_3), 2.22 (s, 4H, CH_2); NMR δ_C (125 MHz, $CDCl_3$) 39.1 (CH_3), 26.7 (CH_2); MS (ESI) 122 $[M+H]^+$, 144 $[M+Na]^+$; HRMS (ESI) $C_3H_8NO_2S$ $[M+H]^+$ requires 122.0276 found 122.0278. This compound further characterised by X-ray crystallography as shown in Fig. 10.12.

8.4 Synthesis 2-Phenylpyridine

8.4.1 *[(4-Bromophenyl)methoxy](tert-butyl)dimethylsilane (25)*

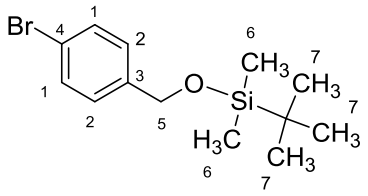

Imidazole (0.36 g, 5.3 mmol), 4-Bromobenzyl alcohol (0.50 g, 2.7 mmol) and *tert*-butyldimethylsilyl chloride (TBDMS-Cl) (0.61 g, 4.04 mmol) were dissolved in dry DMF (1 mL). The reaction was stirred at room temperature and monitored by TLC analysis (R_f = 0.69, 20% EtOAc in hexane). After 20 h the reaction mixture was poured in water (5 mL) and extracted with Et_2O (10 mL x 3). The combined organic layers were dried over $MgSO_4$, filtered and concentrated. The crude residue was purified with normal phase chromatography SiO_2 (10% EtOAc in hexane) to give the title compound as a clear colourless oil (0.66 g, 83%). NMR δ_H (400 MHz, $CDCl_3$) 7.32 (d, 2H, *J* = 8.5, 1-CH), 7.07 (d, 2H, *J* = 8.5, 2-CH), 4.56 (s, 2H, 5-CH_2), 0.84 (s, 9H, 7-CH_3), 0.2 (s, 6H, 6-CH_3); NMR δ_C (100 MHz, $CDCl_3$) 140.5 (3-C), 131.2 (1-C), 127.6 (2-C), 120.6 (4-C), 64.3 (5-C), 25.8, 0.0 (CH_3), 18.3 (C_q); MS (ESI) 301 $[M+H]^+$; HRMS (ESI) $C_{13}H_{20}O^{28}Si^{79}Br$ $[M+H]^+$ requires 299.0467 found 299.0461, $C_{13}H_{20}O^{28}Si^{81}Br$ $[M+H]^+$ requires 301.0446 found 301.0460.

8.4.2 *2-[4-(((tert-butyldimethylsilyl)oxy)methyl)phenyl]pyridine (26)*

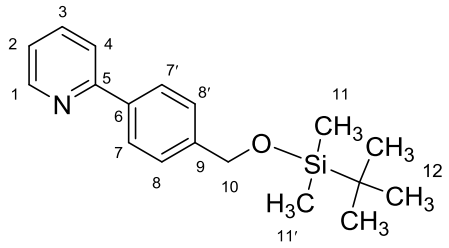

A dry Schlenck tube was evacuated and flushed with Ar (x 3). This was loaded with $Pd(PPh_3)_4$ (0.33 g, 0.3 mmol), **(25)** (1.75 g, 5.8 mmol), 2-tributylstannylpyridine (2.57 g, 6.98 mmol) and dry toluene (10 mL). The reaction was heated in dark at 110 °C for 48 h with monitoring by TLC analysis (R_f = 0.48, 20% EtOAc in hexane). After filtration, the crude residue was purified with normal phase chromatography SiO_2 (hexane: Et_2O 4:1) to give the title compound as a white

solid (0.81 g, 46%), m.p. 66-67 °C. NMR δ_H (400 MHz, $CDCl_3$) 8.69 (ddd, 1H, ^3J = 6.2, ^4J = 1.5, ^5J = 1.1, 1-CH), 7.97 (d, 2H, J= 8.4, 7-CH), 7.64-7.59 (m, 2H, 3,4-CH), 7.31 (d, 2H, J = 8.4, 8-CH), 7.09 (ddd, 1H, ^3J = 6.2,4.8, ^4J = 2.3, 2-CH), 4.81 (s, 2H, 10-CH_2), 0.96 (s, 9H, 12-CH_3), 0.12 (s, 6H, 11-CH_3); NMR δ_C (100 MHz, $CDCl_3$) 157.4 (5-C), 149.6 (1-C), 142.3 (9-C), 138 (6-C), 136.6, 120.3 (4,3-C), 126.7 (7-C), 126.4 (8-C), 120.3 (2-C), 64.7 (10-C), 25.9, 0.0 (CH_3), 18.4 (C_q); MS (ESI) 300, 301 $[M+H]^+$; HRMS (ESI) $C_{18}H_{26}NO^{28}Si$ $[M+H]^+$ requires 300.1784 found 300.1786.

8.4.3 *[4-(pyridin-2-yl)phenyl]methanol (27)*

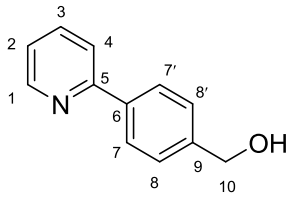

(26) (0.50 g, 1.7 mmol) was dissolved in (60% AcOH: 20% H_2O: 20% THF) (7 mL) and stirred at room temperature. After 48 h the TLC analysis (R_f = 0.05, 2.5 % EtOAc in hexane) shows the compound was fully deprotected. The crude residue was purified with normal phase chromatography SiO_2 (100% EtOAc) to give the title compound as a white solid (0.3 g, 97%). NMR δ_H (400 MHz, $CDCl_3$) 8.66 (ddd, 1H, ^3J = 4.9, ^4J = 1.7, ^5J = 1.0, 1-CH), 7.9 (d, 2H, J = 8.4, 7-CH), 7.76-7.67 (m, 2H, 3,4-CH), 7.4 (d, 2H, J = 8.4, 8-CH), 7.22 (ddd, 1H, ^3J = 7, 4.9, ^4J = 1.4, 2-CH), 4.71 (s, 2H, 10-CH_2), 2.97 (s br, 1H, OH); NMR δ_C (100 MHz, $CDCl_3$) 157.2 (5-C), 149.5 (1-C), 141.9 (9-C), 138.3 (6-C), 136.8, 120.6 (3,4-C), 127.0, 127.1 (8, 7-C), 122 (2-C), 64.6 (10-C); MS (ESI) 186 $[M+H]^+$; HRMS (ESI) $C_{12}H_{12}NO$ $[M+H]^+$ requires 186.0919 found 186.0928.

8.5 Synthesis of Pyridyl-alkynes (Sonogashira cross-coupling)

8.5.1 *5-(Trifluoromethyl)-2-[(trimethylsilyl)ethynyl] pyridine (28)*

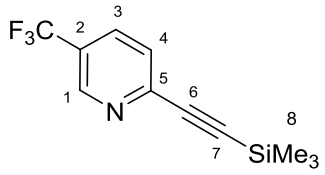

2-Bromo-5-(trifluoromethyl) pyridine (0.50 g, 2.21 mmol), $Pd(PPh_3)_2Cl_2$ (31.0 mg, 40.0 µmol) and CuI (10.0 mg, 50.0 µmol), THF (10 mL) and (TEA) (2 mL) were charged to Schlenck tube. After evacuating and flushing with N_2 (x 3), TMS-acetylene

(0.40 g, 4.08 mmol) were added portion-wise and stirred at ambient temperature for 18 h. The consumption of the bromopyridine was monitored by TLC analysis (R_f = 0.65, 0.5% Ethyl acetate in hexane). The residue was purified by normal phase chromatography SiO_2 (EtOAc: hexane 1:25) to furnish the title compound as white solid (0.36 g, 67%). NMR δ_H (400 MHz, $CDCl_3$) 8.81 (s, 1H, 1-CH), 7.87 (dd, 1H, ^3J = 8.2, ^4J = 2.1, 3-CH), 7.54 (d, 1H, J = 8.2, 4-CH), 0.28 (s, 9H, 8-CH_3); NMR δ_C (100 MHz, $CDCl_3$) 146.7 (q, $^3J_{C\text{-}F}$= 12.7, 1-C), 146.8 (5-C), 133.7 (q, $^3J_{C\text{-}F}$ = 12.7, 3-C), 126.7 (4-C), 125.4 (q, $^2J_{C\text{-}F}$ = 33.5, 2-C), 123.2 (q, $^1J_{C\text{-}F}$ = 273.2, CF_3), 102.3 (6-C), 98.2 (7-C), 0.0 (8-C): NMR δ_F (376 MHz, $CDCl_3$) -62.6 (s); MS (ESI) 244 $[M+H]^+$; HRMS (ESI) $C_{11}H_{13}NF_3{}^{28}Si$ $[M+H]^+$ requires 244.0769 found 244.0764.

8.5.2 *4-(Trifluoromethyl)-2-[(trimethylsilyl)ethynyl]pyridine (29)*

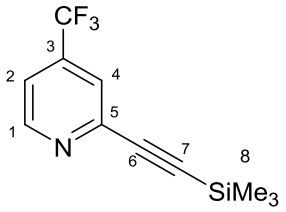

2-Chloro-4-(trifluoromethyl) pyridine (200 mg, 1.10 mmol), $Pd(PPh_3)_2Cl_2$ (38.0 mg, 50.0 μmol), PPh_3 (58.2 mg, 0.22 mmol) and CuI (11.1 mg, 58.28 mmol) were suspensioned with Et_3N (5 mL) and THF (5 mL) in dry Schlenck tube. After evacuation/flushing with N_2 (x 3), TMS-acetylene (141 mg, 1.43 mmol) was added dropwise. The yellow suspension was heated at 90 °C with monitoring by TLC analysis (R_f = 0.24, DCM: hexane 3:7). After 8 h, the yellow residue was purified by normal phase chromatography SiO_2 (hexane: DCM 1:1) to give the title compound as a yellowish oil (140 mg, 52%). NMR δ_H (400 MHz, $CDCl_3$, Me_4Si) 8.76 (d, 1H, J = 5.1, 1-CH), 7.65 (d, 1H, J = 1.0, 4-CH), 7.44 (dd, 1H, ^3J = 5.1, ^4J = 0.9, 2-CH), 0.29 (s, 9H, 8-CH_3); NMR δ_C (125 MHz, $CDCl_3$, Me_4Si) 150.8 (1-C), 144.2 (5-C), 138.6 (q, $^2J_{C\text{-}F}$ = 34.3, 3-C), 123.3 (q, $^3J_{C\text{-}F}$ = 13.2, 4-C), 139.1 (q, $^1J_{C\text{-}F}$ = 273.5, CF_3), 118.8 (q, $^3J_{C\text{-}F}$ = 13.2, 2-C), 102.8 (6-C), 97.7 (7-C), 0.3 (8-C); NMR δ_F (376 MHz, $CDCl_3$, Me_4Si) -65.0 (s); MS (ESI) 244 $[M+H]^+$; HRMS (ESI) $C_{11}H_{13}NF_3{}^{28}Si$ $[M+H]^+$ requires 244.0769 found 244.0768.

8.5.3 *2,6-Bis[(trimethylsilyl)ethynyl]pyridine (30)*

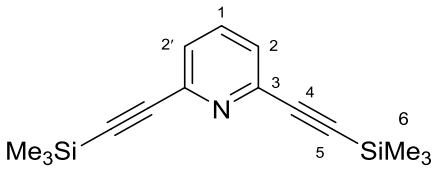

To a degassed Schlenck tube was added 2,6-dibromo pyridine (1.00 g, 4.22 mmol), CuI (16.2 mg, 85.0 μmol), $Pd(PPh_3)_4$ (97.3 mg, 84.2 μmol), THF (8 mL) and DIPA (8 mL). TMS-acetylene (1.05 g, 10.69 mmol) were added in course of 10 min after evacuation/flushing with N_2 (x 3). After heating at 50 °C for 48 h, the consumption of the halide was monitored by TLC analysis (R_f = 0.55, hexane: EtOAc 4:1). After filtration, the yellow residue was purified by normal phase chromatography SiO_2 (hexane:DCM 1:1) to give the title compound as a white solid (0.81 g, 71%). NMR δ_H (400 MHz, $CDCl_3$) 7.58 (t, 1H, *J* = 7.5, 1-CH), 7.38 (d, 2H, *J* = 7.5, 2-CH), 0.25 (s, 18H, 6-CH_3); NMR δ_C (100 MHz, $CDCl_3$) 143.2 (3-C), 136.1 (1-C), 126.4 (2-C), 103 (4-C), 95.3 (5-C), 0.2 (6-C); MS (ESI) 272 $[M+H]^+$; HRMS (ESI) $C_{15}H_{22}N^{28}Si_2$ $[M+H]^+$ requires 272.1291 found 272.1293.

8.5.4 *4-Methoxy-2-((trimethylsilyl)ethynyl)pyridine (31)*

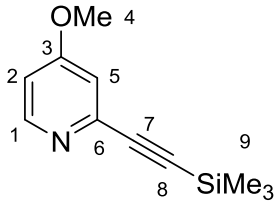

To a degassed Schlenck tube was added 2-Chloro-4-methoxypyridine (500.1 mg, 3.48 mmol), $Pd(PPh_3)_2Cl_2$ (74.3 mg, 0.10 mmol), PPh_3 (91.1 mg, 0.34 mmol), CuI (20.0 mg, 0.10 mmol) and NEt_3:DMF (3:1) 8 mL. After freeze-pump-thaw (x 3), TMS-acetylene (0.69 g, 7.02 mmol) was added drop wised followed by heating at 120 °C for 24 h. After which the reaction was treated with 0.1 M HCl (5 mL), extracted with DE (10 mL x 3) and purified using normal phase chromatography SiO_2 (DE:hexane 2:8). The title compound was isolated as yellow oil (0.36 g, 51%); NMR δ_H (400 MHz, $CDCl_3$) 8.31 (d, 1H, *J* = 5.8, 1-CH), 6.93 (d, 1H, *J* = 2.5, 5-CH), 6.71 (dd, 1H, ^3J = 5.8, ^4J = 2.5, 2-CH), 3.78 (s, 3H, 4-CH_3), 0.22 (s, 9H, 9-CH_3). NMR δ_C (100 MHz, $CDCl_3$) 165.4 (6-C), 150.9 (1-C), 144.1 (3-C), 112.8 (5-C), 109.7 (2-C), 103.6 (7-C), 94 (8-C), 55.1

(4-C), 0.0 (9-C). MS (ESI) 206, 207 $[M+H]^+$, 228, 229 $[M+Na]^+$; HRMS (ESI) $C_{11}H_{16}NO^{28}Si$ $[M+H]^+$ requires 206.1001 found 206.1003.

8.6 Synthesis of Triazoles Using Click Chemistry

Synthesis of 1,2,3 triazoles followed the general synthetic method:

A solution of 3-Bromo-1-propanol 1.1 eq. and sodium azide 1.2 eq. was heated at reflux at 90 °C in (MeOH: H_2O 3:1) (20 mL) for 18 h. The conversion of azide was monitored by TLC analysis EtOAc (100%), TLC plate was dipped in a 10% solution of PPh_3 in DCM this convert the azide to amine and then developed using ninhydrin stain. After cooling to room temperature, NaAsc, $CuSO_4.5H_2O$ and pyridyl-alkyne (0.2, 0.1, 1 equivalent respectively) were added, 1 eq. of K_2CO_3 is also added if the alkyne is protected with TMS. The resulting mixture was stirred under nitrogen at 70 °C. After 16 h saturated. aq. EDTA pH = 10 (10 mL) was added and extracted with EtOAc (3 x 50 mL). The combined organics were dried ($MgSO_4$), filtered and concentrated. The crude residue was subjected to normal phase chromatography SiO_2 (10% ethyl acetate in hexane).

8.6.1 *3-(4-(Pyridine-2-yl)-1H-1,2,3-triazol-1-yl)-propan-1-ol (32)*

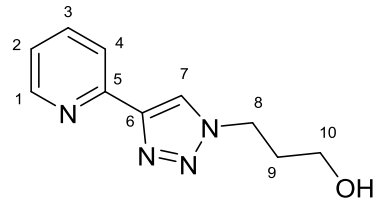

3-Bromo-1-propanol (1.46 g, 10.56 mmol), sodium azide (0.75 g, 11.65 mmol), 2-ethynyl pyridine (1.00 g, 9.69 mmol), $CuSO_4$ (154.6 mg, 0.96 mmol) and NaAsc (0.38 g, 1.93 mmol) were reacted. The title compound was obtained as light brown solid (1.7 g, 86%), m.p. 104-105 °C; NMR δ_H (500 MHz, $CDCl_3$, Me_4Si) 8.53 (ddd, 1H, ^3J = 4.8, ^4J = 1.6, ^5J = 0.8, 1-CH), 8.22 (s, 1H, 7-CH), 8.14 (ddd, 1H, ^3J = 7.7, ^4J = 0.8, ^5J = 0.7, 4-CH), 7.75 (ddd, 1H, ^3J = 7.9, 7.7, ^4J = 1.6, 3-CH), 7.20 (ddd, 1H, ^3J = 7.4, 4.8, ^4J = 1, 2-CH), 4.59 (t, 2H, J = 6.7, 8-CH_2), 3.71 (s br, 1H, OH), 3.67 (t, 2H, J = 5.7, 10-CH_2), 2.17 (quintet, 2H, J = 6.3, 9-CH_2); NMR δ_C (125 MHz, $CDCl_3$, Me_4Si) 150 (5-C), 149.1 (1-C), 147.9 (6-C), 137 (3-C), 122.9 (2-C), 122.6 (7-C), 120.3 (4-C), 58.3 (10-C),

47.1(8-C), 32.6(9-C). MS (ESI) 205 $[M+H]^+$, 227 $[M+Na]^+$; HRMS (ESI) $C_{10}H_{13}N_4O$ $[M+H]^+$ requires 205.1089 found 205.1082.

8.6.2 *3-(4-Phenyl-1H-1,2,3-triazol-1-yl)propan-1-ol (33)*

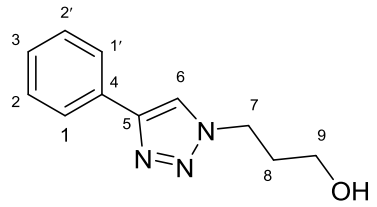

3-Bromo-1-propanol (0.98 g, 7.11 mmol), sodium azide (0.51 g, 7.89 mmol) in (THF: H_2O 4:1) (20 mL) were reacted. After that phenyl acetylene (0.66 g, 6.46 mmol), NaAsc (0.25 g, 1.26 mmol) and $CuSO_4$ (0.16 g, 0.65 mmol) were added. The title compound was obtained as white solid (0.82 g, 63%), m.p. 90-91 °C. NMR δ_H (400 MHz, $CDCl_3$, Me_4Si) 7.83-7.77 (m, 3H, 1,6-CH), 7.44-7.38 (m, 2H, 2-CH), 7.32 (tt, 1H, ^3J = 6.6, ^4J = 1.3, 3-CH), 4.55 (t, 2H, J = 6.6, 7-CH_2), 3.68 (q, 2H, J = 5.4, 9-CH_2), 2.75 (t, 1H, J = 4.8, OH), 2.16 (quintet, 2H, J = 6, 8-CH_2). NMR δ_C (100 MHz, $CDCl_3$, Me_4Si) 147.6 (4-C), 130.4 (5-C), 128.8, 128.2 (1,3-C), 125.6 (2-C), 120.2 (6-C), 58.6 (9-C), 47 (7-C), 32.6 (8-C); MS (ESI) 204 $[M+H]^+$; HRMS (ESI) $C_{11}H_{14}N_3O$ $[M+H]^+$ requires 204.1137 found 204.1127.

8.6.3 *3-{4-[4-(trifluoromethyl) pyridin-2-yl]-1H-1,2,3-triazol-1-yl}propan-1-ol (34)*

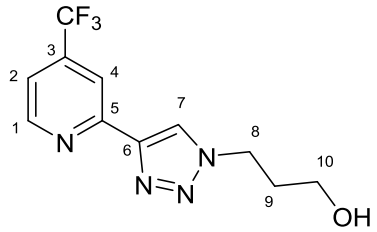

3-Bromo propanol (88.2 mg, 0.63 mmol) and sodium azide (45.0 mg, 0.69 mmol) were reacted. After that NaAsc (23.7 mg, 0.12 mmol), $CuSO_4$ (9.3 mg, 57.7 µmol) K_2CO_3 (95 mg, 0.676 mmol) and **(29)** (140.5 mg, 0.57 mmol) were added. The title compound was obtained as colourless oil (100 mg, 64%). NMR δ_H (500 MHz, $CDCl_3$) 8.67 (d, 1H, J = 5.1, 1-CH), 8.31 (s, 1H, 4-CH), 8.25 (s, 1H, 7-CH), 7.36 (d, 1H, J = 5.1, 2-CH), 4.59 (t, 2H, J = 6.7, 8-CH_2), 3.79 (s br, 1H, OH), 3.66 (t, 2H, J = 5.7, 10-CH_2), 2.17 (quintet, 2H, J = 5.9, 9-CH_2); NMR δ_C (125 MHz, $CDCl_3$) 151.3 (5-C), 150.2

(1-C), 149.8 (6-C), 139.2 (q, $^{2}J_{C\text{-}F}$ = 133.4, 3-C), 123.2 (7-C), 122.5 (q, $^{1}J_{C\text{-}F}$ = 272.5 , CF_3), 118.2 (q, $^{3}J_{C\text{-}F}$ = 12, 4-C), 115.9 (d, $^{3}J_{C\text{-}F}$ = 12, 2-C), 58.2 (10-C), 47.3 (8-C), 32.5 (9-C); NMR δ_F (376 MHz, $CDCl_3$) -64.9 (s); MS (ESI) 273 $[M+H]^+$, 295 $[M+Na]^+$; HRMS (ESI) $C_{11}H_{12}N_4OF_3$ $[M+H]^+$ requires 273.0963 found 273.0968.

8.6.4 *3-{4-[5-(trifluoromethyl)pyridin-2-yl]-1H-1,2,3-triazol-1-yl} propan-1-ol (35)*

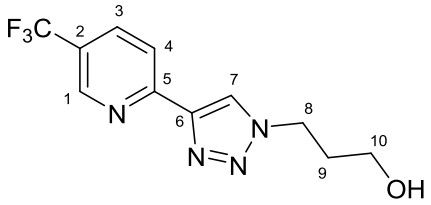

3-Bromo-1-propanol (0.26 g, 1.84 mmol) and sodium azide (0.13 g, 2.027 mmol) were reacted. After that **(28)** (0.41 g, 1.68 mmol), NaAsc (0.33 g, 0.39 mmol), $CuSO_4$ (26.8 mg, 0.16 mmol) and K_2CO_3 (0.2 g, 1.9 mmol) were added. The title compound was obtained as off-white solid (0.39 g, 87%), m.p. 79-80 ^{o}C. NMR δ_H (400 MHz, $CDCl_3$, Me_4Si) 8.78 (s, 1H, 1-CH), 8.3-8.24 (m, 2H, 4,7-CH), 8.01 (dd, 1H, ^{3}J = 8.2, ^{4}J = 1.7, 3-CH), 4.62 (t, 2H, J = 6.7, 8-CH_2), 3.71 (t, 2H, J = 5.3, 10-C), 3.06 (s br, 1H, OH), 2.20 (quintet, 2H, 9-CH_2); NMR δ_C (100 MHz, $CDCl_3$, Me_4Si) 153.3 (5-C), 147.0 (6-C), 146.3 (q, $^{3}J_{C\text{-}F}$ = 12.7, 1-C), 134.1 (q, $^{3}J_{C\text{-}F}$ = 12.7, 3-C), 125.4 (q, $^{2}J_{C\text{-}F}$ = 33.5, 2-C), 123.6 (7-C), 123.4 (q, ^{1}J = 273.2, CF_3), 119.6 (4-C), 58.4 (9-C), 47.2 (8-C), 32.5 (9-C); NMR δ_F (376 MHz, $CDCl_3$, Me_4Si) -62.3 (s); MS (ESI) 273 $[M+H]^+$, 295 $[M+Na]^+$; HRMS (ESI) $C_{11}H_{12}N_4OF_3$ $[M+H]^+$ requires 273.0963 found 273.0969.

8.6.5 *3-(4-(4-Methoxypyridin-2-yl)-1H-1,2,3-triazol-1-yl)propan-1-ol (36)*

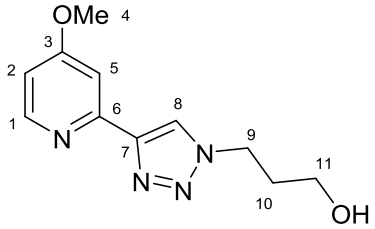

3-Bromo-1-propanol (0.27 g, 1.95 mmol), sodium azide (0.13 g, 2.14 mmol), **(31)** (0.36 g, 1.78 mmol), NaAsc (70.5 mg, 0.35 mmol), K_2CO_3 (247, 1.79 mmol) and $CuSO_4.5H_2O$ (28.4 mg, 0.17 mmol) were reacted. The title compound was obtained after column 10% MeOH:DCM as light brown solid (0.32 g, 76%). NMR δ_H (400 MHz,

$CDCl_3$) 8.31 (d, 1H, *J* = 5.8, 1-CH), 8.21 (s, 1H, 8-CH), 7.70 (d, 1H, *J* = 2.5, 5-CH), 6.74 (dd, 1H, ^3J = 5.8, ^4J = 2.5, 2-CH), 4.58 (t, 1H, *J* = 6.8, 9-CH_2), 3.9 (s, 3H, 11-CH_2, OH), 3.66 (t, 2H, *J* = 5.8, 11-CH_2), 2.16 (quintet, 2H, *J* = 6.2, 10-CH_2); NMR δ_C (125 MHz, $CDCl_3$) 166.5 (3-C), 151.7 (6-C), 150.1 (1-C), 147.8 (7-C), 122.7 (8-C), 110.1 (2-C), 105.2 (5-C), 58.1 (11-C), 55.3 (4-C), 47.0 (9-C), 32.5 (10-C); MS(ESI) 235 $[M+H]^+$, 257 $[M+Na]^+$; HRMS (ESI) $C_{11}H_{15}N_4O_2$ $[M+H]^+$ requires 235.1195 found 235.1196.

8.6.6 *2-(4-(3-Chloropropyl)-1H-1,2,3-triazol-1-yl)pyridine (37)*

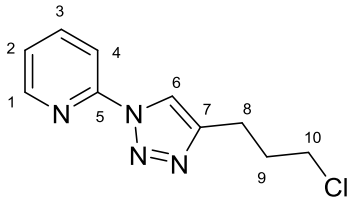

A dry Schlenck tube was loaded with 2-azidopyridine (0.10 g, 0.83 mmol), CuI (15.2 mg, 80.1 µmol) and toluene (5 mL). After evacuation/flushing with N_2 (x 3), 5-chloro-1-pentyne (125 mg, 1.21 mmol) was added and heated at 120 °C. The reaction was monitored by TLC (100% EtOAc) R_f = 0.79. After 72 h, the reaction mixture was filtered and purified by normal phase chromatography (EtOAc:hexan 7:3) to give the title compound as yellow oil (100 mg, 54%). NMR δ_H (400 MHz, $CDCl_3$, Me_4Si) 8.49 (ddd, 1H, ^3J = 4.9, ^4J = 1.8, ^5J = 0.9, 1-CH), 8.38 (s, 1H, 6-CH), 8.18 (ddd, 1H, ^3J = 8.2, ^4J = 1.0, ^5J = 0.9, 4-CH), 7.91 (ddd, 1H, ^3J = 9.3, 7.4, ^4J = 1.9, 3-CH), 7.34 (ddd, ^3J = 7.4, 4.9, ^4J = 0.9, 2-CH), 3.63 (t, 2H, *J* = 3.65, 8-CH_2), 3.00 (t, *J* = 7.24, 10-CH_2), 2.25 (quintet, 2H, *J* = 7.2, 9-CH_2); NMR δ_C (400 MHz, $CDCl_3$, Me_4Si) 149.3 (5-C), 148.5 (1-C), 146.8 (7-C), 139.1 (3-C), 123.3 (2-C), 118.6 (6-C), 113.7 (4-C), 44.0 (8-C), 31.7 (9-C), 22.7 (10-C); MS (ESI) 223, 225 $[M+H]^+$; HRMS (ESI) $C_{10}H_{12}N_4{}^{35}Cl$ $[M+H]^+$ requires 223.0750 found 223.0757, $C_{10}H_{12}N_4{}^{37}Cl$ $[M+H]^+$ requires 225.0721 found 225.0732.

8.6.7 *3-(4-{6-[3-(3-Hydroxypropyl)-3H-pyrazol-5-yl]pyridin-2-yl}-1H-1,2,3-triazol-1-yl)propan-1-ol (38)*

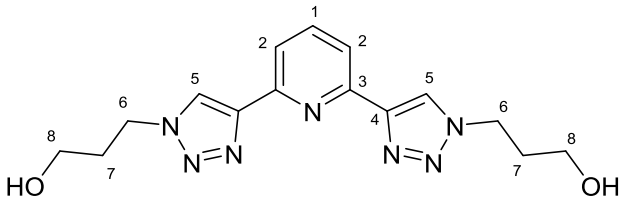

3-Bromo-1-propanol (0.45 g, 3.24 mmol) and sodium azide (0.11 g, 1.81 mmol) were reacted. After that NaAsc (59.8 mg, 0.30 mmol), $CuSO_4$ (0.07 g, 0.29 mmol), K_2CO_3 (0.51 g, 3.68 mmol) and **(30)** (0.41 g, 1.51 mmol) were added. The product was purified by normal phase chromatography Al_2O_3 (1% NH_4OH: 19% MeOH: 80% DCM) to give the title compound as yellow oil (0.39 g, 80%), m.p. 110-111 °C. NMR δ_H (400 MHz, D_2O) 7.80 (s, 2H, 5-CH), 7.25 (t, 1H, *J* = 7.6, 1-CH), 7.04 (d, 2H, *J* = 7.6, 2-CH), 4.18 (t, 4H, *J* = 7.1, 6-CH_2), 3.45 (t, 4H, *J* = 6.8, 8-CH_2), 1.90 (quintet, 4H, *J* = 6.8, 7-CH_2); NMR δ_C (100 MHz, D_2O) 147.8 (3-C), 146.4 (4-C), 137.9 (1-C), 123.4 (5-C), 118.9 (2-C), 58.1 (6-C), 47.2 (8-C), 31.7 (7-C); MS (ESI) 330 $[M+H]^+$, 352 $[M+Na]^+$; HRMS (ESI) $C_{15}H_{20}N_7O_2$ $[M+H]^+$ requires 330.1678 found 330.1688, $C_{15}H_{19}N_7O_2Na$ $[M+Na]^+$ requires 352.1498 found 352.1518.

8.7 Chlorination of Alcohols:

General Synthesis: Thionyl chloride ~20 equivalents was gradually added to the pyta-OH dissolved in dry DCM (10 mL) in ice bath for 3 h. The reaction mixture was left stirred under N_2 at room temperature for 18 h. Aq. 2 M Na_2CO_3 was added cautiously. The reaction mixture extracted with DCM (3 x 30 mL), the organic layer separated, dried over $MgSO_4$ and concentrated to afford the title compound.

8.7.1 *2-[4-(Chloromethyl)phenyl]pyridine (39)*

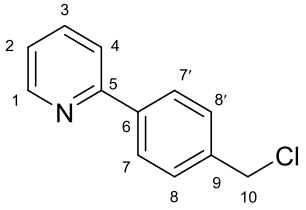

Thionyl chloride (3.28 g, 27.56 mmol) and **(27)** (0.30 g, 1.62 mmol) were reacted. **(39)** was obtained as white solid (0.25 g, 76%), m.p. 205-206 °C. NMR δ_H (400 MHz, $CDCl_3$) 8.71 (ddd, 1H, ^3J = 4.7, ^4J = 1.5, ^5J = 1.0, 1-CH), 8.0 (d, 2H, *J* = 8.1, 7-

CH), 7.8 -7.72 (m, 2H, 3,4-CH), 7.51 (d, 2H, J = 8.1, 8-CH), 7.25 (ddd, 1H, ^{3}J = 6.6, 4.7, ^{4}J = 1.7, 2-CH), 4.65 (s, 2H, 10-CH_2); NMR δ_C (100 MHz, $CDCl_3$) 156.6 (5-C), 149.6 (1-C) 139.4 (9-C), 138 (6-C), 136.7, 120.4 (3, 4-C), 128.9 (8-C), 127.1 (7-C), 122.4 (2-C), 45.8 (10-C); MS (ESI) 204, 206 $[M+H]^+$; HRMS (ESI) $C_{12}H_{11}N^{35}Cl$ $[M+H]^+$ requires 204.0580 found 204.0584.

8.7.2 *2-(1-(3-chloropropyl) - 1H- 1, 2, 3- triazol-4-yl) pyridine (40)*

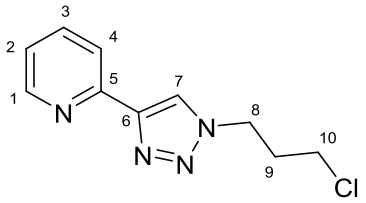

Thionyl chloride (11.31 g, 95.11 mmol) and (**32)** (0.95 g, 4.65 mmol) were reacted. **(38)** was obtained as white solid (0.92 g, 95%), m.p. 80-81 ^{o}C. NMR δ_H (500 MHz, $CDCl_3$, Me_4Si) 8.59 (d, 1H, J = 4.5, 1-CH), 8.26 (s, 1H, 7-CH), 8.21 (d, 1H, 4-CH), 7.79 (ddd, 1H, ^{3}J = 7.7, 7.6, ^{4}J = 1.6, 3-CH), 7.27 (dd,1H, ^{3}J = 7.7, 4.5, 2-CH), 4.61 (t, 2H, J = 6.7, 8-CH_2), 3.54 (t, 2H, J = 5.9, 10-CH_2), 2.42 (quintet, 2H, J = 6.4, 9-CH_2); NMR δ_C (125 MHz, $CDCl_3$, Me_4Si) 149.7 (5-C), 148.8 (1-C), 147.8 (6-C), 137.3 (3-C), 122.9 (2-C), 122.7 (7-C), 120.3 (4-C), 47.2 (8-C), 40.9 (10-C), 32.4 (9-C); MS (ESI) 223, 225 $[M+H]^+$; HRMS (ESI) $C_{10}H_{12}N_4{}^{35}Cl$ $[M+H]^+$ requires 223.0750 found 223.0751, $C_{10}H_{11}N_4{}^{35}ClNa$ $[M+Na]^+$ requires 245.0570 found 245.0578.

8.7.3 *1-(3-chloropropyl)-4-phenyl-1H-1,2,3- triazole (41)*

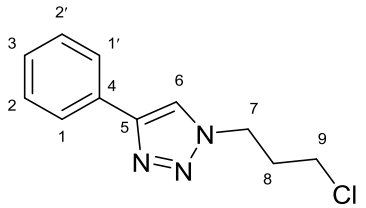

Thionyl chloride (1.9 mL, 25.19 mmol) and **(33)** (0.25 g, 1.23 mmol) were reacted. **(39)** was obtained as white solid (0.26 g, 95%), m.p. 66-67 °C. NMR δ_H (400 MHz, $CDCl_3$, Me_4Si) 7.91-7.71 (m, 3H, 1,6-CH), 7.51-7.28 (m, 3H, 2,3-CH), 4.61 (t, 2H, J = 6.4, 7-CH_2), 3.56 (t, 2H, J = 5.9, 9-CH_2), 2.44 (quintet, 2H, J = 6.2, 8-CH_2); NMR δ_C (100 MHz, $CDCl_3$, Me_4Si) 147.8 (4-C), 130.4 (5-C), 128.8 (1-C), 128.2 (3-C), 125.7 (2-C), 120.2 (6-C), 47 (7-C), 41.1 (9-C), 32.5 (8-C); MS (ESI) 222, 224 $[M+H]^+$; HRMS (ESI) $C_{11}H_{13}N_3Cl$ $[M+H]^+$ requires 222.0798 found 222.0787.

8.7.4 *2-[1-(3-Chloropropyl)-1H-1,2,3-triazole-4-yl]-1-(trifluoromethyl) pyridine (42)*

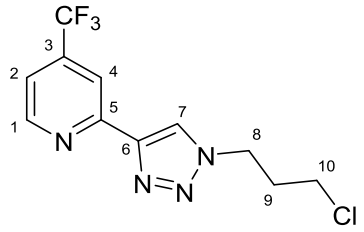

Thionyl chloride (1.64 g, 13.7 mmol) and **(34)** (0.10 g, 0.36 mmol) were reacted. **(40)** was obtained as a yellow oil (100 mg, 94%). NMR δ_H (400 MHz, $CDCl_3$) 8.72 (d, 1H, *J* = 5.1, 1-CH), 8.37 (d, 1H, *J* = 1.1, 4-CH), 8.2 (s, 1H, 7-CH), 7.42 (dd, 1H, ^3J = 5.1, ^4J = 1.1, 2-CH), 4.62 (t, 2H, *J* = 6.6, 8-CH_2), 3.55 (t, 2H, *J* = 6.1, 10-CH_2), 2.44 (quintet, 2H, *J* = 6.2, 9-CH_2); NMR δ_C (125 MHz, $CDCl_3$) 151.4 (5-C), 150.3 (1-C), 147.3 (6-C), 139.2 (q, $^2J_{C\text{-}F}$ = 135.6, 3-C), 123.2 (7-C), 122.7 (q, $^1J_{C\text{-}F}$ = 272.6, CF_3), 118.2 (d, $^3J_{C\text{-}F}$ = 12, 2-C), 115.9 (d, $^3J_{C\text{-}F}$ = 12, 4-C), 47.2 (8-C), 40.9 (10-C), 32.4 (9-C); NMR δ_F (376 MHz, $CDCl_3$) -64.96 (s); MS (ESI) 291, 293 $[M+H]^+$, 313, 315 $[M+Na]^+$; HRMS (ESI) $C_{11}H_{11}N_4ClF_3$ $[M+H]^+$ requires 291.0624 found 291.0621.

8.7.5 *2-[1-(3-Chloropropyl)-1H-1,2,3-triazol-4-yl]-5-(trifluoromethyl) pyridine (43)*

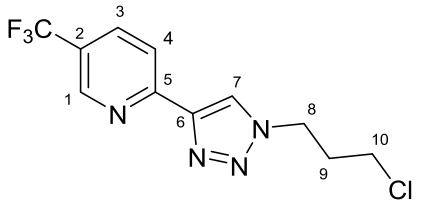

Thionyl chloride (2.62 g, 22.02 mmol) was added gradually to **(35)** (0.29 g, 1.1 mmol). The title compound was obtained as a white solid (0.29 g, 91%), m.p. 122-123 ^oC. NMR δ_H (400 MHz, $CDCl_3$, Me_4Si) 8.84 (d, 1H, *J* = 2.1, 1-CH), 8.31 (d, *J* = 8.2, 1H, 4-CH), 8.25 (s, 1H, 7-CH), 8.01 (dd, 1H, ^3J = 8.2, ^4J = 2.2, 3-CH), 4.66 (t, 2H, *J* = 6.4, 8-CH_2), 3.57 (t, 2H, *J* = 5.8, 10-CH_2), 2.47 (quintet, 2H, *J* = 6.4, 9-CH_2); NMR δ_C (100 MHz, $CDCl_3$, Me_4Si) 153.3 (5-C), 147.3 (6-C), 146.4 (q, $^3J_{C\text{-}F}$ = 3.2, 1-C), 134.1 (q, $^3J_{C\text{-}F}$ = 3.2, 3-C), 125.4 (q, $^2J_{C\text{-}F}$= 33.5, 2-C), 123.6 (7-C), 123.5 (q, $^1J_{C\text{-}F}$ = 273.2, CF_3), 119.6 (4-C), 47.3 (8-C), 40.9 (10-C), 32.4 (9-C); NMR δ_F (376 MHz, $CDCl_3$) -62.35 (s); MS

(ESI) 291,293 $[M+H]^+$, 313,315 $[M+Na]^+$; HRMS (ESI) $C_{11}H_{11}N_4F_3{}^{35}Cl$ $[M+H]^+$ requires 291.0624 found 291.0638.

8.7.6 *2-(1-(3-Chloropropyl)-1H-1,2,3-triazol-4-yl)-4-methoxypyridine (44)*

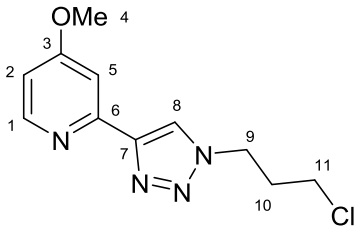

Thionyl chloride (3.28 g, 27.56 mmol) was dissolved in dry DCM 10 mL then **(36)** (320 mg, 1.36 mmol) was dropwise added. The title compound was obtained as light yellow solid (0.31 mg, 90%). NMR δ_H (400 MHz, $CDCl_3$) 9.38 (s, 1H, 8-CH) 8.45 (d, 1H, *J* = 6.5, 1-CH), 7.97 (d, 1H, *J* = 2.4, 5-CH), 7.05 (dd, 1H, ^3J = 2.4, ^4J = 6.4, 1-CH), 4.67 (t, 2H, *J* = 6.7, 9-CH_2), 4.1 (s, 3H, 4-CH_3), 3.59 (t, 2H, *J* = 6.1, 11-CH_2), 2.47 (quintet, 2H, *J* = 6.5, 10-CH_2); NMR δ_C (125 MHz, $CDCl_3$) 170 (3-C), 147.5 (6-C), 143.9 (1-C), 141.4 (7-C), 126.4 (8-C), 111.5 (2-C), 106.2 (5-C), 56.9 (4-C), 40.9 (11-C), 47.4 (9-C), 32.5 (10-C); MS(ESI) 253 $[M+H]^+$, 275 $[M+Na]^+$; HRMS (ESI) $C_{11}H_{14}N_4O^{35}Cl$ $[M+H]^+$ requires 253.0856 found 253.0856, $C_{11}H_{14}N_4O^{37}Cl$ $[M+H]^+$ requires 255.0827 found 255.0832.

8.7.7 *2-[3-(3-Chloropropyl)-3H-pyrazol-5-yl]-6-[1-(3-chloropropyl)-1H-1,2,3-triazole-4-yl] pyridine (45)*

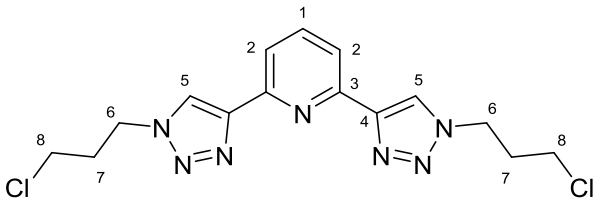

Thionyl chloride (3.28 g, 27.56 mmol) and **(38)** (0.29 g, 0.91 mmol) were reacted. The title compound was obtained as a white solid (0.29 g, 87%). NMR δ_H (400 MHz, $CDCl_3$) 8.45 (s, 2H, 5-CH), 8.16 (d, 2H, *J* = 7.8, 2-CH), 7.93 (t, 1H, *J* = 7.8, 1-CH), 4.65 (t, 4H, *J* = 6.5, 6-CH_2), 3.59 (t, 4H, *J* = 5.9, 8-CH_2), 2.47 (quintet, 4H, *J* = 6.1, 7-CH_2); NMR δ_C (100 MHz, $CDCl_3$) 149.3 (3-C), 147.2 (4-C), 138.5 (1-C), 123.4 (5-C),

119.7 (1-C), 47.3 (6-C), 41 (8-C), 32.5 (7-C); MS (ESI) 388, 390 $[M+Na]^+$; HRMS (ESI) $C_{15}H_{18}N_7{}^{35}Cl_2$ $[M+H]^+$ requires 366.1001 found 366.1007, $C_{15}H_{17}N_7Na^{35}Cl_2$ $[M+Na]^+$ requires 388.0820 found 388.0825.

8.8 Synthesis of Alkyne Precursors.

8.8.1 *2-(Prop-2-yn-1-yloxy)ethan-1-ol (46)*[289]

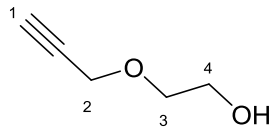

Ethylene glycol (6.98 mL, 125 mmol) and KOH (2.81 g, 50.0 mmol) were suspended in H_2O (4.4 mL) at 0 °C. Propargyl bromide (2.79 mL, 31.3 mmol) was added dropwise over 30 m. The mixture was stirred for 18 h at room temperature, then extracted with DCM (3 x 50 mL). The residue was purified by normal phase chromatography (EtOAc:p. ether 2:2). The title compound was obtained as a yellow oil (1.90 g, 61%). NMR δ_H (500 MHz, $CDCl_3$) 4.21 (d, 2H, *J* = 2.4, 2-CH_2), 3.76 (q, 2H, *J* = 4.1, 3-CH_2), 3.65 (t, 2H, *J* = 4.7, 4-CH_2), 2.79 (t, 1H, *J* = 5.7, OH), 2.49 (t, 1H, *J* = 2.3, 1-CH); NMR δ_C (125 MHz, $CDCl_3$) 79.4 (Cq), 74.7 (1-C), 71.2 (3-C), 61.4 (2-C), 58.3 (4-C); HRMS (ESI) $C_5H_9O_2$ $[M+H]^+$ requires 101.0603 found 101.0604.

8.8.2 *2-(Prop-2-yn-1-yloxy)ethyl 4-methylbenzenesulfonate(47)*[289]

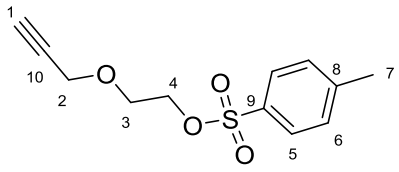

(46) (0.54 g, 5.4 mmol), tosyl chloride (1.23 g, 6.45 mmol) and KOH (1.66 g, 29.64 mmol) were dissolved in diethyl ether (10 mL) at 0 °C. The mixture was stirred for 18 h, then filtered and purified by normal phase chromatography (EtOAc: p. ether 2:1). The title compound was obtained as a colourless oil (1.0 g, 73%). NMR δ_H (400 MHz, $CDCl_3$) 7.77 (d, 2H, *J* = 8.2, 5-CH), 7.34 (d, 2H, *J* = 8.1, 6-CH), 4.17 (t, 2H, *J* = 1.7, 4-CH_2), 4.08 (d, 2H, *J* = 2.4, 2-CH_2), 3.69 (t, 2H, *J* = 1.7, 3-CH_2), 2.42 (s, 4H, 1-CH, CH_3); NMR δ_C (125 MHz, $CDCl_3$) 144.9 (8-C), 132.8 (9-C), 129.8 (6-CH), 127.9 (5-CH), 78.9 (10-C), 75.1 (1-CH), 68.9 (4-CH_2), 67.0 (3-CH_2), 58.3 (2-CH_2), 21.6 (CH_3).

MS (ESI) 277, 278 $[M+Na]^+$; HRMS (ESI) $C_{12}H_{15}O_4S_7$ $[M+H]^+$ requires 255.0691 found 255.0703.

8.8.3 *3-(2-Iodoethoxy)prop-1-yne (48)*

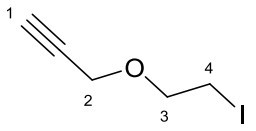

(47) (0.71 g, 2.79 mmol) and KI (2.31 g, 13.95 mmol) were suspended in acetone (15 mL) and heated at reflux. After 48 h the reaction mixture was filtered and the solvent removed under reduced pressure, then diethyl ether (2 x 20 mL) was added and filtered again. The residue concentrated *in vacuo* to give the title compound as a clear, yellowish oil (0.4 g, 68%). NMR δ_H (500 MHz, $CDCl_3$) 4.17 (d, 2H, *J* = 2.4, 2-CH_2), 3.77 (t, 2H, *J* = 6.5, 3-CH_2), 3.24 (t, 2H, *J* = 6.7, 4-CH_2), 2.45 (t, 1H, *J* = 2.3, 1-CH); NMR δ_C (125 MHz, $CDCl_3$) 79.4 (Cq), 74.7 (1-C), 71.2 (3-C), 61.4 (2-C), 58.3 (4-C); MS (ESI) 211 $[M+H]^+$.

8.9 Synthesis of ^{t}BuDO3A Bearing Pendant Triazoles:

General Synthesis: pyridyl-chloride, KI and K_2CO_3 (1.2, 0.1, and 8 equiv.) respectively were added to a solution of **^{t}BuDO3A.HBr** 1 equiv. in dry MeCN (20 mL). The reaction mixture was heated at reflux for 48 h in an inert atmosphere. The reaction was monitored by mass spectroscopy. After filtration, the solvent was concentrated and the crude residue was subjected to normal phase chromatography SiO_2 with (90% DCM: 9% MeOH: 1% NH_4OH) as eluent.

8.9.1 *Tert-butyl2,2',2''-(10-(3-(4-(pyridin-2-yl)-1H-1,2,3-triazol-1-yl)propyl)-1,4,7,10-tetraazacyclododecane (49)*

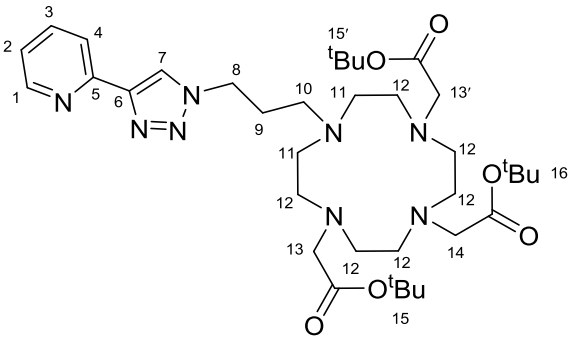

(*t*BuDO3A.HBr) (1.11 g, 1.86 mmol), **(40)** (0.50 g, 2.25 mmol), K_2CO_3 (2.07 g, 15.0 mmol) and KI (29.8 mg, 0.18 mmol) were reacted to afford the title compound as a yellowish oil (0.98 g, 76%). NMR δ_H (500 MHz, $CDCl_3$, Me_4Si) 8.57 (ddd, 1H, ^3J = 4.8, ^4J = 1.6, ^5J = 0.8, 1-CH), 8.19 (s, 1H, 7-CH), 8.13 (d, 1H, J = 8, 4-CH), 7.73 (ddd, 1H, ^3J = 7.7, 7.5, ^4J = 1.6, 3-CH), 7.18 (ddd, 1H, ^3J = 7.5, 4.8, ^4J = 1, 2-CH), 4.51 (t, 2H, J = 7.1, 8-CH_2), 3.26 (s, 2H, 14-CH_2), 3.25 (s, 4H, 13-CH_2), 2.79 (s br, 12H, 12-CH_2), 2.6 (t, 4H, J = 5, 11-CH_2), 2.44 (t, 2H, J = 5.9, 10-CH_2), 2.09 (quintet, 2H, J = 6.7, 9-CH_2), 1.41 (s, 9H, 16-CH_3), 1.40 (s, 18H, 15-CH_3); NMR δ_C (125 MHz, $CDCl_3$, Me_4Si) 171, 170.9 (C=O), 150.4 (5-C),149.3 (1-C), 148.1 (6-C), 136.7 (3-C), 122.6 (2-C), 122.3 (7-C), 120 (4-C), 80.6 (Cq), 56.6, 56.4 (13, 14-C), 53.4, 52.2, 52.1 and 51.8 (CH_2), 48.5 (8-C), 28.4 (9-C), 28.2 (CH_3). MS (ESI) 702 $[M+H]^+$, 724 $[M+Na]^+$; HRMS (ESI) $C_{36}H_{61}N_8O_6$ $[M+H]^+$ requires 701.4714 found 701.4744.

8.9.2 *Tri-tert-butyl 2,2',2''-[10-(3-{4-[4-(trifluoromethyl)pyridin-2-yl]-1H-1,2,3-triazol-1-yl}propyl)-1,4,7,10-tetraazacyclododecane-1,4,7-triyl]triacetate (50)*

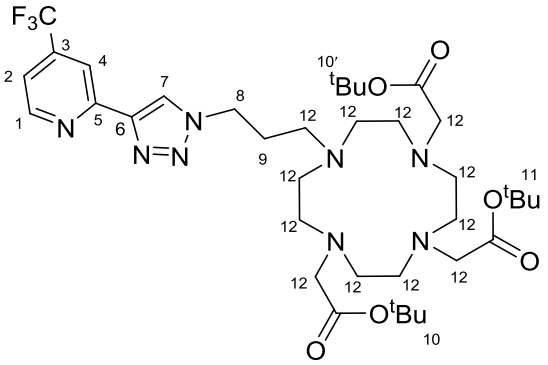

(*t*BuDO3A.HBr) (148 mg, 0.24 mmol), **(42)** (78.4 mg, 0.27 mmol), K_2CO_3 (0.30 g, 1.98 mmol) and KI (6.0 mg, 36.1 μmol) afforded the title compound as a yellowish oil (0.13 mg, 70%). NMR δ_H (400 MHz, $CDCl_3$) 8.68 (d, 1H, J = 5.1, 1-CH), 8.42 (s, 1H,

7-CH), 8.28 (t, 1H, J = 0.9, 4-CH), 7.35 (dd, 1H, ^3J = 5.1, ^4J = 1.0, 2-CH), 4.45 (t, 2H, J = 7, 8-CH_2), 3.4-2.17 (m, 24H, 12-CH_2), 2.12 (t, J = 7, 2H, 9-CH_2), 1.35 (s, 9H, 11-CH_3), 1.34 (s, 18H, 10-CH_3); NMR δ_C (100 MHz, $CDCl_3$) 173.5, 172.5 (C=O), 151.5 (5-C), 150.2 (1-C), 146.8 (6-C), 138.8 (q, $^2J_{C\text{-}F}$ = 34.1, 3-C), 123.2 (7-C), 122.7 (q, $^1J_{C\text{-}F}$ = 273.3, CF_3), 117.8 (q, $^3J_{C\text{-}F}$ = 3.1, 4-C), 115.5 (q, $^3J_{C\text{-}F}$ = 3.1, 2-C), 82.9, 82.5 (Cq), 56.6, 56.3, 55.5, 50.9 (CH_2), 48.7 (8-C), 27.8, 27.7 (11,10-C), 26.5 (9-CH_2); NMR δ_F (376, $CDCl_3$) -64.9 (s); MS (ESI) 769 $[M+Na]^+$; HRMS (ESI) $C_{37}H_{60}N_8O_6F_3$ $[M+H]^+$ requires 769.4588 found 769.4611, $C_{37}H_{59}N_8O_6F_3Na$ $[M+Na]^+$ requires 791.4407 found 791.4442.

8.9.3 *Tri-tert-butyl 2,2',2''-[10-(3-{4-[5-(trifluoromethyl)pyridin-2-yl]-1H-1,2,3-triazol-1-yl}propyl)-1,4,7,10-tetraazacyclododecane-1,4,7-triyl]triacetate (51)*

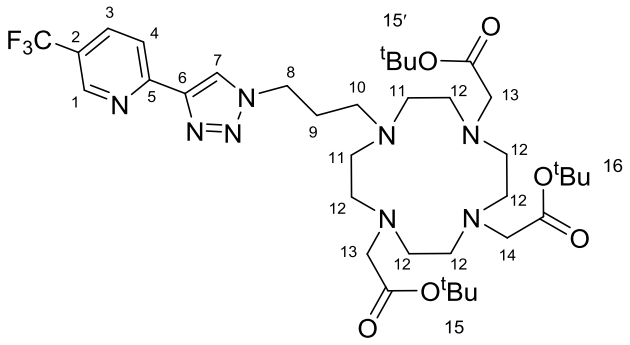

(^{t}BuDO3A.HBr) (0.26 g, 0.43 mmol), **(43)** (0.14 g, 0.48 mmol), K_2CO_3 (0.48 g, 3.5 mmol) and KI (7.0 mg, 42.1 μmol) afforded the title compound as a yellowish oil (0.25 g, 74%). NMR δ_H (400 MHz, $CDCl_3$, Me_4Si) 8.82 (d, 1H, J = 1, 1-CH), 8.4 (s, 1H, 7-CH), 8.25 (d, J = 8.4, 1H, 4-CH), 8.01 (dd, 1H, ^3J = 8.3, ^4J = 2.1, 3-CH), 4.5 (t, 2H, J = 7.2, 8-CH_2), 3.18 (s, 4H, 13-CH_2), 3.05 (s, 2H, 14-CH_2), 2.99-2.24 (m, 18H, 12-CH_2), 2.2 (t, 2H, J = 7.6, 9-CH_2), 1.43 (s, 9H, 16-CH_3), 1.42 (s, 18H, 15-CH_3); NMR δ_C (100 MHz, $CDCl_3$, Me_4Si) 173.7, 172.5 (C=O), 153.4 (5-C),147 (6-C), 146.46 (q, $^3J_{C\text{-}F}$ = 3.1, 1-C), 133.9 (q, $^3J_{C\text{-}F}$ = 3.1, 3-C), 125.2 (q, $^2J_{C\text{-}F}$= 33.5, 2-C), 123.7 (7-C), 123.5 (q, $^1J_{C\text{-}F}$ = 273.2, CF_3), 82.9, 82.5 (Cq), 56.6, 55.7, 53.4 and 51.1 (CH_2), 48.9 (8-C), 27.9, 27.8 (15,16-C), 26.7 (9-C); NMR δ_F (376 MHz, $CDCl_3$) -62.3 (s); MS (ESI) 770 $[M+H]^+$; HRMS (ESI) $C_{37}H_{60}N_8O_6F_3$ $[M+H]^+$ requires 769.4588 found 769.4613.

8.9.4 *Tri-tert-butyl 2,2,2-{10-[3-(4-phenyl-1H-1,2,3-triazol-1-yl)propyl]-1,4,7,10-tetraazacylododecane-1,4,7-triyl]triacetate (52)*

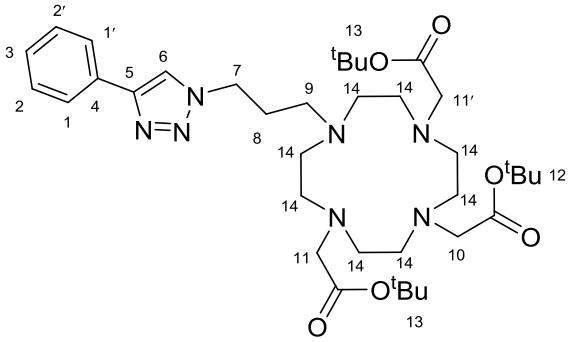

(*t*BuDO3A.HBr) (0.55 g, 0.93 mmol), **(41)** (0.22 g, 0.99 mmol), K_2CO_3 (1.03 g, 7.47 mmol) and KI (0.01 g, 0.09 mmol) afforded the title compound as yellowish oil (0.53 g, 82%). NMR δ_H (400 MHz, $CDCl_3$) 8.45 (s, 1H, 6-CH), 7.82-7.76 (m, 2H, 1-CH), 7.35- 7.28 (m, 2H, 2-CH), 7.21 (tt, 1H, ^3J = 6.6, ^4J = 1.1, 3-CH), 4.61 (t, 2H, J = 6.6, 7-CH_2), 3.57-3.42 (m, 6H, 14-CH_2), 3.35 (s, 2H, 10-CH_2), 3.22 (s, 4H, 11-CH_2), 2.94 (s br, 4H, 14-CH_2), 2.68 (d, 8H, J = 4.8, 14-CH_2), 2.5 (quintet, 2H, J = 6.7, 8-CH_2), 1.35 (s, 9H, 12-CH_3), 1.35 (s, 18H, 13-CH_3); NMR δ_C (100 MHz, $CDCl_3$) 170.2, 169.9 (C=O), 147.4 (4-C), 130.4 (5-C), 128.5 (2-C), 127.7 (3-C), 125.5 (1-C), 121.3 (6-C), 81.7, 81.6 (Cq), 56.6 (11-C), 55.4 (10-C), 53.0, 52.3, 49.9, 49.7, 47.8 (CH_2), 47.2 (7-C), 27.9, 27.8 (12,13-C), 23.7 (8-C); MS (ESI) 701 $[M+H]^+$, 722 $[M+Na]^+$; HRMS (ESI) $C_{37}H_{62}N_7O_6$ $[M+H]^+$ requires 700.4762 found 700.4753.

8.9.5 *Tri-tert-butyl 2,2',2''-(10-(3-(4-(4-methoxypyridin-2-yl)-1H-1,2,3-triazol-1-yl)propyl)-1,4,7,10-tetraazacyclododecane-1,4,7-triyl)triacetate (53)*

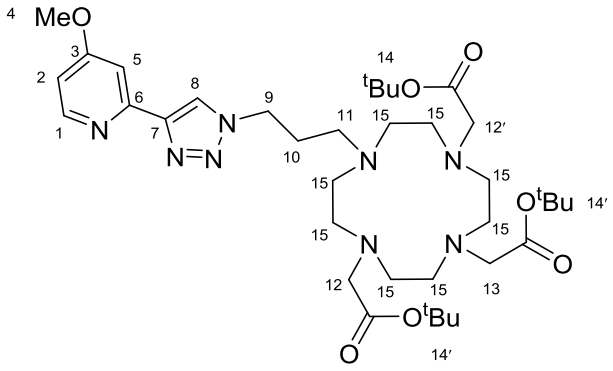

(*t*BuDO3A.HBr) (0.70 g, 1.17 mmol), **(44)** (0.36 g, 1.42 mmol), KI (19.9 mg, 0.12 mmol) and K_2CO_3 (0.90 g, 6.52 mmol) afforded the title compound as yellow oil (0.62 mg, 72%); NMR δ_H (400 MHz, $CDCl_3$) 8.39 (s, 1H, 8-CH), 8.37 (d, 1H, *J* = 5.6, 1-CH), 7.67 (d, 1H, *J* = 2.5, 5-CH), 6.76 (dd, 1H, ^3J = 5.6, ^4J = 2.5, 1-CH), 4.64 (t, 2H, *J* = 6.4, 9-CH_2), 3.92 (s, 2H, 4-CH_3), 3.68-3.50 (m, 2H, 11-CH_2), 3.45 (s, 2H, 13-CH_2), 3.31 (s, 4H, 12-CH_2), 3.04 (s br, 4H, 15-CH_2), 2.79 (s br, 12H, 15-CH_2), 2.56 (qui, 2H, *J* = 6.6, 10-CH_2), 1.42 (s, 27H, 14-CH_3); NMR δ_C (125 MHz, $CDCl_3$) 170, 169.8 (Cq), 166.4 (3-C), 151.5 (6-C), 150.3 (1-C), 148.2 (7-C), 123.2 (8-C), 110 (2-C), 105.4 (5-C), 82.0, 81.9 (Cq), 56.7 (12-C), 55.7 (13-C), 55.3 (4-C), 53.2, 50.2, 48.3 (CH_2), 52.3 (10-C), 47.6 (9-C), 28.0 (14-C), 24.0 (10-C); MS(ESI) 731 $[M+H]^+$, 753 $[M+Na]^+$; HRMS (ESI) $C_{37}H_{63}N_8O_7$ $[M+H]^+$ requires 731.4820 found 731.4805, $C_{37}H_{62}N_8O_7Na$ $[M+Na]^+$ requires 753.4639 found 753.4626.

8.9.6 *Tri-tert-butyl 2,2',2''-(10-(3-(1-(pyridin-2-yl)-1H-1,2,3-triazol-4-yl)propyl)-1,4,7,10-tetraazacyclododecane-1,4,7-triyl)triacetate (54)*

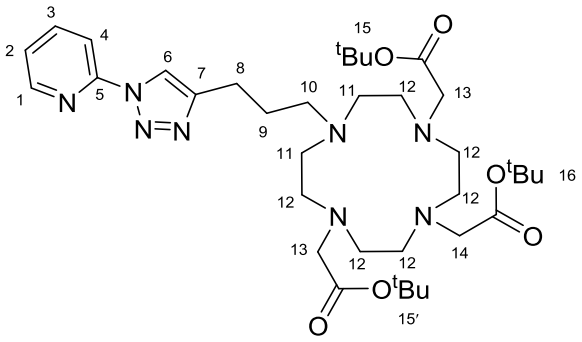

(*t*BuDO3A.HBr) (0.22 g, 0.37 mmol), **(37)** (0.09 g, 0.40 mmol), KI (10.0 mg, 70.0 µmol) and K_2CO_3 (0.40 g, 2.89 mmol) afforded the title compound as a yellowish oil (0.17 g, 66%). NMR δ_H (400 MHz, $CDCl_3$) 8.46 (ddd, 1H, ^3J = 4.8, ^4J = 1.7, ^5J = 1.0, 1-CH), 8.29 (s, 1H, 6-CH), 8.12 (d, 1H, ^3J = 8.2, 4-CH), 7.9 (ddd, 1H, ^3J = 7.4, 7.6, ^4J = 1.7, 3-CH), 7.34 (ddd, 1H, , ^3J = 7.4, 7.6, ^4J = 4.8, 2-CH), 3.35-2.15 (m, 26H, 12-CH_2), 1.87 (quintet, 2H, *J* = 7.8, 9-CH_2), 1.4 (s, 9H, 16-CH_3), 1.39 (s, 9H, 15-CH_3); NMR δ_C (400 MHz, $CDCl_3$) 173.5, 172.6 (C=O), 149.1 (5-C), 148.5 (1-C), 147.5 (7-C), 139.2 (3-C), 123.6 (2-C), 118.2 (6-C), 113.6 (4-C), 82.8, 82.4 (Cq), 56.5, 55.8, 53.8, 53.5, 50.3 (CH_2), 27.9, 27.8 (15,16-C), 26.2 (9-C), 23.7 (8-C). MS (ESI) 701 $[M+H]^+$, 735 $[M+Na]^+$; HRMS (ESI) $C_{36}H_{61}N_8O_6$ $[M+H]^+$ requires 701.4714 found 701.4747.

8.9.7 *Tri-tert-butyl2,2',2''-(10-{[7-(pyridine-2-yl)phenyl]methyl} 1,4,7,10-trtraazacyclododecane-1,4,7-triyl)triacetate (55)*

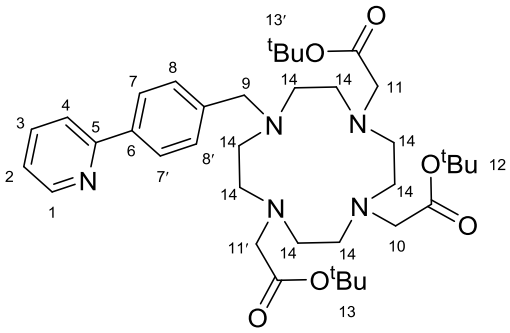

(*t*BuDO3A.HBr) (0.66 g, 1.11 mmol), **(39)** (0.25 g, 1.23 mmol), KI (10.0 mg, 70.0 μmol), K_2CO_3 (1.20 g, 8.68 mmol) afforded the title compound as colourless oil (0.65 g, 86%). NMR δ_H (500 MHz, $CDCl_3$) 8.67 (d, 1H, *J* = 4.7, 1-CH), 7.92 (d, 2H, *J* = 8.1, 7-CH), 7.76-7.70 (m, 2H, 3, 4-CH), 7.47 (d, 2H, *J* = 8.1, 8-CH), 7.2 (ddd, 1H, ^3J = 6.5, ^4J = 4.8, ^5J = 2, 2-CH), 3.62 (s br, 2H, 9-CH_2), 3.34 (s, 2H, 10-CH_2), 3.22 (s, 4H, 11-CH_2), 2.84 (s, 12H, 14-CH_2), 2.66 (br s, 4H, 14-CH_2), 1.45 (s, 9H, 12-CH_3), 1.4 (s, 18H, 13-CH_3); NMR δ_C (125 MHz, $CDCl_3$) 171.1, 171 (C=O), 157.3 (5-C), 149.5 (1-C), 136.6, 120.3 (3, 4-C), 129.5 (8-C), 126.6 (7-C), 121.9 (2-C), 80.6 (Cq), 59.8 (9-C), 56.4, 52.1, 51.7 (CH_2), 28.2, 28.1 (12,13-C); MS (ESI) 683 $[M+H]^+$, 705 $[M+Na]^+$; HRMS (ESI) $C_{38}H_{60}N_5O_6$ $[M+H]^+$ requires 682.4544 found 682.4559.

8.9.8 *Tri-tert-butyl 2,2',2''-(10-{2-[(methanesulfonyl)amino]ethyl}-1,4,7,10-tetraazacyclododecane-1,4,7-triyl)triacetate (56)*

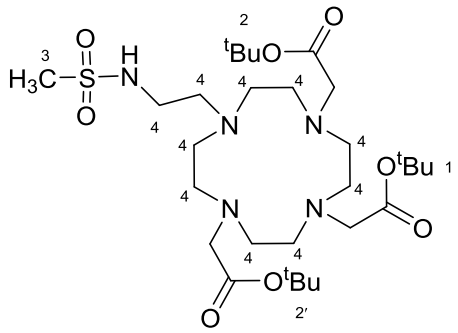

(*t*BuDO3A.HBr) (0.50 g, 0.84 mmol), **(24)** (0.12 g, 1.0 mmol) and K_2CO_3 (0.11 g, 0.84 mmol) afforded the title compound as a colourless oil (0.34 g, 64%). NMR δ_H (400 MHz, $CDCl_3$) 6.32 (t, 1H, *J* = 6.2, NH), 3.42-1.84 (m overlap, 29H, 4-CH_2), 1.46 (s, 18H, 2-CH_3), 1.42 (s, 9H, 1-CH_3); NMR δ_C (100 MHz, $CDCl_3$) 173, 172.4 (C=O), 82.8,

82.3 (Cq), 56.5, 55.4, 53.4, 53.2, 50.1, 40.5 (CH_2), 39 (3-C), 28, 27.8 (1,2-C); MS (ESI) 637 $[M+H]^+$, 658 $[M+Na]^+$, MS (ES-) 634 $[M-H]^-$; HRMS (ESI) $C_{29}H_{58}N_5O_8S$ $[M+H]^+$ requires 636.4006 found 636.4030

8.9.9 *Tri-tert-butyl 2,2',2''-[10-(but-3-yn-1-yl)-1,4,7,10-tetraazacyclododecane (57)*

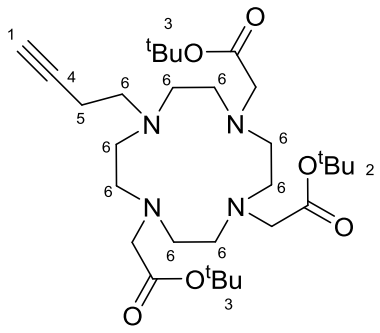

Tert-Butyl bromoacetate (204 mg, 1.05 mmol) was added to a suspension of **(22)** (74.1 mg, 0.33 mmol) and K_2CO_3 (186 mg, 1.32 mmol) in MeCN (10 mL) and heated at 70 °C. The reaction was monitored by TLC analysis (R_f = 0.26, 1% NH_4OH: 9% MeOH: 90% DCM). The title compound was obtained as a pale yellow oil (126 mg, 67%). NMR δ_H (400 MHz, $CDCl_3$) 3.25-2.23 (m, 26H, 6-CH_2), 1.89 (t, 1H, *J* = 2.5, 1-CH), 1.45 (s, 9H, 2-CH_3), 1.43 (s, 18H, 3-CH_3); NMR δ_C (125 MHz, $CDCl_3$) 170.7, 170.6 (C=O), 80.5 (4-C), 80.2, 79.8 (Cq), 77.5 (1-C), 67.5, 54.4, 53.6, 50.1, 47.9 (CH_2), 25.7 (2,3-C), 14.0 (5-C); MS (ESI) 568 $[M+H]^+$, 589 $[M+Na]^+$; HRMS (ESI) $C_{30}H_{55}N_4O_6$ $[M+H]^+$ requires 567.4122 found 567.4150, $C_{30}H_{54}N_4O_6Na$ $[M+Na]^+$ requires 589.3941 found 589.3964.

8.9.10 *Tri-tert-butyl 2,2',2''-[10-(3-{4-[6-(3-{3-[4,7,10-tris(2-tert-butoxy-2-oxoethyl)-1,4,7,10-tetraazacyclododecan-1-yl]propyl}-3H-pyrazol-5-yl)pyridin-2-yl]-1H-1,2,3-triazol-1-yl}propyl)-1,4,7,10-tetraazacylododecane (58)*

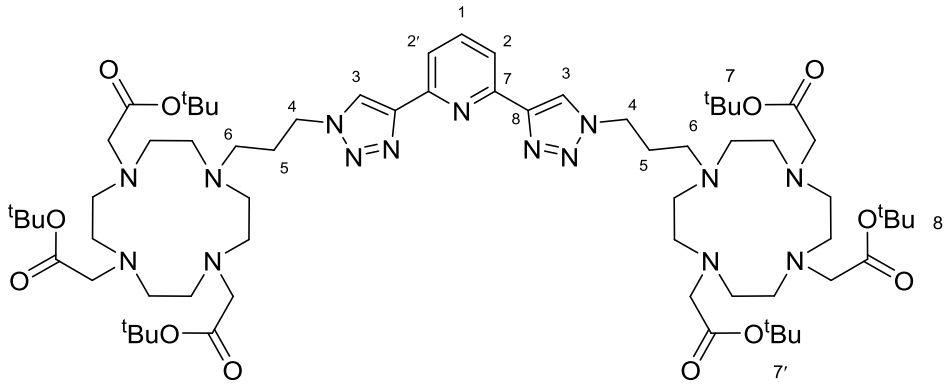

(*t*BuDO3A.HBr) (0.80 g, 1.34 mmol), **(45)** (0.29 g, 0.80 mmol), KI (0.02 g, 0.13 mmol) and K_2CO_3 (0.74 g, 5.38 mmol) afforded the title compound as a yellow oil (0.68, 77%). NMR δ_H (400 MHz, $CDCl_3$) 9.41 (s, 2H, 3-CH), 7.99 (d, 2H, *J* = 7.8, 2-CH), 7.81 (t, 1H, *J* = 7.8, 1-CH), 4.63 (t, 4H, *J* = 6.7, 4-CH_2), 3.74-3.39 (m, 16H, CH_2), 3.31 (s, 8H, CH_2), 3.05 (s br, 8H, CH_2), 2.87-2.60 (m, 16H, CH_2), 2.58-2.1 (m, 4H, CH_2), 1.45 (s, 9H, 8-CH_3), 1.42 (s, 18H, 7-CH_3); NMR δ_C (125 MHz, $CDCl_3$) 170.3, 170 (C=O), 149.9 (7-C), 149.1 (8-C), 137 (3-C), 124.9 (1-C), 118 (2-C), 81.8 (Cq), 57, 52.9, 50.3, 48.1, 47.4 (CH_2), 28.1 (7,8-C), 23.8 (5-C); MS (ESI) 663 $[M+2H]^{2+}$, 673 $[M+H+Na]^{2+}$; HRMS (ESI) $C_{67}H_{116}N_{15}O_{12}$ $[M+H]^+$ requires 1322.8928 found 1322.8943, $C_{67}H_{115}N_{15}O_{12}Na$ $[M+Na]^+$ requires 1344.8747 found 1344.8730.

8.9.11 *Tri-tert-butyl 2,2',2''-(10-{2-[(prop-2-yn-1-yl)oxy]ethyl}-1,4,7,10-tetraazacylododecane-1,4,7-triyl]triacetate (59)*

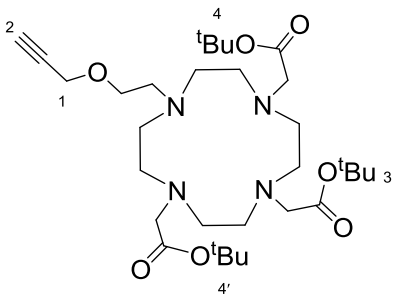

(*t*BuDO3A.HBr) (160 mg, 0.26 mmol), **(48)** (56.7 mg, 0.27 mmol), K_2CO_3 (298 mg, 2.15 mmol) afforded the title compound as a yellow oil (106 mg, 66%). NMR δ_H (400 MHz, $CDCl_3$) 4.1 (d, 2H, *J* = 2.3, 1-CH_2), 3.82-2.48 (m, 26H, CH_2), 2.45 (t, 1H, *J* = 2.3, 2-CH), 1.48 (s, 18H, 4-CH_3), 1.45 (s, 9H, 3-CH_3); NMR δ_C (125 MHz, $CDCl_3$) 171.9, 172.4 (C=O), 82.0, 81.9 (Cq), 78.9 (1-C), 75.6 (2-C), 65.2, 58.4, 56.4, 55.5 and 51.2

(CH_2), 27.9, 27.8 (3,4-C); MS (ESI) 598 $[M+H]^+$, 620 $[M+Na]^+$; HRMS (ESI) $C_{31}H_{57}N_4O_7$ $[M+H]^+$ requires 597.4227 found 597.4253.

8.10 Synthesis of Pro-ligands:

General Synthesis: a solution of (DCM:TFA 1:1) (10 mL) was gradually added to the appropriate ^{t}BuDO3A-derivatives with stirring for 20 h under an open atmosphere. The reaction was monitored by MS. DCM (2 x 5 mL) was added and concentrated, followed by diethyl ether (5 mL) and concentrated, yielding a hydroscopic white solid. The resulted compounds purified by reverse phase chromatography (method A).

8.10.1 *2,2',2''-(10-(3-(4-(Pyridin-2-yl)-1H-1,2,3-triazol-1-yl)propyl) 1,4,7,10-tetraazacyclododecane (H_3L1)*

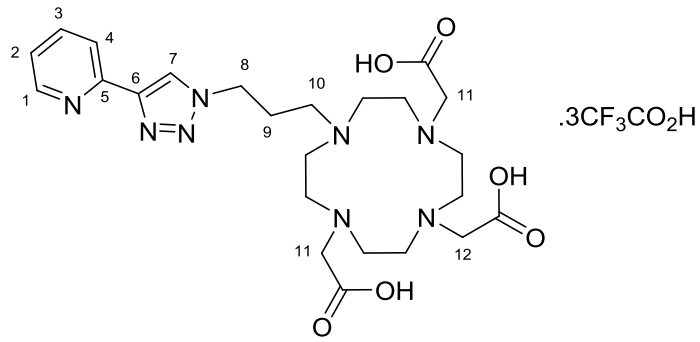

(49) (1.44 g, 2.05 mmol), RP-HPLC t_R = 16.8 min. The title compound was obtained as a hygroscopic white powder (1.31 g, 73%). NMR δ_H (500 MHz, 329K, MeOD) 8.61 (ddd, 1H, ^3J = 6, ^4J = 1.6, ^5J = 1.0, 1-CH), 8.52 (s, 1H, 7-CH), 8.14 (ddd, 1H, ^3J = 8.5, 8.2, ^4J = 1.5, 4-CH), 8.01 (d, 1H, J = 8.0, 4-CH), 7.45 (ddd, 1H, ^3J = 7.6, 6.1 , ^4J = 1.2, 2-CH), 4.64 (t, 2H, J = 6.7, 8-CH_2), 4.01 (s, 2H, 12-CH_2), 3.7-3.54 (br s, 4H, 11-CH_2), 3.5-3.34 (m, 10H, CH_2), 3.24-3.07 (m, 8H, CH_2), 2.4 (quintet, 2H, J = 7.4, 9-CH_2); NMR δ_C (125 MHz, D_2O) 174, 169.9(C=O), 162.9 (q, $^2J_{C\text{-}F}$ = 36.8, $CF_3CO_2^-$), 147.4 (3-C), 142.3 (5-C), 141 (1-C), 139.2 (6-C), 126.8 (7-C), 126 (2-C), 124.5 (4-C), 116.3 (q, $^1J_{C\text{-}F}$ = 290.3, $CF_3CO_2^-$), 54.6 (9-C), 52.9, 51.5, 51.3, 50, 48.5, 48.2 and 47.7 (CH_2), 24.1 (9-C); NMR δ_F (376 MHz, $CDCl_3$) -75.5 (s) ($CF_3CO_2^-$); MS (ESI) 534 $[M+H]^+$, 556 $[M+Na]^+$; HRMS (ESI) $C_{24}H_{37}N_8O_6$ $[M+H]^+$ requires 533.2836 found 533.2844, $C_{24}H_{36}N_8O_6Na$ $[M+Na]^+$ requires 555.2656 found 555.2656.

8.10.2 *2,2',2''-10-[3-(4-Phenyl-1H-1,2,3-triazol-1-yl) propyl]- 1,4,7,10-tetraazacyclododecane (H_4L2)*

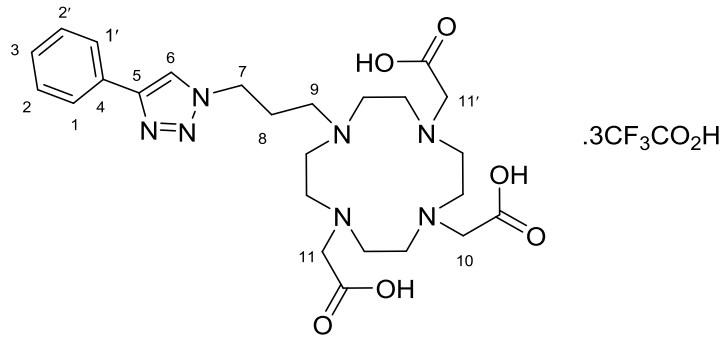

(52) (1.35 g, 1.93 mmol), RP-HPLC t_R = 18.51 min. The title compound was obtained as a white solid (1.44 g, 86%). NMR δ_H (400 MHz, D_2O) 8.31 (s, 1H, 6-CH), 7.77 (d, 2H, *J* = 7.2, 1-CH), 7.49 (t, 2H, *J* = 7.2, 2-CH), 7.42 (tt, 1H, ^3J = 7.2, ^4J = 1.9, 3-CH), 4.56 (t, 2H, *J* = 6.5, 7-CH_2), 3.84 (s, 2H, 10-CH_2), 3.64-2.87 (m, 22H, CH_2), 2.39 (quintet, 2H, *J* = 6.7, 8-CH_2); NMR δ_C (100 MHz, D_2O) 174.9, 170.3 (C=O), 162.9 (q, $^2J_{C\text{-}F}$ = 36.8, $CF_3CO_2^-$), 148.5 (5-C), 140.2 (4-C), 130.2 (2-C), 129.9 (3-C), 126.6 (1-C), 123.3 (6-C), 116.3 (q, $^1J_{C\text{-}F}$ = 290.3, $CF_3CO_2^-$), 56.1 (10-C), 54.0, 52.4, 52.1, 50.8, 49.5, 49.3 (CH_2), 48.4 (7-C), 24.8 (8-C); NMR δ_F (376 MHz, $CDCl_3$) -75.5 (s) ($CF_3CO_2^-$); MS (ESI) 533 $[M+H]^+$, 555 $[M+Na]^+$; HRMS (ESI) $C_{25}H_{38}N_7O_6$ $[M+H]^+$ requires 532.2884 found 532.2879.

8.10.3 *2,2',2''-[10-(3-{4-[5-(Trifluoromethyl)pyridine-2-yl]-1H-1,2,3-triazol-1-yl}propyl)- 1,4,7,10-tetraazacyclododecane (H_3L3)*

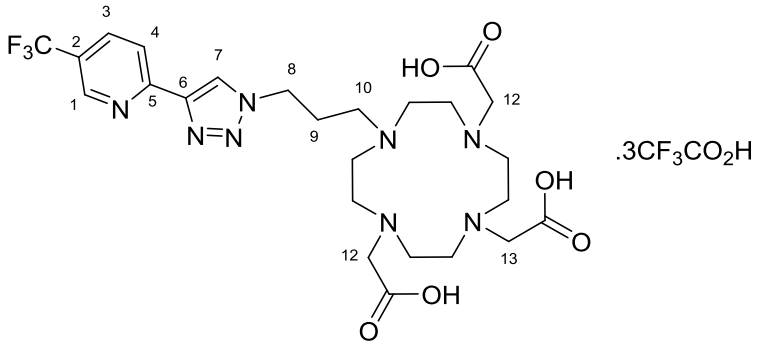

(51) (1.00 g, 1.30 mmol), RP-HPLC t_R = 19.45 min. The title compound was obtained as a white solid (1.03 g, 85%). NMR δ_H (500 MHz, MeOD, 313 K) 8.89 (d, 1H, *J* = 1.0, 1-CH), 8.62 (s, 1H, 7-CH), 8.25 (d, 1H, *J* = 8.4, 4-CH), 8.22 (dd, 1H, ^3J = 8.3, ^4J = 1.1, 3-CH), 4.65 (t, 2H, *J* = 6.8, 8-CH_2), 4.1 (s, 2H, 13-CH_2), 3.8-3.35 (m, 16H, CH_2),

3.14 (br s, 8H, CH_2), 2.45 (quintet, *J* = 6.8, 2H, 9-CH_2); NMR δ_C (125 MHz, MeOD, 313 K) 174.4, 169.5 (C=O), 162.5 (q, $^2J_{C\text{-}F}$ = 35.1, 2-C), 162.3 (q, $^2J_{C\text{-}F}$ = 36.8, $CF_3CO_2^-$), 154.7 (5-C), 148.1 (6-C), 147.5 (q, $^3J_{C\text{-}F}$ = 4, 1-C), 135.8 (q, $^3J_{C\text{-}F}$ = 4, 3-C), 125.7 (7-C), 125 (q, $^1J_{C\text{-}F}$ = 272, CF_3), 121 (4-C), 116.2 (q, $^1J_{C\text{-}F}$ = 290.3, $CF_3CO_2^-$), 55.9, 53.9, 53.2, 52.7, 51.4, 50.2, and 50 (CH_2), 25.8 (9-C); NMR δ_F (376 MHz, $CDCl_3$) -62.4 (s) (CF_3-pyta), -75.5 (s) ($CF_3CO_2^-$); MS (ESI) 602 $[M+H]^+$; HRMS (ESI) $C_{25}H_{36}N_8O_6F_3$ $[M+H]^+$ requires 601.2710 found 601.2731.

8.10.4 *2,2',2''-[10-(4-{4-[5-(Trifluoromethyl)pyridine-2-yl]-1H-1,2,3-triazol-1-yl}propyl)- 1,4,7,10-tetraazacyclododecane (H_3L4)*

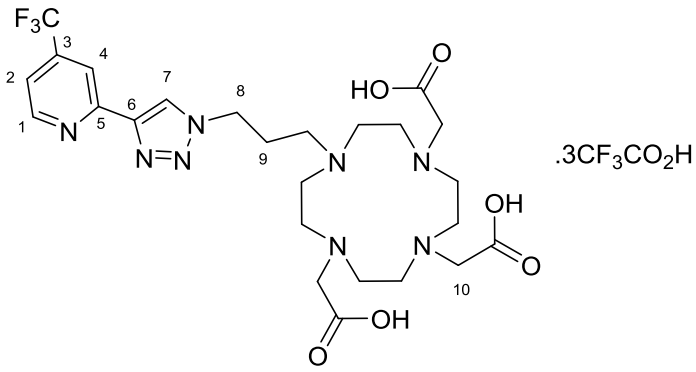

(50) (185 mg, 0.24 mmol), RP-HPLC t_R = 25.1 min. The title compound was obtained as a yellow solid (174 mg, 77%). NMR δ_H (400 MHz, D_2O) 8.75 (d, 1H, *J* = 5.2, 1-CH), 8.59 (s, 1H, 7-CH), 8.3 (s, 1H, 4-CH), 7.85 (d, 1H, *J* = 5.1, 2-CH), 4.6 (t, 2H, *J* = 6.2, 8-CH_2), 4.06 (s, 2H, 10-CH_2), 3.62-3.22 (m, 14H, CH_2), 2.15-2.83 (m, 8H, CH_2), 2.42 (quintet, 2H, *J* = 7.0, 9-CH_2); NMR δ_C (100 MHz, D_2O) 173.8, 168.9 (C=O), 162.3 (q, $^2J_{C\text{-}F}$ = 36.8, $CF_3CO_2^-$), 148.6 (1-C), 148.2 (5-C), 144.1 (6-C), 140.8 (q, $^2J_{C\text{-}F}$ = 34.1, 3-C), 122 (q, $^1J_{C\text{-}F}$ = 273, CF_3), 119.9 (2-C), 116.3 (q, $^1J_{C\text{-}F}$ = 290.3, $CF_3CO_2^-$), 117.3 (4-C), 54.8 (10-C), 52.9, 51.4, 51.3, 49.9, 48.4, 48.2 (CH_2), 47.5 (8-C), 24 (9-C); NMR δ_F (376, D_2O) -65.27 (s) (CF_3-pyta), -75.5 (s) ($CF_3CO_2^-$); MS (ESI) 601 $[M+H]^+$; HRMS (ESI) $C_{25}H_{36}N_8O_6F_3$ $[M+H]^+$ requires 601.2710 found 601.2734.

8.10.5 *2,2',2''-(10-(3-(1-(pyridin-2-yl)-1H-1,2,3-triazol-4-yl)propyl)-1,4,7,10-tetraazacyclododecane (H_3L5)*

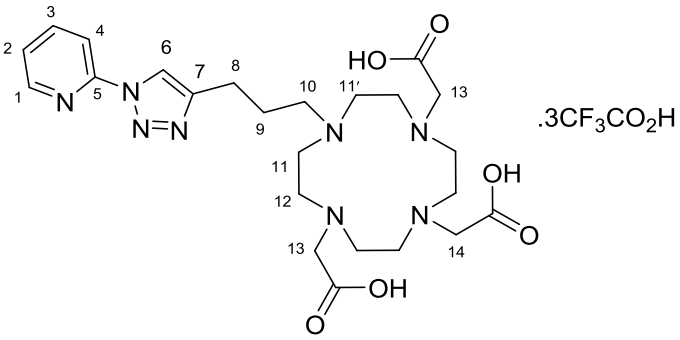

(53) (150 mg, 0.21 mmol), RP-HPLC t_R = 20.62 min. The title compound was obtained as a white solid (141 mg, 76%). NMR δ_H (400 MHz, D_2O) 8.41 (d, 1H, *J* = 4.3, 1-CH), 8.36 (s, 1H, 6-CH), 8.01 (ddd, 1H, ^3J = 7.6, 7.8, ^4J = 1.3, 3-CH), 7.84 (d, 1H, *J* = 8.2, 4-CH), 7.47 (dd, 1H, *J* = 5, 7.4, 2-CH), 4.09 (s, 2H, 14-CH_2), 3.59-3.25 (m, 14H, CH_2), 3.16-2.87 (m, 8H, CH_2), 2.82 (t, 2H, *J* = 7.2, 10-CH_2), 2.13 (quintet, 2H, *J* = 7.4, 9-CH_2); NMR δ_C (100 MHz, D_2O) 174.2, 168.6 (C=O), 162.3 (q, $^2J_{C\text{-}F}$ = 36.8, $CF_3CO_2^-$), 148.4 (1-C), 147.9 (3-C), 146.7 (5-C), 140.7 (7-C), 124.9 (2-C), 120.7 (6-C), 117.5 (8-C), 116.3 (q, $^1J_{C\text{-}F}$ = 290.3, $CF_3CO_2^-$), 114.9 (4-C), 54.8 (14-C), 53.5, 52.9, 51.8, 50.0, 48.4, 48.0 (CH_2), 22.7 (9-C), 21.5 (10-C); NMR δ_F (376 MHz, $CDCl_3$) -75.5 (s) ($CF_3CO_2^-$); MS (ESI) 533 $[M+H]^+$; HRMS (ESI) $C_{24}H_{37}N_8O_6$ $[M+H]^+$ requires 533.2836 found 533.2861.

8.10.6 *2,2',2''-(10-{[7-(Pyridine-2-yl)phenyl]methyl}1,4,7,10-trtraazacyclododecane (H_4L6)*

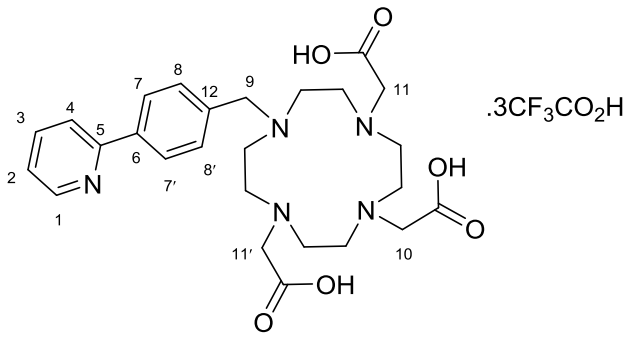

(54) (0.60 g, 0.87 mmol), RP-HPLC t_R = 6.65 min. The title compound was obtained as colourless oil (0.49 g, 66%). NMR δ_H (500 MHz, MeOD, 343 K) 9.17 (d, 1H, *J* = 5.8, 1-CH), 9.05 (t, 1H, *J* = 8.0, 3-CH), 8.69 (d, 1H, *J* = 8.0, 4-CH), 8.43 (t, 1H, *J* = 6.5, 2-CH), 8.3 (d, 2H, *J* = 8.0, 7-CH), 8.19 (d, 2H, *J* = 8.0, 8-CH), 4.25 (s, 2H, 10-CH_2), 4.04-3.45 (m, 22H, CH_2); NMR δ_C (125 MHz, MeOD, 343 K) 171.8, 171.6 (C=O), 162.4

(q, $^{2}J_{C\text{-}F}$ = 36.8, $CF_3CO_2^-$), 151.9 (5-C), 147.9 (1-C), 141.9 (3-C), 132.3 (8-C),132.2 (11-C), 129.4 (7-C), 126.8 (4-C), 126.3 (2-C), 116.2 (q, $^{1}J_{C\text{-}F}$ = 290.3, $CF_3CO_2^-$), 57.6 (9-C), 55, 54.3, 50.6, 50.2, 49.9, 49.7 (CH_2); NMR δ_F (376 MHz, $CDCl_3$) -75.5 (s) ($CF_3CO_2^-$); MS (ESI) 514 $[M+H]^+$, 536 $[M+Na]^+$; HRMS (ESI) $C_{26}H_{36}N_5O_6$ $[M+H]^+$ requires 514.2666 found 514.2646.

8.10.7 *2,2',2''-[10-(3-{4-[6-(3-{3-[4,7,10-Tris(carboxymethyl)-1,4,7,10-tetraazacyclododecan-1-yl]propyl}-3H-pyrazol-5-yl)pyridin-2-yl]-1H-1,2,3-triazol-1-yl}propyl)-1,4,7,10-tetraazacyclododecane (H_6L7)*

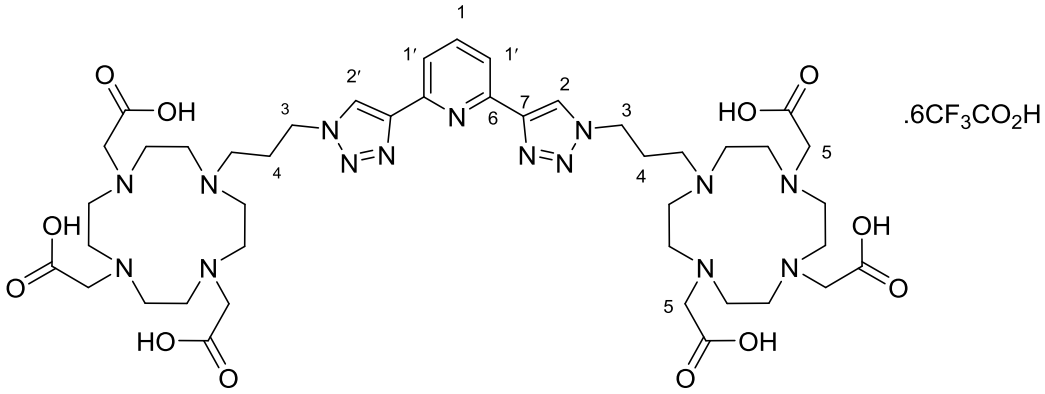

(57) (0.51 g, 0.37 mmol), RP-HPLC t_R = 18.27 min. The title compound was obtained as a pale yellow solid (0.44 g, 70%). NMR δ_H (500 MHz, MeOD, 323K) 8.66 (s, 2H, 2-CH), 7.97 (s, 3H, 1-CH), 4.66 (t, 4H, *J* = 6.9, 3-CH_2), 4.06 (s, 4H, 5-CH_2), 3.63 (s br, 8H, CH_2), 3.53-3.35 (m, 20H, CH_2), 3.15 (s br, 16H, CH_2), 2.55 (quintet, 4H, *J* = 7.9, 4-CH_2); NMR δ_C (125 MHz, MeOD, 323K) 174.2, 169.6 (C=O), 162.3 (q, $^{2}J_{C\text{-}F}$ = 36.8, $CF_3CO_2^-$), 151.1 (6-C), 149.3 (7-C), 139.3 (1-C), 125 (2-C), 120.4 (1-C), 116.3 (q, $^{1}J_{C\text{-}F}$ = 290.3, $CF_3CO_2^-$), 56 (5-C), 54.3, 53.2, 52.8, 51.5 and 50.3 (CH_2), 25.9 (4-C) ; NMR δ_F (376 MHz, $CDCl_3$) -75.5 (s) ($CF_3CO_2^-$); MS (ESI) 986 $[M+H]^+$, 1008 $[M+Na]^+$, 505 $[M+H+Na]^{2+}$, 494 $[M+2H]^{2+}$; HRMS (ESI) $C_{43}H_{68}N_{15}O_{12}$ $[M+H]^+$ requires 986.5172 found 986.5201.

8.10.8 *2,2',2''-(10-{2-[(Prop-2-yn-1-yl)oxy]ethyl}-1,4,7,10-tetraazacylododecane (H_3L8)*

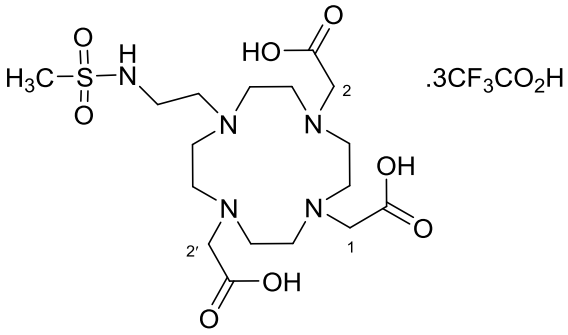

(55) (300 mg, 0.47 mmol), RP-HPLC t_R = 5.51 min. The title compound was obtained as a white solid (179 mg, 47%). NMR δ_H (500 MHz, MeOD) 4.01 (s br, 2H, 1-CH_2), 3.71 (s br, 4H, 2-CH_2), 3.58-3.36 (m, 12H, CH_2), 3.19 (s br, 8H, CH_2), 3.02 (s, 3H, CH_3); NMR δ_C (125 MHz, MeOD) 174, 170.6 (C=O), 162.3 (q, $^2J_{C\text{-}F}$ = 36.8, $CF_3CO_2^-$), 55.6, 54.9 (CH_2), 116.3 (q, $^1J_{C\text{-}F}$ = 290.3, $CF_3CO_2^-$), 54.3 (1-C), 52.2 (2-C), 51.3, 50.5, 50.3, 39.5 (CH_2), 39.4 (CH_3); NMR δ_F (376 MHz, $CDCl_3$) -75.5 (s) ($CF_3CO_2^-$); MS (ESI) 468 $[M+H]^+$, 490 $[M+Na]^+$; HRMS (ESI) $C_{17}H_{34}N_5O_8S$ $[M+H]^+$ requires 468.2128 found 468.2135.

8.10.9 *2,2',2''-[10-(But-3-yn-1-yl)-1,4,7,10-tetraazacyclododecane (H_4L9)*

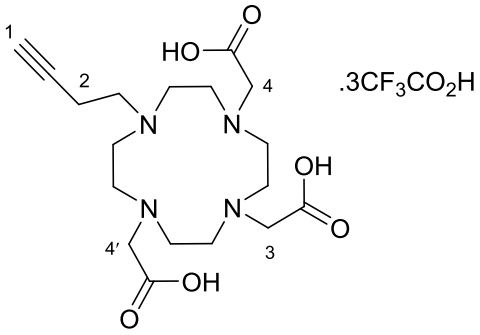

(56) (109 mg, 0.19 mmol), RP-HPLC t_R = 7.35 min. The title compound was obtained as a yellowish oil (112 mg, 79%). NMR δ_H (500 MHz, D_2O) 4.03 (s, 2H, 3-CH_2), 3.78-3.61 (m, 4H, 4-CH_2), 3.59-3.38 (m, 10H, CH_2), 3.33-3.06 (m, 8H, CH_2), 2.8 (s br, 2H, 2-CH_2), 2.58 (s, 1H, CH). NMR δ_C (125 MHz, D_2O) 163, 162.7 (C=O), 162.4 (q, $^2J_{C\text{-}F}$ = 36.8, $CF_3CO_2^-$), 116.2 (q, $^1J_{C\text{-}F}$ = 290.3, $CF_3CO_2^-$), 73.5 (1-C), 55.3 (3-C), 53.2, 51.9, 51.1, 49.9, 48.4, 48 (CH_2), 14 (2-C); NMR δ_F (376 MHz, $CDCl_3$) -75.5 (s) ($CF_3CO_2^-$); MS (ESI) 399 $[M+H]^+$, 437 $[M+K]^+$; HRMS (ESI) $C_{18}H_{31}N_4O_6$ $[M+H]^+$ requires 399.2244 found 399.2257.

8.10.10 *2,2',2''-[10-(But-3-yn-1-yl)-1,4,7,10-tetraazacyclododecane (H_4L10)*

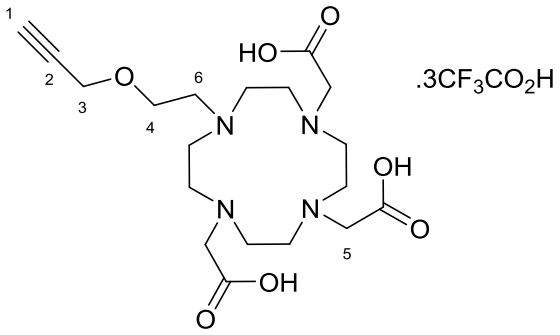

(58) (0.61 g, 1.02 mmol), RP-HPLC t_R = 11.62 min. The title compound was obtained as a colourless oil (0.68 g, 88%). NMR δ_H (500 MHz, D_2O) 4.18 (d, 2H, *J* = 2.3, 3-CH_2), 4.14 (s, 2H, 4-CH_2), 3.9 (t, 2H, *J* = 4.6, 6-CH_2), 3.66- 3.34 (m, 14H, CH_2), 3.2-2.94 (m, 8H, CH_2), 2.87(t, 1H, *J* = 2.3, 1-CH); NMR δ_C (125 MHz, D_2O) 173.1, 167.8 (C=O), 162.3 (q, $^2J_{C\text{-}F}$ = 36.8, $CF_3CO_2^-$), 116.3 (q, $^1J_{C\text{-}F}$ = 290.3, $CF_3CO_2^-$), 77.9 (2-C), 75.3 (1-C), 62.2 (4-C), 57.3 (4-C), 53.8 (5-C), 52.6, 52.1, 50.7, 49.8, 47.5, 47 (CH_2); NMR δ_F (376 MHz, $CDCl_3$) -75.5 (s) ($CF_3CO_2^-$); MS (ESI) 429 $[M+H]^+$; HRMS (ESI) $C_{19}H_{33}N_4O_7$ $[M+H]^+$ requires 429.2358 found 429.2358.

8.10.11 *2,2',2''-(10-(3-(4-(4-methoxypyridin-2-yl)-1H-1,2,3-triazol-1-yl)propyl)-1,4,7,10-tetraazacyclododecane-1,4,7-triyl)triacetic acid (H_3L11)*

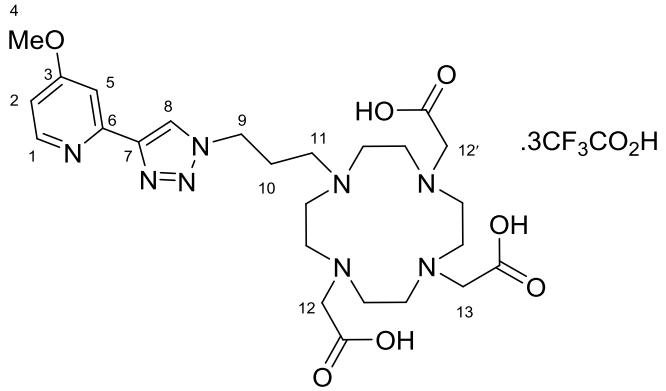

(59) (379 mg, 0.51 mmol), R_f =16.61 min. The title compound was obtained as a white solid (251 mg, 86%). NMR δ_H (400 MHz, D_2O) 8.66 (s, 1H, 8-CH), 8.40 (d, 1H, *J* = 7, 1-CH), 7.65 (d, 1H, *J* = 2.7, 5-CH), 7.29 (dd, 1H, ^3J = 2.6, ^4J = 7, 2-CH), 4.55 (t, 2H, *J* = 6.6, 9-CH_2), 4.02 (s, 3H, 4-CH_3), 3.98 (s, 2H, 13-CH_2), 3.59-2.77 (m, 22H, CH_2), 2.36 (quintet, 2H, *J* = 6.6, 10-CH_2); NMR δ_C (100 MHz, $CDCl_3$) 173.9, 172.6 (Cq), 163.9 (q,

$^{2}J_{C\text{-}F}$ = 35, $CF_3CO_2^-$), 143.5 (3-C), 142.1 (1-C), 139.2 (6-C), 126.3 (8-C), 116 (q, $^{1}J_{C\text{-}F}$ = 290, $CF_3CO_2^-$), 111.8 (2-C), 109.1 (2-C), 57.5 (4-C), 54.6, 52.8, 51.3, 49.9, 48.4, 47.6 (CH_2), 24.1 (10-C); NMR δ_F (376 MHz, $CDCl_3$) -75.5 (s) ($CF_3CO_2^-$); MS(ESI) 563 $[M+H]^+$; HRMS (ESI) $C_{25}H_{39}N_8O_7$ $[M+H]^+$ requires 563.2942 found 563.2941.

8.11 Synthesis of Lanthanide Complexes

General synthesis: the pro-ligand 1 equiv. was dissolved in H_2O then $LnCl_3.6H_2O$ 1.05 equivalent was added, the pH to ~6 was adjusted using 1M NaOH. The reaction mixture was heated to 90 °C and monitored by MS. After 20 h the reaction mixture was cooled and pH raised to 10 (1 M NaOH) then filtered through a celite® plug. The pH was then adjusted to 7 using 1M HCl. The solution was tested for free Ln(III) with xylenol orange. The complexes were purified using RP-HPLC (method B).

8.11.1 *Europium(III) 2,2',2''-(10-(3-(4-(pyridin-2-yl)-1H-1,2,3-triazol-1-yl)propyl) 1,4,7,10-tetraazacyclododecane (EuL1)*

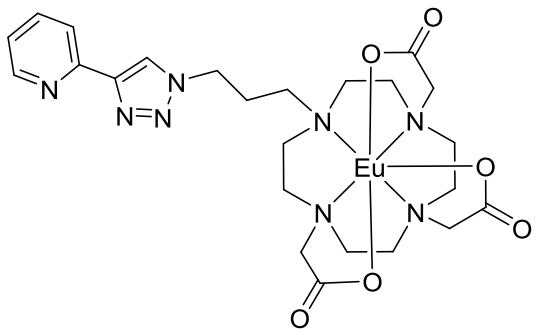

H_3L1 (80.0 mg, 91.8 μmol) and $EuCl_3.6H_2O$ (36.0 mg, 96.4 μmol). **EuL1** was obtained (50.2 mg, 80%) after RP-HPLC t_R = 22.72 m as white solid. MS (ESI) 681 $[M+H]^+$; HRMS (ESI) $C_{24}H_{34}N_8O_6{}^{151}Eu$ $[M+H]^+$ requires 681.1800 found 681.1822. UV-Vis (H_2O): λ_{max}/nm 230 and 280. The ^{1}H NMR spectrum (400 MHz, D_2O) showed broad resonances that were not sufficiently resolved at 273 K.

8.11.2 *Gadolinium(III) 2,2',2''-(10-(3-(4-(pyridin-2-yl)-1H-1,2,3-triazol-1-yl)propyl) 1,4,7,10-tetraazacyclododecane (GdL1)*

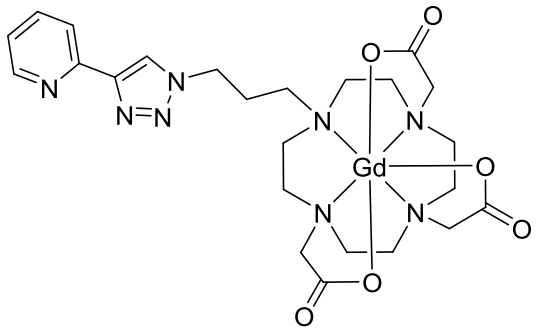

H_3L1 (100 mg, 114.7 µmol) and $GdCl_3.6H_2O$ (45.0 mg, 120.5 µmol). **GdL1** (61 mg, 77%) was obtained after RP-HPLC t_R = 21.53 m as white solid. MS (ESI) 686 $[M+H]^+$, 710 $[M+Na]^+$, HRMS (ESI) $C_{24}H_{34}N_8O_6{}^{158}Gd$ $[M+H]^+$ requires 688.1842 found 688.1858, $C_{24}H_{34}N_8O_6{}^{158}GdNa$ $[M+Na]^+$ requires 710.1662 found 710.1649. UV-Vis (H_2O): λ_{max}/nm 230 and 280.

8.11.3 *Terbium(III) 2,2',2''-(10-(3-(4-(pyridin-2-yl)-1H-1,2,3-triazol-1-yl)propyl) 1,4,7,10-tetraazacyclododecane (TbL1)*

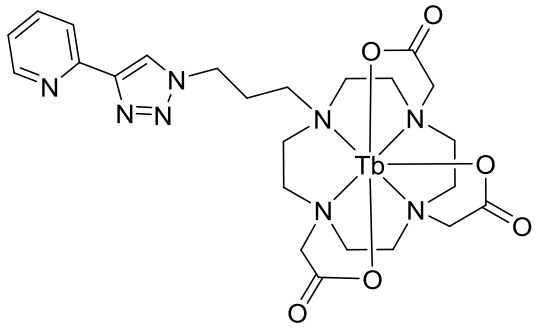

H_3L1 (100 mg, 114.8 µmol) and $TbCl_3.6H_2O$ (32.0 mg, 120.5 µmol). **TbL1** (60.3 mg, 76%) was obtained after RP-HPLC t_R = 21.50 m as white solid. MS (ESI) 689 $[M+H]^+$, 711 $[M+Na]^+$; HRMS (ESI) $C_{24}H_{33}N_8O_6Na^{159}Tb$ $[M+Na]^+$ requires 711.1674 found 711.1675. UV-Vis (H_2O): λ_{max}/nm 230 and 280.

8.11.4 *Yttrium(III) 2,2',2''-(10-(3-(4-(pyridin-2-yl)-1H-1,2,3-triazol-1-yl)propyl) 1,4,7,10-tetraazacyclododecane (YL1)*

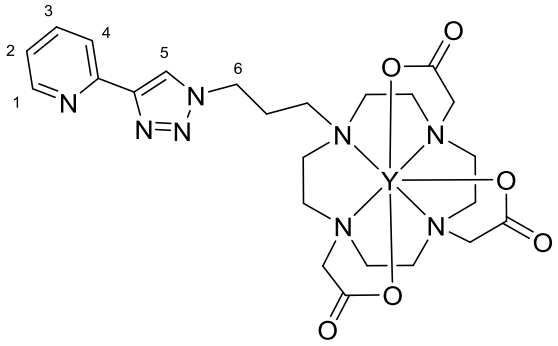

H_3L1 (25.5 mg, 29.2 μmol) and $YCl_3.6H_2O$ (10 mg, 30.1 μmol). **YL1** (13 mg, 73%) was obtained after RP-HPLC t_R = 20.69 m as white solid. NMR δ_H (400 MHz, D_2O) 8.45 (d, *J* = 4.3, 1H, 1-CH), 8.31 (s, 1H, 5-CH), 7.95-7.9 (m, 1H, 4-CH), 7.86-7.82 (m, 1H, 3-CH), 7.42-7.38 (m, 1H, 2-CH), 4.42 (s br, 2H, 6-CH_2), 3.8-1.98 (m, 26H, CH_2); MS (ESI) 620 $[M+H]^+$, 657 $[M+K]^+$; HRMS (ESI) $C_{24}H_{33}N_8O_6Na^{89}Y$ $[M+Na]^+$ requires 641.1479 found 641.1479.

8.11.5 *Europium(III) 2,2',2''-{10-[3-(4-phenyl-1**H**-1,2,3-triazol-1-yl)propyl]-1,4,7,10-tetraazacyclododecane (EuHL2)*

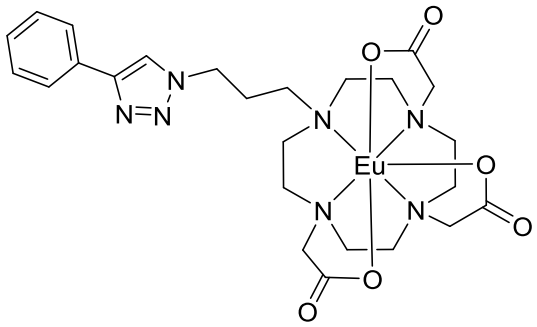

H_4L2 (133 mg, 153 μmol) and $EuCl_3.6H_2O$ (59.0 mg, 160 μmol). **EuHL2** was obtained after RP-HPLC t_R = 20.25 m as white solid (80.3 mg, 77%); MS (ESI) 682 $[M+H]^+$; HRMS (ESI) $C_{25}H_{34}N_7O_6Na^{151}Eu$ $[M+Na]^+$ requires 702.1667 found 702.1675, $C_{25}H_{34}N_7O_6Na^{153}Eu$ $[M+Na]^+$ requires 704.1680 found 704.1681.

8.11.6 *Gadolinium(III) 2,2',2''-{10-[3-(4-phenyl-1**H**-1,2,3-triazol-1-yl)propyl]-1,4,7,10-tetraazacyclododecane (GdHL2)*

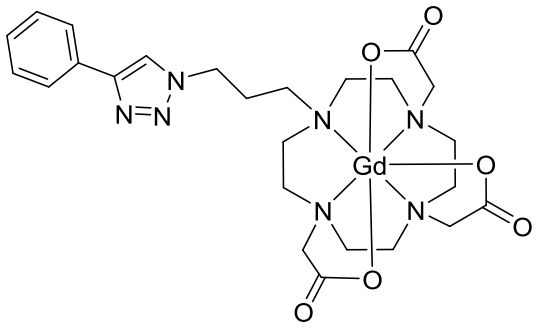

H_4L2 (110 mg, 126 μmol) and $GdCl_3.6H_2O$ (50.0 mg, 133 μmol). **GdHL2** was obtained after RP-HPLC t_R = 19.54 m as white solid (66.7 mg, 76%); MS (ESI) 687 $[M+H]^+$; HRMS (ESI) $C_{25}H_{34}N_7O_6Na^{158}Gd$ $[M+Na]^+$ requires 709.1699 found 709.1709, $C_{25}H_{34}N_7O_6Na^{160}Gd$ $[M+Na]^+$ requires 711.1739 found 711.1781.

8.11.7 *Europium(III) 2,2',2''-[10-(3-{4-[5-(trifluoromethyl)pyridin-2-yl]-1**H**-1,2,3-triazol-1-yl}propyl)-1,4,7,10-tetraazacyclododecane (EuL3)*

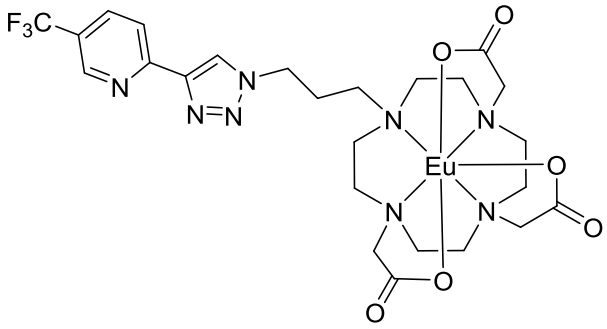

H_3L3 (55.0 mg, 58.5 μmol) and $EuCl_3.6H_2O$ (23.0 mg, 61.5 μmol). **EuL3** was obtained after RP-HPLC t_R = 30.63 m as white solid (31.1 mg, 70%); MS (ESI) 751 $[M+H]^+$; HRMS (ESI) $C_{25}H_{33}N_8O_6F_3^{151}Eu$ $[M+H]^+$ requires 749.1674 found 749.1729, $C_{25}H_{33}N_8O_6F_3^{153}Eu$ $[M+H]^+$ requires 751.1688 found 751.1724.

8.11.8 *Gadolinium(III) 2,2',2''-[10-(3-{4-[5-(trifluoromethyl)pyridin-2-yl]-1**H**-1,2,3-triazol-1-yl}propyl)-1,4,7,10-tetraazacyclododecane (GdL3)*

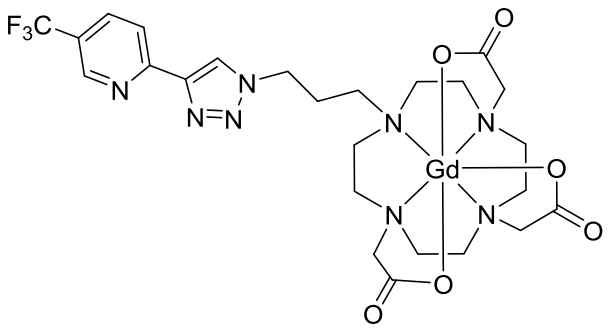

H_3L3 (41.1 mg, 38.5 μmol) and $GdCl_3.6H_2O$ (15.0 mg, 40.4 μmol). **GdL3** (26 mg, 65%) was obtained after RP-HPLC t_R = 21.44 m as white solid; MS (ESI) 777 $[M+Na]^+$; HRMS (ESI) $C_{25}H_{33}N_8O_6F_3Na^{158}Gd$ $[M+Na]^+$ requires 778.1536 found 778.1553, $C_{25}H_{33}N_8O_6F_3Na^{156}Gd$ $[M+Na]^+$ requires 776.1516 found 776.1512.

8.11.9 *Yttrium(III) 2,2',2''-[10-(3-{4-[5-(trifluoromethyl)pyridin-2-yl]-1*H*-1,2,3-triazol-1-yl}propyl)-1,4,7,10-tetraazacyclododecane (YL3)*

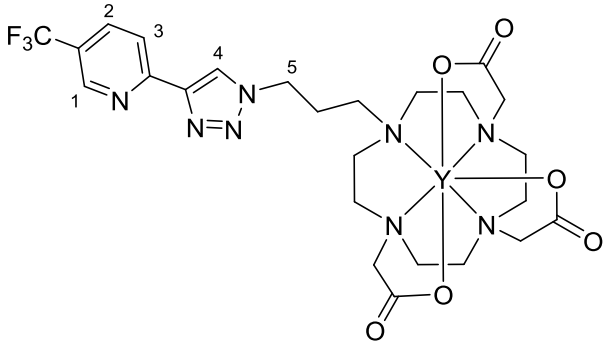

H_3L3 (50.0 mg, 53.2 μmol) and $YCl_3.6H_2O$ (17.0 mg, 55.9 μmol). **YL3** (27 mg, 74%) was obtained after RP-HPLC t_R = 29.56 m as white solid; NMR δ_H (400 MHz, D_2O) 8.8 (d, 1H, *J* = 1.8, 1-CH), 8.46 (s, 1H, 4-CH) 8.18 (dd, 1H, ^3J = 8.3, ^4J = 1.8, 2-CH), 8.02 (d, *J* = 8.3, 1H, 3-CH), 4.49 (s br, 2H, 5-CH_2), 3.7-2.18 (m, 26H, CH_2); NMR δ_F (376 MHz, $CDCl_3$) -62.4 (s); MS (ESI) 687 $[M+H]^+$, 709 $[M+Na]^+$; HRMS (ESI) $C_{25}H_{32}N_8O_6F_3Na^{89}Y$ $[M+Na]^+$ requires 709.1353 found 709.1328.

8.11.10 *Europium(III) 2,2',2''-[10-(3-{4-[4-(trifluoromethyl)pyridin-2-yl]-1H-1,2,3-triazol-1-yl}propyl)-1,4,7,10-tetraazacyclododecane (EuL4)*

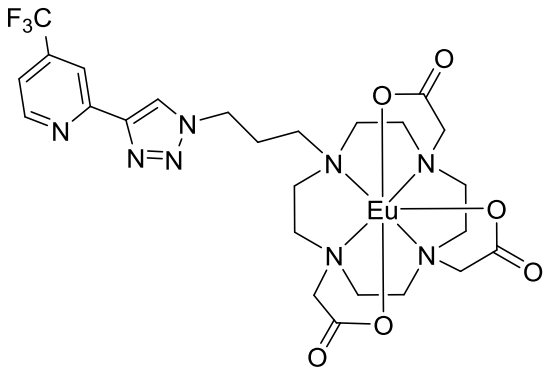

H_3L4 (80.1 mg, 85.19 μmol) and $EuCl_3.6H_2O$ (33.5 mg, 89.4 μmol). **EuL4** was obtained after RP-HPLC t_R = 30.63 m as white solid (48 mg, 75%); MS (ESI) 773 $[M+Na]^+$; HRMS (ESI) $C_{25}H_{32}N_8O_6F_3{}^{151}EuNa$ $[M+Na]^+$ requires 771.1493 found 771.1505, $C_{25}H_{32}N_8O_6F_3{}^{153}EuNa$ $[M+Na]^+$ requires 773.1507 found 773.1539.

8.11.11 *Gadolinium(III) 2,2',2''-[10-(3-{4-[4-(trifluoromethyl)pyridin-2-yl]-1H-1,2,3-triazol-1-yl}propyl)-1,4,7,10-tetraazacyclododecane (GdL4)*

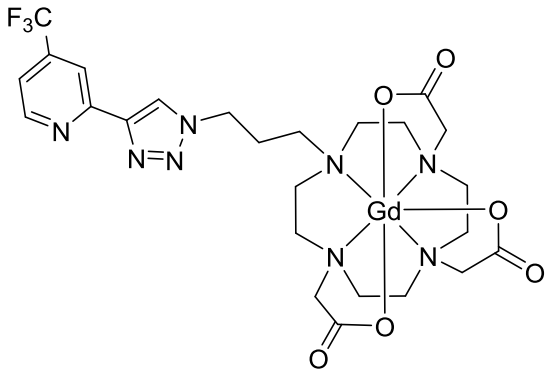

H_3L4 (41.0 mg, 38.5 μmol) and $GdCl_3.6H_2O$ (15.2 mg, 40.4 μmol). **GdL4** (26.2 mg, 65%) was obtained after RP-HPLC t_R = 21.44 m as white solid; MS (ESI) 777 $[M+Na]^+$; HRMS (ESI) $C_{25}H_{33}N_8O_6F_3Na^{158}Gd$ $[M+Na]^+$ requires 778.1536 found 778.1553, $C_{25}H_{33}N_8O_6F_3Na^{156}Gd$ $[M+Na]^+$ requires 776.1516 found 776.1512.

8.11.12 *Europium (III) 2,2',2''-(10-(3-(1-(pyridin-2-yl)-1H-1,2,3-triazol-4-yl)propyl)-1,4,7,10-tetraazacyclododecane (EuL5)*

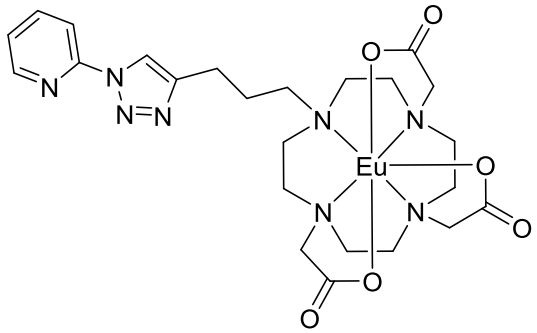

H_3L5 (41.0 mg, 47.0 μmol) and $EuCl_3.6H_2O$ (18 mg, 49.4 μmol). **EuL5** was obtained after RP-HPLC t_R = 20.25 m as white solid (17 mg, 68%); MS (ESI) 705 $[M+Na]^+$; HRMS (ESI) $C_{25}H_{34}N_7O_6Na^{151}Eu$ $[M+Na]^+$ requires 702.1667 found 702.1675, $C_{25}H_{34}N_7O_6Na^{153}Eu$ $[M+Na]^+$ requires 704.1680 found 704.1680.

8.11.13 *Gadolinium(III) 2,2',2''-(10-(3-(1-(pyridin-2-yl)-1H-1,2,3-triazol-4-yl)propyl)-1,4,7,10-tetraazacyclododecane (GdL5)*

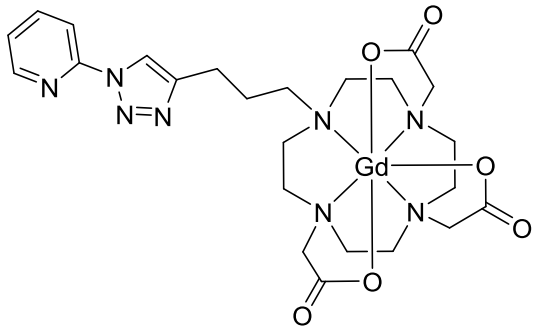

H_3L5 (100 mg, 115 μmol) and $GdCl_3.6H_2O$ (45.0 mg, 121 μmol). **GdL5** (58 mg, 73%) was obtained after RP-HPLC t_R = 23.4 m as white solid. MS (ESI) 710 $[M+Na]^+$; HRMS (ESI) $C_{24}H_{33}N_8O_6{}^{156}GdNa$ [M+Na] requires 708.1647 found 708.1642.

8.11.14 *Europium(III) 2,2',2''-(10-{[4-(pyridin-2-yl)phenyl]methyl}-1,4,7,10-tetraazacyclododecane (EuHL6)*

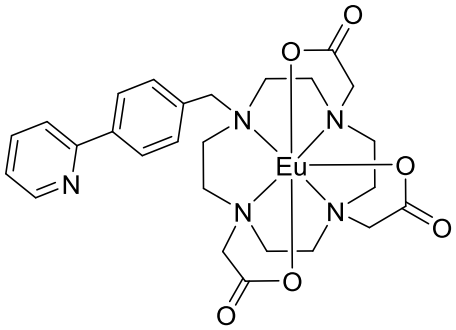

H_4L6 (26.0 mg, 30.5 μmol) and $EuCl_3.6H_2O$ (12.1 mg, 32.2 μmol). **EuL6** (13.4 mg, 65%) was obtained after RP-HPLC t_R = 18.37 m as white solid; MS (ESI) 664 $[M+H]^+$, 682 $[M+Na]^+$; HRMS (ESI) $C_{26}H_{33}N_5O_6{}^{151}Eu$ $[M+H]^+$ requires 662.1629 found 662.1655, $C_{26}H_{33}N_5O_6{}^{153}Eu$ $[M+H]^+$ requires 664.1643 found 664.1667.

8.11.15 *Gadolinium(III) 2,2',2''-(10-{[4-(pyridin-2-yl)phenyl]methyl}-1,4,7,10-tetraazacyclododecane (GdHL6)*

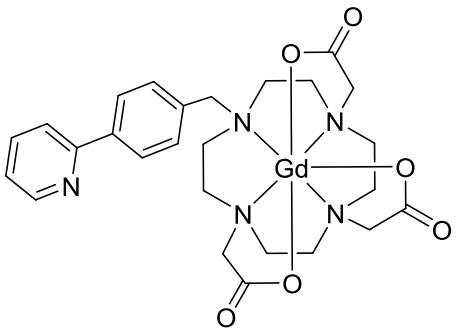

H_4L5 (35.1 mg, 41.2 μmol) and $GdCl_3.6H_2O$ (16.0 mg, 43.1 mmol). **GdL6** was obtained after RP-HPLC t_R = 18.68 m as white solid (20.5 mg, 72%); MS (ESI) 681 $[M+H]^+$, 691 $[M+Na]^+$; HRMS (ESI) $C_{26}H_{32}N_5O_6Na^{156}Gd$ $[M+Na]^+$ requires 689.1472 found 689.1474, $C_{26}H_{32}N_5O_6Na^{158}Gd$ $[M+Na]^+$ requires 691.1491 found 691.1509.

8.11.16 *Europium(III) 2,2',2''-[10-(3-{4-[6-(3-{3-[4,7,10-tris(carboxymethyl)-1,4,7,10-tetraazacyclododecan-1-yl]propyl}-3H-pyrazol-5-yl)pyridin-2-yl]-1H-1,2,3-triazol-1-yl}propyl)-1,4,7,10-tetraazacyclododecane (EuL7)*

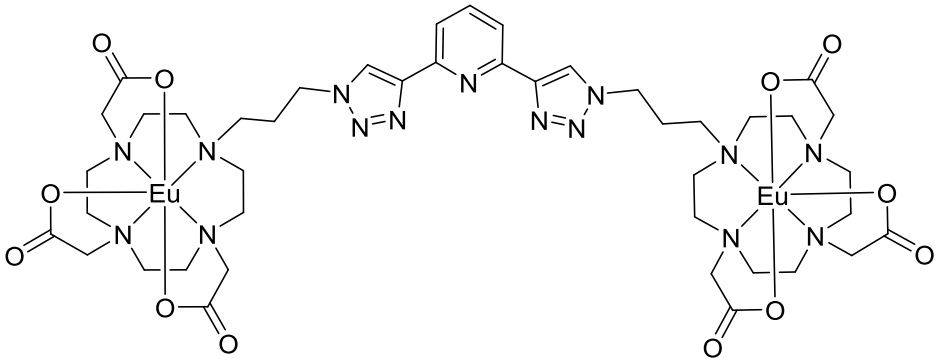

H_6L7 (110 mg, 66.1 μmol) and $EuCl_3.6H_2O$ (51.3 mg, 138.6 μmol). **EuL7** (60.5 mg, 71%) was obtained after RP-HPLC t_R = 22.52 m as white solid; MS (ESI) 1285 $[M+H]^+$, 1306 $[M+Na]^+$; HRMS (ESI) $C_{43}H_{61}N_{15}O_{12}{}^{153}Eu_2Na$ $[M+Na]^+$ requires 1306.2936 found 1306.2905, $C_{86}H_{122}N_{30}O_{24}{}^{153}EuNa$ $[2M+Na]^+$ requires 2591.6003 found 2591.6121.

8.11.17 *Gadolinium(III) 2,2',2''-[10-(3-{4-[6-(3-{3-[4,7,10-tris(carboxymethyl)-1,4,7,10-tetraazacyclododecan-1-yl]propyl}-3H-pyrazol-5-yl)pyridin-2-yl]-1H-1,2,3-triazol-1-yl}propyl)-1,4,7,10-tetraazacyclododecane (GdL7)*

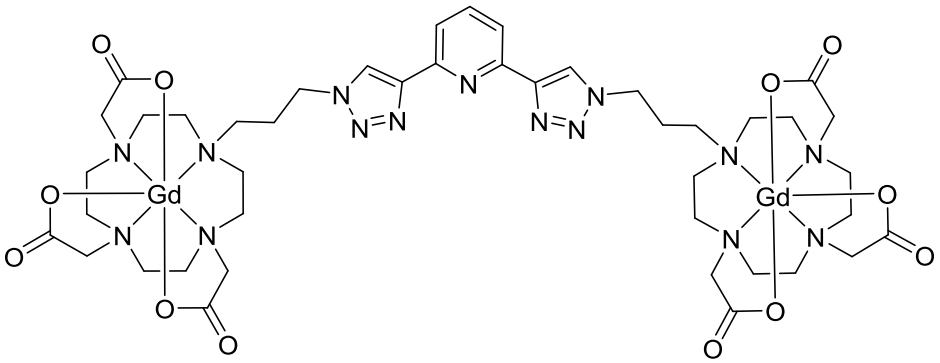

H_6L7 (49.1 mg, 29.4 μmol) and $GdCl_3.6H_2O$ (23.2 mg, 61.7 μmol). **GdL7** (24.7 mg, 63%) was obtained after RP-HPLC t_R = 21.92 m as white solid; MS (ESI) 1296 $[M+H]^+$, 1316 $[M+Na]^+$; HRMS (ESI) $C_{43}H_{61}N_{15}O_{12}{}^{158}Gd_2Na$ $[M+Na]^+$ requires 1318.3015 found 1318.3055, $C_{86}H_{122}N_{30}O_{24}{}^{158}Gd_4Na$ $[2M+Na]^+$ requires 2611.6130 found 2611.6609.

8.11.18 *Yttrium(III) 2,2',2''-[10-(3-{4-[6-(3-{3-[4,7,10-tris(carboxymethyl)-1,4,7,10-tetraazacyclododecan-1-yl]propyl}-3H-pyrazol-5-yl) pyridin-2-yl]-1H-1,2,3-triazol-1-yl}propyl)-1,4,7,10-tetraazacyclododecane (YL7)*

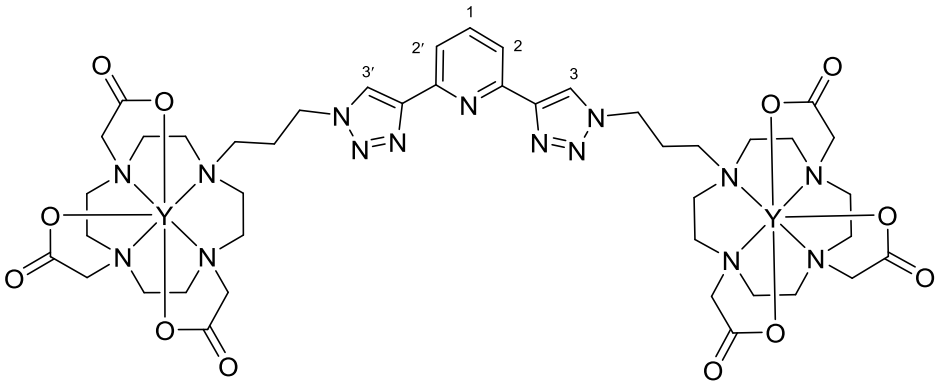

H_6L7 (15.2 mg, 8.5 μmol) and $YCl_3.6H_2O$ (6.1 mg, 18.9 μmol). **YL7** (7.2 mg, 67%) was obtained after RP-HPLC t_R = 22.01 m as white solid. NMR δ_H (400 MHz, D_2O) 8.42 (s br, 2H, 3-CH), 7.95 (s br, 1H, 1-CH), 7.82 (s br, 2H, 2-CH), 3.9-1.65 (m, 56H, CH_2); MS (ESI) 580 $[M+2H]^{2+}$, 591 $[M+H+Na]^{2+}$, 602 $[M+2Na]^{2+}$, 1159 $[M+H]^+$, 1181 $[M+Na]^+$.

8.11.19 *Europium(III) 2,2',2''-(10-{2-[(methanesulfonyl)amino]ethyl}-1,4,7,10-tetraazacyclododecane (EuL8)*

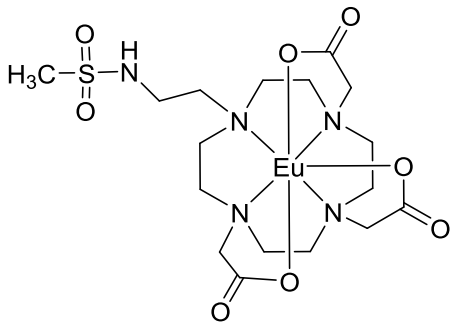

H_3L8 (25.5 mg, 31.6 μmol), $EuCl_3.6H_2O$ (12.3 mg, 32.5 μmol). Giving after RP-HPLC t_R = 6.82 m as white solid (14 mg, 73%); MS (ESI) 616, 618 $[M+H]^+$, 638, 640 $[M+Na]^+$,614, 616 $[M-H]^-$; HRMS (ESI) $C_{17}H_{30}N_5O_8SNa^{151}Eu$ $[M+Na]^+$ requires 638.0911 found 638.0916, $C_{17}H_{30}N_5O_8SNa^{153}Eu$ $[M+Na]^+$ requires 640.0925 found 640.0942.

8.11.20 *Gadolinium(III) 2,2',2''-(10-{2[(methanesulfonyl)amino]ethyl}-1,4,7,10-tetraazacyclododecane (GdL8)*

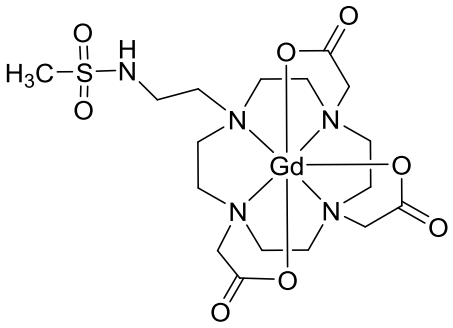

H_3L8 (36.7 mg, 45.5 μmol), $GdCl_3$. $6H_2O$ (18.1 mg, 46.9 mmol). Giving after RP-HPLC t_R = 6.76 m as white solid (16.3 mg, 58%); MS (ESI) 621, 623 $[M+H]^+$, 644, $[M+Na]^+$, MS (ESI) 621, $[M-H]^-$; HRMS (ESI) $C_{17}H_{30}N_5O_8SNa^{156}Gd$ $[M+Na]^+$ requires 643.0934 found 643.0950, $C_{17}H_{30}N_5O_8SNa^{158}Gd$ $[M+Na]^+$ requires 645.0954 found 645.0981.

8.11.21 *Gadolinium(III) 2,2',2''-[10-(but-3-yn-1-yl)-1,4,7,10-tetraazacyclododecane (GdHL9)*

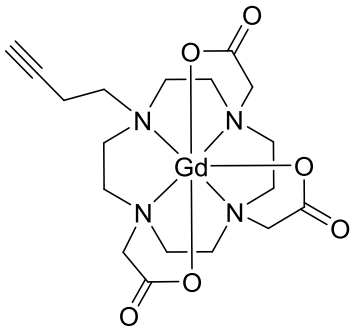

H_4L9 (30.6 mg, 41.7 μmol) with $GdCl_3.6H_2O$ (15.8 mg, 42.7 μmol). **GdHL9** (17.4 mg, 75 %) was obtained as white solid after dissolving in MeOH/DCM and filtering through a celite plug to exclude NaCl; MS (ESI) multipeaks centred on 576 $[M+Na]^+$; HRMS (ESI) $C_{18}H_{27}N_4O_6^{156}GdNa$ $[M+Na]^+$ requires 574.1050 found 574.1052, $C_{18}H_{27}N_4O_6^{157}GdNa$ $[M+Na]^+$ requires 575.1068 found 575.1072.

8.11.22 *Europium(III) 2,2',2''-(10-{2-[(prop-2-yn-1-yl)oxy]ethyl}-1,4,7,10-tetraazacyclododecane (EuHL10)*

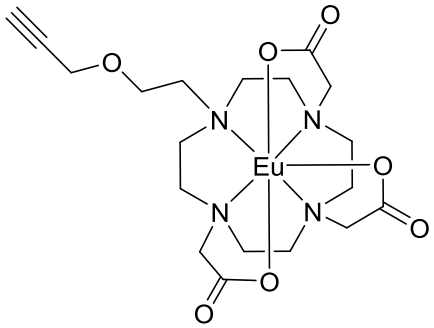

H_4L10 (125 mg, 163.0 µmol) with $EuCl_3.6H_2O$ (62.6 mg, 171.0 µmol) were heated at 50 °C for 18 h. **EuHL10** (72.5 mg, 74%) was obtained as white solid after dissolving in MeOH/DCM and filtering through a celite plug to exclude NaCl; MS (ESI) multipeaks centred on 579 $[M+H]^+$, 599, 601 $[M+Na]^+$; HRMS (ESI) $C_{19}H_{29}N_4O_7{}^{151}EuNa$ $[M+Na]^+$ requires 599.1132 found 599.1140, $C_{19}H_{29}N_4O_7{}^{153}EuNa$ $[M+Na]^+$ requires 601.1146 found 601.1154.

8.11.23 *Gadolinium(III) 2,2',2''-(10-{2-[(prop-2-yn-1-yl)oxy]ethyl}-1,4,7,10-tetraazacyclododecane (GdHL10)*

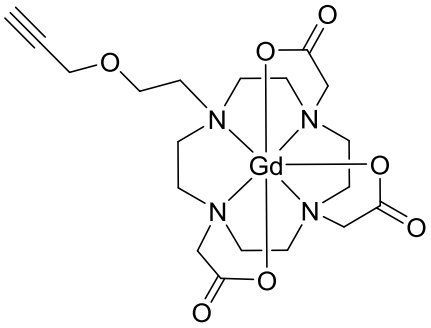

H_4L10 (44.2 mg, 59.9 µmol) with $GdCl_3.6H_2O$ (23.4 mg, 62.9 µmol) were heated at 50 °C for 18 h. **GdHL10** (24.2 mg, 72%) was obtained as white solid after dissolving in MeOH/DCM and filtering through a celite® plug to exclude NaCl; MS (ESI) multipeaks centred on 576 $[M+Na]^+$; HRMS (ESI) $C_{19}H_{29}N_4O_7{}^{156}GdNa$ $[M+Na]^+$ requires 604.1155 found 604.1149, $C_{19}H_{29}N_4O_7{}^{158}GdNa$ $[M+Na]^+$ requires 606.1175 found 606.1172.

8.11.24 *Europium(III) 2,2',2''-(10-(3-(4-(4-methoxypyridin-2-yl)-1H-1,2,3-triazol-1-yl)propyl)-1,4,7,10-tetraazacyclododecane-1,4,7-triyl)triacetic acid (EuL11)*

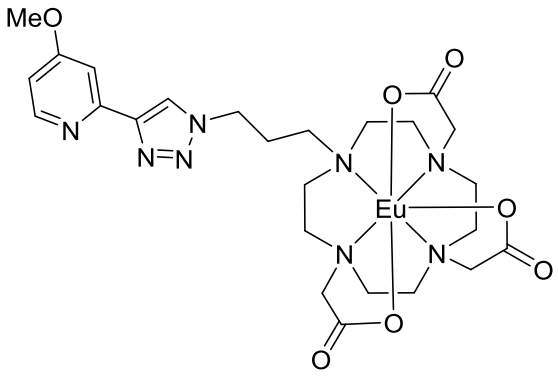

H_3L11 (251 mg, 0.27 mmol) was reacted with $EuCl_3.6H_2O$ (107 mg, 0.29 mmol). The reaction was purified by RP-HPLC (method B) R_f = 26.67 m. The title compound was obtained after freeze drying as white solid (160 mg, 81%). MS (ESI) 713 $[M+H]^+$, 735 $[M+Na]^+$; HRMS (ESI) $C_{25}H_{36}N_8O_7{}^{151}Eu$ $[M+H]^+$ requires 711.1905 found 711.1912, $C_{25}H_{35}N_8O_7{}^{151}EuNa$ requires 733.1725 found 733.1735.

8.12 Synthesis of Iridium Complexes

Ir dimer complexes, General synthesis: 2.1 equiv. (C^N) and 1 equiv. $IrCl_3.xH_2O$ were suspended in 2-propanol:H_2O 3:1 (4 mL). The reaction mixture was heated to 110 °C in microwave reactor for 2 h. For **{Ir(ppy)$_2$Cl}$_2$** dimer, the solvents were removed *in vacuo*, then the crude product was dissolved in DCM (10 mL). The solution was filtered through a celite® plug to remove any undesirable salts produced in the reaction; the organic layer was then washed with 0.1 M HCl (3 x 20 mL) and dried over $MgSO_4$.[145] While with Ir-Ln dimers, the crude products were subjected to RP-HPLC (method B).

Ir-Ln complexes, General synthesis: Ir dimer complex 1 equiv. and (N^N) ancillary complex 2.2 equiv. were dissolved in MeOH (5 mL) and heated at reflux at 90 °C for 18 h. After removing the solvent *in vacuo*, the complexes were purified by RP-HPLC (method B).

8.12.1 *{Ir(ppy)$_2$Cl}$_2$*

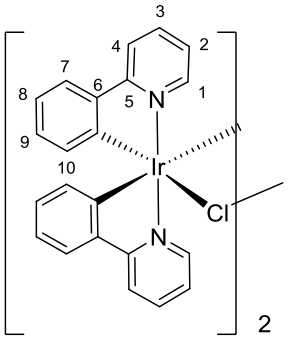

$IrCl_3.xH_2O$ (0.100 g, 0.28 mmol) and phenylpyridin (0.968 g, 0.623 mmol) were afforded the desired product as a yellow solid (0.093 g, 63 %). NMR δ_H (400 MHz, $CDCl_3$) 9.17 (d,4H, *J* = 5.8, 4H, 1-CH), 7.79 (d, 4H, *J* = 7.9, 4-CH), 7.66 (ddd, 4H, *J* = 7.9, 7.8, 1.5, 3-CH) 7.41 (d, *J* = 7.7 Hz, 4H, 7-CH), 6.68 (m , 8H, 2,8-CH), 6.48 (ddd,4H, *J* = 8.3, 8.1, 3.4, 9-CH), 5.85 (d, 4H, *J* = 7.6, 10-CH); NMR δ_C (400 MHz, $CDCl_3$) 168.46 (1-C), 151.91 (2-C), 145.28 (3-C), 144.4 (4-C), 137.08 (5-C), 130.8 (8-C), 129.50 (7-C) , 124.08 (6-C); MS (ESI) m/z 1072 $[M]^+$.

8.12.2 *Ir(ppy)$_2$EuL1*

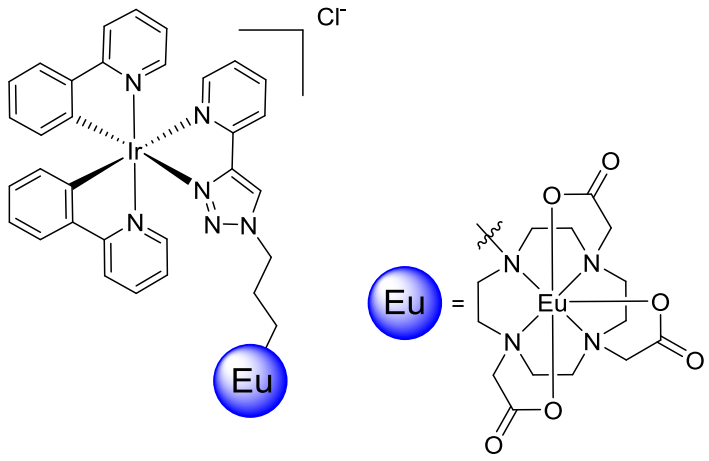

{Ir(ppy)$_2$Cl}$_2$ (26.3 mg, 24.5 μmol) and **EuL1** (36.7 mg, 53.9 μmol), gives the title complex as a pale yellow solid (31.2 mg, 52%) after RP-HPLC t_R = 25.98 m. MS (ESI) multiple peaks centred at 1181 $[M]^+$; HRMS (ESI) $C_{46}H_{49}N_{10}O_6{}^{151}Eu^{193}Ir$ $[M]^+$ requires 1181.2664 found 1181.2678.

8.12.3 *Ir(ppy)$_2$GdL1*

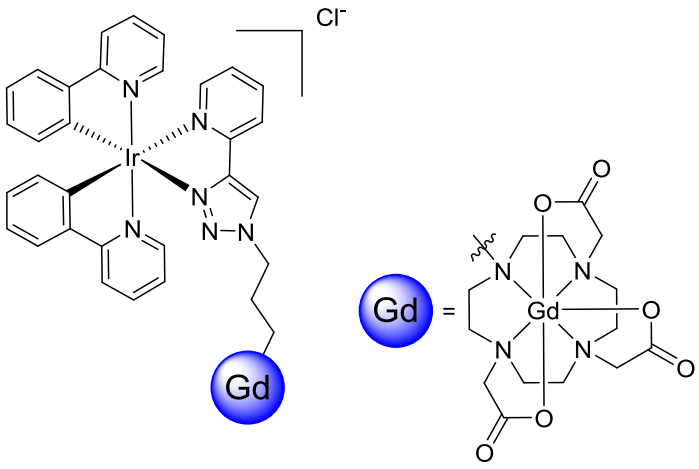

{Ir(ppy)$_2$Cl}$_2$ (10.3 mg, 9.6 µmol) and **GdL1** (14.5 mg, 21.1 µmol), gives the title complex as a bright yellow solid (12 mg, 53%) after RP-HPLC t_R = 25.06 m. MS (ESI) multiple peaks centred at 1188 $[M]^+$;HRMS (ESI) $C_{46}H_{49}N_{10}O_6{}^{158}Gd^{193}Ir$ $[M]^+$ requires 1188.2707 found 1188.2771.

8.12.4 *Ir(ppy)$_2$GdL5*

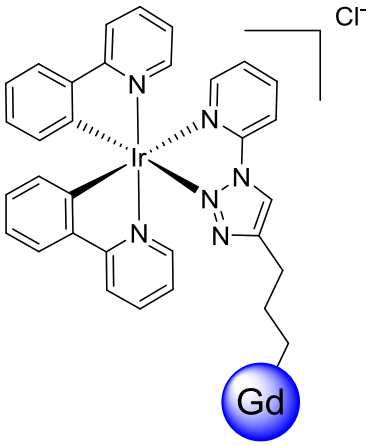

{Ir(ppy)$_2$Cl}$_2$ (15.5 mg, 14.4 µmol) and **GdL5** (21.8 mg, 31.8 µmol) were reacted to give the title complex as a pale yellow solid (19.1 mg, 53%) after RP-HPLC t_R = 30.06 m. MS (ESI) multiple peaks centred at 1186 $[M]^+$; HRMS (ESI) $C_{46}H_{49}N_{10}O_6{}^{160}Gd^{191}Ir$ $[M]^+$ requires 1188.2713 found 1188.2798, $C_{46}H_{49}N_{10}O_6{}^{158}Gd^{193}Ir$ $[M]^+$ requires 1188.2707 found 1188.2798.

8.12.5 ***Ir(ppy)$_2$EuL11***

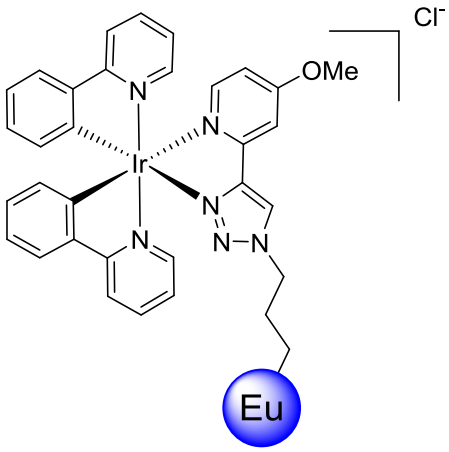

{Ir(ppy)$_2$Cl}$_2$ (9.1 mg, 8.48 µmol) and **EuL11** (13.5 mg, 18.96 µmol) were dissolved in MeOH:DCM (1:1) 6 mL and heated at reflux. The title complex as a pale yellow solid (5.6 mg, 50%). MS (ESI) multiple peaks centred at 1210 $[M]^+$; HRMS (ESI) $C_{47}H_{51}N_{10}O_7{}^{151}Eu^{191}Ir$ $[M]^+$ requires 1209.2747 found 1209.2765, $C_{47}H_{51}N_{10}O_7{}^{151}Eu^{193}Ir$ $[M]^+$ requires 1211.2770 found 1211.2792.

8.12.6 ***IrEuL2*** *(dimer)*

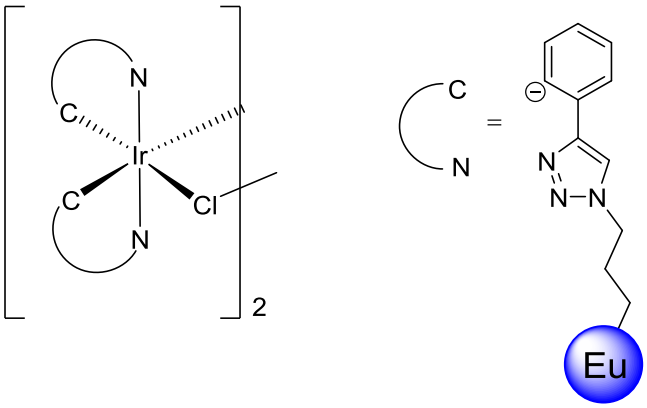

EuHL2 (17.1 mg, 25.1 µmol) and $IrCl_3.xH_2O$ (4.2 mg, 12.0 µmol). The title compound was obtained after RP-HPLC t_R = 16.17 m as a pale yellow solid (8.1 mg, 44%). MALDI (TOF) *m/z* multiple peaks centred at 1551.4646 showing 2 ^{151}Eu and ^{191}Ir isotopes patterns [Ir(**EuL2**)$_2$]$^+$.

8.12.7 ***IrGdL2*** *(dimer)*

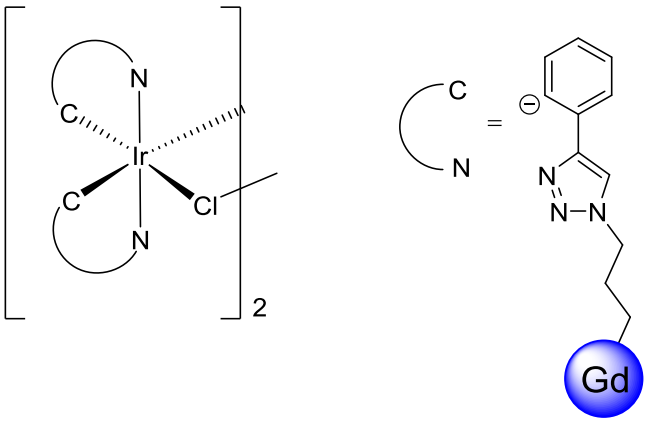

GdHL2 (34.3 mg, 50.0 µmol) and $IrCl_3.xH_2O$ (8.4 mg, 23.8 µmol). The title compound was obtained after RP-HPLC t_R = 15.20 min as a pale yellow solid (18.1 mg, 49%). MALDI (TOF) *m/z* multiple peaks centred at 1560.9862 showing 2 ^{158}Gd and ^{191}Ir isotopes pattern $[Ir(\mathbf{GdL2})_2]^+$.

8.12.8 ***IrEuL6*** *(dimer)*

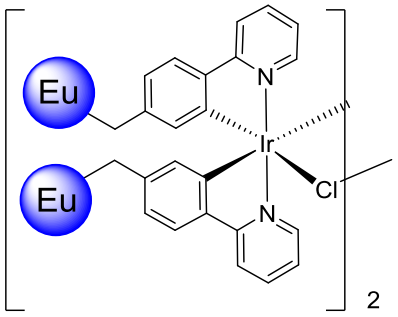

EuHL6 (45.5 mg, 68.6 µmol) and $IrCl_3.xH_2O$ (11.5 mg, 32.7 µmol). The residue was purified by RP-HPLC t_R = 6.83 min to afford the title compound as a pale yellow solid (22.6 mg, 50%). MS (ESI) multiple peaks centred at 1515 $[M]^+$; HRMS (ESI) $C_{52}H_{62}N_{10}O_{12}{}^{151}Eu_2{}^{191}Ir$ $[Ir(EuL6)_2]^+$ requires 1515.2601 found 1515.2593.

8.12.9 ***IrGdL6*** *(dimer)*

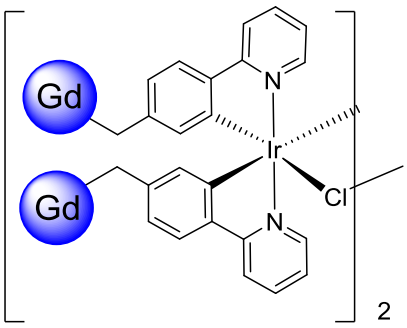

GdHL6 (45.5 mg, 68.1 µmol) and $IrCl_3.xH_2O$ (11.5 mg, 32.5 µmol). The residue was purified by RP-HPLC t_R = 6.86 m to afford the title compound as a pale yellow solid (21.3 mg, 47%). MALDI (TOF) *m/z* multiple peaks centred at 1560.9862 showing 2 ^{158}Gd and ^{195}Ir isotopes pattern [Ir(**GdL6**)$_2$]$^+$.

8.12.10 ***IrEuL2L1***

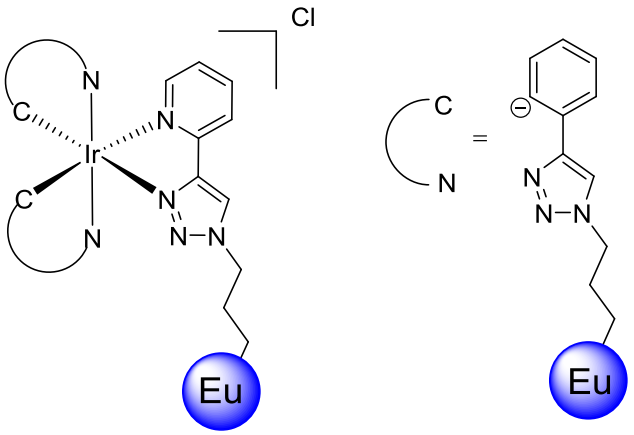

IrEuL2 (12.1 mg, 3.9 µmol) and **EuL1** (5.8 mg, 8.5 µmol), the residue was purified by RP-HPLC t_R = 15.86 m to afford the title compound as a pale yellow solid (6.1 mg, 35%). MALDI (TOF) *m/z* multiple peaks centred at 2233.5378 showing isotopes patterns 3 ^{151}Eu and ^{191}Ir [M]$^+$.

8.12.11 ***IrGdL2L1***

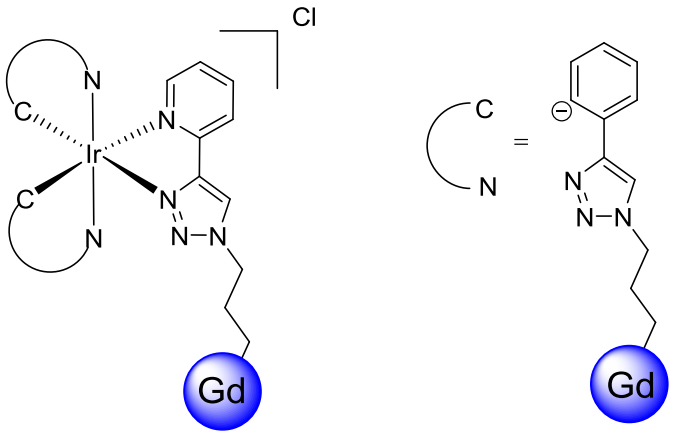

IrGdL2 (15.2 mg, 4.7 µmol) and **GdL1** (7.2 mg, 10.4 µmol), gives after RP-HPLC t_R = 22.54 min the title complex as a pale yellow solid (7.2 mg, 33%). MALDI (TOF) *m/z* multiple peaks centred at 2251.6014 showing isotopes patterns 3 ^{158}Gd and ^{191}Ir $[M]^+$.

8.12.12 ***IrEuL6L3***

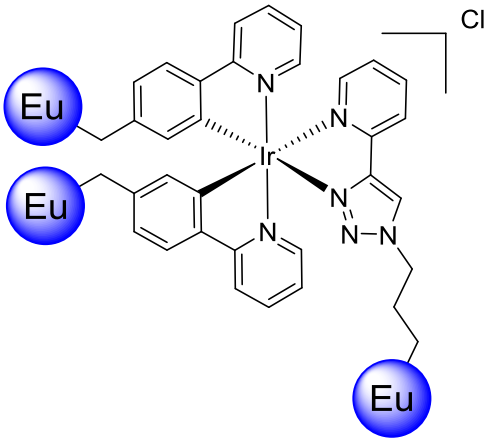

IrEuL6 (10.3 mg, 3.3 µmol) and **EuL1** (4.4 mg, 7.2 µmol). Gives the title complex as a pale yellow solid (6.1 mg, 43%) after RP-HPLC t_R = 18.6 m. MALDI (TOF) *m/z* multiple peaks centred at 2198.1067 showing isotopes patterns 3 ^{151}Eu and ^{195}Ir $[M]^+$.

8.12.13 ***IrGdL6L1***

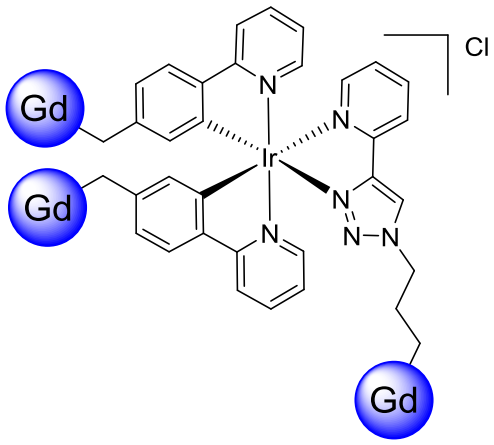

IrGdL6 (10.2 mg, 3.2 μmol) and **GdL1** (5.0 mg, 7.1 μmol), gives the title complex as a pale yellow solid (6.2 mg, 42%) after RP-HPLC t_R = 18.6 min. MALDI (TOF) *m/z* multiple peaks centred at 2212.6676 showing isotopes patterns 3 ^{158}Gd and ^{191}Ir $[M]^+$.

8.12.14 ***IrGdL6L3***

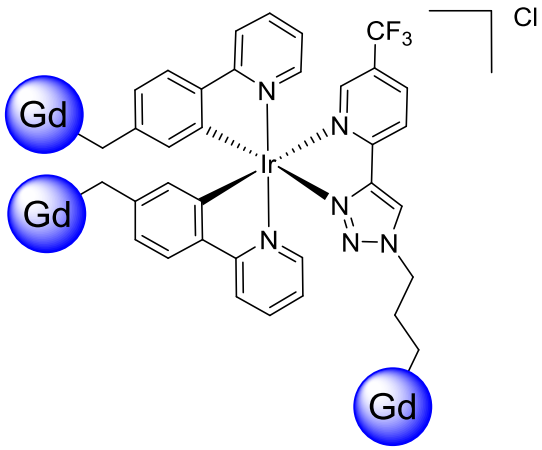

IrGdL6 (10.2 mg, 3.2 μmol) and **GdL3** (5.2 mg, 7.0 μmol), gives the title complex as a pale yellow solid (6.2 mg, 40%) after RP-HPLC t_R = 18.6 min. MALDI (TOF) *m/z* multiple peaks centred at 2282.6501 showing isotopes patterns 3 ^{158}Gd and ^{191}Ir $[M]^+$.

8.13 Synthesis of Platinum Complexes

8.13.1 *Pt(N^C^N)I*

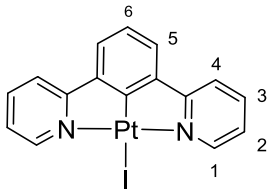

A mixture of **Pt(N^C^N)Cl** (41.5 mg, 90.0 μmol) and KI (149 mg, 0.90 mmol) were stirred in (MeOH:DCM 1:1) (20 mL) at rt. After 18 h, the reaction mixture was filtered through celite® plug followed by removing the solvents *in vacuo*. The residue was purified by normal phase chromatography SiO_2 (100% DCM). The title compound was obtained as bright yellow solid (47.2, 95%). NMR δ_H (500 MHz, $CDCl_3$) 9.89 (d, 2H, J = 5.0, J_{Pt} = 37.9, 1-CH), 7.92 (ddd, 2H, ^3J = 8.7, ^4J = 7.7, ^5J = 1.5, 3-CH), 7.68 (d, 2H, J = 7.5, 4-CH), 7.45 (d, 2H, J = 7.5, 5-CH), 7.2-7.3 (m, 3H, 2,6-CH); Ms (ESI) 425 $[M\text{-}I]^+$; HRMS (ESI) $C_{16}H_{11}IN_2$ ^{194}Pt $[M\text{-}I]^+$ requires 551.9593 found 425.0549.

8.13.2 *PtGdL9*

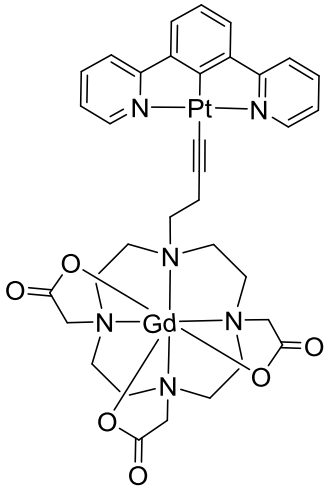

To degassed Schlenk tube **GdHL9** (22.0 mg, 39.8 μmol), CuI (~1 mg), KOH (5 mg, 89.1 μmol), DIPA (2 mL) were added and suspended in (DCM:DMF 1:2) (6 mL). After freeze-pump-thaw (3 x), the suspension was stirred for 30 m then **Pt(N^C^N)Cl** (6.1 mg, 13.2 μmol) was added. After 48 h stirring in the dark at rt, the solvents were

removed *in vacuo*, then the crude product was washed with DCM, MeOH and H_2O. The title compound was obtained as brown solid (8.2 mg, 63 %). MS (ESI) along with isotopic distribution of Pt and Gd in multiple peaks centred on 1018 $[M+K]^+$.

8.13.3 ***PtEuL10***

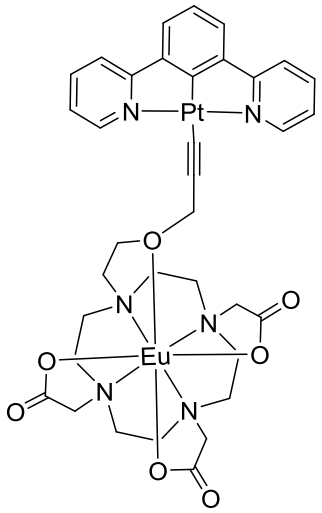

EuHL10 (49.0 mg, 84.8 μmol) and NaOH (20.1 mg, 0.50 mmol) were dissolved in MeOH (5 mL). After stirring for 30 m, **Pt(N^C^N)I** (15.2 mg, 27.4 μmol) was added to the reaction mixture and left to stir at rt for 48 h in the dark. The solvent was removed *in vacuo*, then suspended in DCM (10 mL) and filtered through celite® plug, after that the residue was concentrated, suspended MeOH (5 mL), followed by centrifuging and filtering through celite® plug. The red unfiltered precipitate was taken up in water, then freeze dry it to obtain the title compound as yellow solid and kept in the dark (16.6 mg, 59 %). MS (ESI) along with isotopic distribution of Pt and Gd centred on 1025 $[M+Na]^+$; HRMS (ESI) $C_{35}H_{39}N_6O_7{}^{151}Eu^{194}PtNa$ $[M+Na]^+$ requires 1023.1603 found 1023.1633, $C_{35}H_{39}N_6O_7{}^{151}Eu^{196}PtNa$ $[M+Na]^+$ requires 1025.1626 found 1025.1646.

8.13.4 ***PtGdL10***

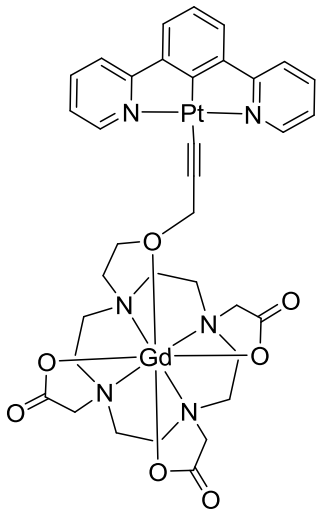

A dry Schlenck tube was charged with **GdHL10** (30.4 mg, 51.1 μmol), KOH (5.0 mg, 89.1 μmol) and CuI (~1 mg) in (DMF:DCM 2:1) (3 mL) and Et_3N (1 mL). The mixture was freeze-pump-thaw (3 x) then left to stir for 30 m, after which **Pt(N^C^N)Cl** (8.1 mg, 17.5 μmol) was added and left to stir at rt for 48 h in the dark. The solvents were removed *in vacuo*, then suspended in DCM (10 mL) and filtered through celite® plug, after that the residue was concentrated, suspended MeOH (5 mL), followed by centrifuging and filtering through celite® plug. The red unfiltered precipitate was taken up in water, then freeze dry it to obtain the title compound as dark red solid and kept in the dark (8.2 mg, 46%). MS (ESI) along with isotopes pattern distribution of Pt and Eu centred on 1030 $[M+Na]^+$; HRMS (ESI) $C_{35}H_{39}N_6O_7{}^{156}Gd{}^{194}PtNa$ $[M+Na]^+$ requires 1028.1626 found 1028.1678, $C_{35}H_{39}N_6O_7{}^{156}Gd{}^{196}PtNa$ $[M+Na]^+$ requires 1030.1648 found 1030.1677.

8.14 Synthesis of Ruthenium Complexes

General synthesis: Ln(III)-complex ~3 equivalents was heated at reflux with 1 equivalent of $RuCl_3$ for 18 h in EtOH (7 mL). The reaction mixture purified by RF-HPLC (method B).

8.14.1 ***RuEuL1***

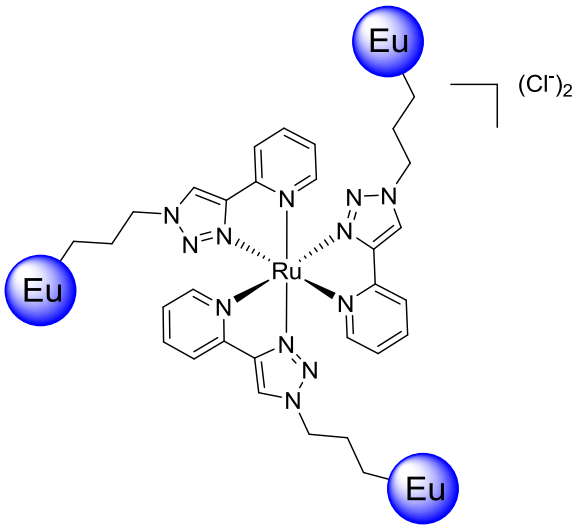

EuL1 (21.0 mg, 30.8 µmol) with $RuCl_3$ (2.1 mg, 10.1 µmol). Giving after RP-HPLC t_R = 7.5 min brown solid (8.1 mg, 37%). MS (ESI) 1072, 1073, 1075 corresponding to Ru, Eu isotopes patterns $[M]^{2+}$; HRMS (ESI) $C_{72}H_{98}N_{24}O_{18}RuEu_3$ $[M]^{2+}$ requires 1073.2130 found 1073.2079.

8.14.2 ***RuGdL1***

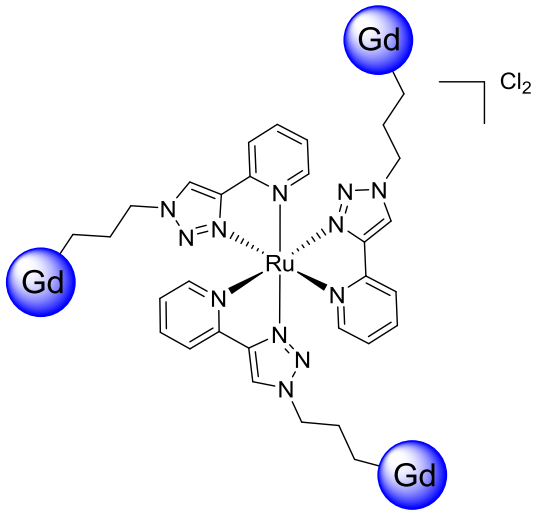

GdL1 (21.0 mg, 30.6 µmol) with $RuCl_3$ (2.1 mg, 10.1 µmol). Giving after RP-HPLC t_R = 6.82 min dark brown solid (6.2 mg, 28%). MS (ESI) corresponding to Ru, Eu isotopes patterns centred on 1080 $[M]^{2+}$; HRMS (ESI) $C_{72}H_{99}N_{24}O_{18}RuGd_3$ $[M]^{2+}$ requires 1080.7180 found 1080.7200.

8.14.3 ***RuYL3***

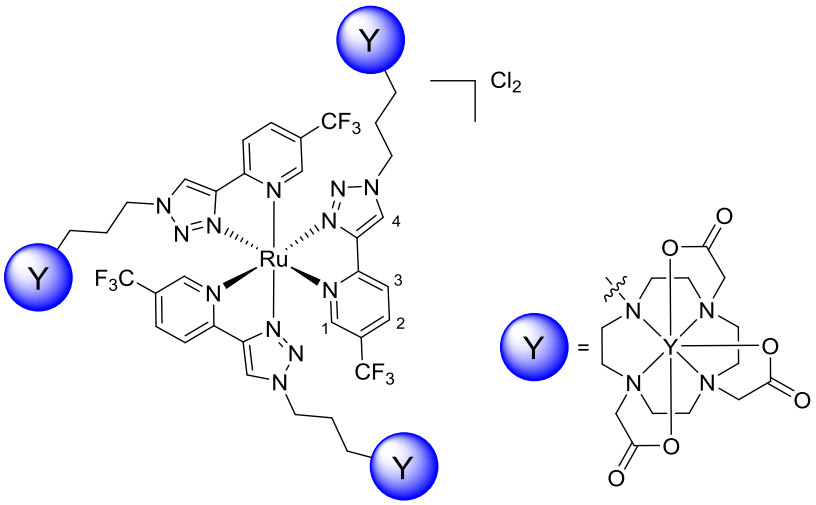

YL3 (26.1 mg, 42.1 µmol) with $RuCl_3$ (2.5 mg, 12.6 µmol). Giving after RP-HPLC t_R = 7.5 min dark green solid (7 mg, 26%); NMR δ_H (400 MHz, D_2O) 9.26-8.96 (m, 3H, 1-CH), 8.48-8.26 (m, 6H, 2,4-CH), 8.08-7.74 (m, 3H, 3-CH) 4.66-4.29 (m, 6H, CH_2), 4.08-1.92 (m, 78H, CH_2); NMR δ_F (376 MHz, $CDCl_3$) -62.57, -62.63, -6279 (s). MS (ESI) corresponding to Ru, Y isotopes patterns centred on 1081 $[M]^{2+}$; HRMS (ESI) $C_{75}H_{98}F_9N_{24}O_{18}RuY_3$ $[M]^{+2}$ requires 1080.1715 found 1080.1497.

8.14.4 ***RuGdL3***

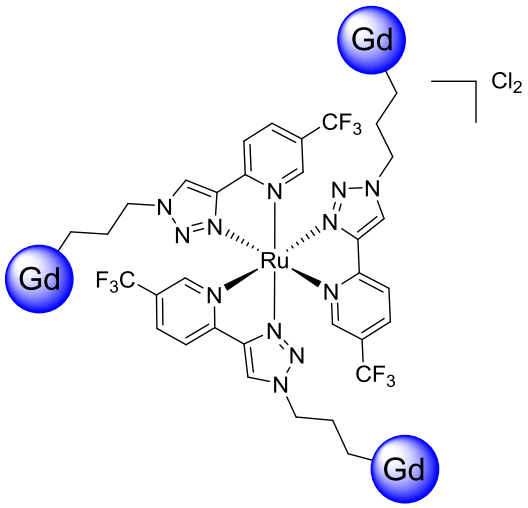

GdL3 (35.2 mg, 46.6 µmol) with $RuCl_3$ (3.1 mg, 14.9 µmol). Giving after semi-prep HPLC t_R = 16.84 min brown solid (12.2 mg, 34%); MS (ESI) corresponding to Ru, Gd isotopes patterns centred on 1183 $[M]^{2+}$.

8.15 Synthesis of Cobalt and Iron Complexes

8.15.1 ***CoGdL1***

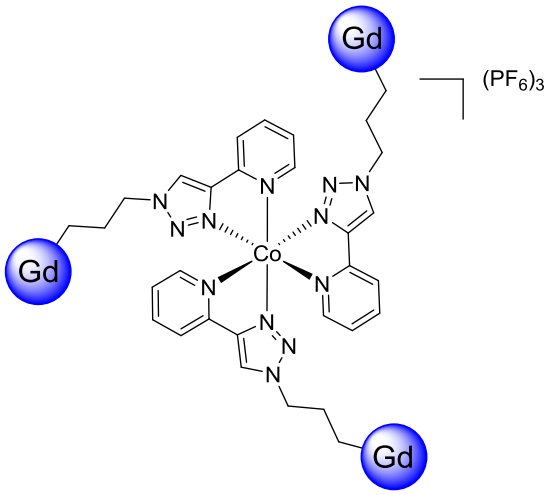

$CoCl_2.6H_2O$ (7.1 mg, 29.4 µmol), **GdL1** (61.2 mg, 89.1 µmol), and KPF_6 (17 mg, 94 µmol) were refluxed at the boiling point in EtOH (5 mL) and H_2O_2 (1 mL). Giving after RP-HPLC t_R = 7.55 min red solid (37.4 mg, 49%); MS (ESI) corresponding to Co, Gd isotopes patterns centred on 1060 $[M+H]^{2+}$.

8.15.2 ***CoEuL1***

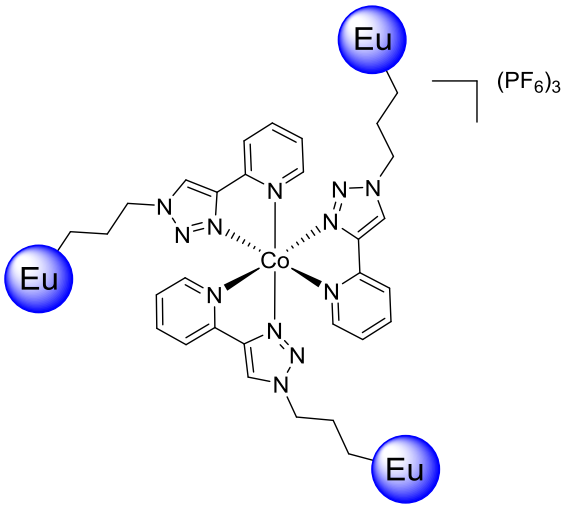

$CoCl_2.6H_2O$ (7 mg, 29.4 µmol), **EuL1** (62 mg, 90 µmol), and KPF_6 (17 mg, 94 µmol) were heated at reflux in EtOH (5 mL) and H_2O_2 (1 mL). Giving after RP-HPLC t_R = 7.45 min red solid (39 mg, 52%); MS (ESI) corresponding to Co, Eu isotopes patterns centred on 1051, 1053 $[M+H]^{2+}$; HRMS (ESI) $C_{72}H_{99}N_{24}Eu_3CoO_{18}$ $[M-H]^{2+}$ requires 1051.7268 found 1051.7244.

8.15.3 ***FeGdL1***

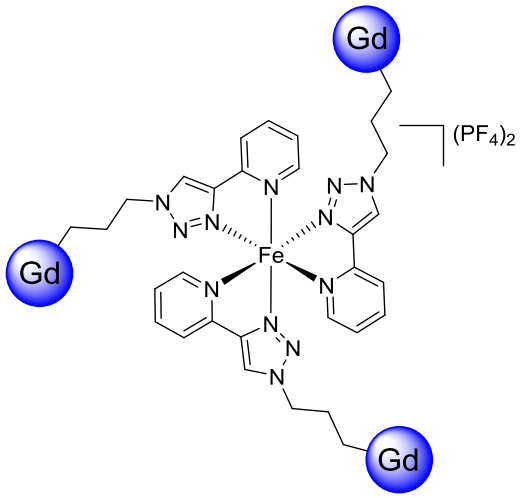

$Fe(BF_4)_2.6H_2O$ (7.0 mg, 20.7 µmol) and **GdL1** (44.1 mg, 64.2 µmol) were heated at reflux in EtOH (5 mL). Giving after RP-HPLC t_R = 8.20 min red solid (21.3 mg, 43%); MS (ESI) corresponding to Fe, Gd isotopes patterns centred on 1060 $[M+H]^{2+}$; HRMS (ESI) $C_{72}H_{99}N_{24}{}^{158}Gd_3FeO_{18}$ $[M]^{+2}$ requires 1059.2130 found 1059.7081.

8.16 Synthesis of Rhenium Complexes

General synthesis: 1 equiv. from Ln(III)-pyta or phta complexes were dissolved in MeOH (7 mL) then 1.05 equiv. $Re(CO)_5Cl$ or $Re(CO)_5(OTf)$[214] was added and heated at reflux for 18 h in inert conditions. After which dry pyridine (100 µL) was added and re-heated at reflux for 18 h. The reaction mixture was purified by RP-HPLC (method B).

8.16.1 ***ReEuL1Cl***

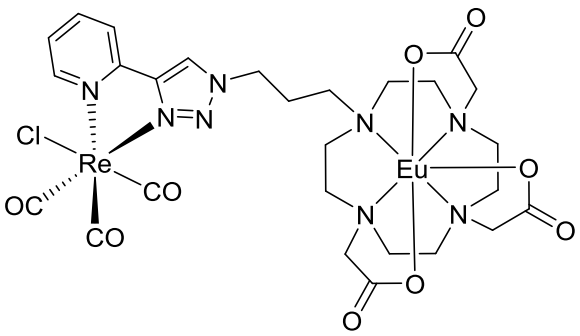

EuL1 (16.1 mg, 23.6 μmol) and $Re(CO)_5Cl$ (9.2 mg, 25.4 μmol) were dissolved in MeOH (5 mL). The reaction mixture was purified by RP-HPLC t_R = 25.34 m to give the title compound as white solid (11.2 mg, 48%). MS (ESI) 494 $[M-Cl]^+$; HRMS (ESI) $C_{27}H_{33}N_8O_9{}^{151}Eu^{185}Re$ $[M-Cl]^+$ requires 949.1092 found 949.1099, $C_{27}H_{33}N_8O_9NaCl^{151}Eu^{185}Re$ $[M+Na]^+$ requires 1007.0749 found 1007.0685.

8.16.2 ***ReGdL1Cl***

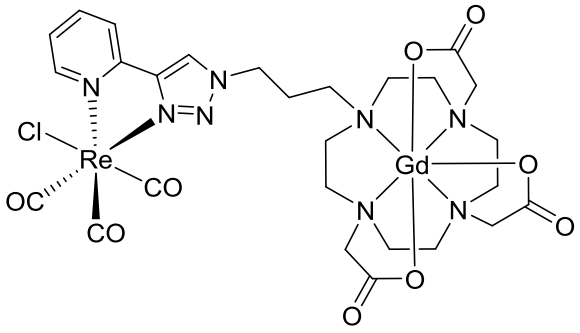

GdL1 (15.6 mg, 22.7 μmol) and $Re(CO)_5Cl$ (8.6 mg, 23.8 μmol) were dissolved in MeOH (5 mL). The reaction mixture was purified by RP-HPLC t_R = 25.30 m to give the title compound as white solid (5.1 mg, 48%). MS (ESI) 956 $[M-Cl]^+$; HRMS (ESI) $C_{27}H_{33}N_8O_9{}^{158}Gd^{185}Re$ $[M-Cl]^+$ requires 956.1216 found 956.1153, $C_{27}H_{33}N_8O_9NaCl^{156}Gd^{185}Re$ $[M+Na]^+$ requires 1016.0749 found 1016.0873.

8.16.3 ***RepyEuL1***

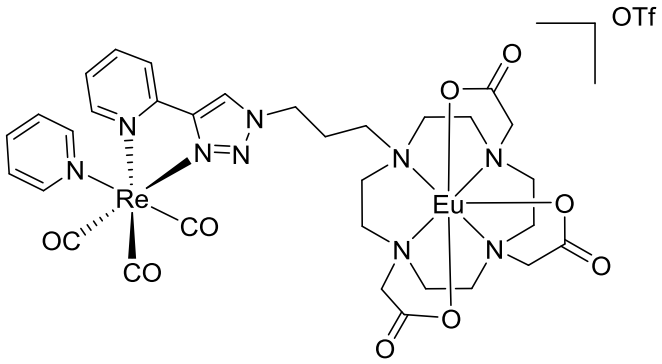

EuL1 (28.3 mg, 41.5 μmol) and $Re(CO)_5OTf$ (21.2 mg, 44.6 μmol). The reaction mixture was purified by RP-HPLC t_R = 23.24 min to give the title compound as white solid (16.1 mg, 33% over two steps). MS (ESI) 1032 $[M]^+$, 951 $[M-py]^+$; HRMS (ESI) $C_{32}H_{38}N_9O_9{}^{151}Eu^{185}Re$ $[M]^+$ requires 1028.1521 found 1028.1499, $C_{32}H_{38}N_9O_9{}^{151}Eu^{187}Re$ $[M]^+$ requires 1030.1549 found 1030.1577.

8.16.4 ***RepyGdL1***

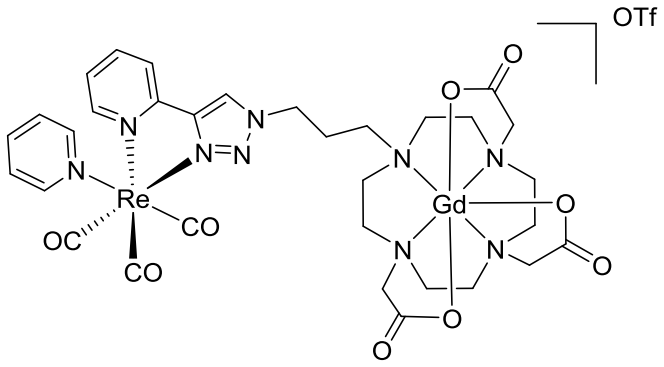

GdL1 (28.5 mg, 41.4 μmol) and $Re(CO)_5OTf$ (21.4 mg, 45.0 μmol). The reaction mixture was purified by RP-HPLC t_R = 23.82 min to give the title compound as white solid (21.5 mg, 43 % over two steps). MS (ESI) 1037 $[M]^+$, 956 $[M\text{-}py]^+$; HRMS (ESI) $C_{32}H_{38}N_9O_9{}^{156}Gd^{185}Re$ $[M]^+$ requires 1033.1544 found 1033.1511, $C_{32}H_{38}N_9O_9{}^{158}Gd^{187}Re$ $[M]^+$ requires 1037.1591 found 1037.1606.

8.16.5 ***RepyYL1***

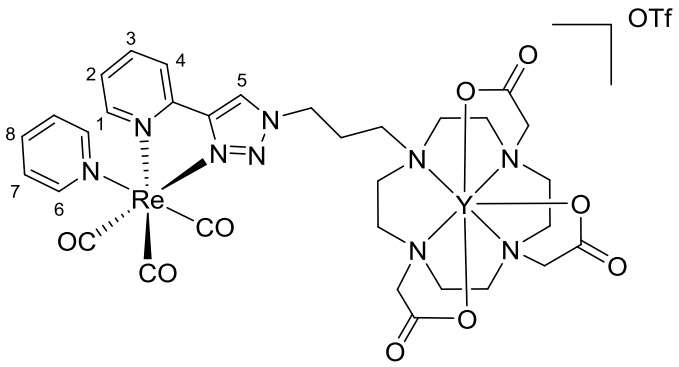

YL1 (12.5 mg, 20.2 μmol) and $Re(CO)_5OTf$ (10 mg, 20.5 μmol). The reaction mixture was purified by RP-HPLC t_R = 23.76 min to give the title compound as white solid (7.5 mg, 33% over two steps). NMR δ_H (400 MHz, D_2O) 9.22 (d, 1H, *J* = 5.3, 1-CH), 8.76 (s, 1H, 5-CH), 8.3 (d, 2H, *J* = 5.1, 6-CH), 8.15 (ddd, ^3J = 7.8 , ^3J = 8, ^4J = 1.1 , 1H, 3-CH), 7.94 (app d, 1H, *J* = 8, 4-CH), 7.81 (tt, 1H, ^3J = 1.3, ^4J = 7.6, 8-CH), 7.64 (ddd, ^3J = 5.5,5.6, ^4J = 1.1, 1H, 2-CH), 7.28-7.25 (m, 2H, 7-CH), 3.83-2.09 (m, 28H, CH_2). MS (ESI) 968 $[M]^+$, 889 $[M\text{-}py]^+$; HRMS (ESI) $C_{32}H_{38}N_9O_9{}^{89}Y^{185}Re$ $[M]^+$ requires 966.1381 found 966.1395, $C_{32}H_{38}N_9O_9{}^{89}Y^{187}Re$ $[M]^+$ requires 968.1409 found 968.1416.

8.16.6 ***ReEuL2***

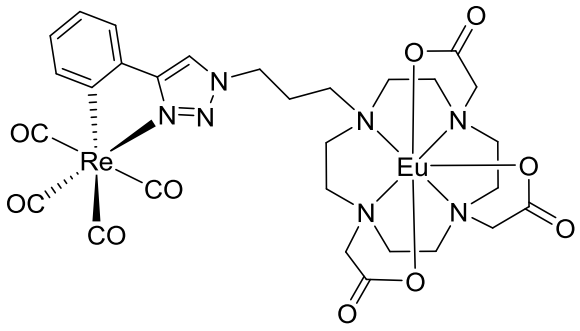

EuL2 (20.5 mg, 30.14 μmol) and $Re(CO)_5Cl$ (11.4 mg, 31.5 μmol) were dissolved in isopropanol:water (3:1) (3 mL) and heated *via* microwave radiation at 90°C for 30 mins (100W), the solution was concentrated and subjected to RP-HPLC t_R = 17.20 min to give white solid (11 mg, 38%). MS (ESI) 952 $[M\text{-}CO+H]^+$; HRMS (ESI) $C_{28}H_{34}N_7O_9{}^{151}Eu^{187}Re$ $[M\text{-}CO+H]^+$ required 950.1174 found 950.1205, $C_{28}H_{34}N_7O_9{}^{153}Eu^{185}Re$ $[M\text{-}CO+H]^+$ required 952.1188 found 952.1260.

8.16.7 ***ReGdL2***

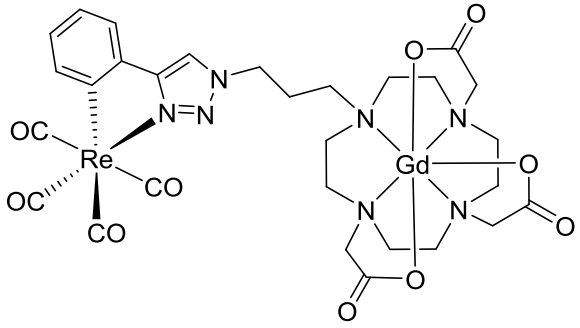

GdL2 (20.5 mg, 30.0 μmol) and $Re(CO)_5Cl$ (11.0 mg, 30.6 μmol) were dissolved in isopropanol:water (3:1) (3 mL) and heated *via* microwave radiation at 90°C for 30 mins (100W), the solution was concentrated and subjected to RP-HPLC t_R = 17.16 min to give white solid (11.2 mg, 38%). MS (ESI) 957 $[M\text{-}CO+H]^+$, 976 $[M\text{-}CO+Na]^+$; HRMS (ESI) $C_{28}H_{34}N_7O_9{}^{156}Gd^{185}Re$ $[M\text{-}CO+H]^+$ required 957.1223 found 957.1280.

8.16.8 ***RepyEuL3***

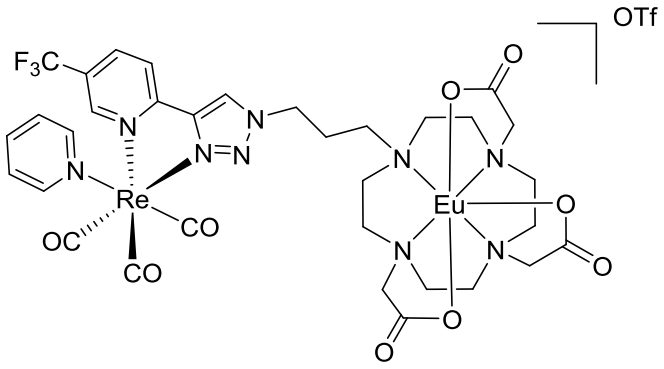

EuL3 (25.6 mg, 34.1 μmol) and $Re(CO)_5OTf$ (17.5 mg, 36.8 μmol). The reaction mixture was purified by RP-HPLC t_R = 22.82 min to give the title compound as white solid (13.6 mg, 32% over two steps). MS (ESI) 1098 $[M]^+$, 1019 $[M\text{-}py]^+$; HRMS (ESI) $C_{33}H_{37}F_3N_9O_9{}^{151}Eu^{187}Re$ $[M]^+$ requires 1098.1423 found 1098.1473, $C_{33}H_{37}N_9O_9{}^{153}Eu^{185}Re$ $[M]^+$ requires 1098.1409 found 1098.1473.

8.16.9 ***RepyGdL3***

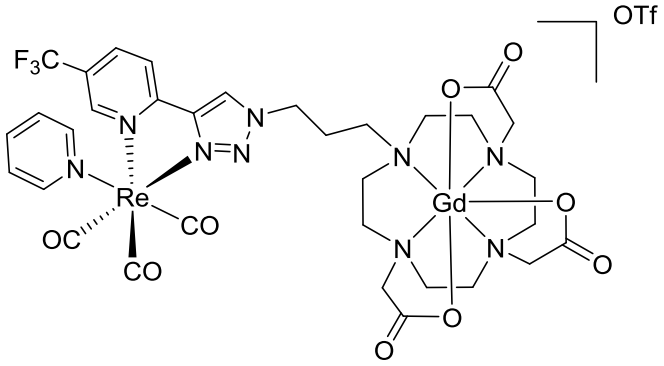

GdL3 (25.5 mg, 33.7 μmol) and $Re(CO)_5OTf$ (16.8 mg, 35.0 μmol). The reaction mixture was purified by RP-HPLC t_R = 22.80 min to give the title compound as white solid (13.5 mg, 32% over two steps). MS (ESI) 1105 $[M]^+$, 1025 $[M\text{-}py]^+$; HRMS (ESI) $C_{33}H_{37}F_3N_9O_9{}^{151}Gd^{187}Re$ $[M]^+$ requires 1102.1368 found 1102.1389, $C_{33}H_{37}N_9O_9{}^{156}Gd^{185}Re$ $[M]^+$ requires 1105.1001 found 1105.1020.

8.16.10 ***RepyEuL4***

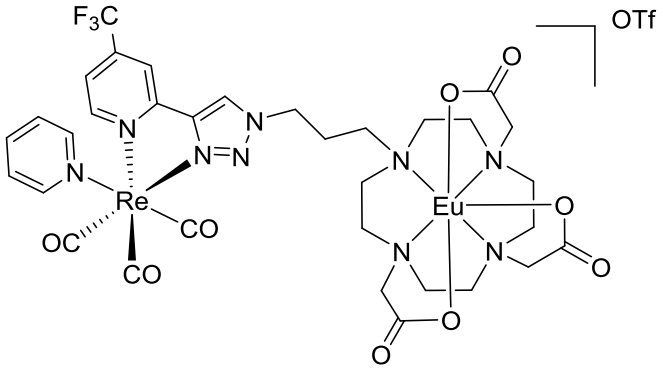

EuL4 (24.2 mg, 32.3 μmol) and $Re(CO)_5OTf$ (16.0 mg, 33.5 μmol). The reaction mixture was purified by RP-HPLC t_R = 22.36 min to give the title compound as white solid (13.2 mg, 33% over two steps). MS (ESI) 1098 $[M]^+$, 1019 $[M\text{-}py]^+$; HRMS (ESI) $C_{33}H_{37}F_3N_9O_9{}^{151}Eu^{185}Re$ $[M]^+$ requires 1096.1395 found 1096.1384, $C_{33}H_{37}N_9O_9{}^{153}Eu^{187}Re$ $[M]^+$ requires 1100.1436 found 1100.1448 .

8.16.11 ***RepyGdL4***

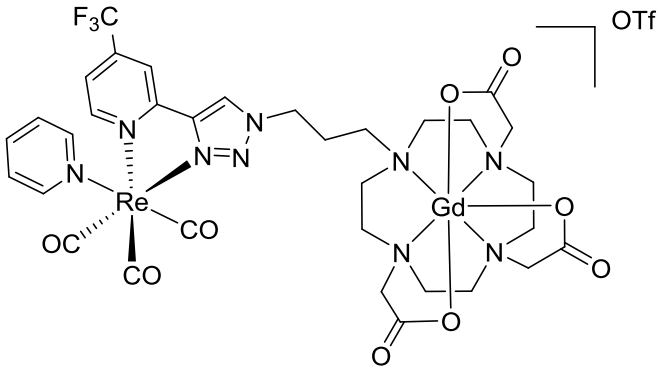

GdL4 (25.5 mg, 33.7 μmol) and $Re(CO)_5OTf$ (16.5 mg, 34.6 μmol). The reaction mixture was purified by RP-HPLC t_R = 22.81 min to give the title compound as white solid (13.5 mg, 32% over two steps). MS (ESI) 1105 $[M]^+$, 1025 $[M\text{-}py]^+$; HRMS (ESI) $C_{33}H_{37}F_3N_9O_9{}^{156}Gd^{185}Re$ $[M]^+$ requires 1101.1417 found 1101.1447, $C_{33}H_{37}N_9O_9{}^{160}Gd^{187}Re$ $[M]^+$ requires 1107.1494 found 1107.1514.

8.16.12 ***RepyEuL5***

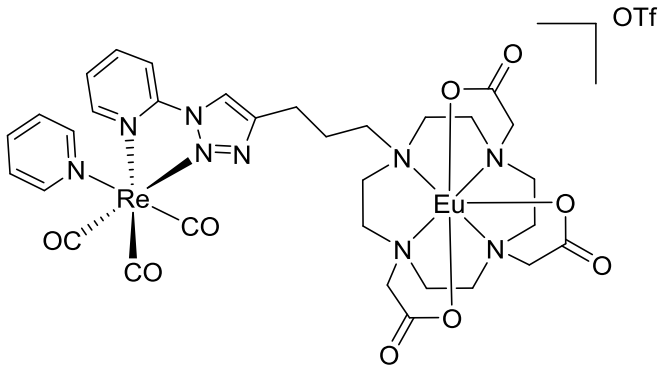

EuL5 (30.5 mg, 44.4 μmol) and $Re(CO)_5OTf$ (22.3 mg, 47.0 μmol). The reaction mixture was purified by RP-HPLC t_R = 28.02 min to give the title compound as white solid (16.1 mg, 31% over two steps). MS (ESI) 1029 $[M]^+$, 951 $[M\text{-}py]^+$; HRMS (ESI) $C_{32}H_{38}N_9O_9{}^{151}Eu^{185}Re$ $[M]^+$ requires 1028.1521 found 1028.1523, $C_{32}H_{38}N_9O_9{}^{151}Eu^{187}Re$ $[M]^+$ requires 1030.1549 found 1030.1584.

8.16.13 ***RepyGdL5***

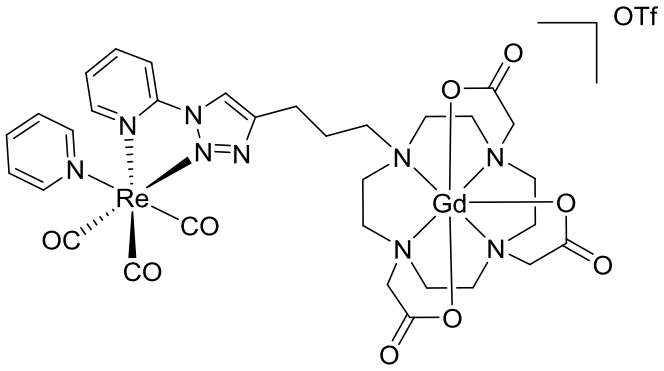

GdL5 (30.1 mg, 43.8 μmol) and $Re(CO)_5OTf$ (22.3 mg, 47.0 μmol). The reaction mixture was purified by RP-HPLC t_R = 29.23 min to give the title compound as white solid (19.2 mg, 37% over two steps). MS (ESI) 1035 $[M]^+$, 957 $[M\text{-}py]^+$; HRMS (ESI) $C_{32}H_{38}N_9O_9{}^{156}Gd^{185}Re$ $[M]^+$ requires 1033.1543 found 1033.1567, $C_{32}H_{38}N_9O_9{}^{158}Gd^{187}Re$ $[M]^+$ requires 1037.1591 found 1037.1608.

8.16.14 ***RepyEuL11***

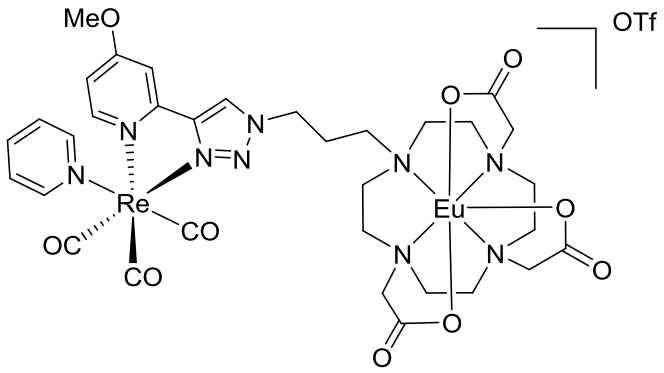

EuL11 (20.4 mg, 28.6 μmol) and $Re(CO)_5OTf$ (13.7 mg, 29.0 μmol) were reacted to give the title compound as white solid (10.3 mg, 31%). MS (ESI) 1059 $[M]^+$, 980 $[M\text{-py}]^+$; HRMS (ESI) $C_{33}H_{40}N_9O_{10}{}^{151}Eu^{185}Re$ $[M]^+$ requires 1058.1626 found 1058.1663, $C_{33}H_{40}N_9O_{10}{}^{153}Eu^{187}Re$ $[M]^+$ requires 1062.1668 found 1062.1704.

9 References

1. V. Gujrati, A. Mishra and V. Ntziachristos, *Chem. Commun.*, 2017, **53**, 4653-4672.

2. M. M. Meloni, S. Barton, L. Xu, J. C. Kaski, W. Song and T. He, *J. Mater. Chem. B*, 2017, **5**, 5714-5725.

3. A. K. Srivastava, D. K. Kadayakkara, A. Bar-Shir, A. A. Gilad, M. T. McMahon and J. W. Bulte, *Dis. Model. Mech.*, 2015, **8**, 323-336.

4. K. Chen and X. Chen, *Curr. Top. Med. Chem.*, 2010, **10**, 1227-1236.

5. Y. Pan, J.-P. Volkmer, K. E. Mach, R. V. Rouse, J.-J. Liu, D. Sahoo, T. C. Chang, T. J. Metzner, L. Kang, M. van de Rijn, E. C. Skinner, S. S. Gambhir, I. L. Weissman and J. C. Liao, *Sci. Transl. Med.*, 2014, **6**, 260-269.

6. A. Marcovich and T. Shinn, *Soc. Sci. Inf.*, 2017, **56**, 348-374.

7. P. Mansfield, *Angew. Chem. Int. Ed.*, 2004, **43**, 5456-5464.

8. A. S. Merbach, L. Helm and É. Tóth, in *The chemistry of contrast agents in medical magnetic resonance imaging*, ed. S. M. Bich-Thuy Doan, and Jean-Claude Beloeil, John Wiley & Sons, United Kindom, Editon edn., 2013, chapter 1, pp. 5-46.

9. M. Balci, *''Basic 1H-13C-NMR Spectroscopy*, Elsevier B.V., Amsterdam, 2005.

10. Neil E. Jacobsen, *''Simplified Theory, Applications and Examples for Organic Chemistry and Structural Biology''*, John Wiley & Sons, Inc., Canada, 2007.

11. P. Libby, *Cardiovascular magnetic resonance imaging*, Springer Science & Business Media, New Jersey, 2008.

12. D. W. McRobbie, E. A. Moore and M. J. Graves, *MRI from Picture to Proton*, Cambridge university press, 2017.

13. C. Westbrook, *MRI at a glance / Catherine Westbrook. – 2nd ed.*, John Wiley & Sons Ltd, United Kingdom, 2010.

14. G. Angelovski, *Angew. Chem. Int. Ed.*, 2016, **55**, 7038-7046.

15. F. G. Shellock and A. Spinazzi, *Am. J. Roentgenol.*, 2008, **191**, 1129-1139.

16. P. Caravan, J. J. Ellison, T. J. McMurry and R. B. Lauffer, *Chem. Rev.*, 1999, **99**, 2293-2352.

17. R. W. Biederman, R. B. Williams, M. Doyle, J. A. Yamrozik, M. Shah, G. Rayarao and S. Napan, *J. Cardiovasc. Magn. Reson.*, 2016, **18**, 519-523.

18. E. Tóth, L. Helm, A. E. Merbach, J. A. McCleverty and T. J. Meyer, *Comprehensive Coordination Chemistry II*, 2004.

19. D. J. Todd and J. Kay, *Annu. Rev. Med.*, 2016, **67**, 273-291.

20. S. P. Fricker, *Chem. Soc. Rev.*, 2006, **35**, 524-533.

21. C. F. G. C. Geraldes and S. Laurent, *Contrast Media. Mol. Imaging*, 2009, **4**, 1-23.

22. E. J. Werner, A. Datta, C. J. Jocher and K. N. Raymond, *Angew. Chem. Int. Ed.*, 2008, **47**, 8568-8580.

23. V. C. Pierre, M. J. Allen and P. Caravan, *J. Biol. Inorg. Chem.*, 2014, **19**, 127-131.

24. H. U. Rashid, M. A. U. Martines, J. Jorge, P. M. de Moraes, M. N. Umar, K. Khan and H. U. Rehman, *Bioorganic Med. Chem.*, 2016, **24**, 5663-5684.

25. J. M. Idée, M. Port, I. Raynal, M. Schaefer, S. Le Greneur and C. Corot, *Fund. Clin. Pharmacol.*, 2006, **20**, 563-576.

26. A. R. Baek, H.-K. Kim, S. Park, G. H. Lee, H. J. Kang, J.-C. Jung, J.-S. Park, H.-K. Ryeom, T.-J. Kim and Y. Chang, *J. Med. Chem.*, 2017, **60**, 4861-4868.

27. A. Vágner, E. Gianolio, S. Aime, A. Maiocchi, I. Tóth, Z. Baranyai and L. Tei, *Chem. Commun.*, 2016, **52**, 11235-11238.

28. Y. Zhang, T. Zou, M. Guan, M. Zhen, D. Chen, X. Guan, H. Han, C. Wang and C. Shu, *ACS Appl. Mater. Interfaces*, 2016, **8**, 11246-11254.

29. D. E. Thurston, *Biomedical Imaging: The Chemistry of Labels, Probes and Contrast Agents*, Royal Society of Chemistry, 2011.

30. S. Mansson and A. Bjornerud, *'The Chemistry of Contrast Agents in Magnetic Resonance Imaging'*, ,ed. A. E. Merbach and E. Toth, Wiley., 2001.

31. P. Caravan, *Chem. Soc. Rev.*, 2006, **35**, 512-523.

32. M. Botta, *Eur. J. Inorg. Chem.*, 2000, **2000**, 399-407.

33. G. Angelovski and É. Tóth, *Chem. Soc. Rev.*, 2017, **46**, 324-336.

34. S. Aime, M. Botta, S. G. Crich, G. Giovenzana, R. Pagliarin, M. Sisti and E. Terreno, *Magn. Reson. Chem.*, 1998, **36**, 200-208.

35. É. Tóth, O. M. N. Dhubhghaill, G. Besson, L. Helm and A. E. Merbach, *Magn. Reson. Chem.*, 1999, **37**, 701-708.

36. E. Debroye and T. N. Parac-Vogt, *Chem. Soc. Rev.*, 2014, **43**, 8178-8192.

37. M. Giardiello, M. Botta and M. P. Lowe, *J. Incl. Phenom. Macrocycl. Chem.*, 2011, **71**, 435-444.

38. S. Aime and P. Caravan, *J. Magn. Reson. Imaging*, 2009, **30**, 1259-1267.

39. L. M. De León-Rodríguez, A. F. Martins, M. C. Pinho, N. M. Rofsky and A. D. Sherry, *J. Magn. Reson. Imaging*, 2015, **42**, 545-565.

40. P. Hermann, J. Kotek, V. Kubíček and I. Lukeš, *Dalton Trans.*, 2008, **23**, 3027-3047.

41. D. R. Broome, *Eur. J. Radiol. Open.*, 2008, **66**, 230-234.

42. Q. Zhu, H. Yang, Y. Li, Y. Tian, W. Wang, W. Tang, Y. Yuan and A. Hu, *J. Mater. Chem. B*, 2016, **4**, 7241-7248.

43. G.-L. Davies, I. Kramberger and J. J. Davis, *Chem. Commun.*, 2013, **49**, 9704-9721.

44. S. Zhang, M. Merritt, D. E. Woessner, R. E. Lenkinski and A. D. Sherry, *Acc. Chem. Res.*, 2003, **36**, 783-790.

45. P. Caravan and Z. Zhang, *Eur. J. Inorg. Chem.*, 2012, **2012**, 1916-1923.

46. G. Gonzalez, D. H. Powell, V. Tissieres and A. E. Merbach, *J. Phys. Chem.*, 1994, **98**, 53-59.

47. S. Aime, A. Barge, J. I. Bruce, M. Botta, J. A. K. Howard, J. M. Moloney, D. Parker, A. S. de Sousa and M. Woods, *J. Am. Chem. Soc.*, 1999, **121**, 5762-5771.

48. A. C. L. Opina, M. Strickland, Y.-S. Lee, N. Tjandra, R. A. Byrd, R. E. Swenson and O. Vasalatiy, *Dalton Trans.*, 2016, **45**, 4673-4687.

49. E. Boros, S. Karimi, N. Kenton, L. Helm and P. Caravan, *Inorg. Chem.*, 2014, **53**, 6985-6994.

50. L. Helm and A. E. Merbach, *Chem. Rev.*, 2005, **105**, 1923-1960.

51. J. H. L. Voncken, *The Rare Earth Elements An Introduction*, SpringerBriefs in Earth Sciences, AG Switzerland, 2016.

52. D. F. Shriver, P. W. Atkins and C. H. Langford, *Inorganic Chemistry*, Oxford University Press, 1994.

53. R. L. Carlin, *''The Rare Earths or Lanthanides'' in''Magnetochemistry''*, Springer, N.Y., 1986.

54. J.-C. G. Bünzli, *J. Coord. Chem.*, 2014, **67**, 3706-3733.

55. H. C. Aspinall, *Chemistry of the F-Block Elements*, CRC Press, 2001.

56. V. Alexander, *Chem. Rev.*, 1995, **95**, 273-342.

57. S. Di Pietro, D. Imbert and M. Mazzanti, *Chem. Commun.*, 2014, **50**, 10323-10326.

58. L. Armelao, S. Quici, F. Barigelletti, G. Accorsi, G. Bottaro, M. Cavazzini and E. Tondello, *Coord. Chem. Rev.*, 2010, **254**, 487-505.

59. J.-C. G. Bünzli, *Acc. Chem. Res.*, 2006, **39**, 53-61.

60. M. C. Heffern, L. M. Matosziuk and T. J. Meade, *Chem. Rev.*, 2014, **114**, 4496-4539.

61. W. T. K. Chan and W.-T. Wong, *Polyhedron*, 2014, **83**, 150-158.

62. J. Vuojola and T. Soukka, *Methods appl. fluoresc.*, 2014, **2**, 1002-1031.

63. D. Parker, *Coord. Chem. Rev.*, 2000, **205**, 109-130.

64. R. M. Supkowski and W. D. Horrocks, *Inorg. Chim. Acta.*, 2002, **340**, 44-48.

65. S. Faulkner and S. J. A. Pope, *J. Am. Chem. Soc.*, 2003, **125**, 10526-10527.

66. A. de Bettencourt-Dias and J. S. K. Rossini, *Inorg. Chem.*, 2016, **55**, 9954-9963.

67. I. M. Clarkson, A. Beeby, J. I. Bruce, L. J. Govenlock, M. P. Lowe, C. E. Mathieu, D. Parker and K. Senanayake, *New J. Chem.*, 2000, **24**, 377-386.

68. Z. Liang, C.-F. Chan, Y. Liu, W.-T. Wong, C.-S. Lee, G.-L. Law and K.-L. Wong, *RSC Advances*, 2015, **5**, 13347-13356.

69. A. de Bettencourt-Dias, in *Luminescence of lanthanide ions in coordination compounds and nanomaterials*, ed. A. de Bettencourt-Dias, John Wiley & Sons, United Kindom, Editon edn., 2014, pp. 1-46.

70. K. Singh, S. Singh, P. Srivastava, S. Sivakumar and A. K. Patra, *Chem. Commun.*, 2017, **53**, 6144-6147.

71. E. G. Moore, A. P. S. Samuel and K. N. Raymond, *Acc. Chem. Res.*, 2009, **42**, 542-552.

72. Z. Liang, T.-H. Tsoi, C.-F. Chan, L. Dai, Y. Wu, G. Du, L. Zhu, C.-S. Lee, W.-T. Wong and G.-L. Law, *Chem. Sci.*, 2016, **7**, 2151-2156.

73. J. D. Routledge, M. W. Jones, S. Faulkner and M. Tropiano, *Inorg. Chem.*, 2015, **54**, 3337-3345.

74. A. J. Amoroso and S. J. Pope, *Chem. Soc. Rev.*, 2015, **44**, 4723-4742.

75. J. Vaněk, F. Smrčka, P. Lubal, I. Třísková and L. Trnková, *Monatsh. Chem.*, 2016, **147**, 925-934.

76. V. V. Rostovtsev, L. G. Green, V. V. Fokin and K. B. Sharpless, *Angew. Chem.*, 2002, **114**, 2708-2711.

77. V. Castro, H. Rodríguez and F. Albericio, *ACS Comb. Sci.*, 2016, **18**, 1-14.

78. L. Liang and D. Astruc, *Coord. Chem. Rev.*, 2011, **255**, 2933-2945.

79. C. Wang, D. Ikhlef, S. Kahlal, J.-Y. Saillard and D. Astruc, *Coord. Chem. Rev.*, 2016, **316**, 1-20.

80. E. Gilbert and W. Voreck, *PEP*, 1989, **14**, 19-23.

81. P. Appukkuttan, W. Dehaen, V. V. Fokin and E. Van der Eycken, *Org. Lett.*, 2004, **6**, 4223-4225.

82. M. Arseneault, C. Wafer and J.-F. Morin, *Molecules*, 2015, **20**, 9263-9294.

83. M. Tropiano, A. M. Kenwright and S. Faulkner, *Chem. Eur. J.*, 2015, **21**, 5697-5699.

84. J. K. Molloy, O. Kotova, R. D. Peacock and T. Gunnlaugsson, *Org. Biomol. Chem.*, 2012, **10**, 314-322.

85. H. Akiba, J. Sumaoka, K. Tsumoto and M. Komiyama, *Anal. Chem.*, 2015, **87**, 3834-3840.

86. W. I. O'Malley, E. H. Abdelkader, M. L. Aulsebrook, R. Rubbiani, C.-T. Loh, M. R. Grace, L. Spiccia, G. Gasser, G. Otting and K. L. Tuck, *Inorg. Chem.*, 2016, **55**, 1674-1682.

87. D. Schweinfurth, S. Strobel and B. Sarkar, *Inorg. Chim. Acta.*, 2011, **374**, 253-260.

88. M. W. a. K. Weisshart, *Imaging Cellular and Molecular Biological Functions*, © Springer-Verlag Berlin Heidelberg, 2007.

89. J. C. Dabrowiak., *Metals in medicine*, John Wiley & Sons, Ltd, 2009.

90. L. Ravotto and P. Ceroni, *Coord. Chem. Rev.*, 2017, **346**, 62-76.

91. A. Sinopoli, C. J. Wood, E. A. Gibson and P. I. P. Elliott, *Inorg. Chim. Acta.*, 2017, **457**, 81-89.

92. Y.-T. Liu, Y.-R. Li, X. Wang and F.-Q. Bai, *Dyes Pigm.*, 2017, **142**, 55-61.

93. D.-L. Ma, M. Wang, C. Liu, X. Miao, T.-S. Kang and C.-H. Leung, *Coord. Chem. Rev.*, 2016, **324**, 90-105.

94. E. Baggaley, J. A. Weinstein and J. G. Williams, *Coord. Chem. Rev.*, 2012, **256**, 1762-1785.

95. T.-T. Meng, H. Wang, Z.-B. Zheng and K.-Z. Wang, *Inorg. Chem.*, 2017, **9**, 4775-4779.

96. B. Laramée-Milette, N. Zaccheroni, F. Palomba and G. S. Hanan, *Chem. Eur. J.*, 2017, **26**, 6370-6379.

97. S. Hostachy, J. M. Swiecicki, C. Sandt, N. Delsuc and C. Policar, *Dalton Trans.*, 2016, **45**, 2791-2795.

98. M. Pastore, *Computation*, 2017, **5**, 2-22.

99. T. U. Connell, J. M. White, T. A. Smith and P. S. Donnelly, *Inorg. Chem.*, 2016, **55**, 2776-2790.

100. L. D. Ramos, H. M. da Cruz and K. P. M. Frin, *Photochem. Photobiol. Sci.*, 2017, **16**, 459-466.

101. M. Wolff, L. Munoz, A. Francois, C. Carrayon, A. Seridi, N. Saffon, C. Picard, B. Machura and E. Benoist, *Dalton Trans.*, 2013, **42**, 7019-7031.

102. W. K. C. Lo, G. S. Huff, J. R. Cubanski, A. D. W. Kennedy, C. J. McAdam, D. A. McMorran, K. C. Gordon and J. D. Crowley, *Inorg. Chem.*, 2015, **54**, 1572-1587.

103. T. Ljungdahl, K. Pettersson, B. Albinsson and J. Mårtensson, *J. Org. Chem.*, 2006, **71**, 1677-1687.

104. S. Thorand and N. Krause, *J. Org. Chem.*, 1998, **63**, 8551-8553.

105. Z. Novák, A. Szabó, J. Répási and A. Kotschy, *J. Org. Chem.*, 2003, **68**, 3327-3329.

106. R. Chinchilla and C. Najera, *Chem. Soc. Rev.*, 2011, **40**, 5084-5121.

107. K. Sonogashira, *J. Organomet. Chem.*, 2002, **653**, 46-49.

108. S. Subramanyam, A. Blumstein and K. P. Li, *Macromolecules*, 1992, **25**, 2065-2069.

109. C. Lang, K. Pahnke, C. Kiefer, A. S. Goldmann, P. W. Roesky and C. Barner-Kowollik, *Polym. Chem.*, 2013, **4**, 5456-5462.

110. S. Ley, R. Noyori and J. Knight, *Science of synthesis: Houben-Weyl methods of molecular transformations*, Thieme, 2004.

111. M. Schilz and H. Plenio, *J. Org. Chem.*, 2012, **77**, 2798-2807.

112. P. Espinet and A. M. Echavarren, *Angew. Chem. Int. Ed.*, 2004, **43**, 4704-4734.

113. C. Cordovilla, C. Bartolome, J. Martínez-Ilarduya and P. Espinet, *ACS Catalysis*, 2015, **5**, 3040-3053.

114. J. Sävmarker, J. Lindh and P. Nilsson, *Tetrahedron Lett.*, 2010, **51**, 6886-6889.

115. P. G. Wuts and T. W. Greene, *Greene's protective groups in organic synthesis*, John Wiley & Sons, 2014.

116. K. Ogata, D. Sasano, T. Yokoi, K. Isozaki, R. Yoshida, T. Takenaka, H. Seike, T. Ogawa, H. Kurata and N. Yasuda, *Chem. Eur. J.*, 2013, **19**, 12356-12375.

117. J. D. Crowley, P. H. Bandeen and L. R. Hanton, *Polyhedron*, 2010, **29**, 70-83.

118. G.-C. Kuang, H. A. Michaels, J. T. Simmons, R. J. Clark and L. Zhu, *J. Org. Chem.*, 2010, **75**, 6540-6548.

119. R. Sun, H. Wang, J. Hu, J. Zhao and H. Zhang, *Org. Biomol. Chem.*, 2014, **12**, 5954-5963.

120. H. Zhang, X. Li, Q. Shi, Y. Li, G. Xia, L. Chen, Z. Yang and Z. X. Jiang, *Angew. Chem.*, 2015, **127**, 3834-3838.

121. S. A. King, B. Pipik, D. A. Conlon and M. Bhupathy, *Synth. Commun.*, 1997, **27**, 701-707.

122. J. Massue, S. E. Plush, C. S. Bonnet, D. A. Moore and T. Gunnlaugsson, *Tetrahedron Lett.*, 2007, **48**, 8052-8055.

123. R. J. Abraham, J. J. Byrne, L. Griffiths and M. Perez, *Magn. Reson. Chem.*, 2006, **44**, 491-509.

124. C. D. Montgomery, *J. Chem. Educ.*, 2013, **90**, 661-664.

125. C. F. Geraldes, M. P. M. Marques and A. D. Sherry, *Inorg. Chim. Acta.*, 1998, **273**, 288-298.

126. W. Grzesiak and B. Brycki, *Molecules*, 2012, **17**, 12427-12448.

127. P. Barbaro, C. Bianchini, G. Capannesi, L. Di Luca, F. Laschi, D. Petroni, P. A. Salvadori, A. Vacca and F. Vizza, *J. Chem. Soc., Dalton Trans.*, 2000, **15**, 2393-2401.

128. P. D. Wadhavane, L. Gorla, A. Ferrer, B. Altava, M. I. Burguete, M. A. Izquierdo and S. V. Luis, *RSC Advances*, 2015, **5**, 72579-72589.

129. J. H. Tomlinson, V. L. Green, P. J. Baker and M. P. Williamson, *Proteins: Struct., Funct., Bioinf.*, 2010, **78**, 3000-3016.

130. A. Barge, G. Cravotto, E. Gianolio and F. Fedeli, *Contrast Media. Mol. Imaging*, 2006, **1**, 184-188.

131. J. Hammell, L. Buttarazzi, C.-H. Huang and J. R. Morrow, *Inorg. Chem.*, 2011, **50**, 4857-4867.

132. J. P. André, C. F. G. C. Geraldes, J. A. Martins, A. E. Merbach, M. I. M. Prata, A. C. Santos, J. J. P. de Lima and É. Tóth, *Chem. Eur. J.*, 2004, **10**, 5804-5816.

133. S. Viswanathan, Z. Kovacs, K. N. Green, S. J. Ratnakar and A. D. Sherry, *Chem. Rev.*, 2010, **110**, 2960.

134. J. Blahut, P. Hermann, Z. Tosner and C. Platas-Iglesias, *Phys. Chem. Chem. Phys.*, 2017, **19**, 26662-26671.

135. G. Sylvain, C. Hak Soo and V. F. John, *Molecular Imaging*, 2010, **9**, 752-761.

136. S. Park, U. Jung, S. Lee, D. Lee and C. Kim, *Biomed. Eng. Lett.*, 2017, **7**, 121-133.

137. Q. Chen, W. Shang, C. Zeng, K. Wang, X. Liang, C. Chi, X. Liang, J. Yang, C. Fang and J. Tian, *Oncotarget*, 2017, **8**, 32741.

138. M. Ceulemans, K. Nuyts, W. M. De Borggraeve and T. N. Parac-Vogt, *Inorganics*, 2015, **3**, 516-533.

139. T. Koullourou, L. S. Natrajan, H. Bhavsar, Pope, J. Feng, J. Narvainen, R. Shaw, E. Scales, R. Kauppinen, A. M. Kenwright and S. Faulkner, *J. Am. Chem. Soc.*, 2008, **130**, 2178-2179.

140. L. Moriggi, A. Aebischer, C. Cannizzo, A. Sour, A. Borel, J.-C. G. Bünzli and L. Helm, *Dalton Trans.*, 2009, **12**, 2088-2095.

141. G. Dehaen, S. V. Eliseeva, P. Verwilst, S. Laurent, L. Vander Elst, R. N. Muller, W. De Borggraeve, K. Binnemans and T. N. Parac-Vogt, *Inorg. Chem.*, 2012, **51**, 8775-8783.

142. H. Yang, L. Ding, L. An, Z. Xiang, M. Chen, J. Zhou, F. Li, D. Wu and S. Yang, *Biomaterials*, 2012, **33**, 8591-8599.

143. H. Kobayashi, M. R. Longmire, M. Ogawa and P. L. Choyke, *Chem. Soc. Rev.*, 2011, **40**, 4626-4648.

144. A. Bogdanov Jr, R. Weissleder, H. Frank, A. Bogdanova, N. Nossif, B. Schaffer, E. Tsai, M. Papisov and T. Brady, *Radiology*, 1993, **187**, 701-706.

145. D. L. Davies, M. P. Lowe, K. S. Ryder, K. Singh and S. Singh, *Dalton Trans.*, 2011, **40**, 1028-1030.

146. Z. D. Deng, G. F. Sigler, N. A. Surridge, C. D. Wilsey, R. J. McEnroe, W. W. Jernigan and R. W. Muddiman, Google Patents, Editon edn., 1996.

147. E. Rossi, L. Murphy, P. L. Brothwood, A. Colombo, C. Dragonetti, D. Roberto, R. Ugo, M. Cocchi and J. A. G. Williams, *J. Mater. Chem.*, 2011, **21**, 15501-15510.

148. J. A. G. Williams, A. Beeby, E. S. Davies, J. A. Weinstein and C. Wilson, *Inorg. Chem.*, 2003, **42**, 8609-8611.

149. W. Lu, B.-X. Mi, M. C. W. Chan, Z. Hui, C.-M. Che, N. Zhu and S.-T. Lee, *J. Am. Chem. Soc.*, 2004, **126**, 4958-4971.

150. Z. Wang, E. Turner, V. Mahoney, S. Madakuni, T. Groy and J. Li, *Inorg. Chem.*, 2010, **49**, 11276-11286.

151. E. Garoni, J. Boixel, V. Dorcet, T. Roisnel, D. Roberto, D. Jacquemin and V. Guerchais, *Dalton Trans.*, 2018, **47**, 224-232.

152. L. Goswami, L. Ma, P. Kueffer, S. Jalisatgi and M. Hawthorne, *Molecules*, 2013, **18**, 9034.

153. P. A. Scattergood, A. Sinopoli and P. I. P. Elliott, *Coord. Chem. Rev.*, 2017, **350**, 136-154.

154. B. N. Siriwardena-Mahanama and M. J. Allen, *Molecules*, 2013, **18**, 9352-9381.

155. A. Beeby, I. M. Clarkson, R. S. Dickins, S. Faulkner, D. Parker, L. Royle, A. S. de Sousa, J. A. Gareth Williams and M. Woods, *J. Chem. Soc., Perkin Trans. 2*, 1999, **3**, 493-504.

156. A. F. Henwood and E. Zysman-Colman, *Chem. Commun.*, 2017, **53**, 807-826.

157. T. U. Connell, J. M. White, T. A. Smith and P. S. Donnelly, *Inorg. Chem.*, 2016, **55**, 2776-2790.

158. B. Beyer, C. Ulbricht, D. Escudero, C. Friebe, A. Winter, L. González and U. S. Schubert, *organomet.*, 2009, **28**, 5478-5488.

159. A. F. Henwood and E. Zysman-Colman, *Chem. Commun.*, 2017, **53**, 807-826.

160. V. Fernandez-Moreira, F. L. Thorp-Greenwood, A. J. Amoroso, J. Cable, J. B. Court, V. Gray, A. J. Hayes, R. L. Jenkins, B. M. Kariuki, D. Lloyd, C. O. Millet, C. F. Williams and M. P. Coogan, *Org. Biomol. Chem.*, 2010, **8**, 3888-3901.

161. C. d. l. Torre, A. Toscani, C. Marín-Hernández, J. A. Robson, M. C. Terencio, A. J. White, M. J. Alcaraz, J. D. Wilton-Ely, R. Martínez-Máñez and F. Sancenón, *J. Am. Chem. Soc.*, 2017, **139**, 18484-18487.

162. J. M. Fernández-Hernández, S. Ladouceur, Y. Shen, A. Iordache, X. Wang, L. Donato, S. Gallagher-Duval, M. de Anda Villa, J. D. Slinker and L. De Cola, *J. Mater. Chem. C*, 2013, **1**, 7440-7452.

163. M. S. Lowry and S. Bernhard, *Chem. Eur. J.*, 2006, **12**, 7970-7977.

164. C. Ulbricht, B. Beyer, C. Friebe, A. Winter and U. S. Schubert, *Adv. Mater.*, 2009, **21**, 4418-4441.

165. C. Ast, E. Schmälzlin, H.-G. Löhmannsröben and J. T. Van Dongen, *Sensors*, 2012, **12**, 7015-7032.

166. M. S. Lowry and S. Bernhard, *Chem. Eur. J.*, 2006, **12**, 7970-7977.

167. M. K. Nazeeruddin, R. T. Wegh, Z. Zhou, C. Klein, Q. Wang, F. De Angelis, S. Fantacci and M. Grätzel, *Inorg. Chem.*, 2006, **45**, 9245-9250.

168. E. P. McCarney, C. S. Hawes, S. Blasco and T. Gunnlaugsson, *Dalton Trans.*, 2016, **45**, 10209-10221.

169. M. Albrecht, S. L. James, N. Veldman, A. L. Spek and G. v. Koten, *Can. J. Chem.*, 2001, **79**, 709-718.

170. P. Shao, Y. Li and W. Sun, *J. Phys. Chem. A*, 2008, **112**, 1172-1179.

171. J. A. G. Williams, in *Photochemistry and Photophysics of Coordination Compounds II*, eds. V. Balzani and S. Campagna, Springer Berlin Heidelberg, Berlin, Heidelberg, Editon edn., 2007, pp. 205-268.

172. Z. Wang, Z. Sun, X.-Q. Hao, J.-L. Niu, D. Wei, T. Tu, J.-F. Gong and M.-P. Song, *organomet.*, 2014, **33**, 1563-1573.

173. M. Hebenbrock, L. Stegemann, J. Kösters, N. L. Doltsinis, J. Müller and C. A. Strassert, *Dalton Trans.*, 2017, **46**, 3160-3169.

174. S. Develay and J. G. Williams, *Dalton Trans.*, 2008, **34**, 4562-4564.

175. V. V. Sivchik, E. V. Grachova, A. S. Melnikov, S. N. Smirnov, A. Y. Ivanov, P. Hirva, S. P. Tunik and I. O. Koshevoy, *Inorg. Chem.*, 2016, **55**, 3351-3363.

176. A. Boulay, C. l. Deraeve, L. Vander Elst, N. Leygue, O. Maury, S. Laurent, R. N. Muller, B. a. Mestre-Voegtlé and C. Picard, *Inorg. Chem.*, 2015, **54**, 1414-1425.

177. S. V. Kumar, S. Ø. Scottwell, E. Waugh, C. J. McAdam, L. R. Hanton, H. J. Brooks and J. D. Crowley, *Inorg. Chem.*, 2016, **55**, 9767-9777.

178. B. Happ, D. Escudero, M. D. Hager, C. Friebe, A. Winter, H. Görls, E. Altuntas, L. González and U. S. Schubert, *J. Org. Chem.*, 2010, **75**, 4025-4038.

179. P. I. Elliott, *Organomet. Chem.*, 2014, **39**, 1-25.

180. J. T. Fletcher, B. J. Bumgarner, N. D. Engels and D. A. Skoglund, *organomet.*, 2008, **27**, 5430-5433.

181. N. Zabarska, A. Stumper and S. Rau, *Dalton Trans.*, 2016, **45**, 2338-2351.

182. E. Badaeva, V. V. Albert, S. Kilina, A. Koposov, M. Sykora and S. Tretiak, *Phys. Chem. Chem. Phys.*, 2010, **12**, 8902-8913.

183. W. J. Evans, J. H. Meadows, A. G. Kostka and G. L. Closs, *organomet.*, 1985, **4**, 324-326.

184. W. Shen, W. Zhang and C. Zhu, *Phys. Chem. Chem. Phys.*, 2017, **19**, 23532-23540.

185. M. Felici, P. Contreras-Carballada, Y. Vida, J. M. M. Smits, R. J. M. Nolte, L. De Cola, R. M. Williams and M. C. Feiters, *Chem. Eur. J.*, 2009, **15**, 13124-13134.

186. H. van der Salm, A. B. S. Elliott and K. C. Gordon, *Coord. Chem. Rev.*, 2015, **282-283**, 33-49.

187. C.-M. Che, J.-L. Zhang and L.-R. Lin, *Chem. Commun.*, 2002, **12**, 2556-2557.

188. S. C. F. Kui, Y.-C. Law, G. S. M. Tong, W. Lu, M.-Y. Yuen and C.-M. Che, *Chem. Sci.*, 2011, **2**, 221-228.

189. J. B. Livramento, L. Helm, A. Sour, C. O'Neil, A. E. Merbach and E. Toth, *Dalton Trans.*, 2008, 1195-1202.

190. S. Sung, H. Holmes, L. Wainwright, A. Toscani, G. J. Stasiuk, A. J. P. White, J. D. Bell and J. D. E. T. Wilton-Ely, *Inorg. Chem.*, 2014, **53**, 1989-2005.

191. J. C. Er, C. Leong, C. L. Teoh, Q. Yuan, P. Merchant, M. Dunn, D. Sulzer, D. Sames, A. Bhinge, D. Kim, S. M. Kim, M. H. Yoon, L. W. Stanton, S. H. Je, S. W. Yun and Y. T. Chang, *Angew. Chem. Int. Ed.*, 2015, **54**, 2442-2446.

192. J. Lohrke, T. Frenzel, J. Endrikat, F. C. Alves, T. M. Grist, M. Law, J. M. Lee, T. Leiner, K.-C. Li, K. Nikolaou, M. R. Prince, H. H. Schild, J. C. Weinreb, K. Yoshikawa and H. Pietsch, *Adv. Ther.*, 2016, **33**, 1-28.

193. A. Hoffmann, J. Bredno, M. Wendland, N. Derugin, P. Ohara and M. Wintermark, *Transl. Stroke Res.*, 2011, **2**, 106-111.

194. V. M. Runge, *Invest. Radiol.*, 2016, **51**, 273-279.

195. M. G. Honig and R. I. Hume, *Trends Neurosci.*, 1989, **12**, 333-341.

196. S. Sreedharan, A. Sinopoli, P. J. Jarman, D. Robinson, C. Clemmet, P. A. Scattergood, C. R. Rice, C. G. W. Smythe, J. A. Thomas and P. I. P. Elliott, *Dalton Trans.*, 2018, **47**, 4931-4940.

197. B. A. Smith and B. D. Smith, *Bioconjugate Chem.*, 2012, **23**, 1989-2006.

198. J. Seelig, *Biochim. Biophys. Acta*, 2004, **1666**, 40-50.

199. M. Saleem, N. G. Choi and K. H. Lee, *Int. J. Environ. Anal. Chem.*, 2015, **95**, 592-608.

200. D. M. Prescott, H. C. Charles, J. M. Poulson, R. L. Page, D. E. Thrall, Z. Vujaskovic and M. W. Dewhirst, *Clin. Cancer Res.*, 2000, **6**, 2501-2505.

201. E. Cordat and J. R. Casey, *Biochem. J.*, 2009, **417**, 423-439.

202. S. J. Butler and D. Parker, *Chem. Soc. Rev.*, 2013, **42**, 1652-1666.

203. J. R. Casey, S. Grinstein and J. Orlowski, *Nat. Rev. Mol. Cell Biol.*, 2010, **11**, 50.

204. Y. Zhou, L. A. Skelton, L. Xu, M. P. Chandler, J. M. Berthiaume and W. F. Boron, *J. Am. Soc. Nephrol.*, 2016, **27**, 2616-2621.

205. J. A. Greenberg and M. E. Meyerhoff, *Anal. Chim. Acta*, 1982, **141**, 57-64.

206. N. Abramova, S. Levichev and A. Bratov, *Talanta*, 2010, **81**, 1750-1754.

207. C. M. Andolina and J. R. Morrow, *Eur. J. Inorg. Chem.*, 2011, **1**, 154-164.

208. A. Thibon and V. C. Pierre, *Anal. Bioanal. Chem.*, 2009, **394**, 107-120.

209. S. J. Bradberry, A. J. Savyasachi, M. Martinez-Calvo and T. Gunnlaugsson, *Coord. Chem. Rev.*, 2014, **273**, 226-241.

210. M. Giardiello and M. P. Lowe, *Inorg. Chem.*, 2009, **48**, 8515-8522.

211. M. L. Cable, J. P. Kirby, H. B. Gray and A. Ponce, *Acc. Chem. Res.*, 2013, **46**, 2576-2584.

212. J. Vaněk, P. Lubal, P. Hermann and P. Anzenbacher, *J. Fluoresc.*, 2013, **23**, 57-69.

213. H. Liu, H. Wang, T. Chu, M. Yu and Y. Yang, *J. Mater. Chem. C*, 2014, **2**, 8683-8690.

214. J. M. Smieja, E. E. Benson, B. Kumar, K. A. Grice, C. S. Seu, A. J. M. Miller, J. M. Mayer and C. P. Kubiak, *Proc. Natl. Acad. Sci.*, 2012, **109**, 15646-15650.

215. L. Sacksteder, A. P. Zipp, E. A. Brown, J. Streich, J. Demas and B. DeGraff, *Inorg. Chem.*, 1990, **29**, 4335-4340.

216. D. Parker, *Coord. Chem. Rev.*, 2000, **205**, 109-130.

217. S. Hostachy, C. Policar and N. Delsuc, *Coord. Chem. Rev.*, 2017, **351**, 172-188.

218. M. Obata, A. Kitamura, A. Mori, C. Kameyama, J. A. Czaplewska, R. Tanaka, I. Kinoshita, T. Kusumoto, H. Hashimoto and M. Harada, *Dalton Trans.*, 2008, **25**, 3292-3300.

219. D. Sykes, A. J. Cankut, N. M. Ali, A. Stephenson, S. J. P. Spall, S. C. Parker, J. A. Weinstein and M. D. Ward, *Dalton Trans.*, 2014, **43**, 6414-6428.

220. S. Faulkner, L. S. Natrajan, W. S. Perry and D. Sykes, *Dalton Trans.*, 2009, 3890-3899.

221. H. Takeda, K. Koike, T. Morimoto, H. Inumaru and O. Ishitani, *Adv. Inorg. Chem.*, 2011, **63**, 137-186.

222. M. Giardiello, PhD. thesis, University of Leicester, 2007.

223. J. I. Bruce, R. S. Dickins, L. J. Govenlock, T. Gunnlaugsson, S. Lopinski, M. P. Lowe, D. Parker, R. D. Peacock, J. J. B. Perry, S. Aime and M. Botta, *J. Am. Chem. Soc.*, 2000, **122**, 9674-9684.

224. L. Burai, V. Hietapelto, R. Király and E. Brücher, *Magn. Reson. Med.*, 1997, **38**, 146-150.

225. C. Y. Chan and P. J. Barnard, *Dalton Trans.*, 2015, **44**, 19126-19140.

226. T. R. Hayes, S. C. Bottorff, W. S. Slocumb, C. L. Barnes, A. E. Clark and P. D. Benny, *Dalton Trans.*, 2017, **46**, 1134-1144.

227. L. Ramos, R. Sampaio, F. De Assis, K. De Oliveira, P. Homem-de-Mello, A. Patrocinio and K. Frin, *Dalton Trans.*, 2016, **45**, 11688-11698.

228. Z. Zhu, C. W. Leung, X. Zhao, Y. Wang, J. Qian, B. Z. Tang and S. He, *Sci. Rep.*, 2015, **5**, 1-9.

229. J. G. Vaughan, B. L. Reid, P. J. Wright, S. Ramchandani, B. W. Skelton, P. Raiteri, S. Muzzioli, D. H. Brown, S. Stagni and M. Massi, *Inorg. Chem.*, 2014, **53**, 3629-3641.

230. X.-Z. Yang, Y.-L. Wang, J.-Y. Guo, T.-T. Zhang, J.-F. Jia and H.-S. Wu, *Mater. Chem. Phys.*, 2016, **178**, 173-181.

231. H. C. Bertrand, S. Clède, R. Guillot, F. Lambert and C. Policar, *Inorg. Chem.*, 2014, **53**, 6204-6223.

232. M. R. Gonçalves and K. P. M. Frin, *Polyhedron*, 2015, **97**, 112-117.

233. A. T. R. Williams, S. A. Winfield and J. N. Miller, *Analyst*, 1983, **108**, 1067-1071.

234. C. Würth, M. Grabolle, J. Pauli, M. Spieles and U. Resch-Genger, *Nature Protocols*, 2013, **8**, 1535-1550.

235. K. K.-W. Lo, M.-W. Louie and K. Y. Zhang, *Coord. Chem. Rev.*, 2010, **254**, 2603-2622.

236. Y. Kang, A. Ito, E. Sakuda and N. Kitamura, *J. Photochem. Photobiol.*, 2015, **313**, 107-116.

237. Y. Chi and P.-T. Chou, *Chem. Soc. Rev.*, 2007, **36**, 1421-1431.

238. G. Zhao, C. Lu, H. Li, Y. Xiao, W. Zhang, X. Fang, P. Wang, X. Fang, J. Xu and W. Yang, *Inorg. Chim. Acta.*, 2013, **406**, 146-152.

239. A. N. W. Kuda-Wedagedara and M. J. Allen, *Analyst*, 2014, **139**, 4401-4410.

240. D. J. Mastarone, V. S. Harrison, A. L. Eckermann, G. Parigi, C. Luchinat and T. J. Meade, *J. Am. Chem. Soc.*, 2011, **133**, 5329-5337.

241. J. B. Livramento, É. Tóth, A. Sour, A. Borel, A. E. Merbach and R. Ruloff, *Angew. Chem. Int. Ed.*, 2005, **44**, 1480-1484.

242. L. H. Bryant, M. W. Brechbiel, C. Wu, J. W. M. Bulte, V. Herynek and J. A. Frank, *J. Magn. Reson. Imaging*, 1999, **9**, 348-352.

243. J. B. Livramento, A. Sour, A. Borel, A. E. Merbach and É. Tóth, *Chem. Eur. J.*, 2006, **12**, 989-1003.

244. J. B. Livramento, L. Helm, A. Sour, C. O'Neil, A. E. Merbach and É. Tóth, *Dalton Trans.*, 2008, **9**, 1195-1202.

245. J. Costa, E. Balogh, V. Turcry, R. Tripier, M. Le Baccon, F. Chuburu, H. Handel, L. Helm, É. Tóth and A. E. Merbach, *Chem. Eur. J.*, 2006, **12**, 6841-6851.

246. W.-S. Li, J. Luo and Z.-N. Chen, *Inorg. Chem. Commun.*, 2011, **14**, 1898-1900.

247. S. Vellas, J. Lewis, M. Shankar, A. Sagatova, J. Tyndall, B. Monk, C. Fitchett, L. Hanton and J. Crowley, *Molecules*, 2013, **18**, 6383-6407.

248. J. R. Cubanski, M. E. Reish, A. G. Blackman, P. J. Steel, K. C. Gordon, D. A. McMorran and J. D. Crowley, *Aust. J. Chem.*, 2015, **68**, 1160-1170.

249. M. Liu, Y. Zheng, U. Avcibasi and S. Liu, *Nucl. Med. Biol.*, 2016, **43**, 732-741.

250. S. E. Howson, L. E. N. Allan, N. P. Chmel, G. J. Clarkson, R. van Gorkum and P. Scott, *Chem. Commun.*, 2009, **13**, 1727-1729.

251. J. Demas, *Anal. Chem.*, 1991, **63**, 829-837.

252. J. Luo, X. F. Zhu and Z. N. Chen, *Eur. J. Inorg. Chem.*, 2015, **19**, 3087-3093.

253. D. M. Corsi, C. Platas-Iglesias, H. v. Bekkum and J. A. Peters, *Magn. Reson. Chem.*, 2001, **39**, 723-726.

254. P. Caravan, C. T. Farrar, L. Frullano and R. Uppal, *Contrast Media. Mol. Imaging*, 2009, **4**, 89-100.

255. C. Tu and A. Y. Louie, *NMR Biomed.*, 2013, **26**, 781-787.

256. S. Rehncrona, H. N. Hauge and B. K. Siesjö, *J. Cereb. Blood Flow Metab.*, 1989, **9**, 65-70.

257. M. Damaghi, J. W. Wojtkowiak and R. J. Gillies, *Front. Physiol.*, 2013, **4**, 1-10.

258. F. K. Kálmán, M. Woods, P. Caravan, P. Jurek, M. Spiller, G. Tircsó, R. Király, E. Brücher and A. D. Sherry, *Inorg. Chem.*, 2007, **46**, 5260-5270.

259. M. P. Lowe and D. Parker, *Chem. Commun.*, 2000, **8**, 707-708.

260. M. P. Lowe, D. Parker, O. Reany, S. Aime, M. Botta, G. Castellano, E. Gianolio and R. Pagliarin, *J. Am. Chem. Soc.*, 2001, **123**, 7601-7609.

261. A. G. Sorensen, A. L. Tievsky, L. Ostergaard, R. M. Weisskoff and B. R. Rosen, *J. Magn. Reson. Imaging*, 1997, **7**, 47-55.

262. L. De Luca and G. Giacomelli, *J. Org. Chem.*, 2008, **73**, 3967-3969.

263. F. G. Bordwell, *Acc. Chem. Res.*, 1988, **21**, 456-463.

264. R. Pal and D. Parker, *Org. Biomol. Chem.*, 2008, **6**, 1020-1033.

265. R. Pal and D. Parker, *Chem. Commun.*, 2007, **5**, 474-476.

266. J. Chen, V. Palani and T. R. Hoye, *J. Am. Chem. Soc*, 2016, **138**, 4318-4321.

267. A. Takács, R. Napolitano, M. Purgel, A. C. Bényei, L. Zékány, E. Brücher, I. Tóth, Z. Baranyai and S. Aime, *Inorg. Chem.*, 2014, **53**, 2858-2872.

268. F. Bordwell and D. Algrim, *J. Org. Chem.*, 1976, **41**, 2507-2508.

269. M. Otagiri, H. Nakamura, Y. Imamura and U. Matsumoto, *Pharmacy World & Science*, 1989, **11**, 207-212.

270. R. C. Crumrine, V. J. Marder, G. M. Taylor, J. C. LaManna, C. P. Tsipis, P. Scuderi, S. R. Petteway and V. Arora, *Exp. Transl. Stroke Med.*, 2011, **3**, 1-14.

271. L. Belayev, O. F. Alonso, R. Busto, W. Zhao and M. D. Ginsberg, *Stroke*, 1996, **27**, 1616-1623.

272. E. M. Nemoto and S. Frinak, *Stroke*, 1981, **12**, 77-82.

273. G. S. Huff, W. K. C. Lo, R. Horvath, J. O. Turner, X.-Z. Sun, G. R. Weal, H. J. Davidson, A. D. W. Kennedy, C. J. McAdam, J. D. Crowley, M. W. George and K. C. Gordon, *Inorg. Chem.*, 2016, **55**, 12238-12253.

274. S.-T. Lam, N. Zhu, V. K.-M. Au and V. W.-W. Yam, *Polyhedron*, 2015, **86**, 10-16.

275. S.-T. Lam, G. Wang and V. W.-W. Yam, *organomet.*, 2008, **27**, 4545-4548.

276. P. A. Scattergood and P. I. P. Elliott, *Dalton Trans.*, 2017, **46**, 16343-16356.

277. J. M. Fernández-Hernández, J. I. Beltrán, V. Lemaur, M.-D. Gálvez-López, C.-H. Chien, F. Polo, E. Orselli, R. Fröhlich, J. Cornil and L. De Cola, *Inorg. Chem.*, 2013, **52**, 1812-1824.

278. K. Y. Zhang, S. Liu, Q. Zhao, F. Li and W. Huang, in *Luminescent and Photoactive Transition Metal Complexes as Biomolecular Probes and Cellular Reagents*, ed. K. K.-W. Lo, Springer Berlin Heidelberg, Berlin, Heidelberg, Editon edn., 2015, pp. 131-180.

279. Y.-T. Liu, Y.-R. Li, X. Wang and F.-Q. Bai, *Dyes Pigm.*, 2017, **142**, 55-61.

280. E. Baggaley, I. V. Sazanovich, J. A. G. Williams, J. W. Haycock, S. W. Botchway and J. A. Weinstein, *RSC Advances*, 2014, **4**, 35003-35008.

281. S. Nowtoarski, P. Woster and R. Casero Jr, *Expert. Rev. Mol. Med.*, 2013, **15**, 1-28.

282. G. K. Balendiran, R. Dabur and D. Fraser, *Cell Biochem. Funct.*, 2004, **22**, 343-352.

283. F. Bolze, S. Jenni, A. Sour and V. Heitz, *Chem. Commun.*, 2017, **53**, 12857-12877.

284. T. J. Prior, H. Savoie, R. W. Boyle and B. S. Murray, *organomet.*, 2018, **37**, 294-297.

285. A. Beeby, I. M. Clarkson, R. S. Dickins, S. Faulkner, D. Parker, L. Royle, A. S. de Sousa, J. A. Gareth Williams and M. Woods, *J. Chem. Soc., Perkin Trans. 2*, 1999, 493-504.

286. D. M. Corsi, C. Platas-Iglesias, H. v. Bekkum and J. A. Peters, *Magn. Reson. Chem.*, 2001, **39**, 723-726.

287. O. Axelsson and A. Olsson, Google Patents, Editon edn., 2012.

288. B. Jagadish, G. L. Brickert-Albrecht, G. S. Nichol, E. A. Mash and N. Raghunand, *Tetrahedron Lett.*, 2011, **52**, 2058-2061.

289. J. Bucher, T. Wurm, K. S. Nalivela, M. Rudolph, F. Rominger and A. S. K. Hashmi, *Angew. Chem. Int. Ed.*, 2014, **53**, 3854-3858.

10 Appendices

10.1 Courses and Modules

Advanced inorganic chemistry, 15 credits,

Advanced structure determination, 15 credits

Chemistry research skills, 15 credits

English Language for academic purposes, ELTU

Preparing to Teach in Higher Education, strand B, LLI

10.2 Conferences

Conferences Attended

RSC, Chemistry Biology and Bio-organic Chemistry Symposium, University of Bristol, 19th May 2015.

Posters presentations

"Synthesis of Dual-Mode Magnetic Resonance / Optical Imaging Contrast Agents" A. H. ALI, M. P. Lowe, RSC, Organic Division Midlands Meeting, University of Leicester, 5th May 2017

"Synthesis of Dual-Mode Magnetic Resonance / optical imaging contrast agents" A. H. ALI, M. P. Lowe, RSC, Molecular Imaging and Chemistry; Defining the future, London, 21st March 2017.

10.3 Demonstrating

5/10/2016 — 25/1/2017, 1st Year, Thin-Layer Chromatography.

15/1/2017 — 3/5/2017, 1st Year, Coordination Chemistry of Tin.

4/10/2017 — 6/12/2017, 1st Year, Thin-Layer Chromatography.

29/1/2018 — 27/2/2018, 3rd Year, Extended Investigation.

10.4 Lifetime, MS, excitation, emission and ^{1}H NMR spectra

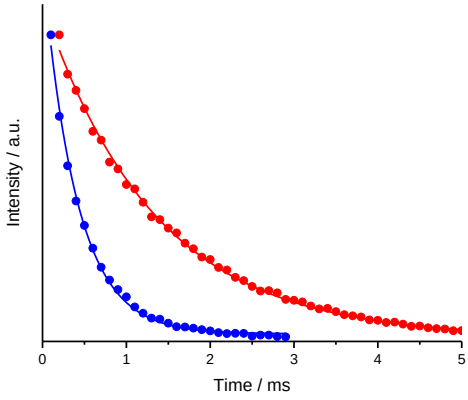

Figure 10.1: **TbL1** lifetime at λ_{ex} = 280 and λ_{em} = 544 nm.

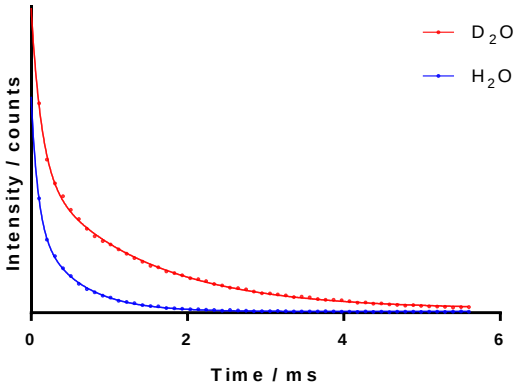

Figure 10.2: Lifetime measurement for **PtEuL10**.

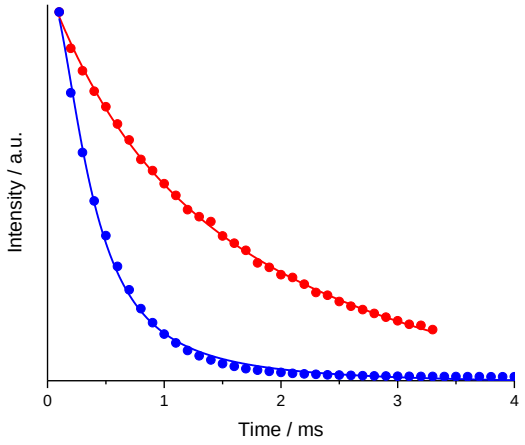

Figure 10.3: Excited state life time studies for **CoEuL1** at 298 K, pH 6, λ_{ex} = 280 nm, λ_{em} = 617 nm. Blue = H_2O, Red = D_2O.

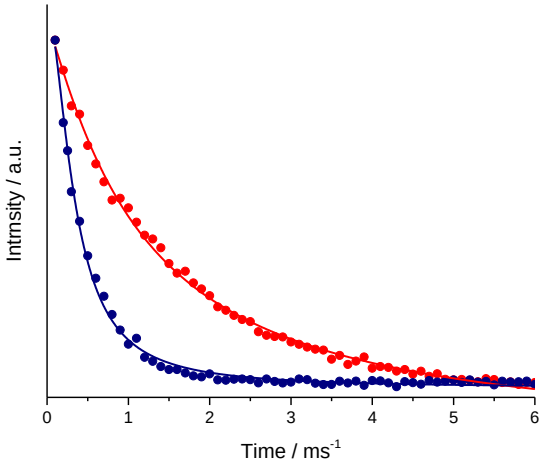

Figure 10.4: Lifetime of **Ru(EuL1)$_3$** in H_2O (blue) and D_2O (red) at delay time 0.5 ms.

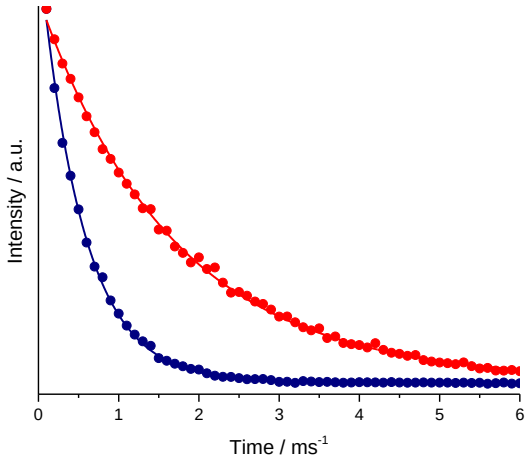

Figure 10.3: Lifetime of **EuL10** in H_2O (blue) and D_2O (red) at λ_{ex} 395 nm, λ_{em} 616.

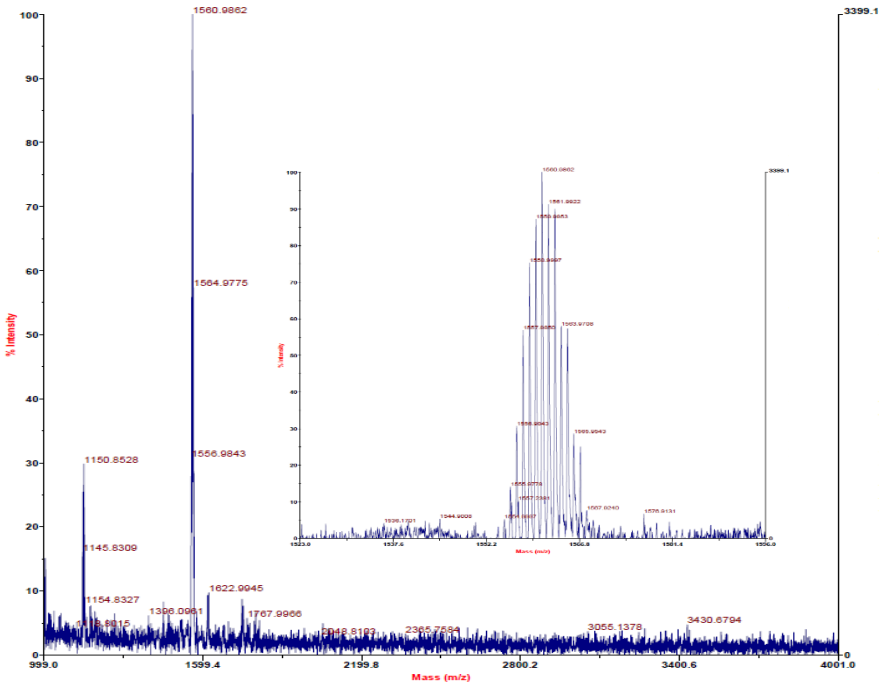

Figure 10.4: **IrGdL2-dimer** MALDI (TOF).

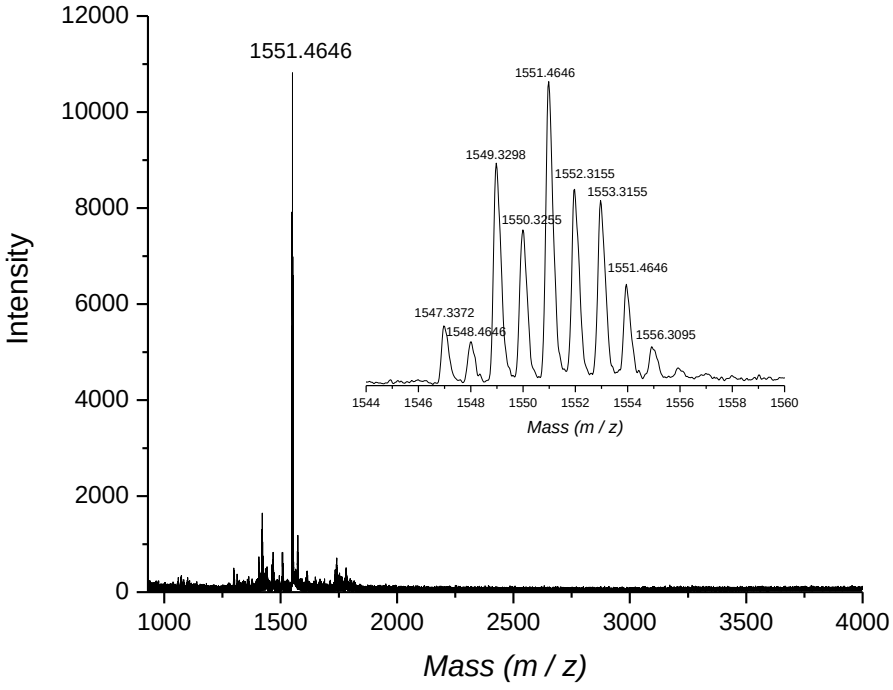

Figure 10.5: **IrEuL2-dimer** MALDI (TOF).

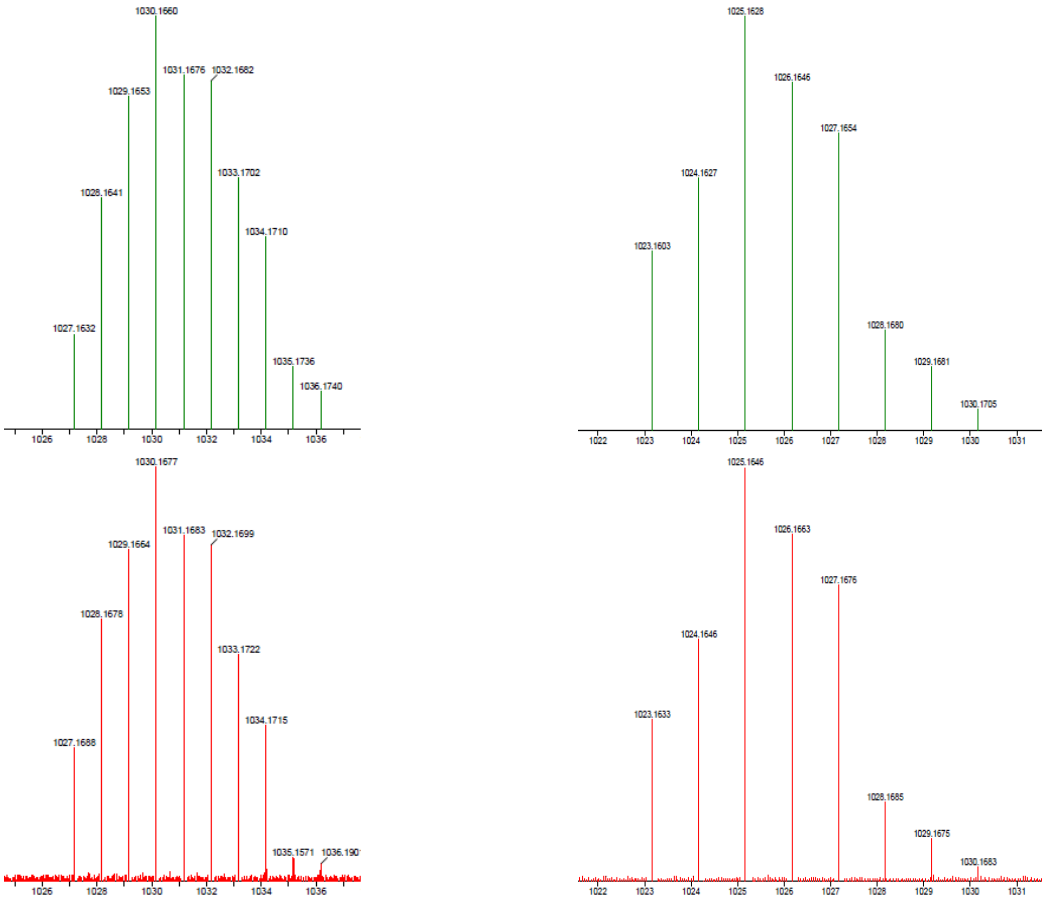

Figure 10.8: HRMS (ESI) for **PtGdL10**(left) and **PtEuL10** (right), observed (bottom) calculated (top).

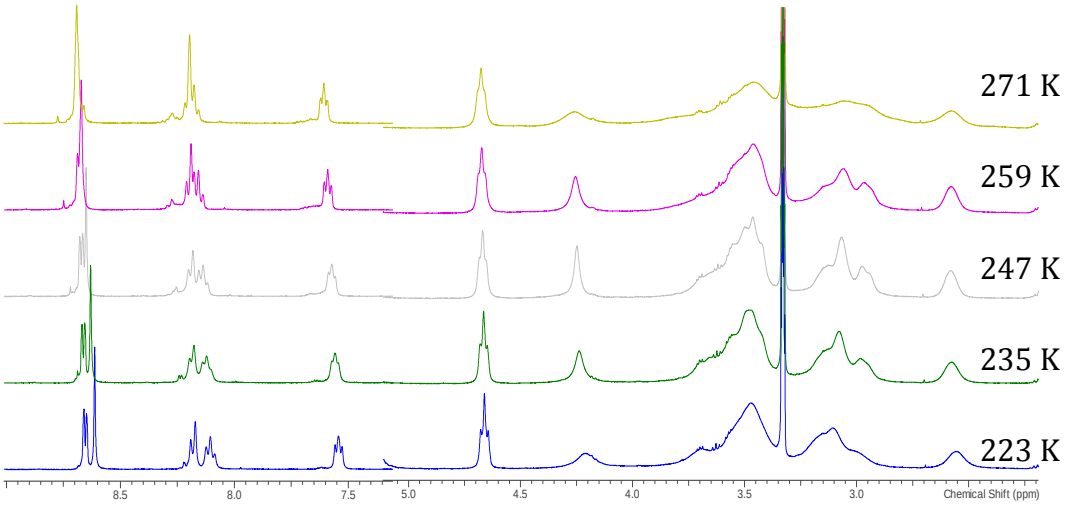

Figure 10.9: ^{1}H NMR spectrum of **H3L1** in CD_3OD. The signals resolve with decreasing temperature.

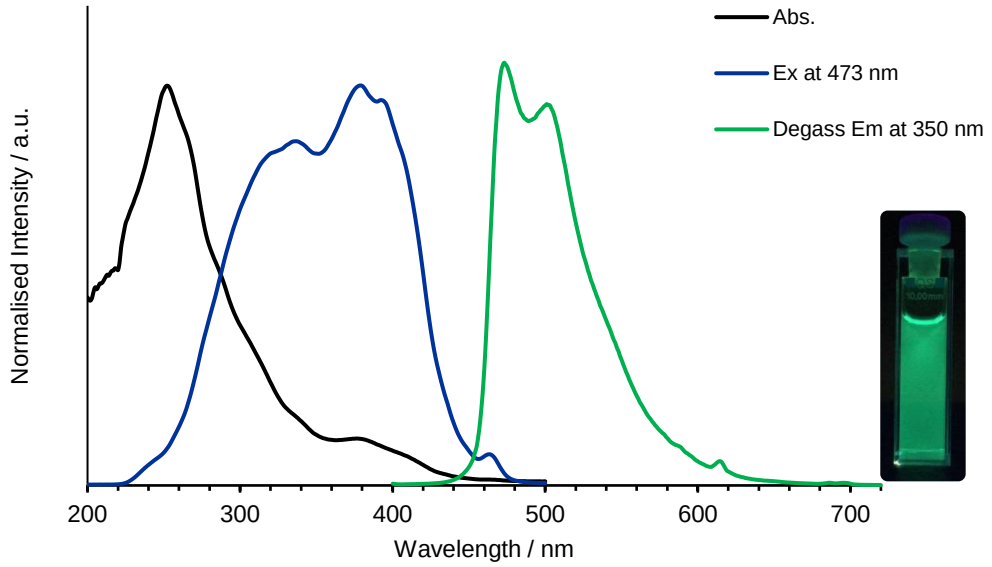

Figure 10.10: **IrEuL6L1** Absorption (black), excitation (blue) and emission (green) spectra 0.1 mM in aerated 50 mM HEPES, pH 7.4. Inset; 0.1 mM solution of **IrEuL6L1** viewed under UV light (365 nm).

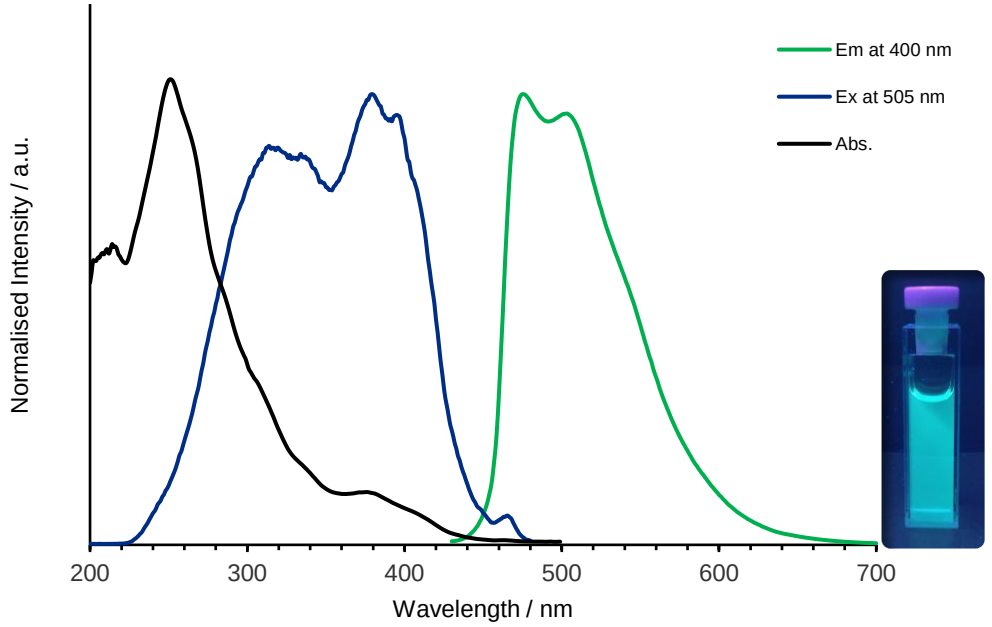

Figure 10.6: Normalised absorption (black), excitation (blue) and emission (green) spectra for **Ir(ppy)$_2$GdL1** 0.1 mM in aerated 50 mM HEPES, pH 7.4. Inset; 0.1 mM solution of **Ir(ppy)$_2$GdL1** viewed under UV light (365 nm).

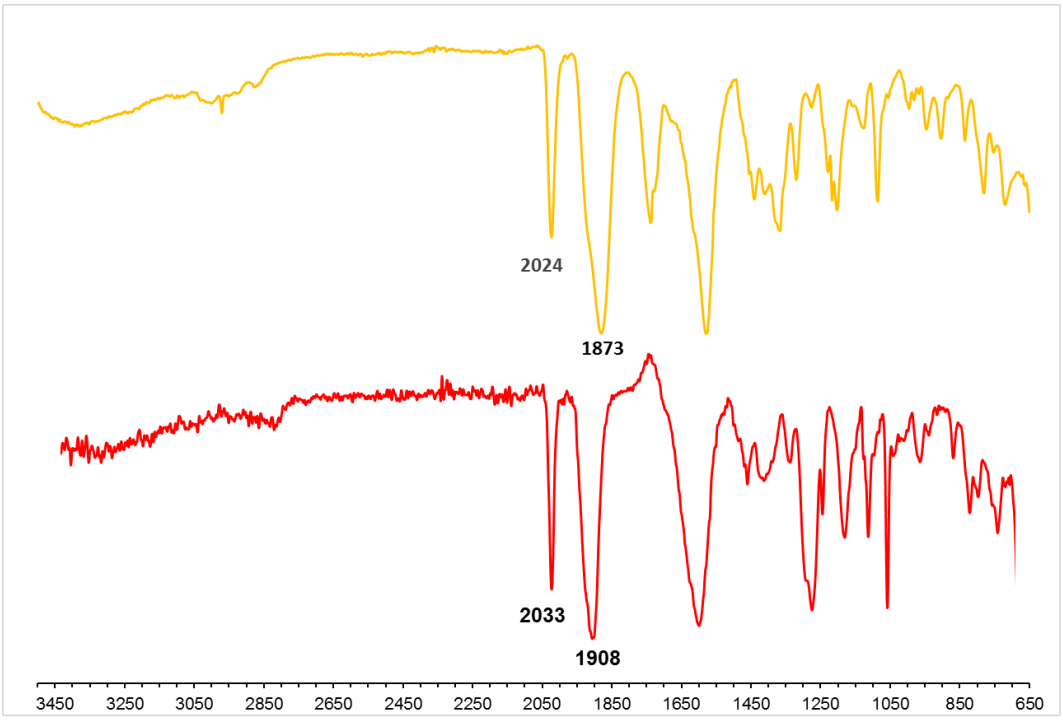

Figure 10.7: FT-IR spectra of **RepyEuL1** (—) and **ReClEuL1** (—).

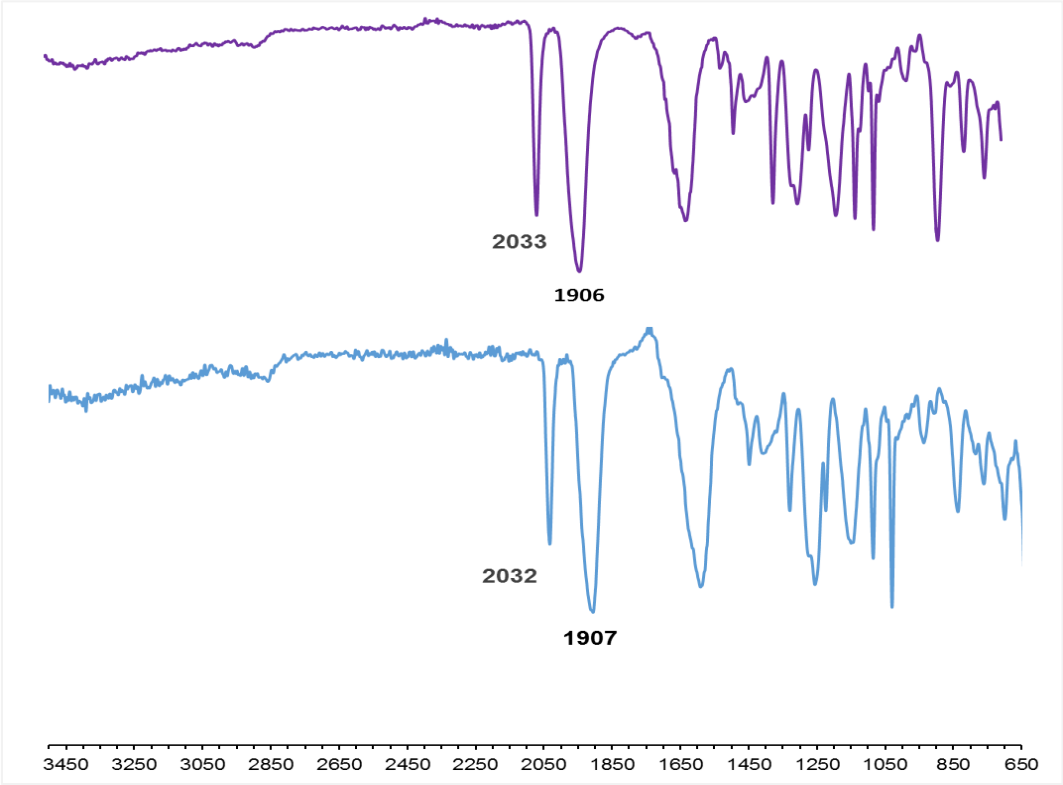

Figure 10.8: FT-IR spectra of **RepyEuL3** (—) and **RepyEuL4** (—).

10.5 X-ray Crystallography Data

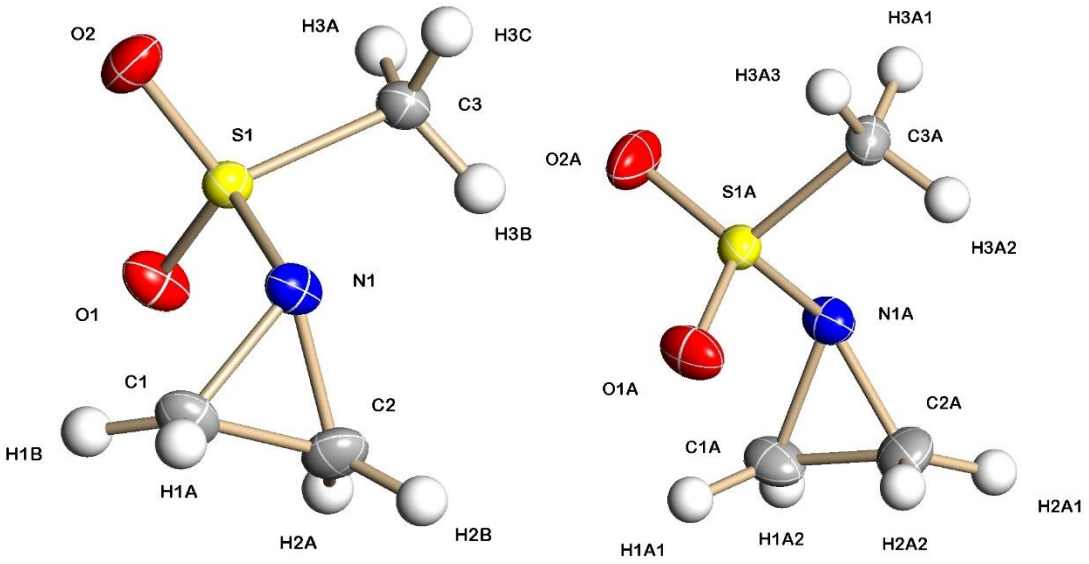

50% displacement ellipsoids. R1 = 0.0409, wR2 = 0.1020.

Figure 10.9: X-Ray crystal structure of Azrdine **4** .

Table 1. Crystal data and structure refinement for 17094.

Identification code	17094	
Empirical formula	C_3 H_7 N O_2 S	
Formula weight	121.16	
Temperature	150(2) K	
Wavelength	0.71073 Å	
Crystal system	Triclinic	
Space group	P-1	
Unit cell dimensions	a = 6.8863(13) Å	δ= 81.179(3)°.
	b = 8.2200(16) Å	β= 83.021(3)°.
	c = 9.5925(19) Å	γ = 89.977(3)°.
Volume	532.50(18) $Å^3$	
Z	4	
Density (calculated)	1.511 Mg/m^3	
Absorption coefficient	0.492 mm^{-1}	
F(000)	256	
Crystal size	0.21 x 0.20 x 0.11 mm^3	

Theta range for data collection 2.16 to 25.99°.

Index ranges -8<=h<=8, -10<=k<=10, -11<=l<=11

Reflections collected 4171

Independent reflections 2077 [R(int) = 0.0339]

Completeness to theta = 25.99° 99.2 %

Absorption correction Empirical

Max. and min. transmission 0.831 and 0.478

Refinement method Full-matrix least-squares on F^2

Data / restraints / parameters 2077 / 0 / 129

Goodness-of-fit on F^2 0.976

Final R indices [I>2sigma(I)] R1 = 0.0409, wR2 = 0.1020

R indices (all data) R1 = 0.0482, wR2 = 0.1051

Largest diff. peak and hole 0.369 and -0.422 e.$Å^{-3}$

Table 1. Atomic coordinates (x 10^4) and equivalent isotropic displacement parameters ($Å^2$x 10^3) for 17094. U(eq) is defined as one third of the trace of the orthogonalized U tensor.

x	y	z	U(eq)	
S(1)	312(1)	4089(1)	8112(1)	18(1)
O(1)	1624(2)	5116(2)	8664(2)	28(1)
O(2)	-1559(2)	4746(2)	7847(2)	29(1)
N(1)	1309(3)	3528(2)	6600(2)	22(1)
C(1)	2470(3)	4849(3)	5617(2)	26(1)
C(2)	3480(3)	3491(3)	6374(3)	27(1)
C(3)	-9(3)	2195(3)	9229(2)	22(1)
S(1A)	5076(1)	8736(1)	7830(1)	20(1)
O(1A)	4854(3)	7940(2)	6628(2)	32(1)
O(2A)	3621(3)	9895(2)	8177(2)	36(1)
N(1A)	7217(3)	9726(2)	7633(2)	24(1)
C(1A)	7899(4)	10520(3)	6155(3)	30(1)
C(2A)	8839(4)	9028(3)	6761(3)	32(1)
C(3A)	5295(3)	7270(3)	9318(2)	23(1)

10.6 Analytical HPLC spectra

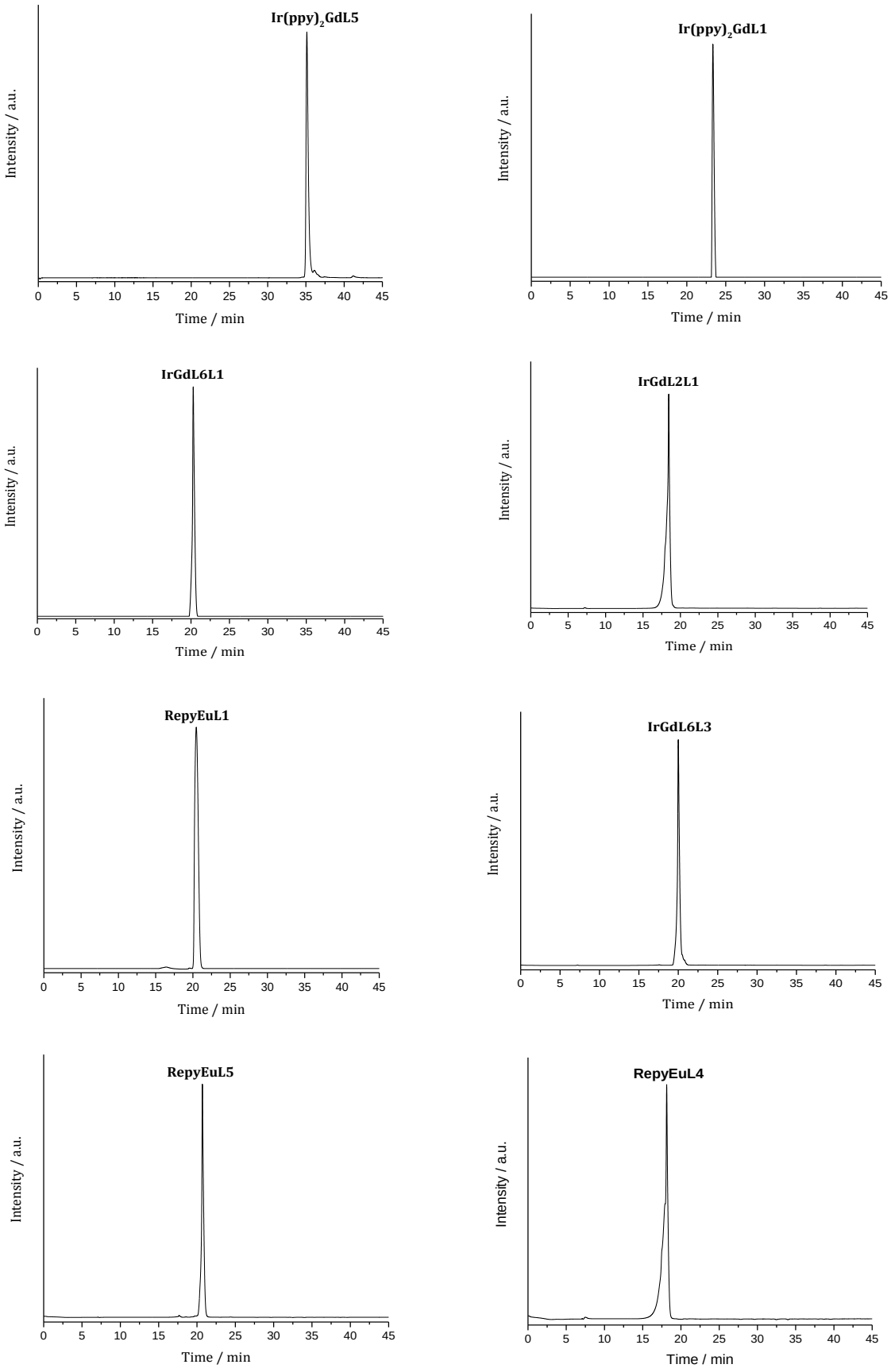

Figure 10.10: **HPLC traces of Ir(III) and Re(I) conjugates**. Solvent A = H_2O, Solvent B = MeCN. 10% B for 5 min, 10-100% B over 30 min, 100% B for 5 min, 100-10% B for 2 min, 10% B for 30 min. Monitor 280 nm.